FACULTY OF ENGINEERING
AND ARCHITECTURE

Thermodynamic Investigation of Converter Slag Characteristics with Industrial Validation

Lotte De Vos

Doctoral dissertation submitted to obtain the academic degree of
Doctor of Materials Engineering

Supervisors

Prof. Kim Verbeken, PhD - Prof. Inge Bellemans, PhD

Department of Materials, Textiles and Chemical Engineering
Faculty of Engineering and Architecture, Ghent University

November 2021

GHENT
UNIVERSITY

FACULTY OF ENGINEERING AND ARCHITECTURE

Thermodynamic Investigation of Converter Slag Characteristics with Industrial Validation

Lotte De Vos

Doctoral dissertation submitted to obtain the academic degree of
Doctor of Materials Engineering

Supervisors
Prof. Kim Verbeken, PhD - Prof. Inge Bellemans, PhD

Department of Materials, Textiles and Chemical Engineering
Faculty of Engineering and Architecture, Ghent University

November 2021

GHENT UNIVERSITY

ISBN 978-94-6355-544-9
NUR 971
Wettelijk depot: D/2021/10.500/92

Members of the Examination Board

Chair

Prof. Hennie De Schepper, PhD, Ghent University

Other members entitled to vote

Soroosh Naghdy, PhD, ArcelorMittal Belgium
Prof. Roumen Petrov, PhD, Ghent University
Prof. Maarten Sabbe, PhD, Ghent University
Johan Zietsman, PhD, Ex Mente Technologies, South Africa

Supervisors

Prof. Kim Verbeken, PhD, Ghent University
Prof. Inge Bellemans, PhD, Ghent University

Dankwoord

Hoe zijn we hier in godsnaam geraakt? Velen die me kennen, stellen zich waarschijnlijk dezelfde vraag. Ik zal hier pogen, en falen, om daar op te antwoorden. Desondanks, is dit ongetwijfeld het meest gelezen gedeelte van dit doctoraat. Ik kan de lezer geen ongelijk geven, hier staat ongetwijfeld het interessantste neergepend van heel dit werk. Want het betekent allemaal niets zonder de mensen die je onderweg tegenkomt.

Zoals het hoort vang ik aan met het bedanken van mijn promotor, Kim, om dit project op poten te zetten en aan mij te denken bij de zoektocht naar een geschikte kandidaat. Vervolgens wil ik graag Inge bedanken voor de dagdagelijkse opvolging. We waren het lang niet altijd eens, maar al van bij de aanvang van mijn doctoraat konden we wel goed samen aan de slag. Bedankt Carina, mijn industriële promotor, voor de vele interessante discussies over mijn doctoraat, de productie van staal en het gewone leven. Geen enkele vraag was een vraag te veel en er was altijd tijd voor ruime toelichting en uitleg. Ik had me geen betere begeleider kunnen wensen.

Gebouw 903, want dat zal het voor mij altijd blijven, eerste verdiep. Dé plek waar ik het grootse deel van mijn doctoraat sleet. Ik wil graag al mijn collega's bedanken, zowel de mensen van de SMS en MMS groep als ook het handjevol collega's dat zijn intrek nam in de gang beneden, voor de fijne werksfeer en de bedrijvigheid die er steeds aanwezig was. En eigenlijk ook wel voor de occasionele portie drama, die nooit veraf was. Line, bedankt voor de open deur en de permanente gelegenheid voor een babbel. Samen met Ives vorm je toch de motor van de hele gang. Aurélie, Linsey, Emilie en Elien dikke merci om zo fantastisch inspirerende topwijven te zijn. Dankzij jullie had ik al vlug door dat je vooral jezelf moet zijn en dat de rest van daar wel weer goed komt. Tom bedankt voor alle café gesprekken op het werk. Tante Liese, met jou op den bureau was het altijd fijn en bovendien slaagden we er in om ook de decoratie op onze persoonlijke voorkeuren af te stemmen. Uiteraard kwam Liesbet er later nog bij om van K3 echte birds of prey te maken! LDV wil SV bedanken voor de vele interessante en diepzinnige gesprekken en de nodige toogfilosofie. Joanna, dearest darling, ich bin immer ganz geil verknallt in dich! Lisa bedankt om ons baken van rust te zijn in een frequent losgeslagen kippenhok. Arne bedankt om altijd je kritische vragen de vrije loop te laten. En dan ja, Keppie en Dikken, ik heb lang getwijfeld of ik jullie bij mijn collega's zou bedanken of toch bij mijn maten, maar omdat onze prachtige driehoeksverhouding zijn oorsprong vond op de werkvloer,

leek het mij gepaster om jullie hier te bedanken voor meer dan ik kan opsommen. Niet alleen waren jullie mijn steun en toeverlaten als het over werk en onderzoek ging - Dikken als de zetel in uw bureau kon vertellen hoe vaak ik daar zat omdat ik weer eens vastgelopen was in mijn onderzoek en het zelf niet meer wist. Keppie als ze onze Teams calls aan elkaar zouden plakken omdat ik aan de lijn hing met dezelfde reden. - maar bovenal werden jullie maten waarmee ik samen kon tafelen, zeveren, zuipen (of dat deden jullie dan vooral), zonnen, dansen, koffie slurpen en zo kan ik nog wel een tijdje doorgaan. Bedankt voor dat alles!

Een doctoraat doen in samenwerking met industrie zorgt er niet alleen voor dat je van twee werelden kan leren, het zorgt er ook voor dat je het geluk hebt twee groepen heel aangename collega's te hebben. De dagen die ik niet spendeerde in Zwijnaarde of al thuiswerkend, was ik te vinden in de gebouwen van de Staalfabriek. Ik wil ook daar graag iedereen bedanken voor de openheid waarmee ik steeds ontvangen werd, de aangename gesprekken aan het koffiemachine, de passie waarmee velen me uitleg gaven en natuurlijk ook voor de vele interessante momenten en gesprekken in de fabriek zelf, waar er steeds heel veel technisch te leren viel en soms ook lessen in 'Wafelijzerpolitiek'. Bedankt Koen om me steeds te verwittigen als er snoep te rapen viel op de koelkast. Ook bedankt aan Joris, Stefan, Soroosh en Karsten die in de loop van de vier jaar elk hun eigen bijdrage hadden aan dit doctoraat. Ivonne, bedankt voor de vele uitstappen naar koude en warme convertoren. Bedankt Roos en Kathleen die me van tijd tot tijd ook mee op sleeptouw namen naar de fabriek.

En zo komen we aan bij de groep mensen die ongetwijfeld de grootste rol spelen in het afronden van dit doctoraat. Bijgevolg zijn het zij, die het meeste lof verdienen omdat we hier vandaag geraakt zijn: mijn geweldige vrienden. Ik wil mijn boys, mijn burgies, mijn matjes, mijn seabirds bedanken omdat ze van mij houden. Dat klinkt triviaal en toch is het dat alles behalve. Zonder hun liefde, steun en geborgenheid, was ik hier vandaag niet geweest. Ik zou boeken kunnen vullen met onze avonturen en mogelijks doe ik dat ooit wel eens, maar misschien is dit niet het geschikte moment dus moet ik het wat kort houden. Namasté bitches, Veerle en Elien! Jana, Bob en Nils bedankt voor de vele mooie herinneringen die ik koester aan het Gesticht. Natuurlijk geldt dat ook voor jou Margot, mijn communicerend vat, al blijf jij voor mij toch altijd het meisje dat wondermooi lippenstiftboodschappen achterliet op de badkamer spiegel. Voor het vele vieren, vijven en zessen om dan terug te vieren moet je bij Seba, Bob, Inti, Simon, Kim, Ruubje en Vincent zijn. Toon, jou wil ik naast het voorgaande ook heel graag bedanken voor onze

vele gewielde avonturen in het voorjaar van 2020 en natuurlijk ook omdat ik dankzij jou ontdekte hoe mega-awesome-geweldig-superzalig-MAF rotsklimmen is. Team Gear Nerd represent en af toe een goed gilletje. Voor de menige uitgebreide maaltijden, de warme knuffels, voor alle keren dat ik jullie mocht voeden en voor de vele keren dat ik mijn benen onder jullie tafel mocht schuiven, voor de koffies, het samen lachen, het samen huilen, het "zegt dat ge een zwientje zijt", het beste Team C, de keren dat we ons koning keizer admiraal van de nachtelijke straten waanden, voor de menige keren dat we de nacht versloegen, voor de oneindige uren aan dansen en nog zo veel meer wil ik graag, in willekeurige volgorde Tira en de Matjes bedanken: Stef, Brecht, Fabrice, Jeroen, Astrid, Aboud, Florian, Ber Ber, Kenny, Natan, SAP!!!!, Jelle en Lieselot bedankt. Op donderdagavond deed ik aan yoga voor lichaam en geest samen met de beste psycholoog van heel Gent en omstreken, Angelos en natuurlijk met de man die de soundtrack bij mijn leven voorziet, Matthijs. "*This world isn't big enough to keep me away from you.*" Boys thanks! Gelukkig hebben jullie mij volledig door. In dat rijtje hoor jij, Simon, natuurlijk ook helemaal thuis. Bedankt om mij steeds uit te dagen, niet te laten vastroesten en op tijd tegen te spreken en steeds op jouw eigen manier zorg voor me te dragen en te koesteren. Robin, een vriendschap met een leeftijd van bijna 20 jaar kan wel tellen, elke brief of postkaart is opnieuw een klein pakketje vreugde. This is how, together, we became geniuses. En dan ontbreken er nog twee, Lieverd en Lieverd, bij het grote publiek ook wel gekend als Yentl en Truc. Het is mogelijks raar dat diegene die het meest bedanking verdienen het minst woorden krijgen. Ik slaag er echter niet in om op papier te zetten hoeveel jullie voor mij betekenen. Soms schiet de taal te kort en dit is zo een voorbeeld. Jullie zijn mijn steun, de armen waar ik steeds naar terugkeer, de wind onder mijn vleugels, de spiegels die me tonen wat ik zelf niet kan zien, de warmte waar ik me in kan nestelen, de rust die mijn onrust nodig heeft.

Om af te ronden Heer Vetje en mijn teerbeminde Spruitje zonder jullie ben ik uiteraard helemaal radeloos en verloren. Al is het natuurlijk duidelijk dat ik de leiding heb ook al ben ik een slechtlopende klok. Deze zinnen zijn "SO FLUFFY I AM gonna die". Tijd om te veranderen van veranda. Chris en Hilde, jullie lieten me veel te vroeg los, maar toch is het vooral mooi om te zien hoe jullie verenigd zijn in ouderliefde en trots. Bedankt voor de vele steun de afgelopen jaren. En zonder enige twijfel hoort de laatste bedanking naar de Kleine Generaal te gaan die me bijbracht dat je "uw gat in uw arms moet nemen" en iets van je leven moet maken.

Lotte (Ericcc, Lottie, Lotteke of Lotje) - Moinho do Comandante, Juni 2021

Summary

Today's worldwide crude steel production reaches up to 1878 million tonnes per year[1]. About 70% of steel is produced via a basic oxygen furnace (BOF) process. During this process, steel is produced alongside a gas and slag. Amongst steelmakers general agreement exists on the importance of this formed slag. Firstly, the slag will play an important role in the refining of the metal bath. Apart from carbon all the other impurities present in the hot metal, such as silicon, phosphorus and manganese, are removed from the metal bath as oxides and thus are part of the slag. Temperature and composition of the slag will affect the equilibrium between the steel and slag bath and hence, the refining. Secondly, the slag will interact with the refractory material of the vessels' lining. This interaction can either be beneficial or damaging and consequently the slag affects the lining's lifespan. A third, and final, important property of the slag is its ability to foam. Foaming is a phenomenon that occurs when gas bubbles are retained in the slag. A foamy slag is on one hand desired due to its beneficial effects on refining and its potential to act as a physical barrier for metal losses via the off-gas stream. However, vigorous foaming is undesired due to the high safety risk and accompanying economic losses. Even though there is agreement on the importance of the slag, a full understanding of the exact mechanisms and the precise effect of the slag's composition or temperature is hitherto lacking. One possible way to gain these fundamental insights would be via experiments. However, the BOF process is very complex and furthermore, the harsh process conditions (high process temperature, large production, CO gas formation, etc.) make representive experiments or industrial sampling very difficult. As a possible alternative, thermodynamic based modelling is proposed in this work. Because this work is a collaboration between Ghent University on one hand and ArcelorMittal Ghent (AMG), one of the worlds leading steel and mining companies, on the other hand, the developed models could be validated with a large amount of available industrial data from AMG.

The first two parts of the work, 'I. Introduction' and 'II. Slag Properties and Behaviour', contain chapters with a general introduction for the process and the role of the slag in the process. Next, a chapter is devoted to the important factors, such as oxygen partial pressure or the used solution models, for thermodynamic modelling. The different

[1] For 2020, data from "http://www.worldsteel.org/media-centre/press-releases/2021/world-steel-in-figures-2021.html"

factors and their effects are demonstrated via consideration of the liquid fraction of the slag. Even though thermodynamically a slag is always a liquid phase, in steelmaking the term is used to describe the complete system of oxides: the liquid oxide solution and the solid solutions. Hence, an industrial slag will have a liquid fraction that is often smaller than 100%. With this knowledge, the possibility to use thermodynamics to describe the industrial slag is explored. For the BOF process, the basis ternary slag consists out of CaO, SiO_2 and FeO_n and different isothermal sections of the basis phase diagram are calculated. The effect of additions of MgO, Al_2O_3 and MnO to the slag system on these basis phase diagrams is discussed and compared to the industrial observations. Already, some interesting similarities are observed between the thermodynamic calculated isothermal sections of the phase diagram and the industrial observations. However, for a more full and thorough understanding of the effects it is clear more complex models are required. Finally, this 'I. Introduction' part of this dissertation, the different models to calculate physical slag properties: viscosity, density and surface tension, are described. These properties have been mentioned in literature to be important to describe the slag foaming behaviour and will influence the overall process to a large extent.

The third part of the work, 'III. Foaming', focusses on the foaming behaviour of the slag. Firstly, a model is developed to describe the slag composition during the process. Even though, in industry different types of foaming are observed, focus is put in this work on the foaming occurring around 30% till 40% oxygen blown into the process. A slag evolution during the process is thus required to verify whether the industrial observations concerning foaming can be linked uniquely to the slag composition. If this would be possible, the foaming could be better predicted and hence better controlled via slag engineering or adaption of the oxygen blowing velocity or lance height. The model to describe the slag evolution for this research on foaming does not have a predictive nature and only actual already produced heats are investigated with it. A combination of mass balances, information of the process' input, industrial measurements during the process, the process' output and thermodynamics is used to describe the slag composition during the process. With these compositions the physical properties are calculated. These physical properties are subsequently used to determine the foaming indices of the slag during the process. A foaming index is a theoretically introduced concept to link physical slag properties to foaming behaviour. However, when these calculated foaming indices are compared to the industrially observed foaming behaviour it is impossible to obtain a unique relation between the two. Hence, it is concluded that the industrial foaming cannot be linked uniquely with the slag physical

properties or accompanying composition. It should be mentioned that there is of course a large discrepancy between the original lab scale experiments to define the concept of the foaming index and the real industrial environment. Furthermore, the viscosity is found to be the most important property to use when describing foaming theoretically.

The fourth part of the work, 'IV. Thermodynamic BOF model', explores the further possibilities to develop a predictive model for the BOF process allowing to vary the input for the process out of the familiar working areas. Firstly, a thorough review is given on different state-of-the-art physicochemical BOF models. Next, the model constructed to describe the process in the current work is discussed, called the TD BOF model. An effective equilibrium reaction zone (EERZ) type model is used. Apart from a thermodynamic scrap melting reaction zone, three different reaction zones are incorporated:

- The jet impact zone
- The interface between slag and metal
- The slag-metal-gas emulsion

Apart from a general homogenisation of the metal and slag, also a second thermal homogenisation is incorporated to integrate the heat transport between the phases with different temperatures. To determine the sizes of the reaction volumes, which is a crucial step in the EERZ model, empirical and theoretical formulae from literature are used. However, preliminary results with the model showed that these reaction volumes sizes were not suited to describe the process sufficiently accurate for the purpose of this work. Due to the large amount of available industrial data for the process, it was decided to introduce a correction factor for each reaction volume size to compensate for the deviations, called a set of parameters. These correction factors are determined via a fitting between the model simulation and the measured data for a set of industrially produced heats. For the fitting two types of deviation between the simulations and the industrial measurements are defined: one describing the overall deviation and one focussing on the deviation at the early stages of the process. Two completely different sets of parameters are obtained which both yield a different solution. Depending upon the research question a different set is used. To show the potential of the model a case study on the effect of MgO to the slag is used. The thermodynamic simulations, mostly show similar trends as industrially observed. A final chapter in this part is devoted to possible further versions of the TD BOF model.

The final part of this work ‘V. Conclusion and future work’ contains the final conclusion of the work and an onset to future possibilities within the research field of the slag in the BOF process.

Samenvatting

Wereldwijd wordt er momenteel 1878 miljoen ton staal per jaar geproduceerd. Ongeveer 70% hiervan wordt geproduceerd via het 'basic oxygen furnace' (BOF) proces, ook wel het converter proces genoemd. Tijdens dit proces worden er naast staal ook een gas en slakfase geproduceerd. Er is een algemene consensus dat deze slakfase een belangrijke rol speelt in het proces. Ten eerste, zal de slakfase de raffinage van de staalfase grotendeels beïnvloeden. Behalve koolstof, dat verdwijnt via de gasfase, worden alle aanwezige onzuiverheden (e.g silicium, fosfor en mangaan) uit het vloeibare ruwijzer verwijdert als oxides die deel uitmaken van de slakfase. Het evenwicht tussen de staal - en slakfase zal grotendeels beïnvloed worden door de slak samenstelling en de temperatuur. Ten tweede zal deze slakfase interageren met het vuurvast materiaal waaruit de convertorwand is opgebouwd. Deze interactie kan zowel een negatieve als positieve impact hebben op de levensduur van de wand. Een derde, en finale, belangrijke eigenschap van de slakfase is de mogelijkheid tot schuimvorming. Schuimvorming is een verschijnsel dat voorkomt indien gasbellen blijven hangen in de slak. Een matige schuimvorming is veelal gewenst in het proces omdat het goed is voor de raffinage en een fysieke barrière vormt voor deeltjes metaal die meegesleurd kunnen worden met de gasstromen naar de afzuiginginstallaties. Anderzijds is ongecontroleerde schuimvorming ongewenst omwille van de grote veiligheidsrisico's en de economische kost die het met zich meebrengt. Ondanks de algemene consensus dat de slakfase belangrijk is voor het proces, is het tot op de dag van vandaag niet helemaal duidelijk welke mechanismen hier een rol en spelen en hoe de slaksamenstelling en de werkingstemperatuur deze verschillende aspecten beïnvloeden. Een mogelijke manier om meer fundamentele inzichten te krijgen in het proces zouden experimenten kunnen zijn. Echter, het BOF-proces is zeer complex en bovendien zorgen de extreme condities (hoge temperatuur, grote volumes, CO-vorming, etc.) ervoor dat experimenten praktisch zeer moeilijk zijn. Als alternatief wordt in dit doctoraat voorgesteld om met modellen die thermodynamisch gebaseerd zijn, te werken. Dit werk is een samenwerking tussen enerzijds de Universiteit Gent en anderzijds ArcelorMittal Gent (AMG), één van 's werelds grootste staal- en mijnbouw-bedrijven, en daarom kunnen de ontwikkelde modellen afgetoetste worden aan een grote hoeveelheid industriële data.

De eerste twee luiken van dit werk, 'I. Introduction' en 'II. Slag Properties and Behaviour', bevatten een algemene inleiding voor het proces en de rol die slak in het proces speelt.

Vervolgens, is er een hoofdstuk gewijd aan verschillende factoren, zoals de partieeldruk zuurstof en gebruikte oplossingsmodellen, die de thermodynamische berekeningen zullen beïnvloeden. Het effect van deze verschillende factoren wordt aangetoond via de zogenaamde vloeibare fractie. Strikt thermodynamisch gezien is een slakfase steeds vloeibaar, industrieel gebruikt men deze term echter om alle oxides te benoemen: zowel de vloeibare fase als de aanwezig vaste oplossingen. Hierdoor heeft een industriële slak een vloeibare fractie die meestal kleiner is dan 100%. Met deze informatie in het achterhoofd worden enkele verkennende berekeningen uitgevoerd om het potentieel van thermodynamische berekeningen om de industriële slak te beschrijven. Voor het convertor proces is het basis slak systeem: CaO, SiO_2 en FeO_n. Voor dit systeem worden verschillende isotherme secties van het fasediagram berekend. Het effect van MgO, Al_2O_3 en MnO op deze diagrammen wordt besproken en vergeleken met industriële observaties. Met deze verkennende berekeningen werden al enkele interessante parallelellen geobserveerd. Het is echter ook zeer duidelijk dat om fundamentele inzichten te verwerven, veel complexere procesmodellen nodig zijn. In dit deel van het werk worden ook de verschillende modellen om fysische slakeigenschappen te berekenen besproken. Viscositeit, dichtheid en oppervlaktespanning worden genoemd als belangrijke eigenschappen om het schuimvormende karakter van de slak te bespreken, maar ze zullen ook een grote invloed hebben op het algemene proces.

Het derde luik van dit werk, 'III. Foaming', focust op de schuimvorming van de slak. Om een link te kunnen maken tussen metingen van de schuimbaarheid van een slak tijdens het proces en de slaksamenstelling is een model nodig dat in staat is om de slaksamenstelling tijdens het proces te beschrijven. Indien het schuimgedrag van de slak uniek gelinkt kan worden aan de slaksamenstelling, of bijhorende fysische eigenschappen, zou schuimvorming veel voorspelbaarder worden en kan er industrieel op geanticipeerd worden door de slaksamenstelling of blaasomstandigheden aan te passen. Het huidige model om de slaksamenstelling tijdens het proces te berekenen, heeft niet als doel voorspellend te werken en wordt enkel gebruikt voor reeds geproduceerde ladingen. Voor dit model wordt een combinatie aan input en output data, metingen van tijdens het proces, massabalansen en thermodynamische berekeningen gebruikt. Van de berekende slak samenstellingen tijdens het proces worden de fysische eigenschappen berekend om op die manier voor elke slaksamenstelling de 'foaming index' te bepalen. Deze 'foaming index' is een theoretisch concept dat gebruikt wordt om fysische slakeigenschappen aan schuimgedrag te linken. Uit het huidige onderzoek blijkt het onmogelijk te zijn om een unieke link te leggen tussen de slaksamenstelling en

de werkelijke schuimvorming. Het is evenwel belangrijk op te merken dat de labo omstandigheden waaronder de 'foaming index' concepten ontwikkeld werden, fundamenteel verschillen van de werkelijke industriële proces omstandigheden. Verder kon besloten worden dat viscositeit de belangrijkste eigenschap is om schuimvorming theoretisch te beschrijven.

In een vierde luik, 'IV. Thermodynamic BOF model', worden de mogelijkheden om een voorspellend model voor het convertor proces op te stellen, verder verkend. Op deze manier zouden ook ongekende werkingsgebieden bestudeerd kunnen worden. Dit luik start dan ook met een overzicht van de huidige state-of-the-art methodes om dit soort modellen te construeren. Vervolgens wordt het model, opgesteld in het huidige werk, grondig beschreven. Dit model wordt TD BOF genoemd. Een 'effective equilibirum reaction zone' model type is hiervoor gebruikt. Naast een reactiezone waar schroot thermodynamisch insmelt worden nog drie andere reactiezones gedefinieerd:

- De impact van de zuurstofstraal op het metaalbad
- Het contactoppervlak tussen staal en slak bad
- De staal – slak – gas emulsie fase

Daarnaast worden ook een algemene homogenisatie van zowel staal als slakfase beschouwd, alsook een warmtetransport gevolgd door een thermische homogenisatie van de aanwezige fasen. Om de grootte van de reactievolumes die cruciaal zijn voor het EERZ-model, te bepalen, worden theoretische en empirische formules uit literatuur gebruikt. De eerste resultaten van het model tonen echter aan dat deze reactievolumes niet geschikt zijn om het proces correct te beschrijven. Door de grote hoeveelheid aan industriële data van het proces dat voorhanden is, werd besloten om dit op te lossen door voor elk reactievolume een correctiefactor voor zijn grootte te introduceren. Deze correctiefactoren, samen een parameterset genoemd, worden bepaald door een fitting tussen de model simulaties en de gemeten dat voor werkelijk geproduceerde ladingen. Voor deze fitting worden twee types afwijkingen tussen de simulaties en de werkelijkheid vooropgesteld: één afwijking die de algemene verschillen tussen beide beschrijft en één afwijking die focust op de verschillen in het begin van het proces. Twee totaal verschillende parametersets met sterk verschillende oplossingen worden gevonden. Afhankelijk van de specifieke onderzoeksvraag wordt de ene dan wel de andere gebruikt. Om het potentieel van het model te tonen, wordt een casus over het effect van MgO in de slak op het proces, gebruikt. De thermodynamisch simulaties tonen meestal de

verwachte trends van industrie. Het finale hoofdstuk van dit luik behandelt de mogelijke verdere versies van het model.

In het laatste luik van dit werk ‘V. Conclusion and future work’, wordt een algemene conclusie geformuleerd en worden enkele ideeën voor vervolgwerk opgesomd.

Table of content

Dankwoord i

Summary v

Samenvatting ix

Table of content xiii

I. Introduction 1

1 General introduction 2

1.1 Research context 2

1.2 Research objectives 3

1.3 Structure of the work 5

2 BOF process and slag 6

2.1 On steelmaking 6

2.2 The BOF Process 8

2.2.1 Refining 8

2.2.2 The BOF vessel 12

2.3 On the role of slag 13

2.3.1 Refining 14

2.3.2 Interaction with refractory 15

2.3.3 Foaming 16

2.4 Conclusion 17

2.5 References 17

II. Slag Properties and Behaviour 21

3 Liquid fraction of the BOF slag 22

3.1 General information about BOF slags 22

3.2 The effect of different modelling settings 24

3.2.1 The effect of the considered slag system 24

3.2.2 The effect of the thermodynamic model 25

3.3 The effect of temperature and oxygen partial pressure 27
3.3.1 On the effect of P_{O2} 28
3.3.2 On the effect of temperature 30
3.4 Conclusion 32
3.5 References 32
4 Linking industrial observations with calculated phase diagrams 36
4.1 General aspects of the BOF slags 36
4.1.1 The importance of saturation 38
4.1.2 The importance of C_2S stability 39
4.2 The effect of different components 40
4.2.1 Effect of MgO 41
4.2.2 Effect of Al_2O_3 44
4.2.3 Effect of MnO 47
4.3 Conclusion 51
4.4 References 51
5 Models for physical slag properties 55
5.1 On structure of slags 55
5.2 On viscosity of slags 58
5.2.1 The modified quasi-chemical viscosity model 60
5.2.2 The viscosity of heterogeneous slags 65
5.3 On density of slags 68
5.4 On surface tension of slags 70
5.5 References 72
6 Intermediate conclusion 79
III. Foaming 81
7 Model to calculate slag compositions during blow of historical heats 82
7.1 General model description 82
7.1.1 Used input data 82

7.1.2 Used output data 84
7.1.3 Implication of the used data on heat selection 86
7.1.4 Calculation of the slag composition 86
7.2 Slag Model Validation 89
7.2.1 Validation via end compostition 89
7.2.2 Validation during the blow 92
7.3 Conclusion 93
7.4 References 93
8 Critical Assessment of the applicability of the foaming index to the industrial BOF process 95
8.1 Introduction 95
8.2 Methodology 100
8.3 Results and discussion 102
8.3.1 Effect of properties on foaming index 102
8.3.2 Relation foaming index and industrial end of blow data 104
8.3.3 Relation foaming index and composition during blow 105
8.3.4 Final discussion 109
8.4 Conclusion 110
8.5 References 111
IV. Thermodynamic BOF Model 95
9 Physicochemical models for the BOF process 116
9.1 Reaction zone models 116
9.1.1 Jet impact zone 116
9.1.2 Metal droplets in the metal-slag emulsion 117
9.2 State-of-the-art of thermodynamic and kinetic models for BOF steelmaking 123
9.2.1 Comprehensive model for oxygen steelmaking (Dogan et al. [23]–[25]) 126
9.2.2 Multi-zone kinetic model (by Rout et al. [9]) 129

9.2.3 Thermodynamic and kinetic model of the converter steelmaking process (Lytvynyuk et al. [66], [67]) 135
9.2.4 Dynamic model for LD converter with gibbs free energy minimization (Sarkar et al. [17]) 137
9.2.5 Mathematical BOF model based upon a Gibbs Energy Minimization Approach (Kruskopf et al. [36]) 139
9.2.6 Effective Equilibrium Reaction Zone model (Van Ende et al. [35]) 142
9.2.7 Additional Models 144
9.3 Comparisson of the discussed models 145
9.4 Future opportunities 150
9.5 References 151
10 Thermodynamic BOF model 162
10.1 Motivation to use thermodynamics 162
10.1.1 The standard closed calculation 162
10.1.2 The standard open calculation 165
10.2 An effective equilibrium reaction zone type model: combining kinetics and thermodynamics 171
10.2.1 General model outline 171
10.2.2 Considered material input 174
10.2.3 Considered thermodynamic specifications 176
10.2.4 Calculation specifications 178
10.3 Model concept and mathematical formulation 178
10.3.1 Calculation at t = 0 s 178
10.3.2 The jet impact zone 178
10.3.3 The slag – metal interface zone 181
10.3.4 The emulsion zone 182
10.3.5 Scrap melting zone 187
10.3.6 Homogenisation 188
10.3.7 Heat transfer between metal and slag phase 189
10.3.8 Temperature homogenisation 191
10.4 Summary of the main model assumptions 191

10.5 Conclusion 194
10.6 References 194
11 Fitting of TD BOF model parameters and model validation 200
11.1 Motivation for fitting 200
11.2 Fitting methodology 207
11.2.1 Defining the error function 208
11.2.2 Optimisation solver 212
11.3 Fitting results 213
11.4 Model validation 220
11.4.1 Validation for parameter set [26.06; 0. 72; 3.03; 0.39] 220
11.4.2 Validation for parameter set [17.58; 0. 78; 0.50; 0.28] 229
11.5 Conclusion 233
11.6 References 234
12 Case study: The effect of MgO 236
12.1 Methodology 236
12.2 Results and discussion 237
12.2.1 Interaction with refractory 237
12.2.2 Foaming behaviour 239
12.2.3 Effect on refining 242
12.3 Conclusion 247
12.4 References 247
13 Towards a more advanced TD BOF model 250
13.1 The combination of different set of model parameters 250
13.1.1 Piecewise combination of the parameter sets 251
13.1.2 Linear combination of the parameter sets 252
13.1.3 Exponential combination of the parameter sets 257
13.1.4 Comparing different combinations 259
13.2 Validation results 261

13.3 Conclusion 268
V. Conclusion and future work 271
14 General conclusion and outlook for the future 272
14.1 Conclusion 272
14.2 Conclusions with respect to the research questions 274
14.3 Outlook for future work 276
Appendix A: Additional figures assessement of the foaming index 280
Appendix B: Input format TD BOF model 285

I. Introduction

"I hate it! I hate the doom you're all waiting for, the giving up, and the senseless question that always sounds like a cry for help. I am sick of hearing pleas for John Galt. I'm going to fight him."

He said quietly, "You are."

"I'm going to build a railroad line for him. Let him come and claim it!"

He smiled sadly and nodded: "He will".

Atlas Shrugged – Ayn Rand

1 General introduction

1.1 Research context

"Make the slag and the steel will make itself" is an old phrase in steelmaking. Slags are liquid oxide phases which play an important role in many pyrometallurgical processes. This is also the case in the basic oxygen process, also known as the converter process. The converter process is a necessary step in traditional steelmaking. During this batch process liquid hot metal from the blast furnace is refined and steel is produced. In a converter, the liquid hot metal from the blast furnace is charged together with scrap, and oxygen is blown through. During this process three main phases are present in the convertor: the liquid metal phase, the slag and a gas phase, which is however immediately removed from the vessel. The slag plays an important role in refining the metal phase (removing C, P, Si, etc.). Furthermore, it has the potential to reduce metal losses via the off-gas stream and due to its interaction with the refractory of the vessel, the durability of the installation is affected.

Even though there is general agreement on the importance of the slag and its functions in steelmaking, a profound understanding of slags is hitherto lacking. Gaining insight in the process, the working principle and the interaction between the slag and metal phase via experiments is rather difficult due to the high working temperature and the extreme process conditions (> 300 ton material, stirring, CO formation, etc.). Thermodynamic modelling of the process is a possibility to gain insight and gather more knowledge about the mechanisms involved.

ArcelorMittal Ghent/Belgium is part of the global ArcelorMittal Group, which is the world's leading steel and mining company. The plant in Ghent is an integrated steel plant where flat steel products are produced starting from raw materials. These products have numerous applications such as automotive industry, packaging and construction. Constant research and innovation allow the company to further optimise both their products and production process. This all adds up to a continuous technological progress and the possibility to increase the productivity, which has already doubled over the past 15 years.

This PhD project is a close collaboration between the Sustainable Materials Science group at Ghent University and the steel shop of ArcelorMittal Ghent. The project was funded

by the Flemish government via a 'Baekeland mandate'. This type of mandates have the specific aim to "*build up scientific or technical knowledge as a basis for economic applications*". The Baekeland mandates support research that, if successful, has clear economic objectives and added value for the company involved in the project, in this case ArcelorMittal Ghent. Consequently, the objectives of this work will be strongly linked to specific process related questions for the steel shop in Ghent. At the steel shop of ArcelorMittal Ghent, models are used to be able to calculate the process' steel and slag end composition based on the material input for each heat. These models are strongly statistically based using regression analyses, neural networks etc. Furthermore, slag and steel samples are taken at the end of each heat and are used to continuously validate these models. Thus, there is knowledge on the start point of each process (the input) and the final conditions of the process. Yet, there are no models or experimental methods present at the steel shop of ArcelorMittal Ghent to provide any descripton on the slag evolution during the process.

Furthermore, as the used industrial data in this work is confidential and it was normalised for display. The normalisation was performed by defining, for each variable, an industrially relevant lower and upper limit. Industrial data points thus have values ranging from 0 to 1. Some exceptions to this method can be found in the work, e.g. when dealing with measurements from during the blow. In this case, the normalisation was not performed in the conventional way, but by dividing the actual measured value by a fixed constant. Whenever this is the case, this is mentioned specifically in the text.

1.2 Research objectives

The goal of this PhD dissertation is to apply thermodynamic models and calculations upon the industrial converter process of ArcelorMittal Ghent, in order to gain scientific knowledge and understanding of the slag and its interactions at this specific steel plant. Combining the results of the thermodynamic software with the enormous amount of process data and knowledge available at ArcelorMittal Ghent, yields the opportunity to create a feedback loop and optimize the currently used models.

Within the context of this work, three important roles for the slag are defined: refining, interaction with refractory and foaming behaviour. Accordingly, the research questions in this work have been divided between these three different roles of the slag. Ideally, working areas which are optimal for all three roles are desired. For each of the slag's

roles specific questions were put forward by ArcelorMittal Ghent. These questions were grouped into some more general research questions.

- What is the effect of slag composition on refining?
  Why has MgO a negative effect on dephosphorisation?
  Does MgO have a negative effect on dephosphorisation for all possible compositions?
  Is it possible to compensate the negative effect of MgO on dephosphorisation via slag engineering[2]?
  Is it beneficial to change the slag's working point for certain heats[3]?
  …
- What is the effect of slag composition on the interaction with the refractory material?
  What is the effect of MgO, CaO and Al_2O_3 on the chemical refractory wear?
  What is the effect of temperature on the chemical refractory wear?
  Is it possible to compensate the negative effect of Al_2O_3 on the refractory wear via slag engineering?
  …
- Is it possible to characterise industrial foaming via the slag compositions?
  Can the slag composition be linked to physical properties such as viscosity and density?
  What is the foaming index for the industrially relevant slag compositions?
  Which parameters are important for this foaming behaviour?

At the start of this PhD project, models or methods to determine the slag composition during the process at ArcelroMittal Ghent were not available. However, to answer the research questions it was found necessary to describe the slag composition during the process. As a consequence, a large part of the work done within the PhD project was the development of methods to either describe or, if possible, predict the slag evolution during the process, specifically for the plant of ArcelorMittal Ghent. These models are not meant for on line industrial process controle but for separate research purposes.

[2] In this context, slag engineering means changing the slag composition or the slag temperature.
[3] Heat is the conventional term in steelmaking used to talk about one batch of material processed during the BOF process.

1.3 Structure of the work

This work is divided into five general parts: 'I. Introduction', II. Slag Properties and Behaviour, 'III. Foaming', 'IV. TD BOF model' and 'V. Conclusions and future work'. The first 'I. Introduction' part of this dissertation contains different chapters and gives an overview on the necessary literature. Both the fundamentals of the process and the importance of slags in the process, divided in the three roles of slag, are discussed. In the second part 'II. Slag Properties and Behaviour', the effect of different conditions on thermodynamic calculations is discussed and the potential of using thermodynamics to gain insight in the process is demonstrated. A last chapter of this part, gives an overview on models used to calculate different physical properties such as viscosity, density and surface tension. An intermediate conclusion is formulated at the end of the second part. In the third part 'III. Foaming' a model to describe the slag evolution of already executed heats is described. Results of the model are used to investigate the foaming behaviour of the industrial slag. The fourth part 'IV. TD BOF model' starts with a thorough review on state-of-the-art physiochemical BOF models. Afterwards a physicochemical BOF model based on the EERZ model, combining thermodynamic and kinetics to describe the process is constructed. A parameter fitting is found to be necessary for the model to yield reliable results. This parameter fitting is thoroughly described and the model is validated with industrial data. A case study on the effect of MgO is used as example to show the potential of this TD BOF model. In the final chapter of this part, a future extension of the TD BOF model is suggested. Part 'V. Conclusions and future work', contains the final chapter of this dissertation with a general conclusion and a discussion for potential future work.

2 BOF process and slag

Today's crude steel production reaches 1878 million ton [1] worldwide. About 70% of this steel is produced via the basic oxygen steelmaking (BOF) process. The main goal of this process is to reduce carbon and impurity content of the hot liquid metal by blowing oxygen through the metal bath. Over the past decades, BOF steelmaking has been extensively researched. Both the metallurgical aspects of the process as well as the design and configuration of the installation, known as the converter, have been addressed in several studies. In this chapter first the BOF process is situated within the steel production process, next the concepts of the BOF process are discussed, both process and the installation are covered. Special focus is put on the slag.

2.1 On steelmaking

Two possible main routes for steel production exist [2]. About 70% [3] of the steel is produced via the Blast Furnace – basic oxygen route (BF-BOF), while the electric arc furnace (EAF) route accounts for about 28% [3] of the steel production. The differences between the two types of production processes are, apart from the installations, the input materials and the energy sources. In EAF processes, the main input material is mainly scrap combined with possibly some pig iron or even direct reduced iron (DRI). Liquid steel with desired composition is produced via electricity, hence the name electric arc furnace. The blast furnace, on the other hand, operates with iron ore and coal to produce 'iron', while the BOF process uses the output from the blast furnace together with scrap to produce 'steel'. Both the BF and BOF process use oxygen rich gases and the heat produced by the chemical reactions to obtain the desired process temperature. Since, this work focuses on the BOF process, only the BF-BOF route is explained in more detail.

In the blast furnace, cokes (C-rich) and iron ores (Fe_xO_y – rich), which are usually sintered, are used as input products. These solid raw materials are charged layer per layer into the furnace and either air or other oxygen rich gases, are introduced at the bottom of the furnace. While the oxygen rich gas is on its way to the top of the furnace, it takes part in a series of combined oxidation and reduction reactions resulting in the production of iron from the ores. Due to the exothermic chemical reactions, the temperature of the process

increases. As a result, liquid iron-rich metal is tapped at the bottom of the furnace. Typically, some BF-slag is produced as well.

The liquid metal tapped from the blast furnace is known as hot metal, or when it is cast and cooled down as pig iron. This hot metal (HM) from the blast furnace contains about 4.5 wt% C, which is considerably higher than the desired carbon content for steel (usually around 0.05 wt% C). Apart from C, the hot metal always contains a substantial amount of Si. The exact quantity is mainly influenced by the blast furnace working point. Furthermore, depending upon the ores and materials used the hot metal will contain considerable amounts of different other impurities, such as P, S, Mn and V. Due to the presence of all these impurities in the hot metal, the BOF process is an essential part of the steelmaking route.

In European steelmaking the used ores, and as a consequence the hot metal, are often P-rich and dephosphorization becomes an important process topic. Removal of P from the steel is essential, due to its detrimental effects on the steel formability and hence, the steel quality. Both the ductility and toughness of the steel require low phosphorus contents. Upon cooling, phosphorus tends to migrate to the central grain boundaries, resulting in the formation of brittle cores within the steel. Especially, for thin sheets for deep drawing or automotive applications or steel intended for pipeline applications, low P contents (< 0.1 wt%) are demanded. [4]

The hot metal, after major sulphur removal, is charged together with scrap into a BOF-vessel, also known as converter, and pure oxygen is blown onto the metal bath to obtain refining. As a result, a CO-rich gas is formed together with a slag which contains the impurities as oxides. Depending upon the desired steel grade and the associated quality, the refining needs to be more thorough. At the end of the process, the steel is tapped and transported to the secondary steelmaking installations where the final composition is obtained by adding alloying elements or performing additional specific refining procedures. When the steel has the final desired composition, it is cast via a continuous casting process and the slabs are cut to the desired dimensions. The steel slabs are rolled in hot and cold rolling mills until they are steel sheets with desired thicknesses. Heat treatments and if required, surface treatments are performed before the steel is shipped.

2.2 The BOF Process

The BOF process was introduced in the 1950's in Austria at Linz and Donawitz. [5], [6] In the batch process, the hot liquid metal, tapped from the blast furnace with main relevant impurities Si, C and P, is refined. The process is known under various names: basic oxygen process (BOP), basic oxygen steelmaking (BOS) and basic oxygen furnace (BOF) process.[7] However, in practice all these processes use pure oxygen and basic slag, which is formed during the process, to convert the hot metal to steel. This is in contrast to much older processes where air was used for this purpose.

2.2.1 Refining

A schematic representation of the BOF process is shown in Figure 2.1. In conventional oxygen steelmaking, scrap and liquid hot metal are charged together in the converter. Pure oxygen is blown through a top lance on the metal bath. As a result, a CO-rich gas phase is formed together with a slag phase, which is a liquid oxide solution phase, that contains impurities such as silicon, phosphorus and manganese. The slag will also contain considerable amounts of iron-rich oxides.

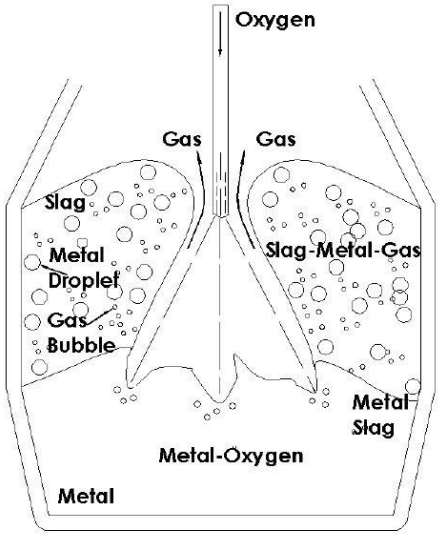

Figure 2.1: Schematic BOF process. Taken from [8]

Refining of the metal is either the result of direct or indirect oxidation of the impurities. The direct oxidation reaction is shown in equation 2.1. In this equation E is every element different from oxygen, the square brackets indicate the elements dissolved in the metal

and the regular brackets indicate the chemical species that are part of a slag. Further oxidation of the formed CO gas with oxygen is possible. Especially, because the CO and O_2 gas streams are flowing next to each other in opposite directions. This further oxidation of the formed CO-gas is called post-combustion. Indirect oxidation occurs when a formed oxide reduces again to the original impurity and by doing so oxidises another impurity. Even though in theory this would be possible between any two elements, if an element with stronger oxygen affinity is in contact with an oxide of an element with lower oxygen affinity, the largest share of indirect oxidations in the BOF process are assumed to be with FeO. The reason for this is twofold. First of all, there is a considerable amount of FeO produced in the beginning of the process, resulting in an abundance of FeO in the slag at the start of the process. Secondly, Fe has by far the lowest affinity with oxygen of all the major mentioned impurities in the process. This can clearly be seen in the Ellingham diagram shown in Figure 2.2. For completeness, the reaction for indirect oxidation with FeO is given in equation 2.2.

$$\begin{aligned} [C] + [O] &\rightleftharpoons CO\ (g) \\ x\,[E] + y\,[O] &\rightleftharpoons \left(E_x O_y\right) \end{aligned} \tag{2.1}$$

$$\begin{aligned} [C] + \ (FeO) &\rightleftharpoons (CO) + \ [Fe] \\ x\,[E] + \ y\,(FeO) &\rightleftharpoons \left(E_x O_y\right) + y\,[Fe] \end{aligned} \tag{2.2}$$

It is well established amongst steelmakers that during the refining process also a metal-slag emulsion exists in the converter, most likely, due to the generation of metal droplets as a result of the gas jet impact upon the steel bath. Research [9]–[11] over the past decades indicated that these metal droplets, and intrinsically the complete metal-slag emulsion, play a crucial role in the refining process of the steel. Often this is attributed to a combination of the increased contact area between metal and slag and the presence of FeO in the slag which acts as an oxidising agent for impurities in the steel. The removal of impurities takes place simultaneously at the droplets' interface. As a result, the droplets falling back from the emulsion into the metal bath are almost entirely refined. [12] More recent work [13]–[15] also indicates the residence time of the metal droplets in the slag-metal emulsion is increased, and with it the refining, due to swelling behaviour of the droplets. Correspondingly, this phenomenon is called 'bloated droplets' or sometimes also 'swollen droplets'. Precise mechanisms of the metal – slag emulsion are nevertheless, still a topic of discussion. [9]

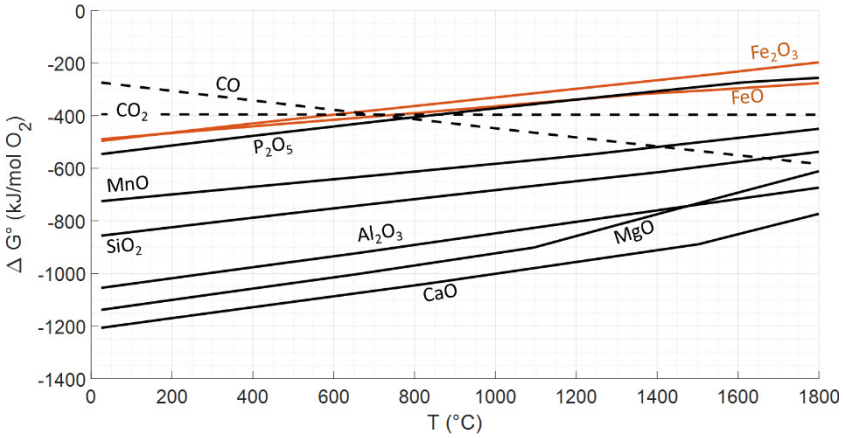

Figure 2.2: Ellingham diagram with relevant oxides for steelmaking. Data from Factsage 7.2 FactPS and FToxid databases.

During the process several different fluxes are added to obtain optimal process conditions. Fluxes are the general name for all the materials added to the process, different than hot metal, oxygen and scrap. Some fluxes, mainly CaO and MgO, are added to obtain an optimal slag, while others e.g. FeSi or coke, are added to control the final temperature of the process.

During the BOF process the hot metal is refined until it's compositions and temperature meet the restrictions and demands for the desired steel grade. However, due to different affinities for oxygen and the kinetics of the process, different elements will have a different refining profile. In this context, reference is often made to work by Hoorn et al. [16], [17] at Hoogovens Ijmuiden BV. Their observations were confirmed in other works [7], [18]. The general profile reported by Turkdogan [6] is given in Figure 2.3. Due to the large affinity for oxygen, the Si present in the hot metal immediately reacts to form silica. For this reason, lime is added at the start of the blow to make sure the formed slag has the desired properties during the complete process. Carbon shows a continuous decrease during the complete process. The rate of this reaction will increase at first, but decreases towards the end of the process due to limited availability of the carbon left in the steel. Both Mn and P show first a decrease and afterwards an increase in their profile before finally decreasing towards the desired levels at the end of the blow. This phenomenon is known as the 'pick-up' of P or Mn and there is still some discussion on the exact responsible mechanisms. Ghosh et al. [19] relate this phenomenon to the FeO-content in the slag, while Hewage et al. [20] point out the complexity it introduces in the

understanding of the kinetics of the BOF refining process. Finally, it is clear from this refining profile that the BOF process is not suited for S removal.

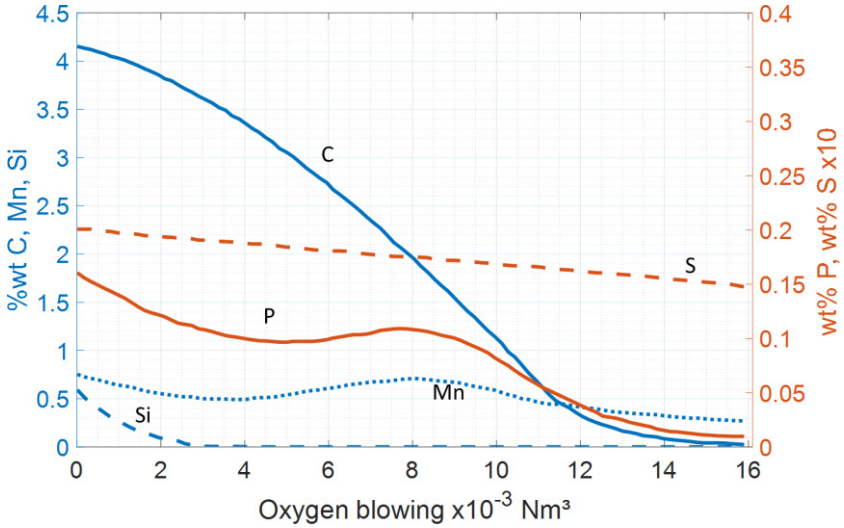

Figure 2.3: General profile of the steel composition during BOF blow. Data from [6].

The basis of a BOF slag is the CaO-FeO_n-SiO_2 system. In steelmaking FeO_n is used instead of FeO or Fe_2O_3 because a mixture of both oxides, in various ratios, will be present. The most important secondary oxides are Al_2O_3, MgO and MnO. Furthermore, the slag will also contain considerable amounts of P_2O_5. Depending upon the steel shop and the conditions of the used hot metal and scrap also V_2O_5, TiO_2 and Cr_2O_3 could be present. Together with changes in the steel composition also the slag composition will vary during blowing. The same works as mentioned before for steel composition report a general corresponding slag composition shown in Figure 2.4. Especially, the initial high FeO content in the slag, followed by a decrease and only at the end of blow an increase is a remarkable feature. Even though there is a general consensus on this composition profile it remains up till today unclear which mechanisms cause it.

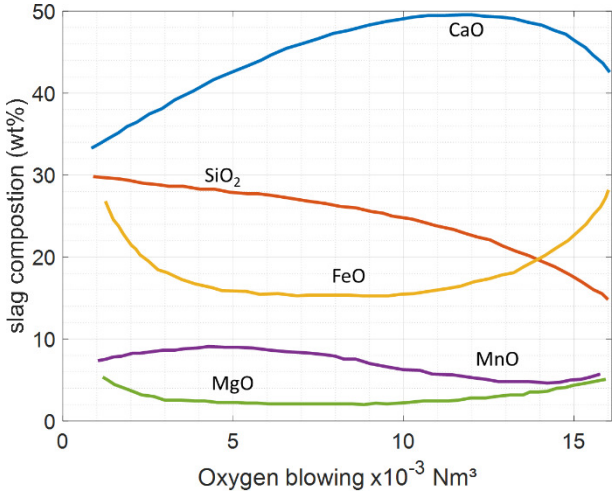

Figure 2.4: General slag composition during BOF blow. Data from [6].

2.2.2 The BOF vessel

A schematic figure of the BOF vessel is shown in Figure 2.5. The vessel consists out of a bottom, cylindrical centre shell, also known as a barrel, and a top cone. Connection to the chimney, to remove the gas from the process, is ensured with a top ring. Furthermore, the vessel has an outer shelf and an inner refractory lining. This refractory material usually consists out of MgO-rich materials which degrade during the process and the lining is said to be consumed. This degradation is due to mechanical, thermal and chemical influences and will cause the refractory to get thinner and thinner during the use of the vessel. As a result, BOF vessels always need replacement of their refractory lining after a certain lifespan. The old refractory materials are removed and new refractory materials are placed into the vessel.

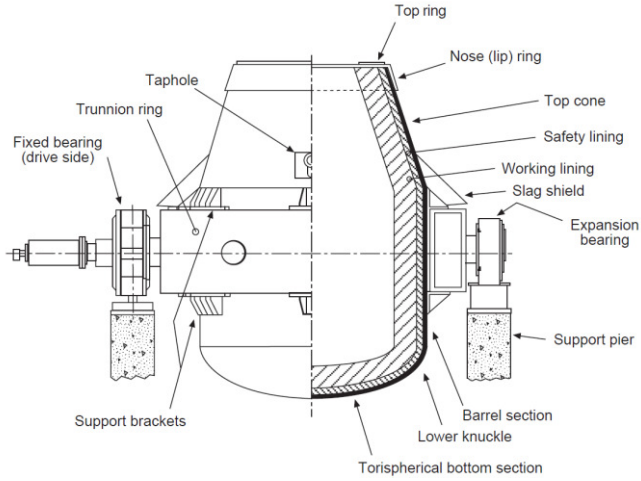

Figure 2.5: Schematic BOF vessel configuration. Taken from [21].

The oxygen is introduced into the vessel with a top blown water-cooled lance. Usually, one lance head has several nozzles which are placed under a specific angle. Mostly, five to six nozzles lances are used in the current BOF vessels. The nozzle angle is important for its effect on the oxygen momentum on the bath and the effect it has on slopping. It is mentioned [21] that the original single nozzle lances with an angle of 0° with respect to the lance central axis showed severe issues with slopping.

To guarantee optimal mixing, today's converters are usually equipped with extra bottom stirring. Inert gas is introduced via tuyères at the bottom into the liquid bath to increase mixing. A number of set ups are reported to have a bottom blowing oxygen option. This last process has been developed from the 70's onwards and also introduces reactive oxygen at the bottom of the bath, [5] adding extra complexity to the process.

2.3 On the role of slag

In steelmaking, slag is used as a general term for all the phases which contain oxides. This in contrast to thermodynamics, where slag usually refers to the liquid oxide phase. Even though the slag contains all the impurities it also has some major functions during the BOF refining, which are discussed here. In chapter 5 more details are given on the theoretical concept of slags such as its structure.

2.3.1 Refining

The first obvious role of slag in the process is the influence on the steel's refining. Whenever two different phases are brought into contact an equilibrium will be established between the two. Depending, upon composition and temperature, this equilibrium will be different. Hence, the refining, which is nothing more than removing impurities from the metal bath via redistribution to the slag, is influenced by the exact composition of the slag system and its temperature. In steelmaking industry it is customary to define either a capacity or a distribution coefficient for an element to express how suited the slag is for refining this specific element. Often empirical relations were developed to describe the effect of different components or temperature on either these capacities or thermodynamic activity coefficients (which are used to calculate the capacities). To make this concept less abstract, an example of the relation for the partition coefficient for P as described by Turkdogan [6], given in equation 2.3, is discussed. Both the definition of the partition coefficient and the empirical expression are given equation 2.3. For optimal dephosphorization K_{PO} should be as large as possible. According to the empirical expression this can either be obtained with a decreasing temperature or an increase of both lime and magnesia. This conclusion is a nice way to illustrate some of the issues with the empirical relations. The first observation that lower temperatures are beneficial for dephosphorization is generally accepted in both steelmaking and fundamental studies [22], [23] on the topic. Also the beneficial effect of CaO on dephosphorization is commonly known amongst steelmakers. Yet, on the role of MgO there is still a lot of discussion, which is accompanied and fed by contradicting observations on the role of MgO. Some steel plants notice no [24] or a beneficial effect [6] of MgO on dephosphorization, while others [25], [26] observe an opposite effect. Even though empirical relations seem convenient and easy to apply, their use is limited to a restricted set of process conditions (composition and temperature) and cannot be applied on just any system.

$$K_{PO} = \frac{(\%P)}{[\%P]} \frac{1}{[\%O]^{2.5}}$$

$$\log(K_{PO}) = \frac{21.740}{T} - 9.87 + 0.071\ (\ wt\%\ CaO + 0.3\ wt\%\ MgO) \tag{2.3}$$

2.3.2 Interaction with refractory

A second role of slag in the BOF process is linked with its interaction with the refractory lining. The refractory material in a regular BOF vessel is usually MgO-rich and can dissolve in the slag. In Figure 2.6 the mechanism of refractory dissolution as described by Dai et al.[27] is shown. Initially (Figure 2.6(a)), a solid slag layer, originating from the previous heat, protects the refractory lining. Due to the concentration gradient the solid layer dissolves/melts in the liquid slag. The flow of material in the vessel facilitates this process (Figure 2.6(b)). When all the solid slag has dissolved/melted, there is direct contact between the liquid slag and the refractory (Figure 2.6(c)). Due to this contact and the concentration gradient between the two phases, MgO particles will precipitate at the interface (Figure 2.6(d)) and diffuse, gradually, into the liquid (Figure 2.6(e)). Due to the flow, the particles are taken away from the interface and they gradually melt into the liquid slag. This process continues until an equilibrium between the liquid slag and the interface is established. As can be seen in Figure 2.6(f) the dissolution of the refractory material results in corrosion of the refractory lining.

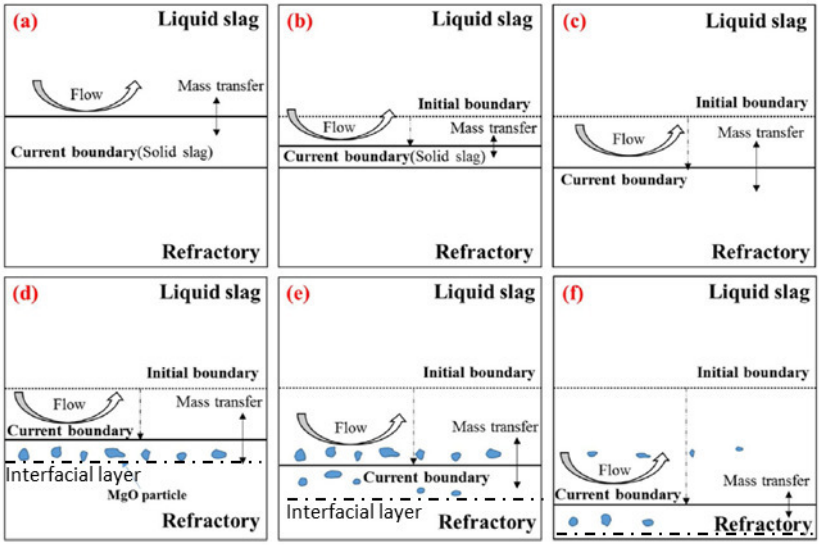

Figure 2.6: Refractory dissolution mechanism as described by Dai et al. [27]. Figure taken and adapted from [27].

The dissolution is largely influenced by the composition and temperature of the slag. When a MgO saturated slag is used, the dissolution of the refractory is reduced. However, other slag components can enhance dissolution of the refractory and increase the wear of the lining. Furthermore, sometimes it is impossible to use MgO saturated

slags, because these slags cause operational issues or they have negative influences on the refining of some important components e.g. P. It should be mentioned that chemical wear is only one possible degradation mechanism for the refractory. Other effects such as mechanical wear (due to e.g. scrap charging) or thermal wear (due to e.g. the nature of the batch process) will also influence the final lifetime of the refractory lining. Yet, from thermodynamic viewpoint only the chemical wear can be studied.

2.3.3 Foaming

A final important slag feature is its foaming or shielding property. Slag foaming occurs whenever gas bubbles, either injected or produced via chemical reactions, are introduced and retained in the molten slag. This phenomenon causes an increase of the slag-gas phase volume and as a consequence an increase in the slag height, schematically shown in Figure 2.7.

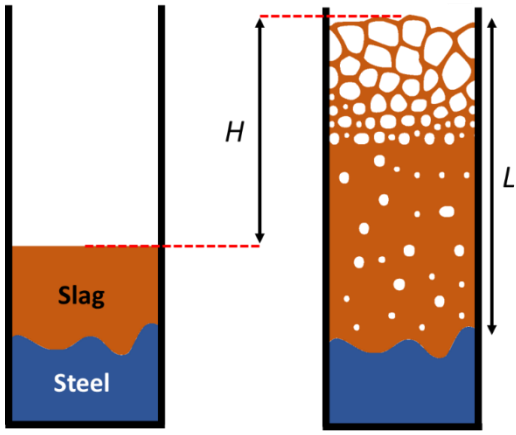

Figure 2.7: Schematic figure illustrating the concept of foaming. Adapted from V. Cnockaert (unpublished work).

In pyrometallurgical processes, gas can either be injected or originate from chemical reactions. In the BOF process the gas could thus either be O_2 from the top lance or produced CO or CO_2 from the decarburisation reactions happening in the converter. Usually, gases from reactive sources will result in smaller bubbles, enhancing foaming, while injected gasses result in larger bubbles which are less beneficial for foaming. [28]

The slag forms a protective layer between the steel bath and the air. Some compositions allow for a more protective layer than others. A good stable and foamy slag will be beneficial for refining and form a good protective layer. This layer is especially important

to reduce the losses of material via the off-gas stream. Small metal droplets are dragged along with off gas stream and either cool down on parts of the installation, resulting in possible obstructions, or are lost in further gas recuperation. The off set of cooled down materials, called sculling, possibly introduces operational or even safety issues. The metal losses are also an undesired economical loss. Foaming of slag is furthermore desired because it also prevents oxidation of the melt and ensures certain thermal insulation. Additionally, a foamy slag has an increased contact area and as such a positive effect on refining of the metal phase. [7], [29] On the other hand slag foaming introduces safety risks. If the foaming is too vigorous, the slag might become uncontrollable and reaches heights, exceeding the height of the vessel. This results in overflowing of the installation, also known as slopping in BOF steelmaking. [29] Both from safety and processing view this is undesired.

2.4 Conclusion

This chapter gives a thorough description of the BOF process. The process' metallurgical description is discussed in detail and the important mechanical aspects are shortly mentioned. The typical refining profiles of both the steel and the slag are given. The role of the formed slag is discussed. The importance of the slag is separated in three different process aspects: refining, interaction with refractory and foaming. For each of these the importance and the requirements for the slag are discussed.

2.5 References

[1] 'World Steel in Figures 2021 now available'. http://www.worldsteel.org/media-centre/press-releases/2021/world-steel-in-figures-2021.html (accessed Jun. 07, 2021).

[2] 'worldsteel | World Steel Assoctiation'. http://www.worldsteel.org/ (accessed Feb. 24, 2020).

[3] 'worldsteel | #steelFacts'. http://www.worldsteel.org/about-steel/steel-facts.html (accessed Jan. 28, 2021).

[4] M. A. Tayeb, S. Spooner, and S. Sridhar, 'Phosphorus: The Noose of Sustainability and Renewability in Steelmaking', *JOM*, vol. 66, no. 9, pp. 1565–1571, Sep. 2014, doi: 10.1007/s11837-014-1093-x.

[5] R. D. Pehlke, W. F. Porter, R. F. Urban, and J. M. Gaines, *BOF Steelmaking, Introduction, Theory and Design*, vol. 1. New York: The Iron and Steel Institute of the American Institute of Mining, 1974.

[6] E. T. Turkdogan, *Fundamentals of steelmaking*. London: The Institute of Materials, 1996.

[7] S. Seetharaman, A. McLean, R. Guthrie, and S. Sridhar, *Treatise on Process Metallurgy*, vol. 2. Elsevier, 2013. Accessed: Oct. 05, 2018. [Online]. Available: http://urn.kb.se/resolve?urn=urn:nbn:se:kth:diva-151111

[8] N. Dogan, 'Mathematical modelling of oxygen steelmaking', PhD thesis, Swinburne University of Technology, Melbourne, Australia, 2011.

[9] J. Martinsson and D. Sichen, 'Decarburization of Pig Iron in Synthetic BOF Converter Slag', *ISIJ Int.*, vol. 59, no. 1, pp. 46–50, Jan. 2019, doi: 10.2355/isijinternational.ISIJINT-2018-472.

[10] Publications Office of the European Union, 'Imphos : improving phosphorus refining.', Dec. 14, 2011. https://publications.europa.eu/en/publication-detail/-/publication/8aecbb7c-f77f-4ee7-bc38-9ebb13b52faf/language-en (accessed Nov. 06, 2018).

[11] H. W. Meyer, W. F. Porter, G. C. Smith, and J. Szekely, 'Slag-Metal Emulsions and Their Importance in BOF Steelmaking', *JOM*, vol. 20, no. 7, pp. 35–42, Jul. 1968, doi: 10.1007/BF03378731.

[12] R. Sarkar, P. Gupta, S. Basu, and N. B. Ballal, 'Dynamic Modeling of LD Converter Steelmaking: Reaction Modeling Using Gibbs' Free Energy Minimization', *Metall. Mater. Trans. B*, vol. 46, no. 2, pp. 961–976, Apr. 2015, doi: 10.1007/s11663-014-0245-2.

[13] B. K. Rout, G. Brooks, M. A. Rhamdhani, Z. Li, F. N. H. Schrama, and J. Sun, 'Dynamic Model of Basic Oxygen Steelmaking Process Based on Multi-zone Reaction Kinetics: Model Derivation and Validation', *Metall. Mater. Trans. B*, vol. 49, no. 2, pp. 537–557, Apr. 2018, doi: 10.1007/s11663-017-1166-7.

[14] B. K. Rout, G. Brooks, and M. Rhamdhani, 'Transient Behavior of Dephosphorization Kinetics in Oxygen Steelmaking', in *AISTech 2015 Iron and Steel Technology Conference*, 2015, pp. 3225–3237.

[15] E. Chen and K. S. Coley, 'Kinetic study of droplet swelling in BOF steelmaking', *Ironmak. Steelmak.*, vol. 37, no. 7, pp. 541–545, 2010.

[16] A. I. van Hoorn, J. T. Konynenburg, and P. J. Kreyger, 'The role of slag in basic Oxygen Steelmaking Processes', in *The role of slag in basic Oxygen Steelmaking Processes*, W. K. Lu, Ed. Toronto: McMaster University Press, 1976.

[17] A. I. Hoorn, J. T. Konijnenburg, and P. J. Kreijger, 'Evolution of Slag Composition during the Blow', in *Proceedings McMaster Symposium on Iron and Steelmaking*, 1976, pp. 2–1.

[18] C. Cicutti, M. Valdez, T. Perez, R. Donayo, and J. Petroni, 'Analysis of slag foaming during the operation of an industrial converter', *Lat. Am. Appl. Res.*, vol. 32, no. 3, pp. 237–240, 2002.

[19] G. Snigdha, B. N. Bharath, and N. N. Viswanathan, 'BOF process dynamics', *Miner. Process. Extr. Metall.*, vol. 128, no. 1–2, pp. 17–33, Apr. 2019, doi: 10.1080/25726641.2018.1544331.

[20] A. K. Hewage, B. K. Rout, G. Brooks, and J. Naser, 'Analysis of steelmaking kinetics from IMPHOS pilot plant data', *Ironmak. Steelmak.*, vol. 43, no. 5, pp. 358–370, 2016.

[21] K. J. Barker, 'Oxygen Steelmaking Furnace Mechanical Description and Maintenance Considerations', p. 94, 1998.

[22] C. Chen, L. Zhang, and J. Lehmann, 'Thermodynamic Modelling of Phosphorus in Steelmaking Slags', *High Temp. Mater. Process.*, vol. 32, no. 3, pp. 237–246, 2013, doi: 10.1515/htmp-2012-0129.

[23] M. Swinnerton, 'The influence of slag evolution on BOF dephosphorisation', 2005.

[24] K. Shimauchi, S. Kitamura, and H. Shibata, 'Distribution of P2O5 between solid dicalcium silicate and liquid phases in CaO–SiO2–Fe2O3 system', *ISIJ Int.*, vol. 49, no. 4, pp. 505–511, 2009.

[25] M. Ek, J.-C. Huber, G. Brosse, and D. Sichen, 'Capacities of some CaO–SiO2–FeO–MnO–MgO slags and slag–solid mixtures in capturing phosphorous', *Ironmak. Steelmak.*, vol. 40, no. 4, pp. 305–311, 2013.

[26] G. J. Chen and S. P. He, 'Effect of MgO content in slag on dephosphorisation in converter steelmaking', *Ironmak. Steelmak.*, vol. 42, no. 6, pp. 433–438, Jul. 2015, doi: 10.1179/1743281214Y.0000000246.

[27] Y. Dai, J. Li, W. Yan, and C. Shi, 'Corrosion mechanism and protection of BOF refractory for high silicon hot metal steelmaking process', *J. Mater. Res. Technol.*, vol. 9, no. 3, pp. 4292–4308, May 2020, doi: 10.1016/j.jmrt.2020.02.055.

[28] Y. Zhang and R. J. Fruehan, 'Effect of the bubble size and chemical reactions on slag foaming', *Metall. Mater. Trans. B*, vol. 26, no. 4, pp. 803–812, Aug. 1995, doi: 10.1007/BF02651727.

[29] M. A. Sattar, J. Naser, and G. Brooks, 'Numerical simulation of slag foaming on bath smelting slag (CaO–SiO2–Al2O3–FeO) with population balance modeling', *Chem. Eng. Sci.*, vol. 107, pp. 165–180, Apr. 2014, doi: 10.1016/j.ces.2013.11.037.

II. Slag Properties and Behaviour

Il ne faut pas craindre la lumière du soleil sous prétexte qu'elle n'a presque toujours servi qu'à éclairer un monde misérable.

René Magritte

3 Liquid fraction of the BOF slag

This chapter focuses on the liquid fraction of the slag. Liquid fractions are important for multiple reasons. Firstly, in the BOF-models the composition and amount of the liquid slag phase will influence final refining. Secondly, when foaming is discussed the considered properties are calculated for the liquid slag. Differences in liquid fractions and related compositions will influence the finally obtained results for the physical slag properties. Even though a liquid fraction sounds as a straightforward 'property', its exact value is influenced by multiple factors such as considered components or model settings. This chapter starts with a general description on the slag composition, to enable the reader to understand the differences in considered components. Next, the effect of model properties and chosen slag system (the set of considered components) on the liquid fraction is discussed. Finally, the effect of temperature and pressure on the liquid fraction is discussed. These effects are important to understand the next chapter where a more in-depth analysis is given on the specific effect of different components on slag features.

3.1 General information about BOF slags

In an industrial context, it is customary to talk about the slag as the collection of all the oxide phases present. An industrial slag will not be fully liquid. Both the liquid and solid oxide rich phases present in the system are thus denoted as the slag. Yet, strictly thermodynamically 'the' slag is only the liquid oxide phase and solid phases are either pure oxides or solid solutions consisting out of different oxides. Thermochemical calculations are often used to determine the liquid fraction and its composition.

As mentioned earlier, the BOF slag system is in essence a CaO-FeO_n-SiO_2 system. Furthermore, the most important other components are MgO, Al_2O_3 and MnO, either due to their mass fraction or the influence they have on the properties and process. Yet, in reality BOF slags will also contain P_2O_5, Cr_2O_3, TiO_2, V_2O_5 and some traces of S. The last component, S, is easily left out of analyses. It is generally known that BOF slags have very low sulphur capacities and the effect of the BOF slag in the refining of sulphur is negligible in the overall steelmaking picture. Furthermore, the amounts of sulphur are also small enough (due to desulfurization prior to the BOF charging) to leave sulphur out of the

general consideration for BOF slag composition and properties. However, it should be mentioned that sulphur is cited [1] to influence refining kinetics ambiguously due to the negative poisoning effect (due to reactive site occupation) it has on the steel surface for O_2 on one hand and the positive effect on emulsification (increasing reaction interface) on the other hand.

Neither Cr_2O_3 nor TiO_2 is ever mentioned to have a major influence upon neither refining nor slag properties. They might have an influence on the liquid fraction and composition, yet the contents for these oxides in industrial slags are small enough to assume their influence is minimal. Additionally, TiO_2 is poorly incorporated in the Factsage [2] solution models for the considered system.

For V_2O_5, the story is even more complicated. In certain industrial BOF slags a considerable amount of V_2O_5 is present, which will influence different process aspects and thus most probably certain slag properties. For example, at the steel plant in Ghent more skulling[4] is observed for periods with high vanadium oxide concentrations in the slag. At the steel shop, this is linked to the observation that the slag is more foamy when higher concentrations of V_2O_5 are present. Nevertheless, V_2O_5 is never considered in thermodynamic calculations nor in models to calculate slag properties. The reason is the lack of experimental data that is available for V_xO_y both for thermodynamic databases and slag physical properties (e.g. viscosity, surface tension, etc.). The Factsage FToxid database does not even contain V_xO_y. This makes it impossible to consider this component in calculations.

Finally, P_2O_5 is, especially in European BOF process, an important oxide and considerable amounts could be present. Yet, experimental data for the physical properties of slags containing P_2O_5 is limited. The phosphorus oxide is claimed to be well described in the Factsage Ftoxid database and thermodynamic calculations are considered trustworthy. Yet, the models to describe the physical slag properties do not contain this component. Consequently, different systems are considered for different calculations. Either a 'complete' or a 'simplified' slag system is considered. CaO-FeO_n-SiO_2-Al_2O_3-MgO-MnO-P_2O_5 (-Cr_2O_3) is the complete slag system.

In the current work, Cr_2O_3 might sometimes be considered for simple calculations, yet for refining calculations the component is left out of the analysis, because it introduced

[4] Skulling is a phenomenon where liquid material deposits and solidifies on different parts of the installation.

unnecessary complexity to the calculation. For similar reasons TiO_2 is not considered unless results between different databases are compared where the other database calculations were performed with TiO_2. Whenever thermodynamic calculations are performed for physical properties, a simplified slag system, without P_2O_5 is considered. The system reduces to: $CaO\text{-}FeO_n\text{-}SiO_2\text{-}Al_2O_3\text{-}MgO\text{-}MnO$. For graphical interpretations sometimes even less components are considered.

3.2 The effect of different modelling settings

3.2.1 The effect of the considered slag system

The effect of including P_2O_5 and Cr_2O_3 in the analyses for the liquid fraction is shown in Figure 3.1. For 100 random BOF heats the liquid fraction was calculated for their compositions with and without considering P_2O_5 and Cr_2O_3. Two important conclusions are drawn from these results. Firstly, the liquid fraction for the system with P_2O_5 and Cr_2O_3 is always higher than the liquid fraction for the system without these components. Secondly, even though absolute values for the liquid fractions are different for the two methods, they are strongly correlated. A heat with a higher liquid fraction for the calculation with P_2O_5 and Cr_2O_3, also has a higher liquid fraction for the calculation without these components. All calculations were performed with the FToxid Factsage 7.3 database. In these specific calculations TiO_2 was included, because the original ArcelorMittal calculations were performed with TiO_2.

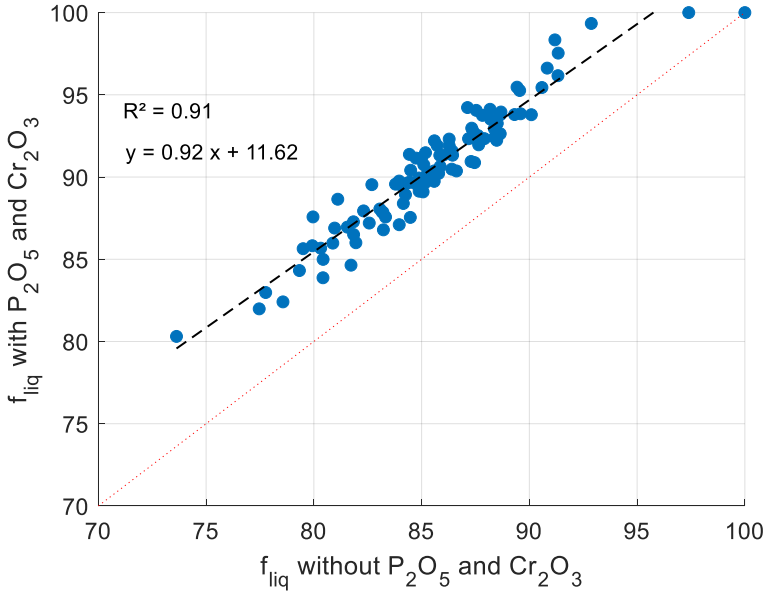

Figure 3.1: Liquid fraction of the complete slag with and without P_2O_5 and Cr_2O_3 included in the calculation.

3.2.2 The effect of the thermodynamic model

For the industrial slag compositions an industrial calculated liquid fraction is available. This liquid fraction is calculated with a statistical neural network based model, which was tuned on thermodynamic calculation with the CEQCSI software [3], [4] of ArcelorMittal Global R&D Maizieres. In Figure 3.2 the results from the CEQCSI calculated liquid fraction are compared to the Factsage 7.2 FToxid liquid fraction. The displayed results are from 3415 reference industrial heats. Identical full slag compositions, considering all components, were used for both calculations. From this figure it is clear the liquid fraction calculated with the CEQCSI model is often higher than the results obtained with Factsage. Especially, for systems with very high liquid fractions, calculations with the CEQCSI model results in considerably higher liquid fractions than the ones with the Factsage model.

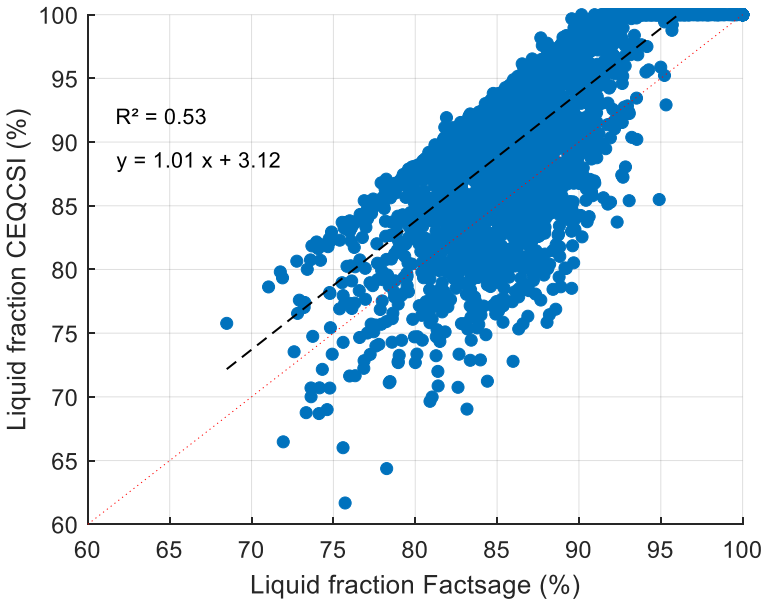

Figure 3.2: Slag calculated liquid fraction for 3415 industrial BOF heats with CEQCSI compared with those from Factsage FToxid (Factsage 7.2).

It is impossible to give one sole reason for the differences in calculations. Thermodynamic modelling depends both upon the used solution model and the data used for model fitting. Considerably different solution models are used in the CEQCSI and Factsage FToxid database. The CEQCSI model uses a central atom model [5]–[7] to describe slags, while Factsage uses a quasi-chemical model [8]–[11] for that purpose. Furthermore, also different data were used to optimise both models. An important difference is observed in the basis ternary BOF slag (CaO-FeO_n-SiO_2) phase diagram in equilibrium with steel: the CEQCSI-model indicates an extra solid region (Ca_3SiO_5). This region is also observed in the basis CaO-SiO_2-FeO_n diagram in the slag Atlas [12], as well as the calculated diagram from the GTox[5] (consulted in 2019) database from Factsage. Nevertheless, the basis ternary diagram calculated with Factsage FToxid 7.2 (or older versions) does not show this region.

From internal communication with the Factsage developers it is known that the FToxid database uses data from Troemel et al. [13] for the optimisation of the CaO-SiO_2 system. Yet, this is not the only data available for this system. Different assessments of the CaO-SiO_2 system have been performed. Different software and thermodynamic database

[5] A commercially available database developed by GTT-Technologies

developers might choose to use different assessments and data of this system based upon their analyses and judgment of the available literature and the quality and reliability of the performed experiments. As illustration two different phase diagrams for the CaO-SiO_2 system are shown in Figure 3.3, e.g. the temperature until which Ca_3SiO_5 is stable is different between the two diagrams (2070°C versus 1800°C). Different used optimisation data can result in differences in the calculation result.

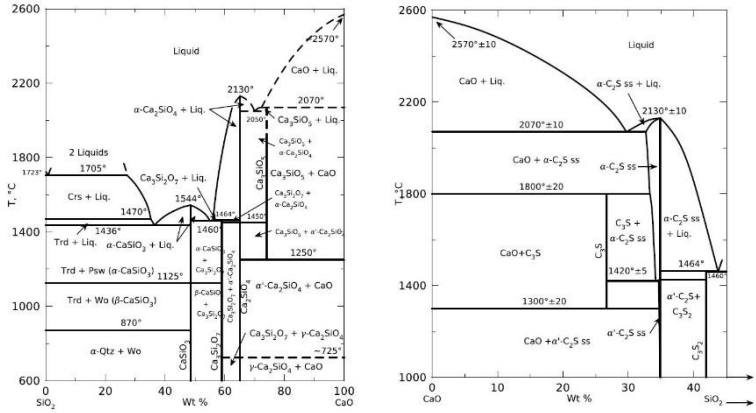

Figure 3.3: Data on the CaO-SiO2 equilibrium system: left side is PED_237 from Philips et al. [14], right side is the PED_6383 from Troemel et al. [13]. (PED = Phase equilibria diagrams database by NIST [15]). Note that the x-axes are reversed in the second figure compared to the first one.

3.3 The effect of temperature and oxygen partial pressure

So far, a general slag system containing all slag components (apart from Cr_2O_3 and P_2O_5) was considered. However, when discussing the effect of temperature and oxygen partial pressure on the liquid fraction, it is much more convenient to reduce the slag system to its three main components: CaO, SiO_2 and FeO_n. Reducing the system, allows to use graphical representations very often encountered in slag engineering and oxide related science: ternary phase diagrams or isothermal sections of the ternary phase diagram. A general lay-out of a classical isothermal section of a pseudo-ternary phase diagram for BOF-slags is shown in Figure 3.4. These phase diagrams are pseudo-ternary and not ternary, because oxides consist out of oxygen and another element. In fact the CaO-SiO_2-FeO_n diagrams, are Ca-Si-Fe-O diagrams. For every phase diagram in the current work, the components are expressed in wt%. Different relevant regions are indicated to ease further discussion in this work. To avoid all confusion, the liquid slag phase is denoted as

$slag_{liq}$ in this figure. The formed CaO phase on this figure, is not a pure calcium oxide but is a solid solution, known as monoxide A in the Factsage databases. The C_2S-phase is the dicalcium silicate phase (Ca_2SiO_4). This phase and its importance for BOF-steelmaking are discussed in more detail in the next chapter of this dissertation. Nevertheless, it should be mentioned that this phase appears in different polymorphs. Under the current circumstances α- Ca_2SiO_4 is calculated as the most stable phase and thus shown on Figure 3.4. The two phase region of slag and C_2S, has a specific nose shape and is therefore, often called the C_2S rich nose or the C_2S nose.

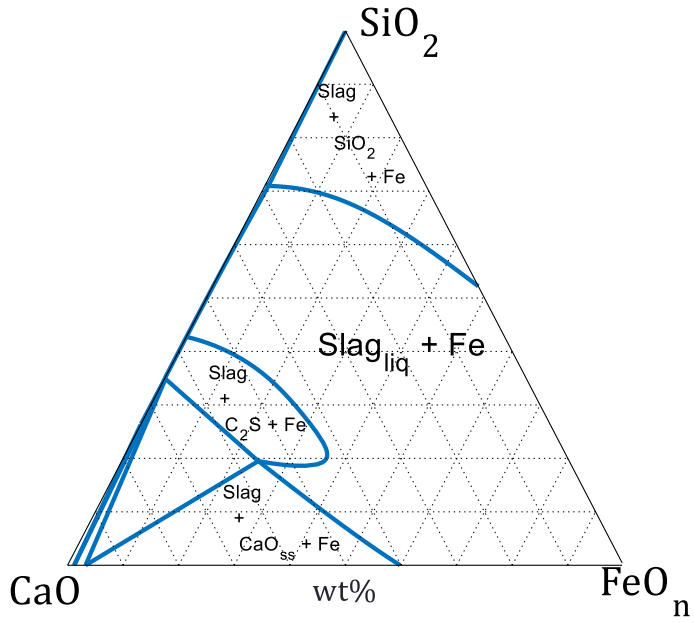

Figure 3.4: Isothermal section of the basis pseudo-ternary slag diagram at 1650°C for a CaO-FeO_n-SiO_2 system in equilibrium with pure Fe(l). The units are wt%. Calculated with Factsage 7.2.

3.3.1 On the effect of P_{O2}

As mentioned before, one of the major components in the BOF slag is FeO_n. The subscript *n* indicates both FeO and Fe_2O_3 are present in the BOF slag, yet, the exact ratio of the two types of oxides is tricky to determine. Due to its multi-valance character, Fe is a challenging component to construct or calculate phase diagrams. Depending upon the oxygen partial pressure, the FeO/Fe_2O_3 ratio will be different and this will influence the thermodynamics of the system. In Figure 3.5 the implications for phase diagram constructions of the varying *n*-value are shown. In essence, a different *n*-value

corresponds to a different plane in the CaO – SiO_2 – FeO – Fe_2O_3 tetrahedron. As a consequence, whenever phase diagrams are displayed it is important to state which system is considered. For steelmaking it is customary to assume the slag is in equilibrium with liquid iron or a steel phase. This corresponds to low oxygen partial pressures, a reducing environment, and n-values approaching 1. Another, not often encountered in BOF slag phase diagrams, assumption would be to assume equilibrium with air. In this case the oxygen partial pressure increases till 0.21 atm and this is usually called an oxidising environment.

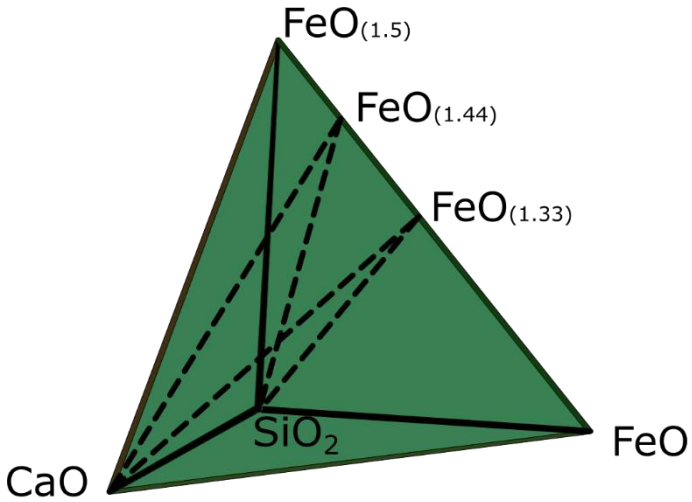

Figure 3.5: Compositional tetrahedron with indication of two different cross sections, corresponding to different n-values.

To illustrate the effect of partial pressure, different phase diagrams for different oxygen partial pressures are superimposed on each other in Figure 3.6. However, care should be taken upon results interpretation. As shown in Figure 3.5, different oxygen partial pressures correspond to different cross section in the compositional tetrahedron. For this reason, the superimposed figure shown in Figure 3.6 is not a true phase diagram collection. Yet, it is clear that oxygen partial pressure is a key parameter for phase diagram calculations. Upon increasing the oxygen partial pressure, the position of the C_2S nose shifts together with a substantial increase of the three phase area: CaO_{ss} – C_2S – *Slag-liq*, decreasing the two phase: CaO_{ss} – *Slag-liq* area. For all the calculated phase diagram in this chapter and in this work, the slag is in equilibrium with pure liquid iron hence a low oxygen partial pressure.

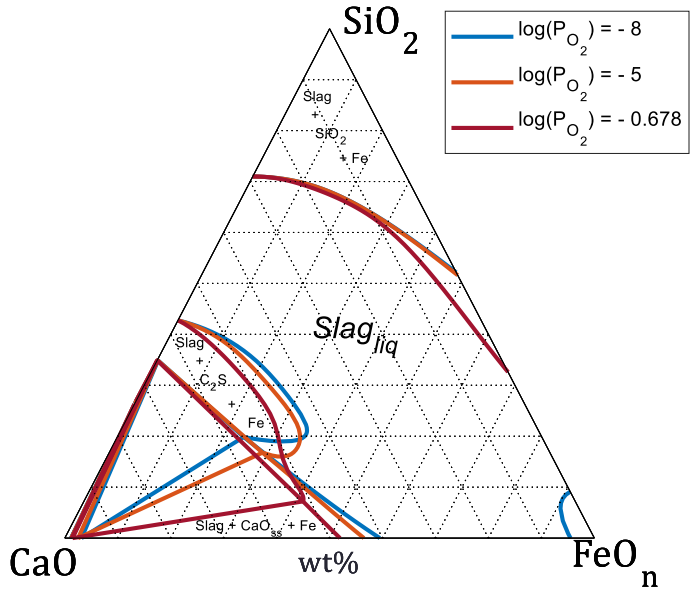

Figure 3.6: Effect of oxygen partial pressure on the basis phase diagram for BOF slag. Calculation at 1650°C with FToxid and FactPS database. Calcualtions are performed with fixed oxygen partial pressures via imposing a fixed activity for the oxygen gas.

3.3.2 On the effect of temperature

To study the effect of both composition and temperature on the equilibrium state of a system, often liquidus projections are used. An example of such a liquidus projection for the basis BOF slag system, is shown in Figure 3.7. On this figure both the primary phase fields, as well as the liquidus lines for different temperatures (colour scale indicated on the right side of the figure) are shown. Even though these types of diagrams contain a lot of information, they are rather complex to read and to compare the effect of different added components or temperature variation. Additionally, calculations of these types of diagram are also computationally intensive and hence time consuming.

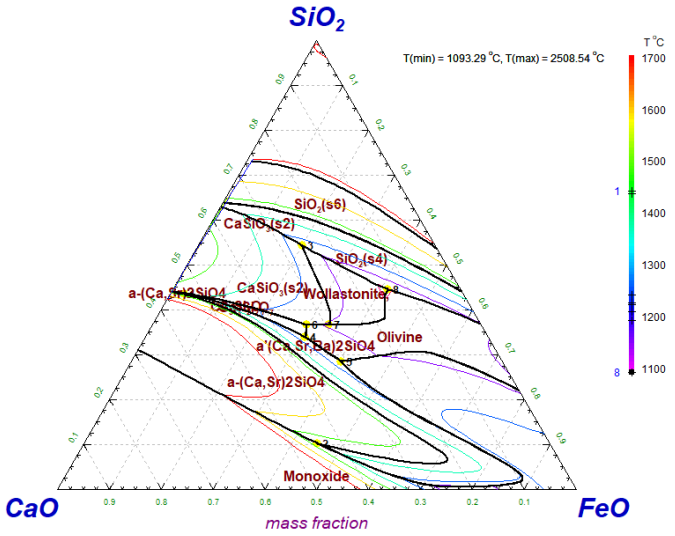

Figure 3.7: Liquidus temperature projection of the CaO-SiO_2-FeO_n system in equilibrium with Fe(l) calculated with Factsage 7.2 Ftoxid and FactPS.

In this work the isothermal sections of the pseudo-ternary phase diagram are more often used than the liquidus projections. An isothermal section gives information for one temperature. However, by combining different isothermal sections, more information can be displayed in one figure. An example is shown in Figure 3.8. It is clear that increasing the temperature increases the liquid slag area. Moreover, it can also be observed that increasing the temperature has a stronger effect on the C_2S nose than on the two phase CaO_{ss}-*Slag-liq* area.

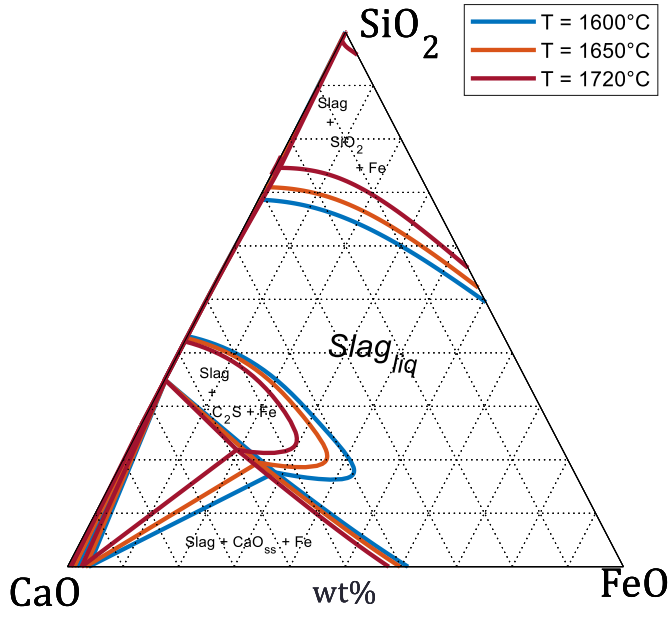

Figure 3.8: Superimposed figure of three different isothermal sections for the basis CaO-SiO_2-FeO_n system in equilibrium with Fe (l). Calculated with Factsage 7.2 Ftoxid and Fsstel.

3.4 Conclusion

From the discussion in this chapter it is clear the liquid fraction of the BOF-slag is influenced by multiple factors. Firstly, it is clear that liquid fractions calculated with P_2O_5 and Cr_2O_3 will always be higher than the ones calculated without. Secondly, the calculated liquid fraction with Factsage will in most cases, be lower than the corresponding industrially calculated liquid fraction which are calculated based on the CEQCSI model. This difference is due to the different used models to calculate liquid fractions. Finally, it was demonstrated that the oxygen partial pressure and considered temperature are also crucial factors in the thermochemical calculation.

3.5 References

[1] B. K. Rout, G. Brooks, M. Akbar Rhamdhani, Z. Li, F. N. H. Schrama, and A. Overbosch, “Dynamic Model of Basic Oxygen Steelmaking Process Based on Multizone Reaction Kinetics: Modeling of Decarburization,” *Metall. Mater. Trans. B*, vol. 49, no. 3, pp. 1022–1033, Jun. 2018, doi: 10.1007/s11663-018-1244-5.

[2] C. W. Bale *et al.*, “FactSage thermochemical software and databases, 2010–2016,” *Calphad*, vol. 54, pp. 35–53, 2016.

[3] J. Lehmann, “The main thermo-statistical models of metallurgical slags: theory and applications,” p. 19.

[4] J. Lehmann, “Applications of Arcelormittal Thermodynamic Computation Tools to Steel Production,” p. 10.

[5] C. H. P. Lupis and J. F. Elliott, “Prediction of enthalpy and entropy interaction coefficients by the ‘central atoms’ theory,” *Acta Metall.*, vol. 15, no. 2, pp. 265–276, Feb. 1967, doi: 10.1016/0001-6160(67)90202-7.

[6] J.-C. Mathieu, F. Durand, and É. Bonnier, “L’atome entouré, entité de base d’un modèle quasichimique de solution binaire - I. — Traitement général,” *J. Chim. Phys.*, vol. 62, pp. 1289–1296, 1965, doi: 10.1051/jcp/1965621289.

[7] J.-C. Mathieu, F. Durand, and É. Bonnier, “L’atome entouré, entité de base d’un modèle quasichimique de solution binaire - II. — Influence de deux formes d’énergie potentielle sur l’enthalpie de mélange,” *J. Chim. Phys.*, vol. 62, pp. 1297–1303, 1965, doi: 10.1051/jcp/1965621297.

[8] A. D. Pelton, S. A. Degterov, G. Eriksson, C. Robelin, and Y. Dessureault, “The modified quasichemical model I—Binary solutions,” *Metall. Mater. Trans. B*, vol. 31, no. 4, pp. 651–659, Aug. 2000, doi: 10.1007/s11663-000-0103-2.

[9] A. D. Pelton and P. Chartrand, “The modified quasi-chemical model: Part II. Multicomponent solutions,” *Metall. Mater. Trans. A*, vol. 32, no. 6, pp. 1355–1360, Jun. 2001, doi: 10.1007/s11661-001-0226-3.

[10] P. Chartrand and A. D. Pelton, “The modified quasi-chemical model: Part III. Two sublattices,” *Metall. Mater. Trans. A*, vol. 32, no. 6, pp. 1397–1407, Jun. 2001, doi: 10.1007/s11661-001-0229-0.

[11] A. D. Pelton, P. Chartrand, and G. Eriksson, “The modified quasi-chemical model: Part IV. Two-sublattice quadruplet approximation,” *Metall. Mater. Trans. A*, vol. 32, no. 6, pp. 1409–1416, Jun. 2001, doi: 10.1007/s11661-001-0230-7.

[12] M. Allibert and V. D. Eisenhüttenleute, *Slag atlas*. Verlag Stahleisen, 1995.

[13] G. Troemel, W. Fix, and R. Heinke, “High Temperature X-Ray Measurements on the Calcium Silicates 2Ca0. SiO2 and 3CaO-SiO2 uv to 1900° C,” *Tonind-Ztg Keram Rundsch.*, vol. 93, no. 1, pp. 1–8, 1969.

[14] H. Gaye, J. Lehmann, P. Rocabois, and F. Ruby-Meyer, “Computational thermodynamics and slag modelling applied to steel elaboration,” *Steel Res.*, vol. 72, no. 11–12, pp. 446–451, 2001, doi: 10.1002/srin.200100150.

[15] “PED Editor,” *NIST*, Oct. 24, 2013. https://www.nist.gov/srd/ped-editor (accessed Nov. 26, 2020).

4 Linking industrial observations with calculated phase diagrams[6]

In this chapter the classic phase diagram for BOF steelmaking slags, that was introduced in the previous chapter 'Chapter 3: Liquid fraction of the BOF slag', is discussed in more detail. Firstly, the different areas on the diagram and their importance for the BOF process are discussed. Next, the effect of different slag components on this classic diagram is analysed. This analysis is combined with observations from the ArcelorMittal Ghent steel plant.

4.1 General aspects of the BOF slags

In Figure 4.1 the already familiar CaO-FeO_n-SiO_2 diagram is repeated. On the diagram the completely liquid slag area is labelled, as well as the three phase regions (since Fe(l) is always present at each point in the diagram, these are phase areas with liquid slag and one solid oxide present). In the previous chapter, focus was put on the liquid fraction and no distinction was made between different formed solids. Yet, for practical BOF steelmaking a slag system that has a liquid fraction of 95 wt% with 5 wt% CaO-rich solids has a completely different meaning than one with identical liquid fraction and 5 wt% Ca_2SiO_4 (C_2S). In this chapter, the effect of different slag components on the liquid fraction, as well as on the formed solids, is discussed. The most convenient method to do this is to use the isothermal pseudo-ternary phase diagrams. All the diagrams are calculated in equilibrium with pure liquid iron and at a temperature of 1650°C, unless stated otherwise. As final note, it is important to mention that phase diagram analyses can give some insight in general observed trends, yet does hardly explain the complete picture of the process.

[6] Part of this chapter was used for a poster presentation: *L. De Vos, I. Bellemans, K. Overmeire, C. Vercruyssen, and K. Verbeken, "Interactive industrial application to represent isothermal sections of multi component phase diagram," in CALPHAD XLVIII, Conference on Computer Coupling of Phase Diagrams and Thermochemistry : proceedings, Singapore, 2019, pp. 149–159.*

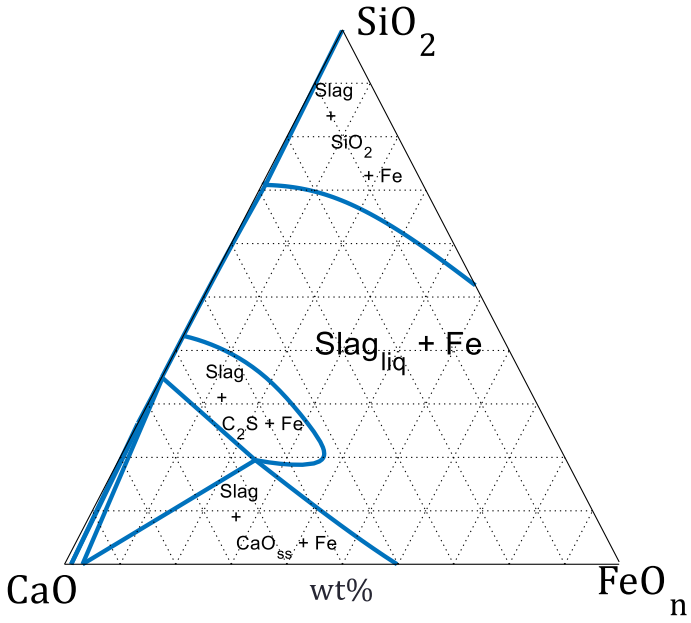

Figure 4.1: Isothermal section of the basis pseudo-ternary slag diagram at 1650°C for a CaO-FeO_n-SiO_2 system in equilibrium with pure Fe(l). The units are wt%. Calculated with Factsage 7.2.

The basis slag diagram is repeated in Figure 4.2, with indication of the compositional area which is relevant for BOF slags: the green dashed rectangle. Often in BOF steelmaking a slag is described by its basicity. Different definitions for basicity can be found. However, the simplest definition of basicity is the ratio of CaO and SiO_2 on weight basis, as is shown in equation 4.1. On Figure 4.2 two lines of constant basicity are indicated. In an industrial BOF slag, the silicon content is determined by the amount of silicon in the hot liquid metal. The amount of lime added to the system, will depend upon the desired basicity. The FeO_n-content will vary during the process. This is easily visualised by reading the line of constant basicity in the direction of the indicated arrows. Constant basicity lines allow for an easy visualisation to try and understand certain phenomena.

$$B = \frac{wt\%\ CaO}{wt\%\ SiO_2} \tag{4.1}$$

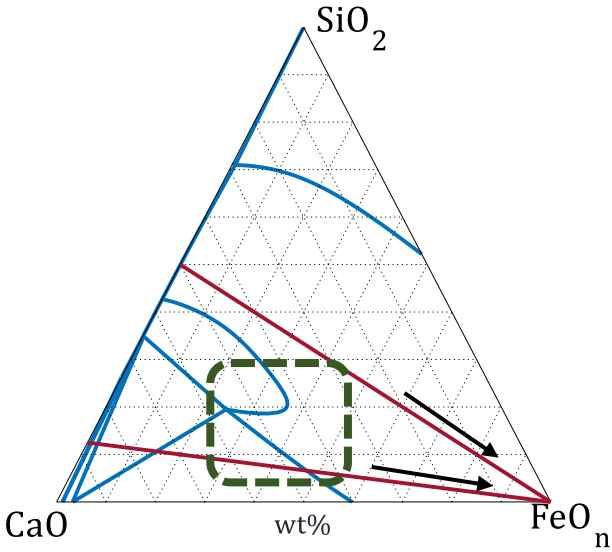

Figure 4.2: Isothermal section of the basis pseudo-ternary phase diagram with indication of two constant B lines (B = 1 and B = 7) in red and highlight of the composition area relevant for BOF steelmaking slags with the green dashed rectangle.

Multiple aspects of these diagrams could be discussed. Yet, for industrial steelmaking, there are two very relevant features on this diagram: regions in which C_2S (the dicalcium silicate Ca_2SiO_4) is thermodynamically stable and the so called saturation of either CaO_{ss} or MgO_{ss}. Before the effect of different components can be discussed it is important to point out why these two specific features are important.

4.1.1 The importance of saturation

Generally, when a component X is dissolved into a solution, saturation indicates that the full dissolution capacity of this component X is reached. Hence, when reaching the saturation point, it is no longer possible to dissolve more of the component X into the solution. For slags, when a component reaches saturation, the activity of the phase becomes one and the phase could start to precipitate from the liquid solution, forming solids. In BOF steelmaking saturation is usually used to discuss the presence of solid CaO. For more complex systems, saturation is also used to describe the presence of solid MgO. Even though these two components are not identical, they are believed to have a similar beneficial effect upon the interaction with refractory.

As explained briefly in the introductory chapters, the chemical refractory wear is largely a consequence of the dissolution of the refractory material (MgO-rich) into the liquid slag. This explains the importance of saturation of MgO or CaO for industrial slags: when

the liquid slag is saturated in a certain component, there is, at equilibrium, no driving force to dissolve this component into the slag. Consequently, a slag saturated in MgO will result in less refractory wear, compared to a slag that is not saturated in MgO. Similar effects are observed in industry for CaO saturated slags.

In Figure 4.3, it is indicated how it can be deduced from the graphical isothermal sections, whether a certain system composition is saturated in CaO or not. As can be seen, the increase in temperature results in a shift of the CaO saturation line to the CaO corner. Increasing the temperature thus, decreases the CaO saturation. Decreasing the temperature has the opposite effect.

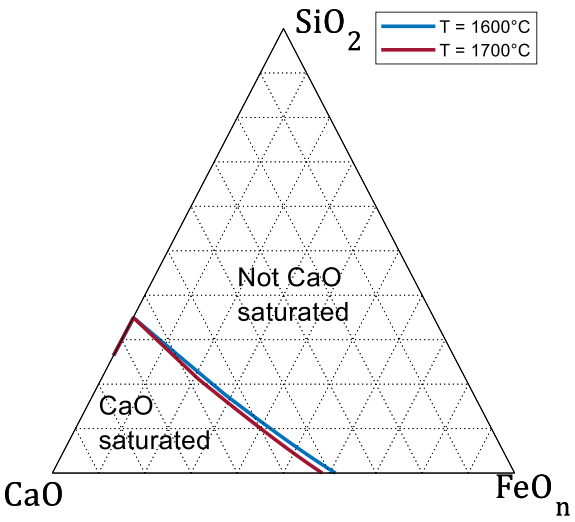

Figure 4.3: Isothermal section with indication of the CaO zero fraction line for two different temperatures to show the effect of temperature on CaO stability The corresponding diagrams where calculated in equilibrium with Fe (l).

4.1.2 The importance of C_2S stability

The dicalcium silicate solid solution stability region is shown in Figure 4.4. The temperature effect is similar to the one observed for CaO saturation. Multiple authors [1]–[6] concluded that calcium silicates are important for the dephosphorisation of the liquid steel phase: the formed P_2O_5 reacts with C_2S and forms a new solid solution, $(2CaO.SiO_2).(3CaO.P_2O_5)$. Therefore, it is said [2] the calcium silicates act as a sink for the phosphorus. These hypotheses are supported by observations [7]–[9] from microstructural investigations of the BOF slags. Even though general consensus exists in scientific literature on the importance of these calcium silicates, the exact mechanisms

remain unclear. The proposed substitution is complex and within one slag sample, calcium silicates from different origins with different morphologies and phosphorous contents have been observed [7].

Furthermore, the dicalcium silicate appears in different polymorphs. For the high temperature BOF process only the α (hexagonal structure) and α' (orthorhombic structure) type polymorphs are of interest. Both structures are stated to be built around isolated SiO_4^{-4} tetrahedral molecule [10] with differences in the orientation and the movement of the Ca-ions for the different types [11]. The C_2S regions which are shown on Figure 4.4 are solid solutions of the α type. Both α and α' structure solid solutions are included in the thermodynamic calculations, yet the α is most stable for the current system.

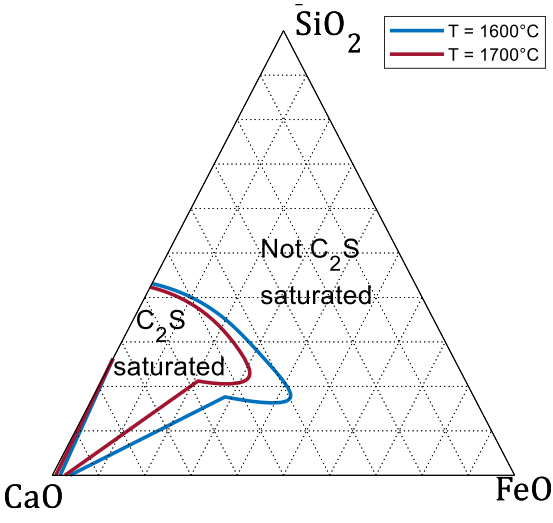

Figure 4.4: Isothermal section with indication of the C_2S zero fraction line for two different temperatures to show the effect of the temperature on C_2S stability. The corresponding diagrams where calculated in equilibrium with Fe (l).

4.2 The effect of different components

So far only the major slag components have been considered for the calculated isothermal sections of the phase diagram. In this section, the effect of different components on the liquid slag phase area of the BOF slag is discussed. For these analyses, isothermal sections at 1650°C and 1 atm are used. The considered concentrations of these species in the overall BOF-slag are shown in Table 4-1.

Table 4-1: Overview of different components and their considered contents

Component	Contents
MgO	0 wt%, 2 wt%, 5 wt%
Al_2O_3	0 wt%, 2 wt%, 5 wt%
MnO	0 wt%, 2 wt%, 4 wt%, 6 wt%

All the isothermal diagrams are calculated with either the Factsage 7.1 or the Factsage 7.2 FToxid and FactPS databases. For the considered oxides and databases no changes were reported between the Factsage 7.1 and 7.2 database versions. All the calculations are performed in equilibrium with pure liquid Fe.

4.2.1 Effect of MgO

Thermodynamic calculation

Figure 4.5 and Figure 4.6, the superimposed isothermal sections, show the effect of adding MgO to the slag system. A distinct difference is observed for the system with 5 wt% MgO compared to the ones with 0 wt% or 2 wt% MgO. While adding 2 wt% MgO results in minor changes in the isothermal section, nearly identical CaO saturation line and only a small shrinkage of the C_2S-nose is observed, the addition of 5 wt% MgO results in the appearance of a new stable phase region in the relevant composition area for BOF steelmaking. The new phase area is related to the MgO_{ss} and is indicated with a green transparent colour on the figures. Specifically, for these calculations, this is a (Mg,Fe) – oxide, called magnesio wustite, phase. Figure 4.5 shows that this phase is also present upon addition of 2 wt% MgO. However, only for very small concentration in FeO_n and without the profound effect on the liquid area of the slag. The importance of this feature should not be underestimated. It clearly shows that, thermodynamically, a slag with 2 wt% MgO will behave completely different than one with 5 wt% MgO. For a system with 5 wt% MgO, the FeO_n content, at constant basicity, needed to obtain a completely liquid slag is considerably higher than for a system without or with 2 wt% MgO. Furthermore, the slag will be saturated in MgO. Since refractory linings in BOF-vessels normally consists out of MgO-rich bricks, a slag saturated in MgO yields the advantage of being more protective towards this lining. As a final remark, this effect of adding MgO is clearly not a linear effect. The beneficial effect of MgO_{ss} stability and thus refractory wear, will only appear from a certain threshold value of MgO in the system onwards. This behaviour of MgO is generally known and used in BOF steelmaking. [12]

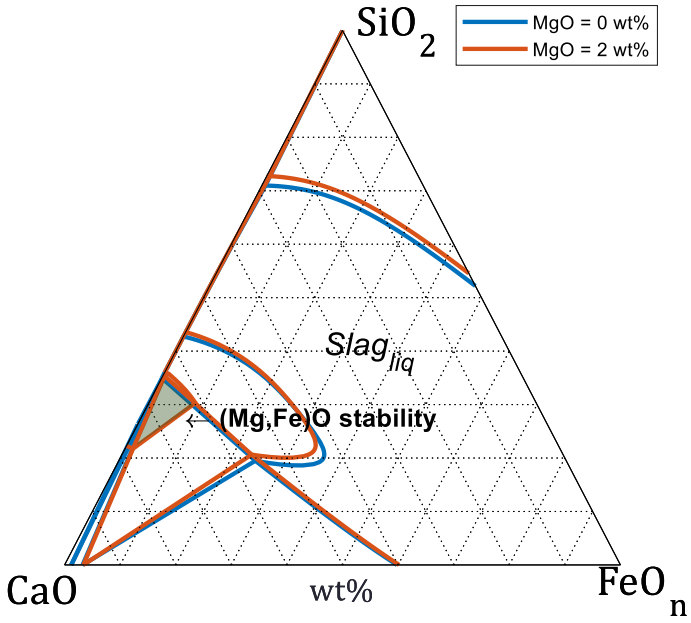

Figure 4.5: Effect of MgO on the phase stability of the isothermal pseudo-ternary phase diagram. The green coloured phase area for the 2wt% MgO isothermal section, indicates the area with magnesiowustite (Mg,Fe)O stability. Calculation at 1650°C, in equilibrium with pure Fe(l), performed with FToxid and FactPS Factsage 7.2.

A second observation from the superimposed isothermal sections in Figure 4.6 is the impact of MgO on the C_2S nose. For 5 wt% MgO it is observed this area decreases. As indicated with arrow 2 on Figure 4.6. On the other hand, arrow 1 on this figure, shows the decrease of the liquid slag area due to the magnesiowustite stability. This is an interesting observation since it means that adding MgO to the slag system will increase the liquid fraction for certain compositions while for others a clear decrease of liquid fraction is observed. This is different from the effect of temperature as discussed in the previous chapter. For an increase in temperature an unambiguous increase in liquid fraction is, thermodynamically, predicted.

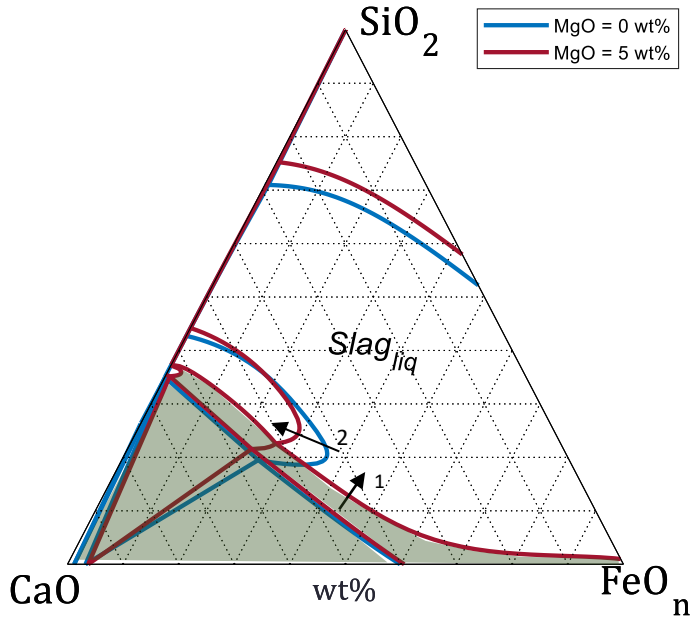

Figure 4.6: Effect of MgO on the phase stability of the isothermal pseudo-ternary phase diagram. The green coloured phase area for the 5wt% MgO isothermal section, indicates the area with magnesiowustite (Mg,Fe)O stability. Calculation at 1650°C, in equilibrium with pure Fe (l), performed with FToxid and FactPS Factsage 7.2.

Industrial observations

It is generally accepted [1]–[6], [13] in BOF steelmaking, that C_2S solids are required to obtain sufficient and good dephosphorisation during the BOF process. Decrease of the areas in which calcium-silicate solid solutions are thermodynamically stable, can impair the dephosphorisation capability of the slag. From the isothermal sections shown in Figure 4.5, it is clear that increasing the MgO content of the slag causes a decrease of these areas. This behaviour is also observed when looking at industrial data. In Figure 4.7 the phosphorus distribution coefficient[7] ($(P)_{slag}/[P]_{steel}$) as a function of the MgO content of the slag is shown. For confidentiality, both variables are normalised. For normalisation, a fixed industrial relevant minimum and maximum value was determined. As a result the normalised values range between 0 and 1. To exclude temperature effects only data from heats with a temperature in a fixed temperature interval (around 1650°C) are displayed. If the dephosphorisation is better, the phosphorus distribution coefficient will be higher, or rephrasing, when the phosphorus content of the slag increases and the phosphorus

[7] (X) denotes the concentration of a species in the liquid slag phase, while [X] denotes the concentration of a species in the liquid steel phase.

content of the steel decreases. From the results in Figure 4.7 it is clearly observed that increasing the MgO content decreases the phosphorus distribution coefficient and hence, the dephosphorisation will be worse. This observation matches with the results from the thermodynamic calculations.

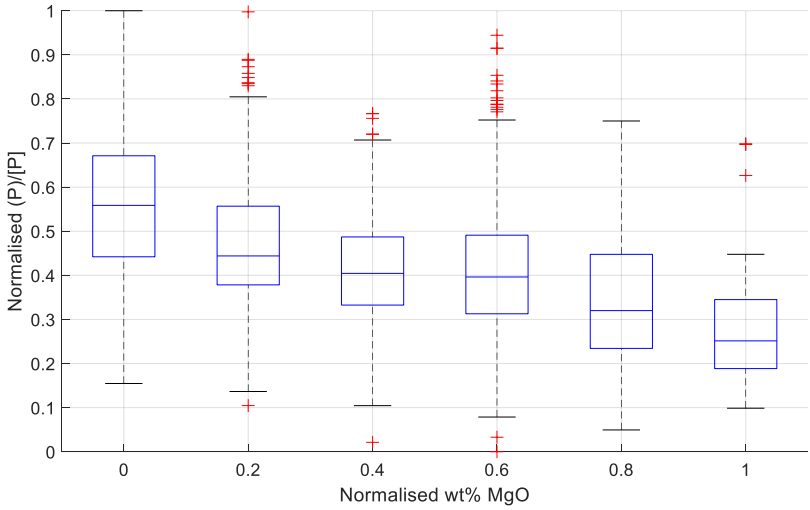

Figure 4.7: Effect of MgO content of the slag on the phosphorus distribution coefficient ($(P)_{slag}/[P]_{steel}$)) from industrial ArcelorMittal Ghent data for a fixed temperature interval around 1650°C. The box plots show the median value with indication of the first and third quartile. The error bars the lowest and largest datapoints without the outliners. The outliners are shown with red crosses. Both variables are normalised between the industrial relevant minimum and maximum value.

4.2.2 Effect of Al_2O_3

Thermodynamic calculation

In Figure 4.8 the effect of an increased Al_2O_3 content on the equilibrium behaviour of the complete BOF slag system is shown. Two features are immediately clear from this figure. Firstly, the increase in Al_2O_3 content results in an increase of the liquid area. Increasing the alumina content, decreases the liquidus point of the slag and for a fixed temperature this results in an increase in liquid area. For this reason, alumina is often mentioned [14]–[16] as a slag 'flux' (not be confused with the general term flux for BOF process additions, but used in a context of a species which will decrease the slag melting point, hence increasing liquid slag phase area and the slag's workability in practical applications e.g. increasing the liquid fraction). Secondly, the increase in Al_2O_3, induces an immiscibility of

the SiO_2-rich regions of the isothermal section. However, this second feature is of no importance for the industrial BOF-slag system because it occurs at compositions far from those used (and observed) in industrial steelmaking.

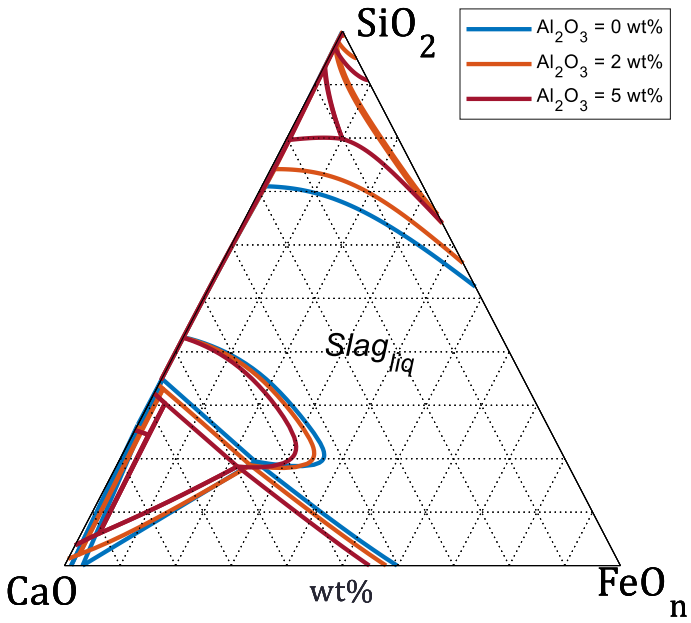

Figure 4.8: Effect of Al_2O_3 on the phase stability of the isothermal section of the pseudo-ternary phase diagram. Calculation at 1650°C in equilibrium with pure Fe(l), performed with FToxid and FactPS Factsage 7.1.

The increase in liquid area, is observed for both the C_2S saturation area as well as the CaO_{ss} saturation area. Thus, an immediate consequence of adding Al_2O_3 is the effect upon the so called saturation lines of the system. An alumina rich slag will be able to dissolve more CaO than an alumina poor slag. Practically, this means that more CaO needs to be added to the system with higher Al_2O_3 content to guarantee CaO saturation. Or that for a system with constant basicity the amount of FeO_n for which there is still CaO saturation decreases for Al_2O_3 rich BOF-slags. The saturation of CaO is desired because it is beneficial for the protection of the refractory lining. On the other hand, to obtain a completely liquid slag, then a 100% liquid slag system can be obtained with lower FeO_n contents at identical basicity in alumina rich slag systems. For the C_2S stability similar conclusions can be formulated.

Industrial observation

Increasing the liquid slag CaO capacity[8] is mentioned to have a negative impact on the refractory lining wear of the BOF vessel. From the results in Figure 4.8 it is observed that increasing the Al_2O_3 content of the slag system, increases the liquid slag CaO capacity. This observation is supported when looking at industrial data. In Figure 4.9 the effect of increasing the Al_2O_3 content of the slag on refractory wear is shown. Refractory wear is expressed as the ratio of MgO/CaO (on weight basis). Out of more than 5000 industrial heats a selection was made of heats for which the MgO target in the slag is identical and the MgO rich flux (dolomite lime) is not added. An increase in MgO/CaO ratio of the slag, for an identical MgO target, indicates higher refractory wear. In Figure 4.9 it can be seen that increasing the Al_2O_3 content increases the refractory wear. The significance of this effect is supported with T-tests, because this effect cannot be sufficiently described with a linear regression. For this T-test the industrial data was divided in a group with Al_2O_3 contents higher and Al_2O_3 contents smaller than the average of the total group. Next, the hypothesis that both groups have identical means for the MgO/CaO ratio is tested against the alternative hypothesis that these means are different from each other. The results for this student's t-test are shown in Table 4-2.

Table 4-2: T-test results for the effect of Al_2O_3 on the refractory wear. Showing both the T-value and the probability (p-value).

	|T-value|	P-value
Data Figure 4.9	10.02	0

For this type of T-test with this large number of data points, the null hypothesis is rejected in favour of the alternative hypothesis with a confidence level of 5% if the T-value is larger than 1.96. The current value clearly exceeds the value of 1.96. Additionally, the p-value approaches zero. Thus, for both groups (with high and low Al_2O_3 content) the mean MgO/CaO ratio is significantly different according to this test.

[8] Thus, more CaO can dissolve in the liquid slag and less solid CaO is present.

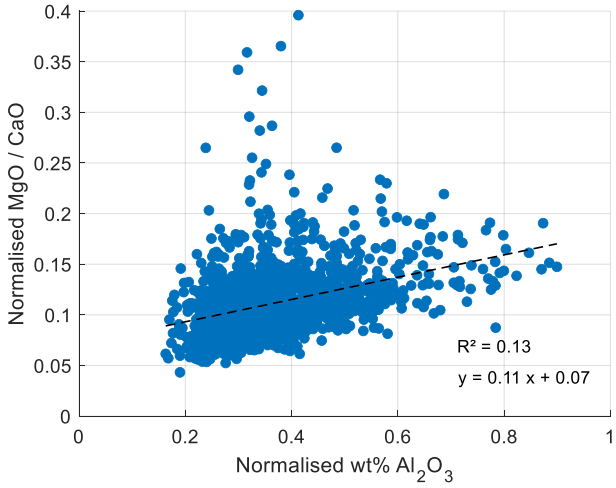

Figure 4.9: Effect of the Al_2O_3 content of the slag on the wear of refractory lining (expressed as the normalised MgO/CaO ratio).

4.2.3 Effect of MnO

Thermodynamic calculation

The effect of MnO is shown in Figure 4.10 via the superimposed isothermal sections. The changes on the isothermal section are minimal even for the addition of 6 wt% MnO. A very small shift in the CaO_{ss} stability line is observed, yet not as pronounced as the effects observed for Al_2O_3 or MgO. A clear shrinkage of the C_2S nose region is observed for increasing MnO content. However, unlike for MgO and Al_2O_3 additions the four phase area with both solid solutions CaO and C_2S present (C_2S (ss) + CaO (ss) + Slag (l) + Fe (l)) remains unchanged for increases in MnO content.

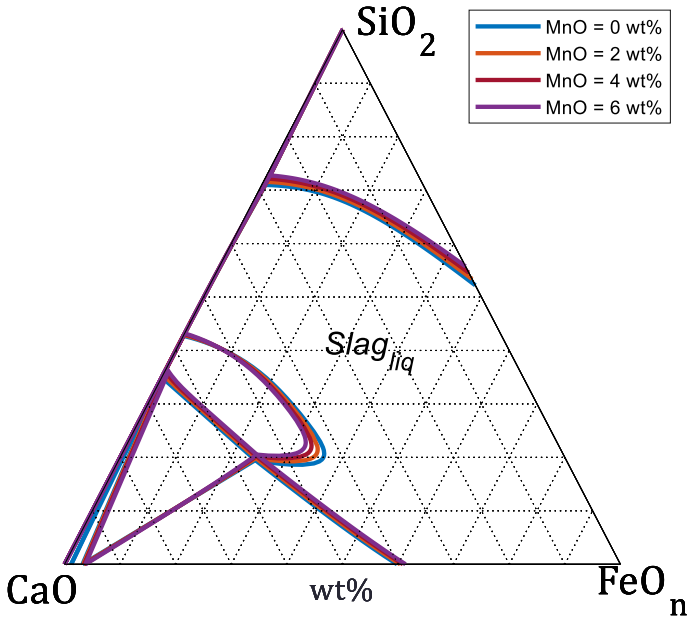

Figure 4.10: Effect of MnO on the isothermal section of the pseudo-ternary diagram. Calculation in equilibrium with pure Fe(l), performed with FToxid and FactPS Factsage 7.2.

Industrial observation

Analysis of the effect of MnO content on the refractory wear for the industrial data is shown in Figure 4.11. Similar methods as those used to describe the effect of Al_2O_3 on the refractory wear are used. The results in Figure 4.10 indicate that MnO has a limited effect on the CaO capacity of the liquid slag. Yet, the results in Figure 4.11 show similarity with the effect of Al_2O_3 which is a component that has a pronounced effect on the CaO capacity of the liquid slag. Just as for Al_2O_3 , a T-test is performed on this data to verify the significance of the effect of MnO on the refractory wear. The same method as described earlier for Al_2O_3 is applied for this purpose. The results for this student's T-test are shown in Table 4-3.

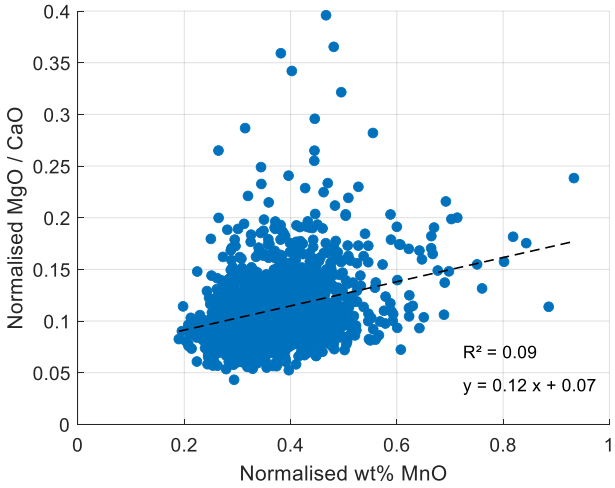

Figure 4.11: Effect of the MnO content of the slag on the wear of refractory lining (expressed as the normalised MgO/CaO ratio).

For this type of T-test with this large number of data points, the null hypothesis is rejected in favour for the alternative hypothesis with a confidence level of 5% if the T-value is larger than 1.96. The current value exceeds the value of 1.96. Additionally, the p-value approaches zero. Thus, for both groups (with high and low MnO content) the mean MgO/CaO ratio is significantly different according to this test.

Table 4-3: T-test results for the effect of MnO on the refractory wear. Showing both the T-value and the probability (p-value).

	|T-value|	p-value
Data Figure 4.11	8.72	0

The result for the industrial data are in contrast with the observations from the thermodynamically calculated isothermal sections. The industrial data clearly shows a similar effect of MnO as for Al_2O_3 and thus an increase in refractory wear. Where the isothermal sections do not show a significant increase in CaO capacity for the liquid slag for increasing MnO content, nor an increase in liquid fraction. If an effect can be observed for this on the isothermal sections, it is rather the opposite.

The changes in the C_2S stability area are, in steelmaking, linked to dephosphorisation. In Figure 4.12 the phosphorus distribution coefficient ($(P)_{slag}/[P]_{steel}$) as a function of the MnO content of the slag is shown. For confidentiality, both variables are normalised. This figure is constructed based on industrial data collected over three years (2019 -2021).

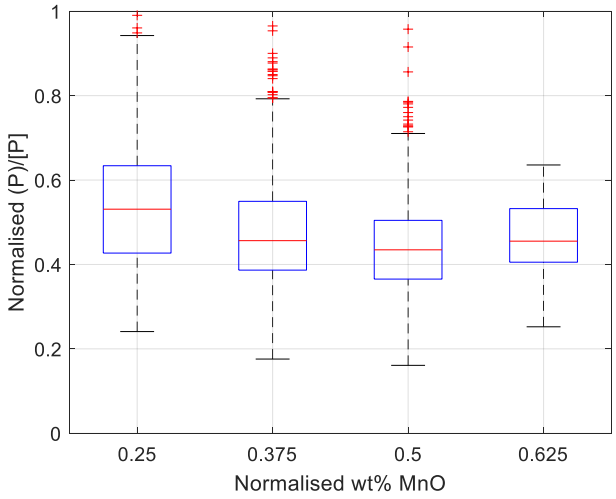

Figure 4.12: Effect of MnO content of the slag on the phosphorus distribution coefficient ($(P)_{slag}/[P]_{steel}$)) from industrial ArcelorMittal Ghent data for a fixed temperature interval around 1650°C. Both the oxygen content of the steel and the basicity of the slag phase are restricted as well to avoid including effects of these factors. The box plots show the median value with indication of the first and third quartile. The error bars the lowest and largest datapoints without the outliners. The outliners are shown with red crosses.

The initial part of the graph shows that an increase in MnO content corresponds with a decrease in the phosphorus distribution coefficient. However, after this first part the distribution coefficient remains stable as the MnO content increases. Thus, for the initial increase in MnO the industrial data corresponds to the effects observed with the thermodynamically calculated isothermal sections. Yet, for further increasing MnO content, there is no pronounced effect on the dephosphorisation of the metal bath. The calculated isothermal sections of the pseudo-ternary phase diagrams, indicate there is negative impact on the stability of the C_2S nose area upon increase of MnO content. Yet, the observed changes in the phase stability are smaller and less pronounced than these observed for Al_2O_3 and MgO. Furthermore, these changes are limited to the C_2S nose (C_2S (ss) + Slag (l) + Fe (l)), while for MgO and Al_2O_3 also a decrease in stability for the phase area with both C_2S and CaO (C_2S (ss) + CaO (ss) + Slag (l) + Fe(l)) is observed in the isothermal sections. Possibly, this is a reason why there is no strong correlation observed between an increase in MnO content and phosphorus distribution coefficient in the industrial data.

4.3 Conclusion

Phase diagrams and isothermal sections are an interesting tool to gain basic insights on the effect of different slag components on industrial slag features. In this chapter special focus was put on the stability of either CaO rich solid solutions (CaO_{ss}) or MgO rich solutions (Magnesiowustite) and on the calcium silicate ($Ca_2SiO_{4,ss}$) rich regions. Both features have a distinct visibility on the isothermal section. Furthermore, they also play an important role in the industrial BOF slag. The effect of three different components: MgO, Al_2O_3 and MnO on the isothermal sections is discussed. The thermodynamically observed trends were verified with industrial observations. Increasing the MgO content will especially decrease refractory wear, yet not in a linear way. Secondly, an increase in MgO content has a negative effect on dephosphorisation. When the Al_2O_3 content of the slag is increased refractory wear will increase as well. Finally, increasing the MnO content of the slag only has minor effects according to the thermochemical data, while for the industrial data effects on refractory wear were observed. It is unclear why there is a discrepancy for this component. For the dephosphorisation the effect of MnO, according to the industrial data, is however limited.

4.4 References

[1] R. Inoue and H. Suito, “Phosphorous partition between 2CaO· SiO2 particles and CaO–SiO2–FetO slags,” *ISIJ Int.*, vol. 46, no. 2, pp. 174–179, 2006.

[2] K. Shimauchi, S. Kitamura, and H. Shibata, “Distribution of P2O5 between solid dicalcium silicate and liquid phases in CaO–SiO2–Fe2O3 system,” *ISIJ Int.*, vol. 49, no. 4, pp. 505–511, 2009.

[3] F. Pahlevani, S. Kitamura, H. Shibata, and N. Maruoka, “Distribution of P2O5 between solid solution of 2CaO· SiO2–3CaO· P2O5 and liquid phase,” *ISIJ Int.*, vol. 50, no. 6, pp. 822–829, 2010.

[4] M. Ek, J.-C. Huber, G. Brosse, and D. Sichen, “Capacities of some CaO–SiO2–FeO–MnO–MgO slags and slag–solid mixtures in capturing phosphorous,” *Ironmak. Steelmak.*, vol. 40, no. 4, pp. 305–311, 2013.

[5] H.-M. Zhou, Y.-P. Bao, and L. Lin, “Distribution of P2O5 between Phosphorus-Enrichment Phase and Matrix Phase in Phosphorus-Containing Slag,” *Steel Res. Int.*, vol. 84, no. 9, pp. 863–869, 2013.

[6] N. Wang, Z. Liang, M. Chen, and Z. Zou, “Phosphorous Enrichment in Molten Adjusted Converter Slag: Part II Enrichment Behavior of Phosphorus in CaO-SiO2-FeOx-P2O5 Molten Slag,” *J. Iron Steel Res. Int.*, vol. 18, no. 12, pp. 22–26, Dec. 2011, doi: 10.1016/S1006-706X(12)60004-1.

[7] C. Duée *et al.*, “Phosphorus speciation in dicalcium silicate phases: Application to the basic oxygen furnace (BOF) slag,” *Cem. Concr. Res.*, vol. 73, pp. 207–214, Jul. 2015, doi: 10.1016/j.cemconres.2015.03.012.

[8] M. Gautier, J. Poirier, F. Bodénan, G. Franceschini, and E. Véron, “Basic oxygen furnace (BOF) slag cooling: Laboratory characteristics and prediction calculations,” *Int. J. Miner. Process.*, vol. 123, pp. 94–101, Sep. 2013, doi: 10.1016/j.minpro.2013.05.002.

[9] F. Bodénan *et al.*, “Phosphorus speciation in dicalcium silicate polymorphs of basic oxygen furnace (BOF) slag–Preliminary results,” *Déchets Sci. Tech.*, no. 57, pp. 5-p, 2010.

[10] N. A. Yamnova, N. V. Zubkova, N. N. Eremin, A. E. Zadov, and V. M. Gazeev, “Crystal structure of larnite β-Ca2SiO4 and specific features of polymorphic transitions in dicalcium orthosilicate,” *Crystallogr. Rep.*, vol. 56, no. 2, pp. 210–220, Mar. 2011, doi: 10.1134/S1063774511020209.

[11] C. Remy, D. Andrault, and M. Madon, “High-Temperature, High-Pressure X-ray Investigation of Dicalcium Silicate,” *J. Am. Ceram. Soc.*, vol. 80, no. 4, pp. 851–860, Apr. 1997, doi: 10.1111/j.1151-2916.1997.tb02914.x.

[12] Process engineer at ArcelorMittal Ghent, “Private communication.”

[13] S. Basu, A. K. Lahiri, and S. Seetharaman, “Phosphorus Partition between Liquid Steel and CaO-SiO2-FeOx-P2O5-MgO Slag Containing 15 to 25 Pct FeO,” *Metall. Mater. Trans. B*, vol. 38, no. 4, pp. 623–630, Aug. 2007, doi: 10.1007/s11663-007-9063-0.

[14] K. Koch, M. Juhart, M. Peter, and J. Lamut, “Influence of alumina and magnesia on phase equilibria in the system Fe-CaO-FeOn-SiO2 at 1600 °C,” *Steel Res.*, vol. 72, no. 9, pp. 331–336, Sep. 2001, doi: 10.1002/srin.200100127.

[15] B. Zhao, E. Jak, and P. C. Hayes, “The effect of Al2O3 on liquidus temperatures of fayalite slags,” *Metall. Mater. Trans. B*, vol. 30, no. 4, pp. 597–605, Aug. 1999, doi: 10.1007/s11663-999-0020-y.

[16] H. Kimura, T. Ogawa, M. Kakiki, A. Matsumoto, and F. Tsukihashi, “Effect of Al2O3 and MgO Additions on Liquidus for the CaO-SiO2-FeOx System at 1573 K,” *ISIJ Int.*, vol. 45, no. 4, pp. 506–512, 2005, doi: 10.2355/isijinternational.45.506.

5 Models for physical slag properties

This chapter gives an overview of the state-of-the-art models for calculation of different slag properties which are relevant for this work. Firstly, the structure of a slag is described. This because the slag structure is important for one of the most important physical material properties of slags in industrial applications: the viscosity. Next, the slag's viscosity is discussed. The concept of structural based viscosity and the model used in this dissertation to calculate the slag viscosity are covered. Methods to integrate solid fractions into liquid slag viscosities are assessed in a separate paragraph. Furthermore, also the slag's density and surface tension are discussed. For both properties a small introduction highlighting their importance for industrial application is given together with a brief description of the model used to calculate these properties in the current dissertation.

5.1 On structure of slags

Generally, slags are described as phases consisting out of a mixture of oxides. However, molten slags are ionic in nature. They consist out of a mixture of cations and anions. [1], [2] Yet, reality is more complex and a silicate network is assumed to be neither covalent or ionic, but to have a fractional ionic character. [3] Even though slags are ionic in nature they are described in terms of the constituent's oxides. Due to difficulties in ion activity determination, the activity of the components is expressed as the activity of the associated oxide.

BOF-slags are silica rich slags and their fundamental building unit is a negatively charged complex silicate anion: SiO_4^{-4}. The silicate anion is also known as the silicate tetrahedron. In this silicate tetrahedron, the silicon atom will be surrounded by four oxygen atoms, while each oxygen atom can have up to two silicon neighbours. The linking oxygen atoms are known as bridging oxygen atoms (BO). In silica the silicate tetrahedrons are joined into a hexagonal network, forming a structure in three dimensions. For solid silica the structure is crystalline. During melting, due to thermal agitation, this network is broken. However, only at very high temperatures the molten silica would decompose into SiO_4^{-4} and Si^{4+} ions.[4] Usually, the working temperatures in pyrometallurgy are high enough to melt the silica, yet not high enough to decompose the network completely. A

schematic drawing for the molten silica is shown in Figure 5.1 (a). The silica will form a network of silica chains. This is sometimes referred to as polymerisation behaviour.

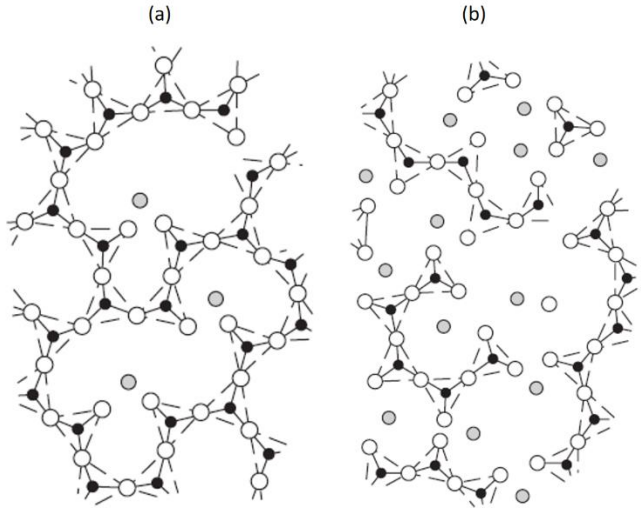

Figure 5.1: (a) Molten silicate network. (b) Broken silicate network. Taken from [2]. The black sphere represent the silicon, the white sphere the oxygen and the grey spheres the network modifier e.g. Ca, Mg, Fe, etc.

In steelmaking a slag consists of multiple oxides, which all will have an influence upon the slag structure. Generally, oxides are classified according to the effect they have upon the network structure. A first category of oxides are those who will, just as SiO_2, form complex anions. These oxides act as network forming oxides and thus accept oxygen ions. The most important network former for oxygen steelmaking slags, apart from silica, is P_2O_5. Also V_2O_5 is mentioned [5],[3], [6] as an network forming oxide. To be a network forming oxide, and thus replace Si^{4+} in its tetrahedral structure, the cation should have similar ionic radius and a formal electrical charge of about 4. If the formal electric charge does not equal 4, charge compensation by other ions will be necessary. [3] Network forming oxides are in general called acidic oxides. [7] A second group of metal oxides will break down the silicate network. This behaviour is schematically represented in equation 5.1 and in Figure 5.1 (b). [2] These oxides modify the network and donate oxygen anions. They are often called basic oxides. [2], [7] Due to the presence of this type of oxides, not only bridging oxygen atoms (BO), but also non-bridging (NBO) or even free oxygen (FO) will be present in the network. The most important basic oxides in BOF-slags are CaO and FeO, but also MgO, MnO and TiO_2 will act as network modifiers, thus breaking down the silicate network. [3]

$$\left(- \begin{array}{c|} \\ Si \\ | \end{array} - O - \begin{array}{c|} \\ Si \\ | \end{array} - \right) + MO \rightarrow 2 \left(- \begin{array}{c|} \\ Si \\ | \end{array} - O \right)^{-} + M^{2+} \qquad (5.1)$$

A third group of metal oxides is known as amphoteric oxides. These oxides will behave differently depending upon the considered system. Al_2O_3, Cr_2O_3 and Fe_2O_3 are considered to be amphoteric oxides, relevant for steelmaking. Aluminium oxide could either act as a network modifying oxide by forming Al^{3+} cations or as a network forming element by forming a complex anion with oxygen. Mysen and Richet [3] mention that the final behaviour of amphoteric oxides is influenced by the possibility of the aluminium ion to be charge compensated by other cations present. According to Virgo and Mysen [8] for the ferric ion (Fe^{3+}) the behaviour can also be linked with the coordination of the ion. When a silicate melt containing iron is oxidised ($\frac{Fe^{3+}}{\sum Fe} > 0.5$), the ferric ion will be in a tetrahedral coordination and act as network former, while when the conditions of the melt are reducing ($\frac{Fe^{3+}}{\sum Fe} < 0.3$) the ion will be in a octahedral coordination and act as network modifier. [9] Yet, one should be careful in linking tetrahedral coordination immediately with the network forming behaviour. [3] In Table 5-1, an overview is given of the nature of different oxides encountered in BOF-slags. It is also important to understand that even when oxides belong to the same category, one oxide might have a much stronger effect than the other.

Table 5-1: Overview of the classification of different oxides relevant for steelmaking slags.

Network former (acid)	Amphoteric	Network modifier (basic)
SiO_2 P_2O_5 V_2O_5	Al_2O_3 Fe_2O_3 Cr_2O_3	CaO MgO FeO MnO TiO_2

The final properties and behaviour of the slag will depend upon composition and temperature. Structure related properties depend on the degree of polymerisation of the slag, or the types and relative amount of oxygen present in the slag under the specific conditions. As mentioned earlier the slag can contain three types of oxygen atoms [10]: bridging oxygen (BO), non-bridging oxygen (NBO) and free oxygen (FO). Their distribution

depends upon the oxides present in the slag. A small example to get some idea of the concept: in a 100% pure silica melt, only BO is present. When lime (CaO) is added to the system also NBO and possibly FO will be present in the slag. The two slags are said to have a different degree of polymerisation. The pure silica has a higher degree of polymerisation than the one with lime added.

5.2 On viscosity of slags

Slag viscosities are strongly linked with the slag structure. Already a vast amount of literature about the viscosity of silicate slags and slag structure based models to calculate this viscosity, is available. In this paragraph a general overview is given on some of the important structure based calculation models (the reader is referred to Kondratiev. et al. [11] for a more in-depth analyses and discussion). The finally implemented model to calculate the viscosity of the BOF slags in this work is the 'modified quasi-chemical' viscosity model. However, first some general aspects of viscosity calculations are given. In industry, the slag is rarely completely liquid. Most often the slag will be a liquid containing one or multiple solid phases. The last part of this section discusses the possibility to integrate solid particles into the viscosity calculation.

Liquid metals will have viscosities within the 10^{-3} – 10^{-2} Pa s range, while molten slags have viscosities within the 10^{-2} – 10^{10} Pa s. [11] In comparison, water has a viscosity of 10^{-3} Pa s. Liquids with viscosities greater than 15-25 Pa s are considered too difficult to tap. [11] The unit of viscosity is either Pa s or poise (1 Pa s = 10 poise). However, in this work either Pa s or mPa s are used unless clearly stated otherwise.

The viscosity of industrially relevant slags is strongly linked with the structure or degree of polymerisation of the slag. Slags which have a complete silicate network, or in other words a strongly polymerised network, will have a high viscosity. Slags which contain a lot of basic (or network modifying) oxides will have a lower viscosity due to the broken down network, i.e. the presence of NBO and FO next to BO. However, considering the composition, the increase or decrease of viscosity is not a linear function. Different models can be proposed to model the viscosity. Often, models are semi-empirical and some experimental data will be needed to define certain parameters to calculate the viscosity for a range of compositions where experiments are lacking.

To include temperature dependence of the molten slag in the viscosity calculation a number of the viscosity models start from an Arrhenius equation, equation 5.2.

$$\ln(\eta) = A + \frac{E}{RT} \tag{5.2}$$

In this equation η is the viscosity, A the pre-exponential factor, T the absolute temperature (K) and R the absolute gas constant. The final parameter in this equation, E (J/mol), is the activation energy. Further linking of these parameters with the considered slag composition, temperature and structure depend upon the used viscosity model. Other models use the Eyring viscosity equation, equation 5.3 [12], to calculate temperature dependent viscosity.

$$\eta = \frac{2RT}{\Delta E_v} \frac{(2\pi m_{SU} kT)^{\frac{1}{2}}}{v_{SU}{}^{\frac{2}{3}}} \exp\left(\frac{E}{RT}\right) \tag{5.3}$$

In this equation R and k are respectively the gas (J/ (K mol)) and Boltzmann (J/K) constant, T is the absolute temperature (K), E and ΔE_v are, respectively, the activation and the vaporization energy (J/mol). The parameters m_{SU} and v_{SU} are the weight (kg) and volume (m^3) of the structural unit of viscous flow.

In a series of articles, Zhang and Chou et al. [9], [13]–[16] propose a structure based viscosity model. for calculation of the viscosities of CaO-MgO-FeO-MnO-SiO_2 completely molten slags. Later on, further extensions were made for addition of more components which have more complex interactions such as Al_2O_3. The model of Zhang and Chou uses the concept of 'flow with cutting – off points' introduced by Nakamoto et al. [17] to define their activation energy. The temperature dependence is integrated with an Arrhenius equation. For more complicated slags (e.g. containing aluminium oxide), the set of equations to calculate the number of different oxygen atoms present in the slag increases to a large number. From the two equations used for the simple slag systems, the set of equations enlarges to 16 equations for industrial relevant slags. This is considered as the first downside of this model. Secondly, the model assumes the principle of complete bridge breaking. This is a very rough estimation. Comparison [13] of the calculated with measured viscosities, shows a good match for relatively low viscosities. However, within the same binary system, the mismatch between measured and calculated viscosities increases for relatively increasing viscosities values. This is never mentioned nor explained by the authors. Yet, general viscosity trends still seem to be correctly represented by this model.

The quasi-chemical (QCV) viscosity model is described by Kondratiev et al. [18]–[21]. Initially, this model was developed to describe the effect of MgO on the slag's viscosity.

The overall aim is to be able to predict the viscosity, for all temperatures and compositions, with the same set of model parameters. [18] For this purpose, a link was established between the physicochemical properties of the slag and the fundamental thermodynamics. The QCV model considers the three different types of oxygen (described as structural units, as shown in Table 5-2) and both activation energy (E) and vaporization energy (ΔE_v) are calculated as a weighted sum of the individual activation and vaporization energies of the different structural units. The temperature dependency is included in the model via an Eyring equation.

Table 5-2: Proposed symbols for the different types of oxygen atoms present.

BO	NBO	FO
Si – Si	Si – Me	Me – Me

Even though the polymerisation behaviour of the slag system is more accurately described within this model compared to the model of Zhang and Chou, this model still requires a large number of parameters that need to be fitted, as also argued by Grundy et al. [22]. For this reason Grundy et al. [22] proposed a different model: modified quasi-chemical viscosity (MQCV) model, which requires less parameters. This last model (the MQCV model) is used in this work and described in the next section.

5.2.1 The modified quasi-chemical viscosity model

Different Canada based authors [22]–[26] developed another approach for the viscosity calculation for liquid slag systems. Their model is known as the modified quasi-chemical viscosity (MQCV) model. The MQCV model is also structure based but with integration of the modified quasi-chemical thermodynamic model to calculate relevant thermodynamic parameters. Thus, in essence the same approach and data is used as by Kondratiev. et al. [19]–[21] in the QCV model. Yet, the MQCV model is claimed to be more simple in use than the previous mentioned ones, due to the simple correlation established between the polymerisation of the silicate melt and the viscosity, resulting in different and simpler expressions for activation energies. Additionally, the few parameters that need to be optimized, are stated to have a physical meaning. Temperature dependence is included with an Arrhenius equation.

The connectivity of the silicate melt, is calculated based upon the concentration of bridging oxygen atoms present in the slag. In the MQCV model the parameters for the

Arrhenius equation are related to temperature, composition and polymerisation degree through the expressions in equation 5.4.

$$E = \sum_M (x_M E_M) + \sum_M \sum_{i,j} (x_M^i x_{Si}^j E_M^{i,j}) + x_{Si}(E_{Si} + E_{Si}^E p^{40} + (p^4 - p^{40}) \frac{\sum_M x_M E_M^R}{\sum_M x_M})$$

$$A = \sum_M (x_M A_M) + \sum_M \sum_{i,j} (x_M^i x_{Si}^j A_M^{i,j}) + x_{Si}(A_{Si} + A_{Si}^E p^{40} + (p^4 - p^{40}) \frac{\sum_M x_M A_M^R}{\sum_M x_M}) \quad (5.4)$$

The composition is described with the parameters x_M and x_{Si} which are the molar fractions of network modifiers and silica. The parameter *p* is the probability of an oxygen atom to be a bridging oxygen. Details on how to calculate this probability are given in the next paragraph. However, as a consequence p^4 is the probability that a silicon atom is surrounded by four BO and p^{40} the probability to find a silica cluster with 40 BO. Alternatively, the later can be read as [26]: "*the probability that a given Si atom is part of a cluster of at least 40 interconnected Si-Si pair*". The integers *i* and *j* are strictly positive, but for most of the work by Grundy et al. [22]–[25] *i* and *j* are both set equal to 1. The different E_M and A_M values in equation 5.4 are statistically fitted. The subscripts *'E'* and *'R'* stand for 'Excess' and 'Remainder' respectively. Both are used to describing the contribution of silicon to the viscosity. The excess contribution is an extra term in the expression, due to the network forming behaviour of silica. The remainder contributions originate from the theory that a critical cluster size of Si-Si pairs exists which will cause a drastic increase in viscosity. However, the clusters with less Si-Si pairs than the critical value, will have a stronger, and thus different, interaction with the basic oxides present in the system. To describe these interactions with the basic oxides, the remainder contributions are used. An overview of the fitted parameters as collected by Cnockaert [27] is given in Table 5-3.

Another, required parameter to be able to calculate E and A, is the degree of polymerisation (p). It is assumed the polymerisation of the network will be one of the main influences on the viscosity of the slag. To determine for a given slag composition and temperature the degree of polymerisation of the system, the concept that three different types of oxygen are present in the slag is used. To explain this approach the notations displayed in Table 5-2 are used to describe the different types of oxygen atoms. [22] The breaking down of the network is expressed as a quasi-chemical reaction, as

shown in equation 5.1. The polymerisation of the network can be calculated as the probability that a silicon atom is connected to another silicon atom in the slag, according to equation 5.6. [26] In this equation, *n* is the total number of pairs (either Si-Si or Si – Me).

$$(\mathrm{Si}-\mathrm{Si})+(Me-Me)\Leftrightarrow 2\,(Si-Me) \tag{5.5}$$

$$p=\frac{2\,n_{Si-Si}}{2\;n_{Si-Si}+\;\;n_{Si-Me}} \tag{5.6}$$

Statistical approaches in which the reaction in equation 5.5 is considered as a forward reaction, are one possibility to calculate the polymerisation. However, to calculate the viscosity more accurately, the reaction given in equation 5.6 should be considered as a true equilibrium. Thermodynamic software, such as Factsage or Chemapp, allows for calculation of the equilibrium amount of each type of bond. These calculations are based on thermodynamics and as such more accurate.

Table 5-3: : Overview of the relevant A and E parameters for the MQCV model. [27]

A		$E\left(\frac{J}{mol}\right)$	
A_{Si}^{E}	-6.128	E_{Si}^{E}	298493
A_{Al}	-9.22	E_{Al}	120400
A_{Si}	-10.559	E_{Si}	217225
A_{Ca}	-12.27	E_{Ca}	137650
$A_{Fe^{2+}}$	-8.75	$E_{Fe^{2+}}$	52500
$A_{Fe^{3+}}$	-8.63	$E_{Fe^{3+}}$	47250
$A_{Al}^{1,1}$	0	$E_{Al}^{1,1}$	-75000
$A_{Si}^{1,1}$	0	$E_{Si}^{1,1}$	0
$A_{Ca}^{1,1}$	0	$E_{Ca}^{1,1}$	-101750
$A_{Fe^{2+}}^{1,1}$	0	$E_{Fe^{2+}}^{1,1}$	-115000
$A_{Fe^{3+}}^{1,1}$	0	$E_{Fe^{3+}}^{1,1}$	-107500
A_{Al}^{R}	-12.30	E_{Al}^{R}	303500
A_{Si}^{R}	0	E_{Si}^{R}	0
A_{Ca}^{R}	0	E_{Ca}^{R}	81400
$A_{Fe^{2+}}^{R}$	0	$E_{Fe^{2+}}^{R}$	87525
$A_{Fe^{3+}}^{R}$	0	$E_{Fe^{3+}}^{R}$	88500

So far only network modifiers, basic oxides breaking down the silicate structure, were mentioned. However, in reality a slag can also contain amphoteric oxides such as Al_2O_3. This means that Al^{3+} could act as network former or modifier. The ion must be charge compensated, to guarantee charge neutrality, to be a network former. This is due to the different partial charge of Al^{3+} compared to Si^{4+}. In BOF slags, Mg^{2+} and Ca^{2+} are considered for charge compensation. Together, these ions will form associates: $CaAl_2O_4$ and $MgAlO_4$. However, when the viscosity of the system is calculated based upon the structure, starting from data of a quasi-chemical model, as will be explained later, there is no possibility to make a distinction between aluminium ions which will act as network formers or modifiers. The model compensates for this fractions of the network forming

Al^{3+} and network modifying Al^{3+} with separate equilibrium reactions [25]. The relevant reactions for the BOF slag system are shown in equation 5.7 and 5.8.

$$2AlO_{1.5} + CaO \leftrightharpoons CaAl_2O_4 \quad (5.7)$$

$$2AlO_{1.5} + MgO \leftrightharpoons MgAl_2O_4 \quad (5.8)$$

For these two reactions the equilibrium constants can be calculated from the activities of each species. Yet, since a thermodynamic database does not include these structural differences, it is impossible to retrieve this activity via standard thermodynamic databases. A separate equilibrium has to be calculated for which new Gibbs free energies are defined. The expression used by Grundy et al. [25] are given in Table 5-4. As can be seen, the formation of the charge compensated tetrahedron with Al^{3+} is influenced by the presence of silica. From these Gibbs free energies, equilibrium constants and thus, activities can be calculated for the considered reactions. For this, it is assumed the activities are equal to the (molar) concentrations of the species.

Table 5-4: Overview of Gibbs free energy for the extra considered reactions

System	*Gibbs free energy*
CaO-$AlO_{1.5}$-SiO_2	$\Delta G^0_{CaAl_2O_4} = 5 - 100\, x_{SiO_2}$
MgO-$AlO_{1.5}$-SiO_2	$\Delta G^0_{MgAl_2O_4} = 13 - 105\, x_{SiO_2}$

With this assumption, so called 'equivalent mole fractions' are calculated. This is symbolically expressed in equation 5.9 in which x'_i is the equivalent mole fraction, x_i is the mole fraction of a component in the considered system (calculated from a standard thermodynamic database), x_{Al}^{form} is the mole fraction aluminium which acts as a network former (calculated with a separate equilibrium calculation) and x_i^{comp} is the mole fraction CaO or MgO required for charge compensation. The mole fractions of CaO and MgO need compensation for their participation in the network forming role of aluminium as charge compensators. Furthermore, it is assumed the network forming aluminium will have identical influence as silica. Resulting a new fraction for silica i.e. the mole fraction of silica plus the mole fraction of alumina network forming oxide and a new fraction for the network modifying aluminium oxide i.e. mole fraction of all alumina minus the mole fraction of alumina network forming oxide. Identical reasoning and expressions are used for Fe^{3+}.

$$x'_{Si} = x_{Si} + x_{Al}^{form}$$
$$x'_{Al} = x_{Al} - x_{Al}^{form} \quad (5.9)$$
$$x'_{Ca,Mg} = x_{Ca,Mg} - x_{Ca,Mg}^{comp}$$

5.2.2 The viscosity of heterogeneous slags

In the previous section, different models are explained to calculate the viscosities of completely molten slags. In reality, slag systems are often not 100% liquid and will contain solid fractions. These solid fractions will influence the effective, or apparent, viscosity of the complete system.

Most often, a relative viscosity is introduced to describe the viscosity of heterogeneous slags. The definition is given in equation 5.10, in which η_S is the viscosity of a suspension and η_L the viscosity of the suspending liquid. This ratio is stated [28] to be mainly influenced by the volume fraction of solids, shape and size of the solid phase particles present in the liquid. Furthermore, recent literature [28], [29] indicates the non-Newtonian characteristics for heterogeneous slags.

$$\eta_r = \frac{\eta_S}{\eta_L} \quad (5.10)$$

The first viscosity model for a solid-liquid system [30] was derived by Einstein [31]. In this model, the solids are assumed to be spherical and monodisperse and the system is treated as a dilute suspension. This model gives rather good results when the solid fractions are extremely low (i.e. < 1 or 2 vol%). The heterogeneous viscosity is given by:

$$\eta_r = \frac{\eta_S}{\eta_L} = 1 + 2.5\,\Phi \quad (5.11)$$

The volume fraction of the solids (Φ) is an important parameter to determine the viscosity of liquids containing solid particles. Different methods could be applied to either measure or calculate this parameter. Measurements based on SEM or OM images of quenched samples are still the most used approach [28] to determine the solid volume fraction of silicate melts. Image processing software is a valuable tool for this purpose. For this method to yield accurate results, the analysed sample area should be sufficiently large and random distribution of particles is required. Calculation of the volume fraction is a much more elegant and easy solution. Kondratiev and Jak [32] suggested the volume fraction for Al_2O_3-CaO-FeO_n-SiO_2 can easily be calculated with an approach also

formulated by Mills et al [33]. They used experimental data obtained by Bottinga et al. [34] and obtained results with an uncertainty of 3% upon assuming the mean partial molar volume as the actual partial molar volume for each oxide component. The expressions for this are given in equations 5.12 and 5.13. The subscripts 'S' and 'L' indicate the solid and liquid volume respectively. To calculate the total volume a linear combination of the partial molar volumes for each oxide (in solid and liquid form) is used.

$$\Phi = \frac{V_S}{V_S + V_L} = 1 - \frac{V_L}{V_S + V_L} \tag{5.12}$$

$$V_{L,S} = \sum \bar{V}_i \, n_i \tag{5.13}$$

When volume fractions of solids are higher, the particle-particle interaction will also influence the viscosity and the equation of Einstein no longer provides reliable values. Yet, this interaction is very complicated and no pure theoretical model, covering all composition ranges, exists at the moment. [28], [30] Empirical relations are used to fill the current gap. The two most often used empirical equations in silicate systems are the Krieger-Dougherty (KD) [35] and the Einstein-Roscoe (ER) [36] type equations. For these equations the assumption is made that all particles are suspended in the liquid and there is no contact between the different particles.

$$KD: \quad \eta_r = \left(1 - \frac{\Phi}{\Phi_m}\right)^{-[\eta]\Phi_m}$$
$$ER: \quad \eta_r = (1 - K\Phi)^{-B} \tag{5.14}$$

In the KD equation $[\eta]$ is the intrinsic viscosity (this is a dimensionless variable) and Φ_m is the maximum packing fraction. [30] Different proposed expression which consider the particle size and shape could be found in literature [28] to determine Φ_m and $[\eta]$. For the ER equation an overview of different empirical parameters is given in Table 5-5.

Table 5-5: Overview of different emperical parameters for the Einstein Roscoe equtions.

K (or R)	B (or n)	Application	Comment	reference
1.35	2.5	Rigid spheres, equal sizes	Good fit	[36]
1	2	Rigid spheres, very diverse sizes	Good fit	[36]
2.04	1.29	Al_2O_3-CaO-FeO-SiO_2 reducing conditions	Up to 30 vol% Dataset Hurst [37], [38]	[32]
7.59	0.64	Industrial BOF slag sample	/	[39]
8.54	0.35	Industrial BOF slag sample	/	[39]

Liu et al. [39] demonstrated that for slags with very similar composition, and fraction of solids, at the same temperature, the viscosity can be considerably different. For their two similar industrial BOF slag samples they found different parameters to fit the measured viscosities with Einstein-Roscoe. Yet, no satisfying explanation was given by the authors for this observation. Furthermore, Liu et al. [40] reported an abrupt viscosity increase when solid particles start to form clusters. In a recent review Liu et al. [28] concluded the effect of particle size and shape upon the viscosity has not yet been fully understood. However, according to their interpretations, it is the longest axis of the particle which will characterize the size concerning viscosity related effects. Furthermore, when the particles are not spherical, the viscosity will increase (compared to when they are assumed to have a perfect spherical size). Rod-like particles are stated to result in the highest viscosity, followed by disk-like, ellipsoidal and spherical particles. Yet, also other parameters such as roughness might have a considerable effect upon the final viscosity

of the heterogeneous system. Up till today, general understanding of the effect of solid particles on the slag viscosity remains limited.

5.3 On density of slags

Density is mentioned as an important parameter for slag foaming. Firstly, because it appears directly in most expressions proposed in literature for the slag foaming index (as will be discussed in one of the next chapter of this dissertation). Secondly, the relation between the liquid viscosity and the viscosity of the liquid with solid particles dispersed into it requires calculation of the solid volume fraction. Standard, the obtained fractions from the thermodynamic calculations are either mole or weight fractions.

Summary of the data found in literature related to slag densities is given by Mills and Keene [33]. Different techniques exist for slag density measurements: hydrostatic weighing method, maximum bubble pressure method and sessile drop method. The experimental uncertainty for density measurements are about ± 2%. Slags containing Fe are quite tricky on this behalf. Both Fe^{2+} and Fe^{3+} will be present yet, the exact ratio will vary over temperature and composition range. This makes the measurement for FeO containing slags extra difficult, due to the different contribution FeO and Fe_2O_3 will have upon the final overall slag density.

Mills and Keene [33] proposed calculation of density via the weighted molar mass and weighted molar volume approach. This is often referred to as the additive model for density. Expressions are shown in equation 5.15, 5.16 and 5.17. M and V are the weighted mass and volume, x_i is the mole fraction, M_i the molar mass and $\bar{V}_i$ the molar volume of the component.

$$V = \sum \bar{V}_i \, x_i \tag{5.15}$$

$$M = \sum M_i \, x_i \tag{5.16}$$

$$\rho = \frac{M}{V} \tag{5.17}$$

Most often molar volume is assumed to be the volume of the pure component. However, slags density will also be influenced by their structure as was pointed out by Lee and Gaskell [41] and Grau and Masson [42]. Especially for silica, which will, depending upon its concentration, arrange differently in the slags (the network forming aspect), errors

are introduced when constant molar volume is assumed. To solve this issue, different approaches are proposed. Bottinga and Weill [43] determined different molar volumes for the oxides components from experimental data, while assuming a constant molar volume for silica within a 40 – 80 wt% SiO_2 range. For BOF steelmaking slags these ranges are nevertheless useless. Bottinga et al. [34] tried to compensate for structural effects, by making the molar volume dependent upon the concentration of silica and alumina in the slag. Mills and Keene [33] argued that this model predicts values within the 2-3% range of measurements, but that it is also a complicated model. Furthermore, the composition ranges considered by Bottinga et al. [34] are not relevant for BOF slags. Mills and Keene [33] propose, an alternative approach to calculate the density of slags containing silica and alumina. A composition dependency is introduced for the molar volumes of SiO_2 and Al_2O_3. For Silica the values are derived from thorough evaluation of the FeO-SiO_2, CaO- SiO_2, MnO- SiO_2, Na_2O- SiO_2, K_2O- SiO_2 and CaO-FeO- SiO_2 systems. Excellent agreement between calculated values and measurements was obtained for all these systems apart for the MnO-SiO_2 system. Mills and Keene [33] argue this is due to the nature of the experimental data for which the reliability has already been questioned. A similar approach is used for the determination of the molar volume expression of alumina with experimental data from the Al_2O_3-CaO, Al_2O_3-CaF_2, Al_2O_3- SiO_2 , Al_2O_3-CaO-MgO and Al_2O_3-MnO- SiO_2 systems. Completeness requires the same approach for phosphate containing slags, since P_2O_5 is also considered as an acid oxide. However, experimental data on systems containing P_2O_5 is limited. From existing data a constant value for the molar volume of P_2O_5 was obtained, rather than a variable one in the method of Mills and Keene [33].

Finally, the molar volume of any oxide component at 1500°C can be calculated [33] with the expression given in equation 5.18. For all the oxides apart from SiO_2 and Al_2O_3 the coefficients B and C in this expression are equal to 0. An overview of the coefficients is given in Table 5-6. The molar volume is expressed in cm^3/mol . To introduce temperature dependencies (dV/dT) a mean value of 0.01 % K^{-1} was adopted. [33]

$$\bar{V}_i = A + Bx_i + Cx_i^2 \tag{5.18}$$

For the density calculation the molar volume was determined with the model described. For the molar mass the data from NIST [44] was used.

Table 5-6: Coefficients for relevant oxides in the BOF-slag for calculation of the molar volume at 1500°C.

	Al_2O_3	SiO_2	CaO	FeO	Fe_2O_3	MgO	MnO	P_2O_5	TiO_2
A	28.31	19.55	20.7	15.8	38.4	16.1	15.6	65.7	24.0
B	32.0	7.966	0.0	0.0	0.0	0.0	0.0	0.0	0.0
C	-31.45	0.0	0.0	0.0	0.0	0.0	0.0	0.0	0.0

5.4 On surface tension of slags

Surface tension of slags, is mentioned as an important property for slag foaming. However, unlike viscosity, experimental data on surface tensions is rather limited and no state of art surface tension models exist for which there is general scientific agreement. The presence of both Fe^{2+} and Fe^{3+} ions, makes the determination of the surface tension even more complicated. FeO can be considered as a regular oxide, while Fe_2O_3 is mentioned as a surface active component causing considerable decrease in the overall slag surface tension due to its presence. Furthermore, slags with high SiO_2 contents are observed to have an increase of surface tension with increasing temperature. This is in contrast to the regular behaviour of surface tensions in function of temperature. The experimental uncertainty for surface tensions of slags is estimated to be 10%. [33] Even though advanced models have been developed e.g. Tanaka et al. [45]–[47] and Nakamoto et al. [48], [49], their use is limited since their accuracy is not necessary better than simpler models, such as the additive surface tension model for slags, while they require more computational effort.[9] Within this work the additive surface tension model is used.

Within the additive surface tension model, it is assumed the surface tension is an additive property with respect to the molar surface tension of each component. This approach was described by Mills and Keene [33] and is only applicable for slag systems with only one surface active component. Including two different surface active components is impossible, since in reality the surface tension can probably not be assumed additive in that case due to a possible concurrency between the two different surface active elements and possible deviations between slag bulk composition and slag surface

[9] *This conclusion was supported by the work of M. Melis in her master dissertation: 'Modelling of the surface tension of liquid silicate slags in pyrometallurgical processes', Ugent, 2020.*

composition. For the considered BOF slags composition in the current work, usually two surface active oxides are present: Fe_2O_3 and P_2O_5.

In equation 5.19 the expression to calculate the surface tension of the slag is given. In this expression γ (N/m or often mN/m for slags) is the surface tension of the slag, γ_i is the partial molar surface tension for component i and x_i its mole fraction. An overview of the partial molar surface tensions at 1500°C given by Mills and Keene [33] is given in Table 5-7.

$$\gamma = \sum \gamma_i \, x_i \tag{5.19}$$

$$\begin{aligned} \gamma_i \, x_i &= A_1 + B_1 x_i + C_1 x_i^2 \quad for \; x_i < N \\ \gamma_i \, x_i &= A_2 + B_2 x_i \quad for \; x_i > N \end{aligned} \tag{5.20}$$

For the surface active components the value of γ_i is zero. The reason is that within this model, their contributions to the surface tensions are calculated slightly differently than for the regular oxides. The expressions for the contribution of surface active components are given in equation 5.20. A threshold molar fraction (*N*) is defined which distinguishes the behaviour of the oxide from surface active, towards regular behaviour for higher concentrations. As can be seen from these expressions, the surface active behaviour is parabolic. In Table 5-8 the parameters at 1500°C from Mills and Keene [33] for the different relevant surface active components are listed.

Table 5-7: partial molar surface tensions for different oxides, used in the additive model. Data from [33].

	Al_2O_3	SiO_2	CaO	FeO	Fe_2O_3	MgO	MnO	P_2O_5	TiO_2
γ_i (mN/m)	655	260	625	645	0	635	645	0	360

Table 5-8: Parameters for the contribution of surface active components to the surface tension. Data from [33].

	Fe_2O_3	P_2O_5
N	0.125	0.12
A_1	-3.7	-5.2
B_1	-2972	-3454
C_1	14312	22178
A_2	-216.2	-142.5
B_2	516.2	167.5

To calculate the surface tension on temperatures higher than 1500°C, a mean value of 0.15 mN/mK was used as temperature coefficient. [33]

5.5 References

[1] E. T. Turkdogan, *Fundamentals of Steelmaking*. Institute of Materials, 1996.

[2] E. T. Turkdogan and R. J. Fruehan, 'Fundamentals of iron and steelmaking', *Mak. Shap. Treat. Steel Steelmak. Refin. Vol. 11th Ed RJ Fruehan Ed AISE Steel Found. Pittsburgh*, pp. 79–132, 1998.

[3] B. O. Mysen and P. Richet, *Silicate Glasses and Melts: Properties and Structure*. Elsevier, 2005.

[4] L. Coudurier, D. W. Hopkins, and I. Wilkomirsky, *Fundamentals of Metallurgical Processes: International Series on Materials Science and Technology*. Elsevier, 2013.

[5] H. JALKANEN, S. NURMI, and S. LOUHENKILPI, 'On the Thermodynamic and Physical properties of Ionic Melts and on Their Role in Ferrous and Nonferrous Metals Production Processes'.

[6] W. D. Kingery, H. K. Bowen, and D. R. Uhlmann, 'Introduction to ceramics', 1960.

[7] R. D. Pehlke, *BOF steelmaking*. New York (N.Y.) : Iron and steel society of the American institute of mining, 1974. [Online]. Available: http://lib.ugent.be/catalog/rug01:000190590

[8] D. Virgo and B. O. Mysen, 'The structural state of iron in oxidized vs. reduced glasses at 1 atm: A57Fe Mössbauer study', *Phys. Chem. Miner.*, vol. 12, no. 2, pp. 65–76, Mar. 1985, doi: 10.1007/BF01046829.

[9] G.-H. Zhang, K.-C. Chou, and K. Mills, 'A Structurally Based Viscosity Model for Oxide Melts', *Metall. Mater. Trans. B*, vol. 45, no. 2, pp. 698–706, Apr. 2014, doi: 10.1007/s11663-013-9980-z.

[10] C. J. B. Fincham and F. D. Richardson, 'The behaviour of sulphur in silicate and aluminate melts', *Proc R Soc Lond A*, vol. 223, no. 1152, pp. 40–62, Apr. 1954, doi: 10.1098/rspa.1954.0099.

[11] A. Kondratiev, E. Jak, and P. C. Hayes, 'Predicting slag viscosities in metallurgical systems', *JOM*, vol. 54, no. 11, pp. 41–45, Nov. 2002, doi: 10.1007/BF02709749.

[12] S. Glasstone, 'KJ Laidler, and H. Eyring', *Theory Rate Process.*, p. 279, 1941.

[13] G.-H. Zhang, K.-C. Chou, Q.-G. Xue, and K. C. Mills, 'Modeling Viscosities of CaO-MgO-FeO-MnO-SiO2 Molten Slags', *Metall. Mater. Trans. B*, vol. 43, no. 1, pp. 64–72, Feb. 2012, doi: 10.1007/s11663-011-9589-z.

[14] G.-H. Zhang, K.-C. Chou, and K. Mills, 'Modelling Viscosities of CaO–MgO–Al2O3–SiO2 Molten Slags', *ISIJ Int.*, vol. 52, no. 3, pp. 355–362, 2012, doi: 10.2355/isijinternational.52.355.

[15] G.-H. Zhang and K.-C. Chou, 'Modeling the Viscosity of Alumino-Silicate Melt', *Steel Res. Int.*, vol. 84, no. 7, pp. 631–637, Jul. 2013, doi: 10.1002/srin.201200196.

[16] G.-H. Zhang and K.-C. Chou, 'Influence of CaF2 on viscosity of aluminosilicate melts', *Ironmak. Steelmak.*, vol. 40, no. 5, pp. 376–380, Jul. 2013, doi: 10.1179/1743281212Y.0000000055.

[17] M. Nakamoto, Y. Miyabayashi, L. Holappa, and T. Tanaka, 'A Model for Estimating Viscosities of Aluminosilicate Melts Containing Alkali Oxides', *ISIJ Int.*, vol. 47, no. 10, pp. 1409–1415, 2007, doi: 10.2355/isijinternational.47.1409.

[18] A. Kondratiev, P. C. Hayes, and E. Jak, 'Development of a Quasi-chemical Viscosity Model for Fully Liquid Slags in the Al2O3–CaO–"FeO"–MgO–SiO2 System. Part 1. Description of the Model and Its Application to the MgO, MgO–SiO2, Al2O3–MgO and

CaO–MgO Sub-systems', *ISIJ Int.*, vol. 46, no. 3, pp. 359–367, 2006, doi: 10.2355/isijinternational.46.359.

[19] A. Kondratiev, P. C. Hayes, and E. Jak, 'Development of a Quasi-chemical Viscosity Model for Fully Liquid Slags in the Al2O3–CaO–"FeO"–MgO–SiO2 System. Part 2. A Review of the Experimental Data and the Model Predictions for the Al2O3–CaO–MgO, CaO–MgO–SiO2 and Al2O3–MgO–SiO2 Systems', *ISIJ Int.*, vol. 46, no. 3, pp. 368–374, 2006, doi: 10.2355/isijinternational.46.368.

[20] A. Kondratiev, P. C. Hayes, and E. Jak, 'Development of a Quasi-chemical Viscosity Model for Fully Liquid Slags in the Al2O3–CaO–"FeO"–MgO–SiO2 System. Part 3. Summary of the Model Predictions for the Al2O3–CaO–MgO–SiO2 System and Its Sub-systems', *ISIJ Int.*, vol. 46, no. 3, pp. 375–384, 2006, doi: 10.2355/isijinternational.46.375.

[21] A. Kondratiev, P. C. Hayes, and E. Jak, 'Development of a Quasi-chemical Viscosity Model for Fully Liquid Slags in the Al2O3–CaO–"FeO"–MgO–SiO2 System. The Experimental Data for the "FeO"–MgO–SiO2, CaO–"FeO"–MgO–SiO2 and Al2O3–CaO–"FeO"–MgO–SiO2 Systems at Iron Saturation', *ISIJ Int.*, vol. 48, no. 1, pp. 7–16, Jan. 2008, doi: 10.2355/isijinternational.48.7.

[22] A. N. Grundy, H. Liu, I.-H. Jung, S. A. Decterov, and A. D. Pelton, 'A model to calculate the viscosity of silicate melts', *Int. J. Mater. Res.*, vol. 99, no. 11, pp. 1185–1194, Nov. 2008, doi: 10.3139/146.101752.

[23] S. A. Decterov, A. N. Grundy, I.-H. Jung, A. D. Pelton, T. E. Simos, and G. Maroulis, 'Modeling the Viscosity of Aluminosilicate Melts', in *AIP Conference Proceedings*, 2007, vol. 963, pp. 404–407. doi: 10.1063/1.2836097.

[24] W.-Y. Kim, A. D. Pelton, and S. A. Decterov, 'A model to calculate the viscosity of silicate melts', *Int. J. Mater. Res.*, vol. 103, no. 3, pp. 313–328, Mar. 2012, doi: 10.3139/146.110637.

[25] A. N. Grundy, I.-H. Jung, A. D. Pelton, and S. A. Decterov, 'A model to calculate the viscosity of silicate melts', *Int. J. Mater. Res.*, vol. 99, no. 11, pp. 1195–1209, Nov. 2008, doi: 10.3139/146.101753.

[26] W.-Y. Kim, A. D. Pelton, and S. A. Decterov, 'A model to calculate the viscosity of silicate melts: Part III: Modification for melts containing alkali oxides', *Int. J. Mater. Res.*, vol. 103, no. 3, pp. 313–328, 2012.

[27] V. Cnockaert, 'Structure based Viscosity models for Molten Slags - Internal Communication'. Sep. 22, 2017.

[28] Z. Liu, L. Pandelaers, B. Blanpain, and M. Guo, 'Viscosity of Heterogeneous Silicate Melts: A Review', *Metall. Mater. Trans. B*, vol. 49, no. 5, pp. 2469–2486, Oct. 2018, doi: 10.1007/s11663-018-1374-9.

[29] A. Ilyushechkin and A. Kondratiev, 'Viscosity of slags with solids: The effect of solids morphology and concentration', *J. Rheol.*, vol. 63, no. 5, pp. 719–733, Sep. 2019, doi: 10.1122/1.5095968.

[30] Z. Liu, L. Pandelaers, B. Blanpain, and M. Guo, 'Viscosity of Heterogeneous Silicate Melts: Assessment of the Measured Data and Modeling', *ISIJ Int.*, vol. 57, no. 11, pp. 1895–1901, Nov. 2017, doi: 10.2355/isijinternational.ISIJINT-2017-288.

[31] A. Einstein, 'Eine neue Bestimmung der Moleküldimensionen', *Ann. Phys.*, vol. 324, no. 2, pp. 289–306, Jan. 1906, doi: 10.1002/andp.19063240204.

[32] A. Kondratiev and E. Jak, 'Modeling of viscosities of the partly crystallized slags in the Al2O3-CaO-"FeO"-SiO2 system', *Metall. Mater. Trans. B*, vol. 32, no. 6, pp. 1027–1032, Dec. 2001, doi: 10.1007/s11663-001-0091-x.

[33] K. C. Mills and B. J. Keene, 'Physical properties of BOS slags', *Int. Mater. Rev.*, vol. 32, no. 1, pp. 1–120, Jan. 1987, doi: 10.1179/095066087790150296.

[34] Y. Bottinga, P. Richet, and D. Weill, 'Calculation of the density and thermal expansion coefficient of silicate liquids', *Bull. Minéralogie*, vol. 106, no. 1, pp. 129–138, 1983, doi: 10.3406/bulmi.1983.7675.

[35] I. M. Krieger and T. J. Dougherty, 'A Mechanism for Non-Newtonian Flow in Suspensions of Rigid Spheres', *Trans. Soc. Rheol.*, vol. 3, no. 1, pp. 137–152, Mar. 1959, doi: 10.1122/1.548848.

[36] R. Roscoe, 'The viscosity of suspensions of rigid spheres', *Br. J. Appl. Phys.*, vol. 3, no. 8, p. 267, 1952, doi: 10.1088/0508-3443/3/8/306.

[37] H. J. Hurst, F. Novak, and J. H. Patterson, 'Viscosity measurements and empirical predictions for some model gasifier slags', *Fuel*, vol. 78, no. 4, pp. 439–444, 1999.

[38] H. J. Hurst, F. Novak, and J. H. Patterson, 'Viscosity measurements and empirical predictions for fluxed Australian bituminous coal ashes', *Fuel*, vol. 78, no. 15, pp. 1831–1840, 1999.

[39] Z. Liu, B. Blanpain, and M. Guo, 'Viscosity of Partially Crystallized BOF Slag', in *7th International Symposium on High-Temperature Metallurgical Processing*, Springer, Cham, 2016, pp. 263–269. doi: 10.1007/978-3-319-48093-0_33.

[40] Z. Liu, L. Chen, B. Blanpain, and M. Guo, 'Effect of Crystallization on the Abrupt Viscosity Increase during the Slag Cooling Process', *ISIJ Int.*, vol. 58, no. 11, pp. 1972–1978, 2018, doi: 10.2355/isijinternational.ISIJINT-2018-176.

[41] Y. E. Lee and D. R. Gaskell, 'The densities and structures of melts in the system CaO-"FeO"-SiO2', *Metall. Trans.*, vol. 5, no. 4, pp. 853–860, Apr. 1974, doi: 10.1007/BF02643138.

[42] A. E. Grau and C. R. Masson, 'Densities and molar volumes of silicate melts', *Can. Metall. Q.*, vol. 15, no. 4, pp. 367–374, Oct. 1976, doi: 10.1179/000844376795050516.

[43] Y. Bottinga and D. F. Weill, 'The viscosity of magmatic silicate liquids; a model calculation', *Am. J. Sci.*, vol. 272, no. 5, pp. 438–475, Jan. 1972, doi: 10.2475/ajs.272.5.438.

[44] P.J. Linstrom and W. G. Mallards, Eds., *NIST Chemistry WebBook, NIST Standard Reference Database Number 69*. Gaithersburg MD: National Institute of Standards and Technology. [Online]. Available: DOI: https://doi.org/10.18434/T4D303

[45] T. Tanaka, K. Hack, and S. Hara, 'Calculation of surface tension of liquid Bi□Sn alloy using thermochemical application library ChemApp', *Calphad*, vol. 24, no. 4, pp. 465–474, Dec. 2000, doi: 10.1016/S0364-5916(00)85001-4.

[46] T. Tanaka, K. Hack, and S. Hara, 'Use of Thermodynamic Data to Determine Surface Tension and Viscosity of Metallic Alloys', *MRS Bull.*, vol. 24, no. 4, pp. 45–51, Apr. 1999, doi: 10.1557/S0883769400052180.

[47] T. Tanaka, T. Kitamura, and I. A. Back, 'Evaluation of Surface Tension of Molten Ionic Mixtures', *ISIJ Int.*, vol. 46, no. 3, pp. 400–406, 2006, doi: 10.2355/isijinternational.46.400.

[48] M. Nakamoto, A. Kiyose, T. Tanaka, L. Holappa, and M. Hämäläinen, 'Evaluation of the Surface Tension of Ternary Silicate Melts Containing Al2O3, CaO, FeO, MgO or MnO', *ISIJ Int.*, vol. 47, no. 1, pp. 38–43, 2007, doi: 10.2355/isijinternational.47.38.

[49] M. Nakamoto, T. Tanaka, L. Holappa, and M. Hämäläinen, 'Surface Tension Evaluation of Molten Silicates Containing Surface-active Components (B2O3, CaF2 or Na2O)', *ISIJ Int.*, vol. 47, no. 2, pp. 211–216, 2007, doi: 10.2355/isijinternational.47.211.

6 Intermediate conclusion

The first 'Introduction' part started with a general outline of the context and research questions of this dissertation. Next, a more detailed description of the BOF process and the important role of slag in the process was given. The difference between the industrial and thermodynamic meaning of 'a slag' was explained. In part II, the thermodynamic calculation of the liquid fraction was used to illustrate the importance of certain parameters for thermodynamic modelling e.g. oxygen partial pressure and the used solution model. In a fourth chapter the potential of thermodynamic modelling to gain insight in the effect of different slag compositions on the industrial process was illustrated. Even though the considered slag systems were strongly simplified, general industrially observed trends could already be explained. However, this method did not give a full insight in the process yet. In the fifth chapter, the nature of slag is explained from a very theoretical view point together with a description of models to predict slag physical properties: viscosity, density and surface tension.

From these two parts it can be concluded that thermodynamic modelling is an interesting tool to study the role of slag in the BOF process. Yet, both for slag foaming, refining and interaction with the refractory an accurate simulation of the slag evolution is necessary. In the next part of this work, two different models will be constructed. The first model uses industrial measurements and is not meant for predictive purposes, while the second model starts from a more physicochemical basis to simulate and predict the BOF process. As a consequence, two separate parts are created in the main part of this work respectively, 'III. Foaming' and 'IV. Thermodynamic BOF model'. In the 'III. Foaming' part, both the model construction as well as the application of the model to investigate the industrial foaming behaviour is discussed. The 'IV. Thermodynamic BOF model' part starts with a thorough literature review, discussing the state-of-the-art physiochemical models. Next, the specific model developed in this work is described, followed by results discussion. Finally, some future developments of the model are explored as well within this part of the dissertation.

III. Foaming

So hold your own
Breathe deep on a freezing beach
Taste the salt of friendship
Notice the movement of a stranger

Hold your own
And let it be catching

Hold your own -The book of traps and lessons – Kae Tempest

7 Model to calculate slag compositions during blow of historical heats

In this chapter, the model used to calculate the composition of the slag for one heat during the process is described. This model uses industrial data, both input and output data as well as data from measurements during the process. For this reason, the model can only be used for already executed heats (called historical heats). The model aims to construct these slag compositions for analysis of slag foaming behaviour. The model is not meant to have a predictive nature.

7.1 General model description

The model described in this chapter, was developed within the context of research on the foaming behaviour of BOF slags. As will be discussed in one of the following chapters, foaming issues or slopping occurs during the converter blowing phase. To be able to perform an analysis on foaming the composition of the slag during blow is required. However, there is no sampling of the steel or slag during the process at the steel shop of ArcelorMittal Ghent. Sampling is only performed at the end of blow, once the process is finished. For this reason, a model was needed and thus, developed that allowed to estimate the slag composition during blow.

7.1.1 Used input data

Both continuous in- and output data of the BOF process are used. Hot metal, scrap (both pig iron and regular scrap), fluxes and oxygen are considered as input. The hot metal composition, mass and temperature for each heat are known. All scrap is added at the very beginning of the process and its melting profile is assumed to be an exponential melting decay for which the parameters are taken as used in the industrial AMG models, shown in equation 7.1. The fraction of scrap that is melted, and as such contributes to the slag composition, is graphically shown in Figure 7.1. No distinction was made between the different types of scrap with regard to their melting profile. Even though the real melting behaviour of scrap materials will depend upon the size and shape of the scrap pieces. [1]

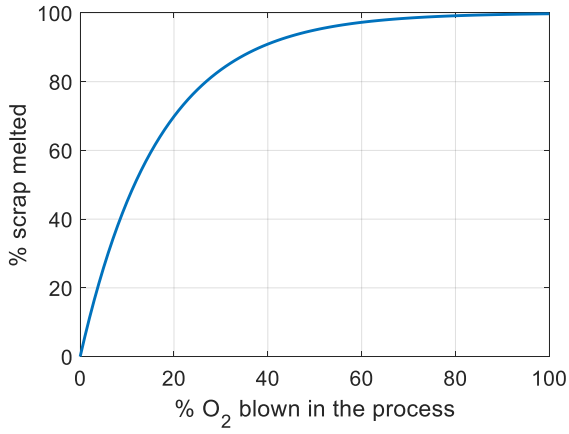

Figure 7.1: Assumed melting profile for scrap. [2]

For the fluxes, the continuous input data during the process is used together with the industrial composition for each flux. The industrial yield for each flux is also incorporated in the calculation. To illustrate this type of input data, the flux addition profiles for one random heat are shown in Figure 7.2. Dissolution of fluxes is considered with a spherical dissolution model which is taken as used in the industrial models, shown in equation 7.2. In these equations i denotes the current calculation step, i_0 is the calculation step in which the flux was added and R_0 is the original radius of the particle.

$$f_{scrap,melted} = (1 - \exp(-0.06 \cdot \%O_2)) \tag{7.1}$$

$$f_{dissolved} = (1 - {R_i^3}/{R_0^3}) \qquad R_i = R_0\left(1 - 0.25\big((i + 0.5) - i_0\big)\right) \tag{7.2}$$

Additionally, refractory dissolution, assumed to be 100% MgO, is accounted for via a fixed linear function of the % O_2 blown. The temperature profile is assumed to be linear, ranging between the hot metal temperature (0% O_2 blown) and the end of blow temperature (100% O_2 blown). The slag is assumed to have the same temperature as the steel phase. Finally, also the amount of oxygen blown at each point during the converter blow is used as input for the model.

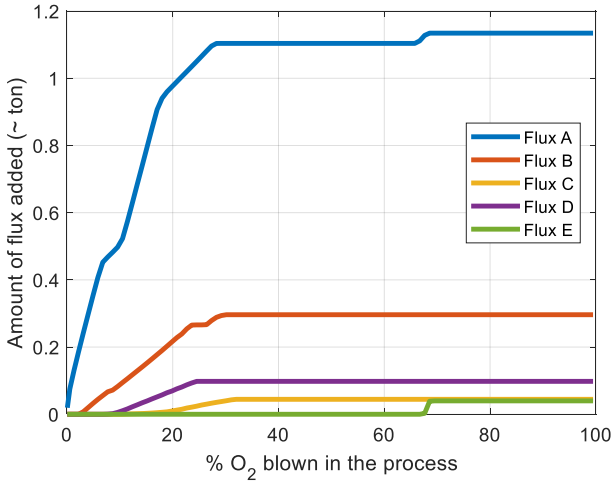

Figure 7.2: Flux addition profiles for one heat produced at the ArcelorMittal Ghent plant. The flux amounts (on the y-axis) were normalised by dividing them by a fixed constant value. Due to confidentiality the flux names are masked.

7.1.2 Used output data

Two main types of output data are used to calculate the slag composition: end of blow compositions and off gas analyses. At the end of the process, steel and slag samples are taken from the BOF vessel. The slag composition is subsequently determined with an XRF measurement. This type of end of blow slag composition is denoted as the industrial XRF composition. Unlike steel sampling, slag sampling is much more complex. As a result, not every heat will have a slag sample of sufficient quality to be analysed in the lab. However, for each heat the slag composition is predicated with the industrial converter model at the ArcelorMittal Ghent plant. This model is used for monitoring of the process and thus, gives good predictions for the measured reality. Ideally, two slag compositions exist for each heat: the predicted one and the XRF composition. Yet, in some cases only the predicted composition is available. To allow the dataset for analyses to be as large as possible, the predicted composition of the slag is used in the model. These end compositions are used for estimation of SiO_2 and Al_2O_3 amounts in the slag. As can be seen in Figure 7.3 , the AMG predicted fraction for these components is a good value for the XRF measured ones.

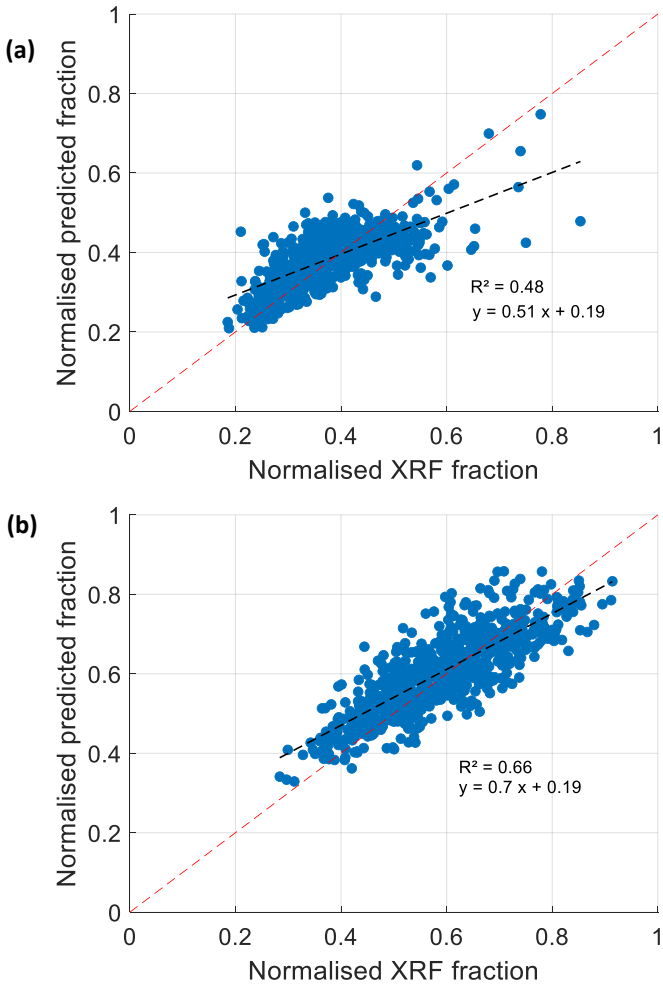

Figure 7.3: Comparison between the industrial XRF fraction and the predicted fraction for relevant components: (a) wt% Al_2O_3 and (b) wt% SiO_2. The first bisector is indicated with a red dashed line.

The second important type of output data that is used, is the off-gas data. During the BOF process CO and CO_2 gas are formed and this off gas is removed from the vessel. The volumetric flow of gas leaving the vessel is measured as well as the composition of this gas phase. This gas composition is measured with a mass spectrometer. The volumetric flow rate for the off gas of one heat is shown in Figure 7.4. Apart from the carbon rich gas which is formed in the converter, ambient air will also be sucked into the off-gas stream. Depending upon the time in the process, the amount of air in the off-gas stream will be higher or lower. The off gas thus consists out of N_2, O_2, CO and CO_2. It is assumed air exists out of 21 vol% O_2 and 78 vol% N_2. Based upon the total amount of nitrogen

measured in the off gas, the amount of oxygen from air in the off gas is calculated and the CO and CO_2 amounts are rescaled if necessary due to post combustion effects.

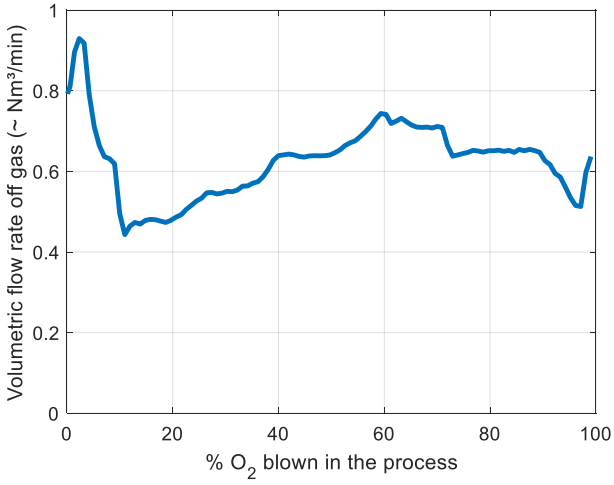

Figure 7.4: Off gas volumetric flow rate for one heat. The volumetric flow rate (on the y-axis) was normalised by dividing it by a fixed constant value.

7.1.3 Implication of the used data on heat selection

As explained above, a lot of different industrial data and assumptions on input and output are used to calculate the slag composition of a heat. As a consequence, the model cannot be used for all the heats. The most important restrictions are summarised here:

- Only five fluxes are considered: lime, dolomitic lime, two types of iron briquettes and iron ore.
- Scrap types that contain slag, e.g. from internal recycling, are not incorporated in the model. These types of material streams contain variable and unknown amounts of bounded oxygen.
- The blow should have happened without any interruptions.
- Only heats blown with specific lance position can be analysed with the model.
- Only heats without maintenance operations for the refractory lining are considered.

7.1.4 Calculation of the slag composition

The model uses a simplified slag system: $CaO – SiO_2 – FeO_n – MgO – Al_2O_3 – MnO$. It is assumed all the CaO in the system originates from added fluxes. The MgO originates from the added fluxes and additionally from refractory dissolution. For SiO_2, three sources are

assumed: fluxes, scrap and the liquid hot metal. The Si in liquid hot metal and in part of the scrap (pig iron) is metallic Si and an oxidation reaction is considered to determine the amount of SiO_2. This Si oxidation is assumed to be stoichiometric with a two pieced linear reaction profile. This is based upon the Si-profiles reported in the Imphos study [3] (European publication 'Improving phosphorus refining'), that are shown in Figure 7.5. Both from this figure as well as the Imphos report, it is clear the Si content of the liquid hot metal decreases fast yet, not at a constant speed. These profiles are mimicked in the current model, with a two piece linear profile. For this profile it is assumed that 80% of the total amount of Si present (both via liquid hot metal as well as solid pig iron) reacts with oxygen during the first 20% of the O_2 blown in the process. The other 20% Si left after this, will all react with oxygen between 20% O_2 blown and 40% O_2 blown. After 40% O_2 blown, no metallic Si is left in the system. The amount of Si for the hot metal is calculated from its composition and mass. For the pig iron the amount of Si is calculated from the industrial composition and input amount of the pig iron added for the heat.

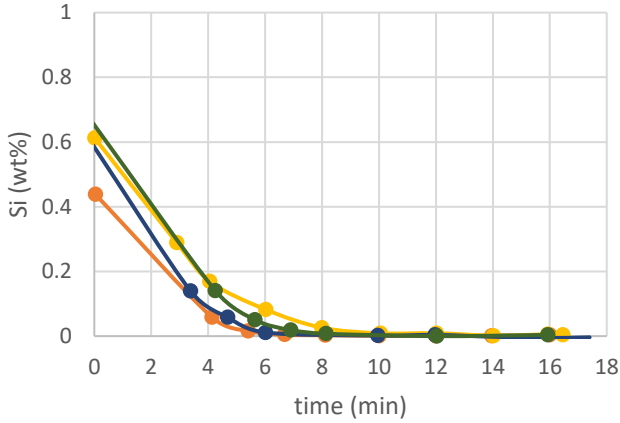

Figure 7.5: Measured Si content profiles for the hot metal phase for different heats. Data was collected from [3].

For the regular scrap, it is assumed SiO_2 enters the system as SiO_2 and this amount is determined based upon a mass balance, as shown in equation 7.3. In this equation $m_{total}^{SiO_2}$ is the amount of SiO_2 in the slag at the end of blow. Both $m_{pig\ iron}^{SiO_2}$ and $m_{hot\ metal}^{SiO_2}$ are the total amounts of SiO_2 from these material streams and are known from input data, as well as the amount of SiO_2 entering via fluxes, $m_{fluxes}^{SiO_2}$.

$$m^{SiO_2}_{regular\ scrap} = m^{SiO_2}_{total} - m^{SiO_2}_{pig\ iron} - m^{SiO_2}_{hot\ metal} - m^{SiO_2}_{fluxes} \quad (7.3)$$

The Al_2O_3 is assumed to originate only from scrap and is calculated from the end of blow composition. The amounts of FeO_n and MnO are calculated based upon the available Fe, Mn and reactive oxygen in the system. To determine the amount of reactive oxygen present in the system, the data on the off gas of the process is used. Based upon the amount of free O_2 entering the system via blowing, fluxes and air (21% O_2 and 78% N_2) together with the amount of O_2 in the off gas, a mass balance gives the amount of O_2 left to react in the converter. This is summarized in equation 7.4. Only the oxidation of Si, Fe and Mn are considered. Once the amount of oxygen consumed for Si oxidation is subtracted, an equilibrium calculation between the left-over reactive oxygen and the total amount of Fe and Mn in the system is performed. The thermodynamic equilibrium is calculated between a FeO_n-MnO slag system and a Fe-Mn melt with Chemapp [4] using Factsage 7.2 [5] FToxid-SlagA and FTmisc-FeLQ.

$$m^{O_2}_{left\ for\ Fe,Si,Mn\ oxidaton} = m^{O_2}_{blown} + m^{O_2}_{fluxes} + m^{O_2}_{air} - m^{O_2}_{off\ gas} \quad (7.4)$$

With $m^{O_2}_{off\ gas} = m^{O_2}_{O_2\ off\ gas} + m^{O_2}_{CO_2\ off\ gas} + m^{O_2}_{CO\ off\ gas}$

Merely as example, the total slag composition of one heat is shown in Figure 7.6.

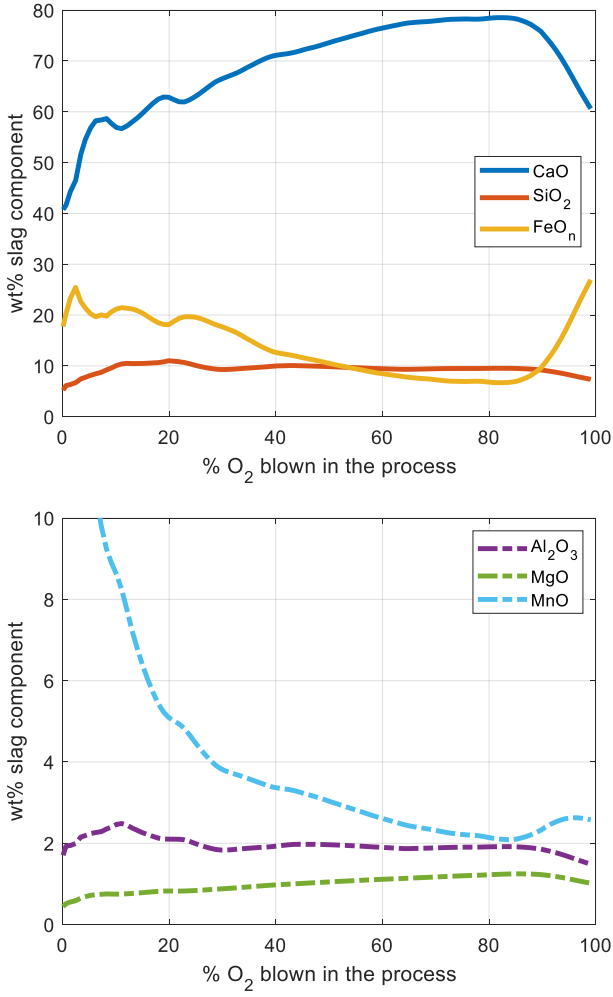

Figure 7.6: Calculated slag composition for one random selected heat

7.2 Slag Model Validation

7.2.1 Validation via end compostition

The model to estimate the slag composition during the process, is validated with a comparison between the calculated end of blow composition and the industrial XRF composition. Whenever the term model is used in the next sections it denotes the model used to calculate the slag composition during blow. Due to confidentiality, displayed results are normalised. Figure 7.7 (a) shows the overall slag mass for which a good correlation ($R^2 = 0.89$) is found. For most of the components, the calculated total mass is

a good predication of the industrial data (for which the mass is also calculated based on the measured XRF composition). In Figure 7.7 (b-d) this is shown for the components which were determined independently of the industrial end of blow composition. For the other components even better correlations than the ones shown in Figure 7.7 (b-d) are observed. However, this was expected since these components were determined, partially, depending upon the industrial end composition. Of all the calculated components MnO, shown in Figure 7.7 (d), shows the poorest correlation. For FeO_n (Figure 7.7 (b)), which is determined based upon a mass balance on the off-gas data, a larger spread is observed in the calculated data compared to the industrial data. This will influence the total slag mass and the finally calculated slag compositions. Especially, for heats with a total normalised FeO_n content smaller than 0.1 according to the model, large deviations are observed in the slag composition.

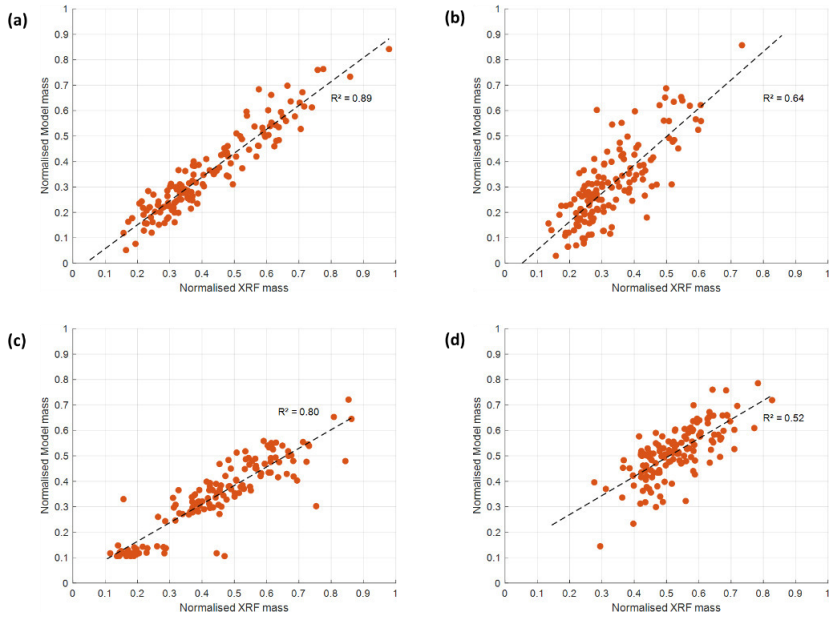

Figure 7.7: Comparison between the industrial and the model's end of blow slag mass. For the industrial end of blow mass the XRF based composition is used. (a) is the total slag mass, (b) the total FeO_n mass, (c) the total MgO mass and (d) is the total MnO mass.

Another important difference, shown in Figure 7.8, is the FeO/Fe_2O_3 ratio (or Fe^{2+}/Fe^{3+}). This difference is due to a difference in oxygen partial pressure between the two calculation methods. For the industrial data this ratio varies between 1.5 and 2, or a corresponding $\log(P_{O2})$ of about -3.67 at 1650°C, while for the model's calculation it ranges between 14 and 15, or a corresponding $\log(P_{O2})$ of about -8.24 at 1650°C. The

industrial ratio is calculated from the overall Fe-content of the slag with an empirical relation which was previously established via industrial slag sampling, involving air cooling, and subsequently a wet chemical analysis. While in the model, this ratio is calculated based upon the assumption of equilibrium between the slag and the metal phase. Consequently, the industrial determination method will result in a larger fraction of Fe_2O_3 due to the higher oxygen partial pressure. However, it is important to consider the limitation of both calculation methods. Firstly, it is important to be aware the industrial slag is believed to be a heterogeneous layer where both temperature and oxygen partial pressure gradients exist. The thermodynamic calculation assumes uniform and unique temperature and oxygen partial pressure, even though the assumption of equilibrium between slag and steel is probably only valid close to the interface. While the equilibrium between slag and air is only valid at their interface. Thus, the model's partial oxygen pressure is expected to be an underestimation. Furthermore, the industrial ratio is probably an overestimation of the oxygen partial pressure due to the nature of industrial slag sampling and the air cooling. The fraction of Fe_2O_3 in the slag mainly influences the calculated surface tension because it is mentioned [6] to be a surface active component. Additionally, the Fe_2O_3 will also influence the liquid fraction of the slag.

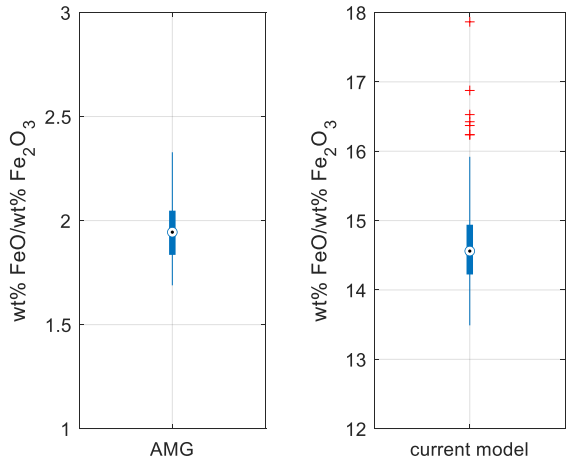

Figure 7.8: The difference in FeO/Fe_2O_3 ratio between AMG data and the current TD model. The boxplots show the median with a circle, the box range from the first to the third quartile value and the line ranges from the minimum to the maximum value of the dataset without the outliners. Outliners are indicated with red crosses.

7.2.2 Validation during the blow

Validation of the slag composition during the blow was attempted with experimental data from literature. An example, of the slag evolution measured in the Imphos study [3] is shown in Figure 7.9. The data points in this figure are taken from [3] and a fitted curve was constructed with the '*polyfit*' function form MATLAB based upon this data. During the Imphos project, slag samples were sampled at different slag heights in a pilot scale set up. For the slag evolutions reported by Turkdogan [7], the reader is referred to the first chapter of this work.

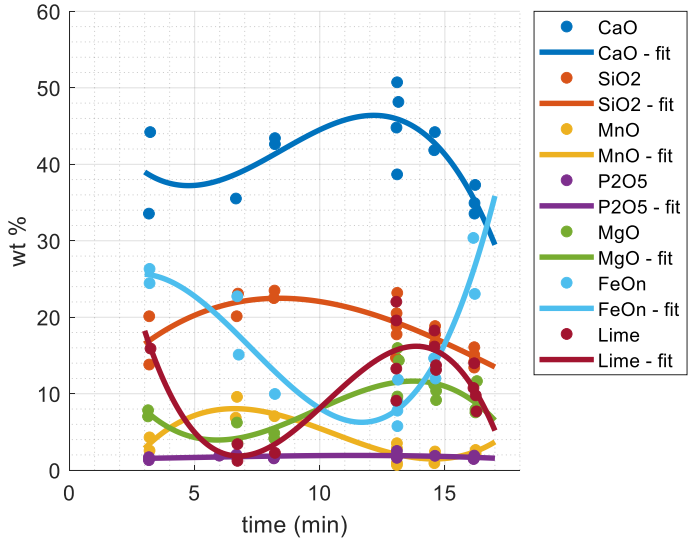

Figure 7.9: Example of slag evolution for one heat measured during the Imphos project [3].

Yet, the slag evolution can only be compared if the processes are comparable. The hot metal used in the Imphos project [3] has a significant different composition than the typical hot metal used at the ArcelorMittal Ghent plant: both Mn and Si content are twice as high for the Imphos hot metal. Furthermore, as can be seen in Table 7-1, the basicity and MgO content for the Imphos process is considerably lower. Consequently, the processes, and their slag evolution, are not comparable. For the slag evolution reported by Turkdogan et al. [7] there is no information available on the composition of the hot metal. Yet, as can be seen in Table 7-1, the basicity for this process is only 60% of the basicity for the AMG process, which again will result in a different process and slag evolution. For Cucicutti et al. [8], [9] no details on process basicity or hot metal composition are, to the best of the authors knowledge, reported either. Thus, it is

impossible to use the available literature on slag evolution to validate the current model calculations for the heats produced at AMG. As a consequence, validation has only been performed with the end of blow composition and is therefore limited.

Table 7-1: Comparison between AMG end of blow slag data and published experimental data. All values are relative with respect to the AMG value, expect the sum of the major components which is an absolute value.

	AMG	Turkdogan	Imphos*
Sum wt% major components	99.32 *Note: total sum > 100%*	95	91.37
$(SiO_2)^R$	1	1.39	1.42
$(MgO)^R$	1 *Note: actually, two regimes*	1.14	0.34 *Note: actually, two regimes*
$(CaO/SiO_2)^R$	1	0.56	0.66
$((CaO+MgO)/SiO_2)^R$	1	0.58	0.64

** The Imphos data was considered without the dissolution effect of the refractory material*

7.3 Conclusion

A model was developed to calculate the simplified slag composition of historical heats during the blowing process. This model uses both input and output measurements from the industrial process to estimate the slag composition. The model was validated via measured slag end compositions. The model's applicability is limited to heats with restriction on the input (types of fluxes and scrap) and blowing conditions (e.g. lance position and no blowing interruptions).

7.4 References

[1] F. M. Penz and J. Schenk, "A Review of Steel Scrap Melting in Molten Iron-Carbon Melts," *Steel Res. Int.*, vol. 90, no. 8, p. 1900124, 2019, doi: 10.1002/srin.201900124.

[2] Process engineer at ArcelorMittal Ghent, "Private communication."

[3] Publications Office of the European Union, “Imphos : improving phosphorus refining.,” Dec. 14, 2011. https://publications.europa.eu/en/publication-detail/-/publication/8aecbb7c-f77f-4ee7-bc38-9ebb13b52faf/language-en (accessed Nov. 06, 2018).

[4] S. Petersen and K. Hack, “The thermochemistry library ChemApp and its applications,” *Int. J. Mater. Res.*, vol. 98, no. 10, pp. 935–945, Oct. 2007, doi: 10.3139/146.101551.

[5] C. W. Bale *et al.*, “FactSage thermochemical software and databases, 2010–2016,” *Calphad*, vol. 54, pp. 35–53, 2016.

[6] K. C. Mills and B. J. Keene, “Physical properties of BOS slags,” *Int. Mater. Rev.*, vol. 32, no. 1, pp. 1–120, Jan. 1987, doi: 10.1179/095066087790150296.

[7] E. T. Turkdogan and R. J. Fruehan, *Fundamentals of iron and steelmaking*, vol. 11. 1998.

[8] C. Cicutti, M. Valdez, T. Perez, R. Donayo, and J. Petroni, “Analysis of slag foaming during the operation of an industrial converter,” *Lat. Am. Appl. Res.*, vol. 32, no. 3, pp. 237–240, 2002.

[9] C. Cicutti *et al.*, “Sudy of slag-metal reactions in an LD-LBE converter,” in *Proceedings of the Sixth International Conference on Molten Slags, Fluxes and Salts*, Stockholm-Helsinki, 2000, pp. 69–78.

8 Critical Assessment of the applicability of the foaming index to the industrial BOF process[10]

The goal of this chapter is to assess the applicability of the concept of a 'slag foaming index' on industrial data. For this purpose, process data from the steel plant of ArcelorMittal Ghent was used. An acoustic measurement was used to identify the heats with high levels of slag foaming. A model based on process data was used to estimate the slag's composition during the converter process. The results of this model, together with industrial data on the slag's end composition, were used as input to calculate the slag's viscosity, density and surface tension. Subsequently, the calculated foaming indices were compared to the acoustic measurements from industry.

8.1 Introduction

Slag foaming occurs whenever gas bubbles, either injected or produced via chemical reactions, are introduced and retained in the molten slag. As a result, the volume of the liquid slag increases, influencing the slag's height. On one hand, foaming of slag is desired due to the creation of a physical protective layer (protection against material and temperature losses) and the beneficial influence on refining. [1], [2] On the other hand, if the foaming is too vigorous, the slag height might become uncontrollable and could reach levels exceeding the height of the vessel. This results in overflow of the installation, also known as 'slopping' in BOF steelmaking [2]. Both from safety and processing view this is undesired.

Bikerman [3] introduced the concept of foaminess based upon the assumed linear relation between the foam height (H in m) and a so-called superficial gas velocity (j in m/s). The latter is defined as the ratio of the gas flow over the cross-sectional area of lance. The proportionality factor is defined as the 'foaming index' (Ω in s) and is an indication of the average residence time of the gas in the foam.

[10] This chapter was published as: *L. De Vos, V. Cnockaert, I. Bellemans, C. Vercruyssen, and K. Verbeken, "Critical Assessment of the Applicability of the Foaming Index to the Industrial Basic Oxygen Steelmaking Process," steel research international, vol. 92, no. 1, 2021.*

$$H = \Omega j \tag{8.1}$$

Several studies [4]–[7] used this foaming index to describe the foaming of the slags in their experiments. Often these studies also attempted to link the measured foaming index to the calculated physical slag properties. An overview of the proposed expressions for the foaming index is given in Table 8-1. The most often mentioned physical properties are the slag's viscosity (μ), surface tension (σ) and density (ρ). Both Jiang and Fruehan [4] and Kim et al. [7] used an additive model to calculate the surface tension and density. For the slag's viscosities the Urbain model was used. Ito and Fruehan [6] referred to Japanese work [8] for their calculation of the surface tension of which the authors of the present work could not find an English translation. Some expressions also contain other interface related properties such as the bubble diameter (D) and effective surface elasticity of the bubble film (E_{eff}). For industrial processes, the exact bubble diameters are unknown and calculation of the surface elasticities is tedious [9] since it requires the knowledge of the surface tension of the slag, the activity and diffusivity of silica and the oscillation frequencies of the gas bubbles [10].

More complex relations are suggested by e.g. Pilon and co-workers [11], [12], [9]. Even though Lotun and Pilon [9] report a good fit for these correlations with collected experimental data, they also argue to apparent contradiction in the correlations of Pilon [11], [12] because the surface tension is present in the numerator. It is argued that this is effect is however, countered by the bubble radius (a property affected by the surface tension) which is in the denominator. Most of the established equations in Table 8-1 identify the viscosity of the liquid slag as the dominant property in the slag's foaming behaviour. However, other research on slag foaming, in which no foaming indices are defined, reports different conclusions. Hara and Ogino [13] link vigorous foaming with the presence of surface active components (e.g. SiO_2,P_2O_5, etc.), which stabilise the bubble lamella, rather than to the viscosity of these slags. Furthermore, Wu et al. [14] mentioned the foam height does not follow simple increasing trends as function of viscosity or superficial gas velocity.

Table 8-1: Overview of proposed expression of the foaming index as function of physical slag properties.

Authors	Slag system	Expression	Eq.
Ito – Fruehan [5], [6]	$CaO – SiO_2 – FeO$ 1250°C – 1400°C	$\Omega = 570 \frac{\mu}{\sqrt{\rho\ \sigma}}$	(8.2)
Jiang – Fruehan [4]	$CaO – SiO_2 – FeO$ $CaO – SiO_2 – FeO – MgO – Al_2O_3$ 1500 °C	$\Omega = 115 \frac{\mu}{\sqrt{\rho\ \sigma}}$	(8.3)
Kim – Min – Park [7]	$CaO – SiO_2 – FeO – Al_2O_3$ 1500°C	$\Omega = 214 \frac{\mu}{\sqrt{\rho\ \sigma}}$	(8.4)
Kim – Min – Park [7]	$CaO – SiO_2 – FeO – MgO_{sat.} – X$ (X= Al_2O_3 , MnO, CaF_2, P_2O_5) 1500°C	$\Omega = 999 \frac{\mu}{\sqrt{\rho\ \sigma}}$	(8.5)
Skupien – Gaskell [15]	$CaO – SiO_2 – FeO$ 1300°C – 1435°C	$\Omega = 100 \frac{\mu^{0.54}}{\rho^{0.39}\ \sigma^{0.15}}$	(8.6)
Zhang – Fruehan [16]	$CaO – SiO_2 – FeO – Al_2O_3$	$\Omega = 115 \frac{\mu^{1.2}}{\rho\ \sigma^{0.2} D^{0.9}}$	(8.7)
Ghag – Hayes – Lee [10], [17], [18]	Water – Glycerol *Verification with CaO – SiO2 – FeO slags at 1550°C*	$\Omega = 10^6 \frac{\mu\ E_{eff}}{\rho^2 g^2 D^3}$	(8.8)

In industrial processes, the slag is not always completely liquid and contains solid particles which can also influence the slag's foaming behaviour. Jiang and Fruehan [4] used the modified Einstein equation to calculate the complete slag system's viscosity and determined the foaming index for solid containing slags using the relation as given in equation 8.3. Cicutti et al. [19] used the same approach for calculating the foaming index of industrial BOF slags, based on collected samples. On the other hand, Luz et al. [20] and Almeida et al. [21] mentioned the existence of a range of solid fractions for which the increase in total viscosity will increase the foaming behaviour. However, a too high solid fraction will have a destructive effect on foaming. This is shown in Figure 8.1, where Θ indicates the fraction of solid particles.

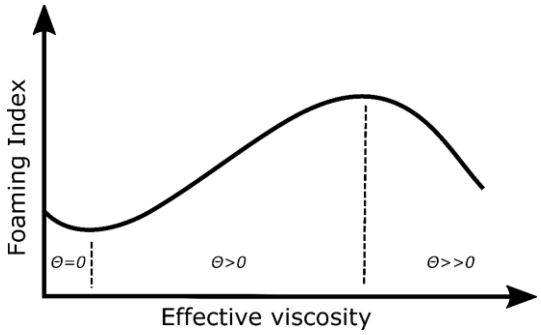

Figure 8.1: The relationship between foaming index and effective viscosity. Adapted from [20] .

Apart from the intrinsic slag properties, also the gas evolution rate will contribute to the finally obtained foaming height. Wu et al. [14] mentioned the foaming behaviour does not follow simple trends for variation of viscosity or superficial gas velocity and a Gaussian distribution was proposed as valid approximation both for the effect of viscosity and superficial velocity on the foaming height. Other research [22] identifies the gas generation rate as the main influence upon the foaming behaviour of slags, rather than the slag properties. Cnockaert et al. [22] focused on undesired and uncontrolled slopping in the industrial copper smelting process, where they identified the gas generated during the process to be the main influence in the foaming. The unpredictability of foaming was linked with the possible imbalance between oxidation and reduction in the slag – matte system. And Khadhraoui et al. [23] linked the effect of solid particles on foaming to their role in the CO-nucleation rather than their effect upon slag viscosity.

Even though a vast amount of lab scale experimental studies on foaming indices are reported, the studies performed on industrial data remain limited. Especially, for the BOF

process a thorough assessment of the applicability of this 'slag foaming index' concept is, to the best of the author's knowledge, lacking. In their work from 2001, Cicutti et al. [19] used a calculated foaming index of samples taken during the industrial blow to estimate the foaming height during a heat. The results were used to discuss slag heights during a blow, but not to compare different heats (and slag composition) to each other. Jung and Fruehan [24] focused on slag compositions which were relevant for the first stages of the BOF blowing process. Yet, to investigate compositional influences, lab scale set ups were used. However, the industrial BOF process is fundamentally different than the lab set ups e.g. reactive gas versus inert gases and strong mixing of different phases versus static slag phase. In recent literature CFD calculations [2] are used to study foaming. Yet, even though this research investigated the relevant slag system with variation of the FeO content, it still is a large simplification from the real industrial process. For instance, only a slag phase was considered and the gas was an injected inert gas.

The current chapter aims to investigate the possibility to apply this concept of 'foaming index' in an industrial environment. If the industrial slag foaming can be linked with the calculated foaming indices and hence, the slag's physical properties and composition, these indices could be used as a predictive tool. Furthermore, the possibility to identify compositions for which slopping occurs via the foaming indices, could be an important step in gaining insight in and controlling the industrial foaming. For this purpose, a set of heats produced at the ArcelorMittal Ghent steel shop was selected. For each heat both the industrial end of blow slag composition as well as the calculated composition during blow were used to calculate foaming indices. The slopping behaviour of the heat was quantified with an acoustic measurement. In this chapter the foaming index is always calculated according to the formula given in relation 8.9 [4]–[7].

$$\Omega \propto \frac{\mu}{\sqrt{\rho\,\sigma}} \tag{8.9}$$

In the 'Methodology' section of this chapter the industrial converter characteristics and process data are discussed. Furthermore, a model was developed to calculate the slag composition of each heat during blow. A thorough overview of this model and its assumptions is given in the 'Model development' part of this work and can be consulted in chapter 7. Yet, for the convenience of the reader the most important features and assumptions of this model are summarized here as well. Finally, the models used to calculate the physical slag properties are discussed. In the 'Results and Discussion'

section, the influence of different physical properties on the foaming index is discussed. Next, it is investigated if a link can be established between foaming indices and acoustic measurements. Finally, a general conclusion is given of all the discussed results.

8.2 Methodology

A selection of heats produced in 2019 at the ArcelorMittal Ghent plant is made. All these heats are produced on the same 330 ton top blown converter. Only heats with the same oxygen blowing pattern (both volumetric flow rate and lance height) are selected. For each of these heats, all the input and output data of the industrial process are available for the authors of this work. The end of blow slag composition is the industrially calculated composition. Additionally, an industrial slag sample at the end of blow is available. The composition of these samples is determined using X-ray fluorescence (XRF). The slag mass is calculated from this measured composition with a CaO mass balance. Hence, for the heats also an XRF-composition at the end of blow is available. For the industrial compositions the FeO and Fe_2O_3 content is calculated from the overall Fe-content with an empirical relation, which was established previously using wet chemical analyses. For some calculations in this work, the continuous off gas analysis is used. The composition of the off gas is measured with a mass spectrometer.

The foaming behaviour of slags during the blow is monitored using a continuous acoustic measurement. This measurement of the sound's intensity is part of the company's expertise and has been used for slag foaming monitoring, and for certain installations also for automated controlling purposes, in industry for many years. This is a relative measurement, dependent on the installation and its geometry, which will alter over time due to refractory wear. Because of this geometrical dependency, the successive heats are grouped according to identical geometrical conditions to correctly compare the acoustic measurements. A foaming slag covers the oxygen lance and damps the noise [1], resulting in a lower acoustic measurement. Thus, low acoustic measurements correspond to high foam heights, while high acoustics measurements correspond to low foam heights. Two examples of the acoustic signal for two randomly selected heats with identical geometrical settings are shown in Figure 8.2. The steep decrease around 10% O_2 blown, is associated with the increase in slag mass due to slag formation. At the start of the process, there is no slag present. Once the process starts, slag is formed due to oxidation reactions and dissolution of fluxes. Thus, it takes some time before a sufficient amount of slag is formed and acoustic signals are muted. From industrial experience, it

is known that slopping for regular heats usually occurs at a time in the process when 30 to 40% of the total required O_2 has been blown. For the two heats shown in Figure 8.2, heat A has a lower acoustic signal during this interval than heat B and thus heat A has more slag foaming than heat B in the 30 to 40% O_2 interval. In a first stage, the acoustic measurements during this interval are used to verify if a relation can be found between the acoustic measurement and the slag foaming index corresponding to the end of blow composition.

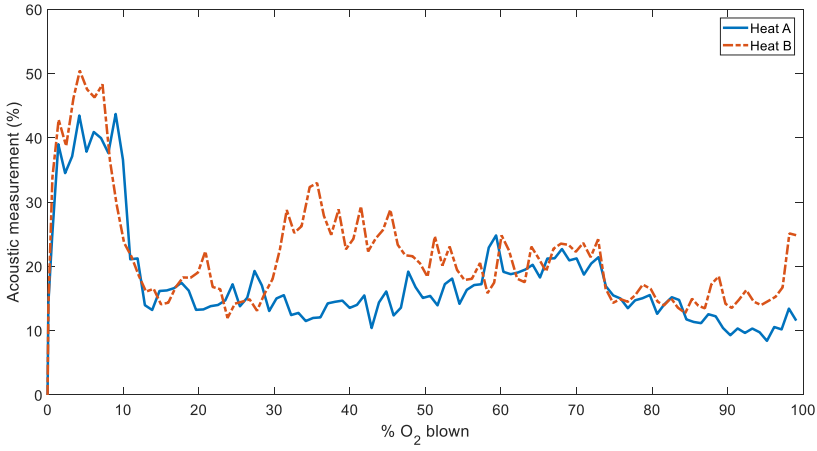

Figure 8.2: Example of an acoustic signal in function of the oxygen blown for two random heats with identical geometrical settings.

Secondly, also the possibility to establish a relation between the continuous acoustic measurement and the slag foaming index corresponding to the instantaneous slag composition is examined. For this the composition of a simplified slag system, $CaO - SiO_2 - FeO_n - MgO - Al_2O_3 - MnO$, during the blow, is estimated with a model using the continuous in- and output data of the BOF process. Details on this model can be consulted in the previous chapter (Chapter 7).

The foaming index is calculated from the physical properties of the liquid slag using the relation as proposed in equation 8.9. The liquid fraction and its composition are calculated with Chemapp [26] using Factsage 7.2 [27] thermodynamic FToxid databases. The liquid slag viscosity is calculated with a modified quasi-chemical viscosity model [28]–[32]. The density and surface tension are estimated with additive models as proposed by Mills and Keene [33]. Details on these models to calculate the physical slag properties can be found in the 'Introduction' part to this work. Since solids are reported to have an

ambiguous effect on foaming (possibility to increase viscosity drastically, but also possibility to have a destructive effect on foam), the solid fraction is considered separately and is not integrated into the calculated foaming index.

The linear relation between the foaming index calculated with the industrial end of blow composition and the acoustic measurement during the blow is discussed. Next, the acoustic measurement is compared to the foaming index calculated with the estimated slag composition during the refining process. For these discussions five groups, containing heats with identical geometrical converter settings, are selected from the 760 considered heats. These groups are chosen in such a way that they contain the largest amount of data. The amount of heats in these groups range from 13 to 25.

8.3 Results and discussion

8.3.1 Effect of properties on foaming index

From the expression for the foaming index as defined in equation relation 8.9, it is clear that to double the foaming index, either the viscosity needs to be doubled or the product of density and surface tension needs to decrease with a factor four. However, when evaluating the ranges for viscosities, densities and surface tensions, the viscosity is the only property which varies over a wide range. For all the considered slag compositions at every moment in the process, the viscosity varies between 10 mPa·s and 100 mPa·s, the surface tension between 500 mN/m and 600 mN/m and densities between 2.8 g/cm³ and 3.6 g/cm³. Upon considering only the industrial end compositions, values between 10 mPa·s and 30 mPa·s are calculated for the viscosity. The density only ranges between 3 g/cm³ and 3.25 g/cm³, and the surface tension between 450 mN/m and 500 mN/m.

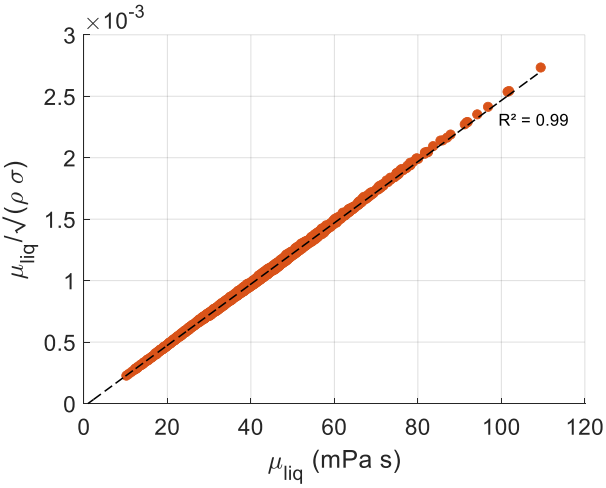

Figure 8.3: Foaming index as function of the viscosity for all the compositions during the blow.

From Figure 8.3 and Figure 8.4 it is clear that the viscosity is the dominant parameter in the calculated foaming indexes. Even though density and surface tension are also temperature and composition dependant, their relative variations are much smaller than the relative variation of viscosity for the considered compositions and temperatures, resulting in a merely constant contribution to the foaming index.

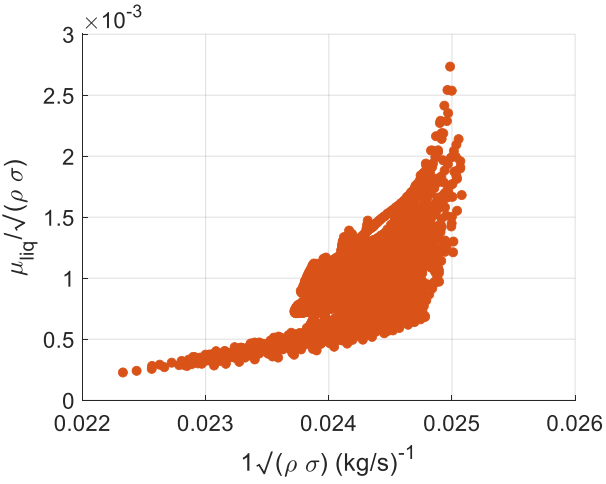

Figure 8.4: Foaming index as function of the inverse ratio of the square root of the density and the surface tension for all the compositions during the blow.

8.3.2 Relation foaming index and industrial end of blow data

For each heat, the calculated foaming index is compared to its average acoustic measurement from the 30% - 40% O_2 blown interval. This interval was selected based upon the industrial experience as explained earlier. In Figure 8.5, the comparison together with the linear fit between the two variables is shown. The Pearson correlation coefficients for each fit are shown in Table 8-2. It is not immediately possible to find a unique linear relation between acoustic measurements and the calculated foaming index of a slag from the end of blow composition, even though all the linear fits confirm the expected trend.

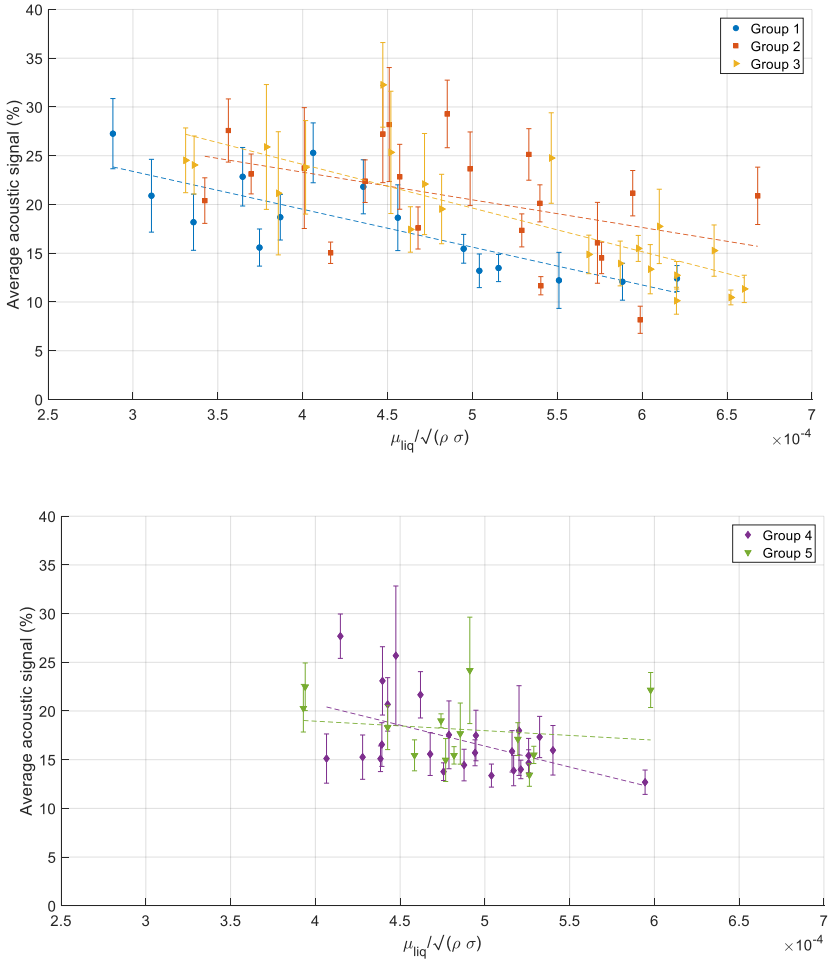

Figure 8.5: Linear relation between the foaming index at end of blow and the average acoustic measurement between 30% and 40% O2 blown.

From the five groups, the best correlation was found for group 1 and 3. However, as shown in Figure 8.5 and Table 8-2, it is clear that this is still insufficient to establish a distinct correlation between the foaming index and the acoustic signal. Furthermore, for the other three groups only a very poor correlation is observed between the two variables. One reason could be that the end of blow composition might be considerably different from the composition of the slag at 30% O_2, when slopping issues occur. The foaming index calculated with the composition during blow is therefore discussed in the next section.

Table 8-2: Correlation coefficients for the linear relations shown in Figure 8.5.

	Correlation coefficient
Group 1	-0.80
Group 2	-0.44
Group 3	-0.80
Group 4	-0.51
Group 5	-0.16

8.3.3 Relation foaming index and composition during blow

For the same five groups the slag composition during the process is estimated with the earlier described model. The same procedure, as described earlier, to calculate the physical properties and the foaming index are used. For every heat, there is data both for the acoustic measurement and the slag composition at each considered measuring point during the process. An example of this data, for one heat, is shown in Figure 8.6.

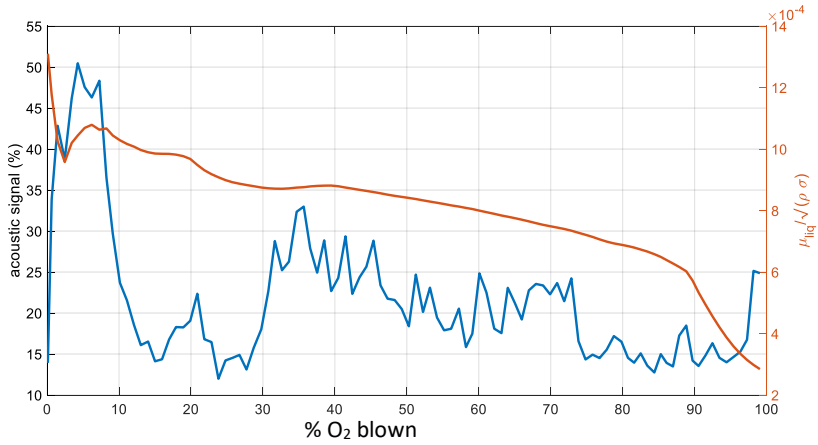

Figure 8.6: Acoustic signal (%) and foaming index as function of the oxygen blown for one specific heat.

To verify if a relation can be established between the calculated foaming index and the acoustic measurement the two variables are compared to each other for all measuring points during each heat. Results are shown for group 1 and 3 in Figure 8.7, for the other groups results are shown in the Appendix A. Each figure only shows five randomly selected heats to reduce the number of data points on the figures and enhance readability. Only data points for more than 20% of the total oxygen blown are shown since the very start of the acoustic measurement is linked to slag formation.

It is observed that for some of the heats (e.g. group 3 – heat 2 and 4) the foaming indices remain constant for a wide range of acoustic measurements. This is remarkable because it indicates the acoustic measurement and hence foaming, is affected by another feature (e.g. gas evolution) than the slag composition and corresponding physical properties, which remain more or less constant according to the foaming indices. Similar results were observed for group 2, 4 and 5.

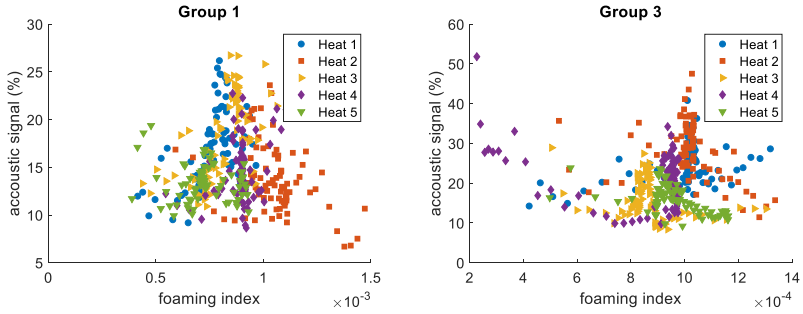

Figure 8.7: foaming index of the liquid slag as function of the acoustic signal for five random selected heats in group 1 and group 3.

For all the heats considered in the five groups, the Pearson correlation coefficient between the calculated foaming index and the acoustic measurement is determined. The results are shown in the histogram in Figure 8.8. For some heats this correlation coefficient is negative, indicating a higher foaming index corresponds to a lower acoustic measurement. This would be the expected relation. Yet, for even more heats, a positive correlation coefficient is determined, indicating that for these heats a higher foaming index corresponds to a higher acoustic measurement. This is the opposite of the expected relation between the two variables. Furthermore, nearly all the correlation coefficients lie within the [-0.6;0.6] range. Thus, there is only a very poor linear relation between the foaming index and the acoustic measurement.

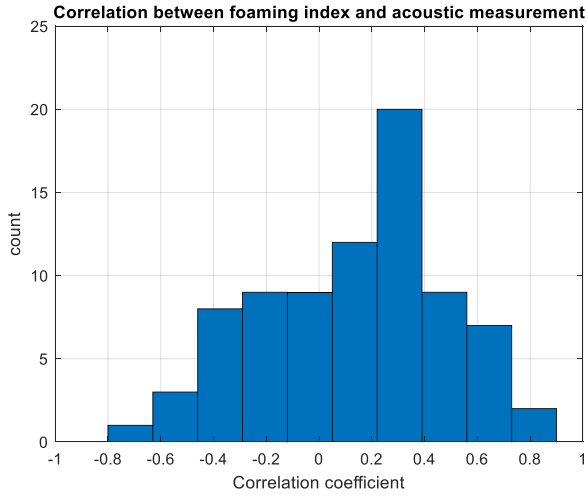

Figure 8.8: Correlation coefficients of the continuous foaming index and the acoustic measurement.

Up till this point, the total slag mass was left out of the analyses and as such it was assumed all heats had comparable masses. However, this is not the case. Within the same group some heats have slag masses which are double the mass of other heats. For the foaming index the slag mass is irrelevant, since the physical properties are only dependent upon the composition and not on the total amount of material present. Yet, the acoustic measurement is a relative measurement which is low for high slag heights and high for low slag heights. Heats for which more slag is produced, will have higher volumes and thus have higher slag heights, even without the foaming effect considered. To integrate this effect into the acoustic signal a scaling of this signal according to the slag volume is proposed. The density of the slags for the considered heats in the five groups at 30% O2 blown nearly all lie in the 2% range of 3.2 kg/dm³, which is within the range of experimental uncertainty for density measurements [33]. To avoid inserting any dependency between the foaming index and the scaled acoustic signal and because the densities for the slags of the compared heats are similar, the scaled acoustic signal is defined as the acoustic signal per ton slag rather than per m³ slag. For the two groups the relation between the scaled acoustic signal and the foaming index is shown in Figure 8.9. The result for the other three groups can again be consulted in Appendix A. From these results, it is also concluded that no linear relation can be established between the foaming index and the weighted acoustic measurement.

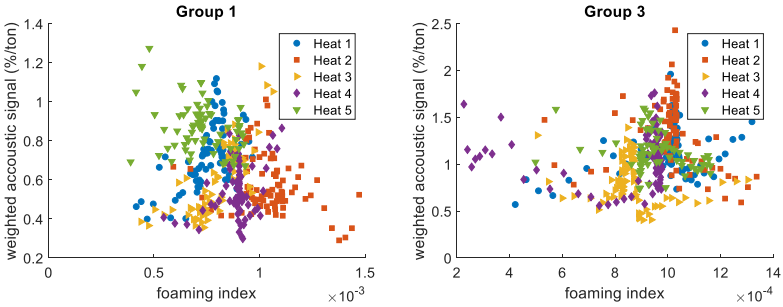

Figure 8.9: foaming index of the liquid slag as function of the weighted acoustic signal for five random selected heats in group 1 and group 3.

Finally, it should be mentioned Kim et al. [7] distinguish MgO-saturated slags from slags without MgO saturation in their foaming index calculation. Even though the ratio of the physical slag properties remains unchanged, the scaling factor is different for the two types of slags. For this reason, the considered heats were divided into two groups, one with the MgO saturated slags and one with the other slags. Yet, analyses of the results, are analogous to the previous figures and discussions and it was impossible to find a good correlation between acoustic measurement and calculated foaming indices. As an illustration, an example of such an analysis is included in the Appendix to this work.

8.3.4 Final discussion

From these results and analyses, the calculated liquid slag foaming indices based only upon physical slag properties cannot be linked to the industrial observations of foamy slags. For the considered industrial compositions, the viscosity seems to be the property with the largest influence upon the final calculated foaming index. It might be more interesting to focus on the variation of the viscosity for these heats rather than considering a ratio of properties. It should, however, also be mentioned that only a simplified slag system was considered. Often P_2O_5 is mentioned [7], [13], [33] as a surface active component, influencing the slag's surface tension. Yet, this component was left out of the analyses in this work. The main reason for this is that the used models for viscosity and surface tension are not optimised for P_2O_5. Furthermore, this component is also not considered to be a major component in the slag systems. On the other hand, the original experiments used to construct the investigated foaming index also consider a simplified slag system, without P_2O_5. Only Kim et al. [7] investigated slags containing P_2O_5 and which were MgO saturated.

To the best of the author's knowledge, the proposed foaming indices are always derived from lab scale experiments in which the injected gas is inert. Other research [24] investigated the applicability of the foaming index, as proposed in equation 8.9. Yet, this was also done in a lab scale set up with introduction of inert gas. These foaming indices thus hold for homogeneous slag systems with steady state inert gas flow. This is fundamentally different from industrial applications. The gas, responsible for foaming or slopping, in the industrial BOF vessel is not inert. It is either oxygen, which has not reached the metal bath, or it is CO/CO_2-gas, which is formed during refining. The CO-gas is either formed from direct oxidation, yet, most CO is probably produced during the indirect oxidation with FeO_n in the slag itself. Resulting in a system, which might behave completely different than the lab scale set ups used to derive the foaming index. Furthermore, gases from reactive sources are stated [16], [21] to have a smaller diameter and thus increase foaming behaviour compared to gases which are injected. Additionally, the slag in the BOF vessel is probably not homogeneous and gradients in temperature, oxygen partial pressure and composition might exist during the process. This might contribute to the unpredictable nature of the foaming behaviour. Cnockaert et al. [22] investigated foaming during the copper smelting process and concluded the foaming index and flow rate of injected gases was not sufficient to describe the observed foaming. Furthermore, they argued this unpredictable foaming is due to the sudden changes in the system and a possible imbalance between oxidation and reduction reactions in the slag. Even though their research focussed on copper smelting, they also linked unpredictable foaming to changes in the reaction conditions during the industrial process, rather than to slag properties alone.

8.4 Conclusion

In this chapter, the applicability of the calculated foaming index in the context of an industrial BOF process was investigated. The conclusion is twofold. Firstly, the calculated foaming index is inadequate to identify heats with higher foaming heights in the investigated industrial BOF process. It is not possible to establish a simple relationship between the foaming index, calculated from slag compositions determined using the industrial data, and the acoustic measurements. This foaming index cannot be applied in the considered industrial context to identify foamy slags. Secondly, the variation in calculated viscosities, even without consideration of solid particles, is much higher than the variation in either surface tension or density of these industrial slags. As a result, the calculated foaming index is dominated by the viscosity of the slag.

8.5 References

[1] S. Seetharaman, A. McLean, R. Guthrie, and S. Sridhar, *Treatise on Process Metallurgy*, vol. 2. Elsevier, 2013. Accessed: Oct. 05, 2018. [Online]. Available: http://urn.kb.se/resolve?urn=urn:nbn:se:kth:diva-151111

[2] M. A. Sattar, J. Naser, and G. Brooks, 'Numerical simulation of slag foaming on bath smelting slag (CaO–SiO2–Al2O3–FeO) with population balance modeling', *Chem. Eng. Sci.*, vol. 107, pp. 165–180, Apr. 2014, doi: 10.1016/j.ces.2013.11.037.

[3] J. J. Bikerman, *Foams*. Springer Science & Business Media, 2013.

[4] R. Jiang and R. J. Fruehan, 'Slag foaming in bath smelting', *Metall. Trans. B*, vol. 22, no. 4, pp. 481–489, Aug. 1991, doi: 10.1007/BF02654286.

[5] K. Ito and R. J. Fruehan, 'Study on the foaming of CaO-SiO2-FeO slags: Part I. Foaming parameters and experimental results', *Metall. Trans. B*, vol. 20, no. 4, pp. 509–514, Aug. 1989, doi: 10.1007/BF02654600.

[6] K. Ito and R. J. Fruehan, 'Study on the foaming of CaO-SiO2-FeO slags: Part II. Dimensional analysis and foaming in iron and steelmaking processes', *Metall. Trans. B*, vol. 20, no. 4, pp. 515–521, Aug. 1989, doi: 10.1007/BF02654601.

[7] H. S. Kim, D. J. Min, and J. H. Park, 'Foaming Behavior of CaO–SiO2–FeO–MgOsatd–X (X = Al2O3, MnO, P2O5, and CaF2) Slags at High Temperatures', *ISIJ Int.*, vol. 41, no. 4, pp. 317–324, Apr. 2001, doi: 10.2355/isijinternational.41.317.

[8] Y. Kawai, K. Mori, H. Shiraishi, and N. Yamada, 'Surface Tension and Density of FeO-CaO-SiO₂ Melts', *Tetsu--Hagane*, vol. 62, no. 1, pp. 53–61, 1976, doi: 10.2355/tetsutohagane1955.62.1_53.

[9] D. Lotun and L. Pilon, 'Physical Modeling of Slag Foaming for Various Operating Conditions and Slag Compositions', *ISIJ Int.*, vol. 45, no. 6, pp. 835–840, 2005, doi: 10.2355/isijinternational.45.835.

[10] S. S. Ghag, P. C. Hayes, and H.-G. Lee, 'The Prediction of Gas Residence Times in Foaming CaO–SiO2–FeO Slags', *ISIJ Int.*, vol. 38, no. 11, pp. 1216–1224, 1998, doi: 10.2355/isijinternational.38.1216.

[11] L. Pilon and R. Viskanta, 'Bubble transport in three-dimensional laminar gravity-driven flow – numerical results', *J. Non-Cryst. Solids*, vol. 336, no. 2, pp. 84–95, May 2004, doi: 10.1016/j.jnoncrysol.2004.01.007.

[12] L. Pilon, A. G. Fedorov, and R. Viskanta, 'Steady-State Thickness of Liquid–Gas Foams', *J. Colloid Interface Sci.*, vol. 242, no. 2, pp. 425–436, Oct. 2001, doi: 10.1006/jcis.2001.7802.

[13] S. Hara and K. Ogino, 'Slag-foaming Phenomenon in Pyrometallurgical Processes', *ISIJ Int.*, vol. 32, no. 1, pp. 81–86, Jan. 1992, doi: 10.2355/isijinternational.32.81.

[14] L. S. Wu, G. J. Albertsson, and D. Sichen, 'Modelling of slag foaming', *Ironmak. Steelmak.*, vol. 37, no. 8, pp. 612–619, Nov. 2010, doi: 10.1179/030192310X12690127076550.

[15] D. Skupien and D. R. Gaskell, 'The surface tensions and foaming behavior of melts in the system CaO-FeO-SiO2', *Metall. Mater. Trans. B*, vol. 31, no. 5, pp. 921–925, Oct. 2000, doi: 10.1007/s11663-000-0068-1.

[16] Y. Zhang and R. J. Fruehan, 'Effect of the bubble size and chemical reactions on slag foaming', *Metall. Mater. Trans. B*, vol. 26, no. 4, pp. 803–812, Aug. 1995, doi: 10.1007/BF02651727.

[17] S. S. Ghag, P. C. Hayes, and H.-G. Lee, 'Model Development of Slag Foaming.', *ISIJ Int.*, vol. 38, no. 11, pp. 1208–1215, 1998, doi: 10.2355/isijinternational.38.1208.

[18] S. S. Ghag, P. C. Hayes, and H.-G. Lee, 'Physical Model Studies on Slag Foaming.', *ISIJ Int.*, vol. 38, no. 11, pp. 1201–1207, 1998, doi: 10.2355/isijinternational.38.1201.

[19] C. Cicutti, M. Valdez, T. Perez, R. Donayo, and J. Petroni, 'Analysis of slag foaming during the operation of an industrial converter', *Lat. Am. Appl. Res.*, vol. 32, no. 3, pp. 237–240, 2002.

[20] A. P. Luz, T. A. Ávila, P. Bonadia, and V. C. Pandolfelli, 'Slag Foaming: Fundamentals, Experimental Evaluation and Application in the Steelmaking Industry', *Refract. WorldForum*, vol. 3, p. 91, 2011.

[21] R. A. M. de Almeida *et al.*, 'Slag Foaming Fundamentals - A Critical Assessment', *Mater. Res.*, vol. 20, no. 2, pp. 474–480, Apr. 2017, doi: 10.1590/1980-5373-mr-2016-0059.

[22] V. Cnockaert, I. Bellemans, K. Verbeken, T. Crivits, and B. Blanpain, 'On the origin of sudden slag foaming during copper smelting', presented at the Copper 2019, Vancouver, 21/08 2019.

[23] S. Khadhraoui *et al.*, 'Modeling and Control of the BOF process: Challenges, solutions and latest developments in SMS group', presented at the METEC and 4th European Steel Technology and Application Days (ESTAD) 2019, Düsseldorf, Jun. 2019.

[24] S.-M. Jung and R. J. Fruehan, 'Foaming Characteristics of BOF Slags.', *ISIJ Int.*, vol. 40, no. 4, pp. 348–355, 2000, doi: 10.2355/isijinternational.40.348.

[25] Publications Office of the European Union, 'Imphos : improving phosphorus refining.', Dec. 14, 2011. https://publications.europa.eu/en/publication-detail/-/publication/8aecbb7c-f77f-4ee7-bc38-9ebb13b52faf/language-en (accessed Nov. 06, 2018).

[26] S. Petersen and K. Hack, 'The thermochemistry library ChemApp and its applications', *Int. J. Mater. Res.*, vol. 98, no. 10, pp. 935–945, Oct. 2007, doi: 10.3139/146.101551.

[27] C. W. Bale *et al.*, 'FactSage thermochemical software and databases, 2010–2016', *Calphad*, vol. 54, pp. 35–53, 2016.

[28] A. N. Grundy, H. Liu, I.-H. Jung, S. A. Decterov, and A. D. Pelton, 'A model to calculate the viscosity of silicate melts', *Int. J. Mater. Res.*, vol. 99, no. 11, pp. 1185–1194, Nov. 2008, doi: 10.3139/146.101752.

[29] A. N. Grundy, I.-H. Jung, A. D. Pelton, and S. A. Decterov, 'A model to calculate the viscosity of silicate melts', *Int. J. Mater. Res.*, vol. 99, no. 11, pp. 1195–1209, Nov. 2008, doi: 10.3139/146.101753.

[30] A. N. Grundy, I.-H. Jung, A. D. Pelton, and S. A. Decterov, 'A model to calculate the viscosity of silicate melts: Part II: The NaO0. 5–MgO–CaO–AlO1. 5–SiO2 system', *Int. J. Mater. Res.*, vol. 99, no. 11, pp. 1195–1209, 2008.

[31] S. A. Decterov, A. N. Grundy, I.-H. Jung, and A. D. Pelton, 'Modeling the viscosity of aluminosilicate melts', in *AIP Conference Proceedings*, 2007, vol. 963, pp. 404–407.

[32] W.-Y. Kim, A. D. Pelton, and S. A. Decterov, 'A model to calculate the viscosity of silicate melts: Part III: Modification for melts containing alkali oxides', *Int. J. Mater. Res.*, vol. 103, no. 3, pp. 313–328, 2012.

[33] K. C. Mills and B. J. Keene, 'Physical properties of BOS slags', *Int. Mater. Rev.*, vol. 32, no. 1, pp. 1–120, Jan. 1987, doi: 10.1179/095066087790150296.

IV. Thermodynamic BOF Model

"Of course it is happening inside your head, Harry, but why on earth should that mean that it is not real?"

Harry Potter and the Deathly Hallows – J.K. Rowling

9 Physicochemical models for the BOF process[11]

In this dissertation focus is put on modelling of the BOF process rather than on experimental work. In this chapter, state of the art modelling techniques are discussed. Modelling of the basic oxygen furnace (BOF) process, both for online monitoring and fundamental research, has gained importance in steelmaking industry over the past decades. Especially models integrating fundamental physicochemical relations are appealing. In the introductory sections, an overview is given on the assumptions and models for underlying BOF phenomena, which are frequently used in the BOF models and sub models. Focus was put on six models with emphasis on the chemical aspect of the BOF process. For each model, its assumptions are given and subsequently evaluated, highlighting both their strengths and limitations. The six different models are also compared to each other. Finally, opportunities for future research are discussed.

9.1 Reaction zone models

Within a BOF-vessel different reaction zones are identified during the process, as was already briefly mentioned in the first chapter of this dissertation. Over the past decades, several models, both theoretical as well as empirical, have been proposed to model these different reaction zones. An overview of the state-of-the-art models and assumptions for the relevant reaction zones, or phenomena in the BOF process, in this work are summarized here. These are often used as submodels in the more general BOF process models, that are the main focus of this chapter.

9.1.1 Jet impact zone

The impingement of the supersonic oxygen jet from the top lance onto the metal bath plays a crucial role in the process. Not only does this introduce the oxygen necessary for the oxidation reactions and accompanied refining, it also provides [1] stirring kinetic energy for gaining spontaneous emulsification. [2] The impingement gas creates a cavity.

[11] This chapter is based on the following publication: L. De Vos, I. Bellemans, C. Vercruyssen, and K. Verbeken, "Basic Oxygen Furnace: Assessment of Recent Physicochemical Models," *Metall. Mater. Trans. B*, vol. 50, no. 6, pp. 2647–2666, Dec. 2019

Molloy [3] identified three different cavity modes i.e. dimpling, splashing and penetrating, as shown in Figure 9.1.

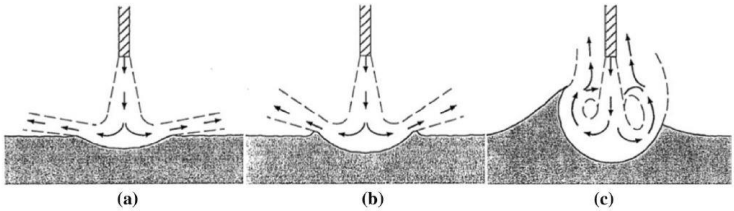

Figure 9.1: Cavity modes as proposed by Molloy [3]: a) dimpling, b) splashing, c) penetrating. Taken from [2].

The lance configuration and blowing parameters (e.g. height of the lance above the bath and blow velocity) will influence the dimensions of the cavity and the cavity mode. Modern top lances in the BOF process are typically multi-hole nozzles, consisting out of 4 to 7 nozzles [4], introducing extra difficulty for theoretical relations between lance parameters and penetration depths. These nozzles are placed in the water-cooled lance under a certain angle with respect to the centre line of the lance. This is known as the inclination angle of the nozzles and a variety of values is found in literature.

In recent literature [2], [5]–[7] computational fluid dynamics (CFD) are used in attempts to model the cavity formation due to the impinging gas jet and link cavity dimensions with process parameters. Nevertheless, in BOF modelling often empirical relations are still used to relate process conditions with the cavity formation.

Koria and Lange [8] described the depression produced by the impinging jet as a parabola in two dimensions. In three dimensional modelling [9], [10] this results in the assumption that the formed cavity can be described as a paraboloid. Koria and Lange [8] linked the height and diameter of the formed cavity with a dimensionless momentum flow rate number, which depends on lance height, nozzle diameter, oxygen blowing pressure, inclination angle of the nozzle and physical parameters of the metal bath. In this approach, the dimensions of the cavity are mainly influenced by number of nozzles, lance distance (with respect to the metal bath) and the oxygen blowing pressure.

9.1.2 Metal droplets in the metal-slag emulsion

During the BOF process, metal droplets are generated which form together with the slag, the so called metal-slag emulsion. Research over the past decades indicated that these

droplets play a crucial role in the steel refining process. More recent, it was observed that these droplets can also swell, which will increase their residence time.

9.1.2.1 Droplet generation

To describe the generation of droplets as a function of the process and material parameters, a dimensionless parameter is introduced. Even though several approaches are available in literature, the approach developed by Coley et al. [11] and Rout et al. [12] is described as this approach is used by most of the state-of-the-art BOF model authors reviewed here. Therefore, it seems more relevant compared to other approaches [13] proposed in literature.

Splashing of the metal bath leads to the generation of metal droplets. This splashing is believed to be related to instability of the surface waves generated at the interface between the liquid and the gas, thus the impinging gas jet from the top lance. This is illustrated in Figure 9.2 as taken from Rout et al.[12].

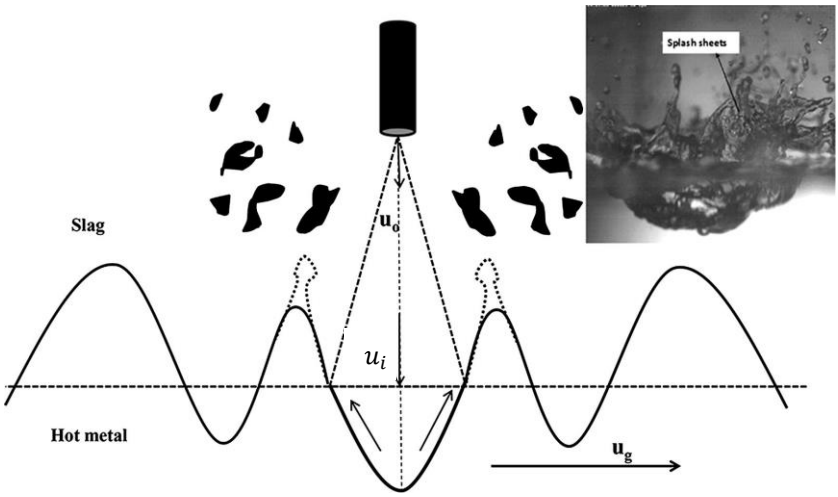

Figure 9.2: Schematic representation of onset of splashing due to Kelvin-Helmholtz surface instability. Taken from [12].

The onset of splashing due to top lance blowing, was mathematically described by Li and Harris [14] with an equation based upon the Kelvin-Helmholtz instability criterion, given in equation 9.1.

$$\frac{\rho_G u_G^2}{2\sqrt{\sigma g \rho_L}} = 1 \tag{9.1}$$

In this equation ρ_G and ρ_L are the densities (kg/m³) of, respectively, gas and liquid. The surface tension (N/m) of the liquid metal is denoted by σ, g is the gravitational acceleration (m/s²) and u_G is the critical gas velocity (m/s). This velocity is the critical tangential velocity at the liquid metal interface and is related to the axial velocity (m/s) of the impinging gas jet from the lance, u_i, according to equation 9.2 [14].

$$u_G = \eta\, u_i \tag{9.2}$$

In equation 9.2, η is a constant. Deo and Bloom [15] fitted this constant to industrial data and found a value of 0.447 and made the observation that droplet generation will be almost negligible when the Weber number ($N_{we} = \frac{\rho_G u_i^2}{2\sqrt{\sigma g \rho_L}}$) is less than 10. This is in line with accepted values when compared to the values collected by Li and Harris [14] for different liquids. However, Subagyo et al. [16] demonstrated that the term expressed in equation 9.1 could be set equal to a blowing number N_B. This number can be used to describe the generation of metal droplets in the BOF process. Thus, the blowing number can be seen as the number of times the critical Kelvin-Helmholtz velocity has been exceeded.

$$\frac{\rho_G u_G^2}{2\sqrt{\sigma g \rho_L}} = N_B \tag{9.3}$$

The relation between the blowing number and the droplet generation rate per unit volume of blown gas is given in equation 9.4. This relationship was empirically established under constant lance height. Coley et al. [11] demonstrated a good graphical fit between this equation and the data from Li and Harris [14] and Subagyo et al. [16].

$$\frac{R_B}{F_G} = \frac{(N_B)^{3.2}}{[2.6e6 + 2e(-4)(N_B)^{12}\,]^{0.2}} \tag{9.4}$$

In this equation R_B ,is the amount of droplets generated (kg/min) and F_G is the volumetric gas flow rate (Nm³/min).

Even though this is a physical approach, several studies [17]–[19] reported the underestimation of the amount of metal in the emulsion as calculated with equation 9.4. Also, an underestimation of dephosphorization was reported when this equation was applied. Equation 9.4 was established under conditions of constant lance height and without considering the effects of flow on the cavity formation.

More recent work by Sabah et al. [20] identified the existence of two splashing modes, depending upon the lance height and operational conditions on one hand and blowing number on the other. One of their conclusions was that a higher blowing number did not necessary result into a higher droplet generation rate. Another aspect is that the density of the gas in equation 9.1, is the density calculated at normal temperature and pressure, while the impact of the jet happens at the metal bath and temperatures largely deviating from the normal temperature. For these reasons, Rout et al. [12] established a corrected version of the theory formulated by Subagyo and co-workers [16]. In their definition of the blowing number, both local conditions for pressure and temperature of the jet and operating conditions, i.e. lance height, are considered. The general form of the expression remains the same, however, both gas density and gas velocity are calculated differently.

9.1.2.2 Residence time

Apart from generation rate and the number of droplets, the residence time of the droplets in the slag-metal emulsion is also an important parameter. The residence time can be significantly increased due to a swelling phenomenon.

Brooks et al. [21] constructed a model to calculate the residence time of the metal droplets in the slag-metal-gas emulsion with consideration of the bloated droplet phenomenon. Their approach starts from a ballistic motion principle, shown in Figure 9.3. Starting from a force balance considering gravitational, buoyancy, drag and added masses forces, the velocity in two dimensions (z,r) is calculated. Finally, the velocities can be written as differential equations, which need to be solved to calculate the final residence time assuming that a droplet enters the slag at position z=0 and also re-enters the metal bath at this position. To integrate the effect of the bloating of the droplets, which leads to an apparent decrease of the droplet density, the decarburisation rate needs to be calculated. First, the critical decarburisation rate, as a function of the FeO content of the slag, is calculated to distinguish between regimes with and without the droplet swelling phenomenon. When the decarburisation rate exceeds the critical value, the initial droplet density is compensated by dividing it through the number of times the critical decarburisation rate is exceeded. This apparent density is used for further calculations.

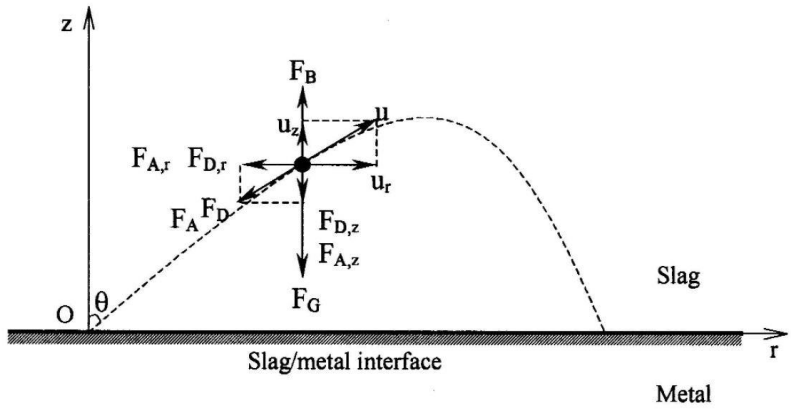

Figure 9.3: Schematic illustration of ballistic motion of a metal droplet in slag. Taken from [21]. In this figure u is the velocity of the droplet relative to the slag, and F_B,F_G,F_D and F_A are respectively the buoyancy, gravitation, drag and added mass forces.

9.1.2.3 Droplet size

Next to the number of droplets and their residence time, the size of the droplets will also play its role in refining. It has been observed [22] that for the same volume of material, several smaller droplets instead of one large droplet will result in faster refining. Instinctively, this can be linked with the increased total interfacial area.

Even though distribution functions for the droplet size have been proposed, some attempts to model the BOF process such as the one by Dogan et al. [23]–[26], do not consider a size distribution but assumes a uniform size for the droplets.

Other state-of-the-art models [9] assume the Rosin-Rammler-Sperling (RRS) distribution [9], [16] for the droplet size. Koria and Lange [27] proposed the RRS distribution for droplet size distribution based on an experimental study. The proposed RRS distribution by Koria and Lange [27] is given in equation 9.5, in which *R* is the cumulative weight (expressed in percentages) of drops remaining on a sieve with diameter *d*. The parameters *n* and *d'* are both distribution parameters expressing homogeneity and the measure fineness, respectively. The dependence of these two parameters upon the blowing conditions in the BOF converter has been discussed by Koria and Lange [27] and Subuyago et al. [16].

$$R = 100\ exp\left[-\left(\frac{d}{d'}\right)^{n}\right] \tag{9.5}$$

9.1.2.4 Bloated droplet theory

There is general agreement that decarburisation of metal in the emulsion zone takes place due to FeO reduction. As a result the carbon content of the metal decreases and CO-gas bubbles are formed. This probably causes extra stirring in the emulsion zone, but will also play its role in foaming behaviour. Many researchers [28]–[30] report the formation of a gas halo around the metal droplets, especially for those with high carbon contents.[24]

At the metal-slag interface of an emulsified metal droplet both carbon and oxygen are available to take part in reactions. The carbon is present in the metal or as CO and the oxygen is present from the decomposition of the slag or dissolved in the metal. An overview of the possible reactions and interfaces is given in Figure 9.4. The bloated droplet theory [9], [31], [32] starts from the concept that when the oxygen absorption rate is higher than the rate at which it can be consumed, there will be an excess of oxygen in metal droplets resulting in an oxygen build up. This oxygen build up can decrease the surface energy of the metal and when the energy related to the internal CO pressure exceeds the energy required to create the interface between the metal droplet and the gas phase, the CO gas bubble will start to form inside the metal droplet. Another approach is to say that once the CO pressure exceeds the ambient pressure, due to oxygen diffusion, there is super saturation in the droplet, making the reaction of oxygen and carbon more favourable. [33] After the internal nucleation of the gas, the droplet is bloated or swollen. [32]

Certain minor elements, such as sulphur, in the slag might have a considerable influence upon the mechanism. It is believed sulphur plays an ambiguous role [32], [34] in the process. On one hand, sulphur will decrease the metal surface tension which accelerates the decarburisation rate and thus CO nucleation rate, due to the reduction of the energy barrier for nucleation. On the other hand, sulphur will also segregate to the surface of the droplet and poison the possible reaction sites. This causes a decrease of the amount of oxygen that can diffuse into the metal droplet, causing on its turn a lower super saturation and as such a decrease of the CO nucleation rate.

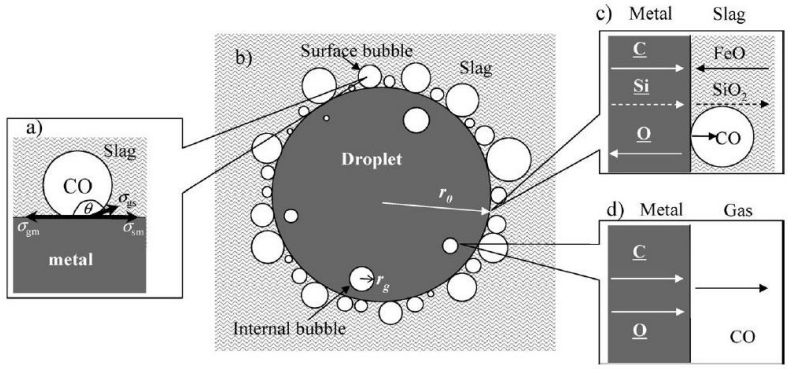

Figure 9.4: Liquid Fe-C droplet in a slag containing FeO. (a) A gas bubble at slag-metal interface, (b) a droplet surrounded by gas bubbles, (c) mass transfers at slag-metal interface, and (d) mass transfers at gas-metal interface. Taken from [33].

The bloating behaviour of droplets has some considerable influence upon the metal-slag interactions. Firstly, the surface area increases. Secondly, the residence time of the metal droplets in the emulsion will also increase. This is believed to have a considerable effect on the kinetics of the complete process. Finally, it is believed the reaction kinetics will also increase due to the turbulence that accompanies the bloated droplet formation process, resulting in a faster mass transfer.

9.2 State-of-the-art of thermodynamic and kinetic models for BOF steelmaking

In literature, already a vast amount of models to simulate the BOF process exist. Some of these models have the goal to be used as in-line process control tool, while others are constructed to gain fundamental insight into the reactions and principles of the refining process. The complexity and assumptions of different models differs since, as often in modelling, there is a trade-off between complexity and computing time.

This work aims to give an overview of six recent developed BOF models which put emphasis on the chemical aspects of the process. Firstly, a small summary of fundamental assumptions and important underlying models to describe reaction zones is given. Focus is put on models describing the interaction with the oxygen jet and the subsequently created metal droplets, which will result in the emulsification of the process. Next, a thorough description for each state-of-the-art model, describing the BOF process, is given. For each model, the assumptions together with both strengths and

limitations are discussed in depth. Subsequently, the six models are also compared to each other and a summary table is given, listing and comparing the main features for each model. In a final chapter, some of the opportunities for future work are discussed.

In general, one could consider two different approaches to construct dynamic BOF models: mathematical or statistical. A mathematical model starts from fundamental physicochemical relations and equations, e.g. thermodynamics and kinetics [9], [17], [23], [35], [36]. Yet, a statistical model [37]–[39] is based on a purely statistical approach in which industrial data is used as input and statistical methods are applied to fit the process to the final output. Nevertheless, due to the complexity of the process, very often even the mathematical models will also need a certain amount of empirical data to fit model parameters.

Further subdivision [36] in the dynamic mathematical models , which are discussed later on, is possible. Loosely two categories can be distinguished: reaction volume models and reaction interface models, schematically shown in Figure 9.5. In reaction interface models, a boundary layer is defined and the rate of reaction is assumed to be controlled by the resistance against mass transfer in the diffusion boundary layers. Interesting information on micro kinetic behaviour (e.g. kinetics of a single droplet in the emulsion phase [9]) can be obtained. However, this approach requires defining reaction interfaces and mass transport coefficients which is often complex. Also parallel rate determining reactions add extra complexity to this approach. The reaction volume models, on the other hand, do not consider reaction interfaces, but emphasis is put on mass exchange between passive bulk volumes and active reaction volumes. In the active reaction volumes, it is assumed equilibrium composition is obtained at every time step. However, to estimate the sizes of the reaction volumes also kinetic assumptions need to be made. An extra appealing aspect of this approach is its compatibility with thermodynamic software.

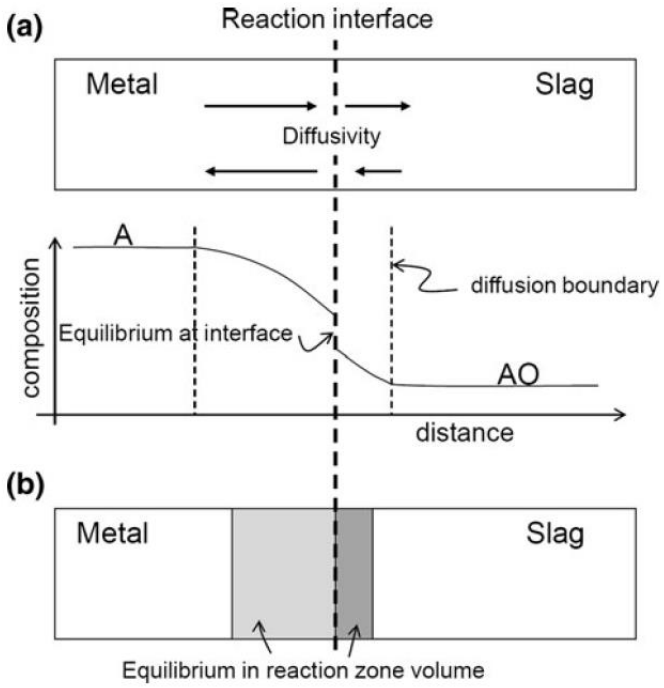

Figure 9.5: schematic representation of the concept of (a) reaction interface model and (b) reaction volume model, applied to metal – slag reaction. Taken from [40].

Modern process models which include thermodynamic and possibly kinetic aspects, can either be single- or multiple zone models. In the case of the single zone model, the complete reactor is considered as one homogeneous unit with complete mixing. Some examples [41], [42] can be found in literature. Yet, the work of Deo and Shukla [41] clearly shows that this single reaction zone is not sufficient to describe all relevant refining phenomena in the BOF process. Especially the initial increase in FeO content of the slag and the dephosphorization are not accurately described by their model. All state-of-the-art models reviewed here are multi-zone models, where different reaction zones are distinguished within the converter. Each model will have its own assumptions made in order to define the number and types of reaction zones.

Only models for which, in the view of the authors of this work, both sufficient and thorough explanation is available in literature and validation is given, are described in detail and discussed in the following sections. For completeness, other recent interesting examples are briefly summarized in the end.

9.2.1 Comprehensive model for oxygen steelmaking (Dogan et al. [23]–[25])

Dogan et al. [23]–[26] built a comprehensive model for the oxygen steelmaking process to gain insights into the decarburisation of the metal. An overview of the model structure is given in Figure 9.6. The model approaches the BOF process from a kinetic viewpoint. Flux dissolution, scrap melting, slag chemistry, temperature profile, formation and residence time of metal droplets in the emulsion zone and different kinetics for the decarburisation in different reaction zones are included. For the model, a mass balance on carbon is used, considering the kinetics of the process. The overall system is divided into two different zones: 'Emulsion zone' and 'Bath zone'. These zones are linked through material flows.

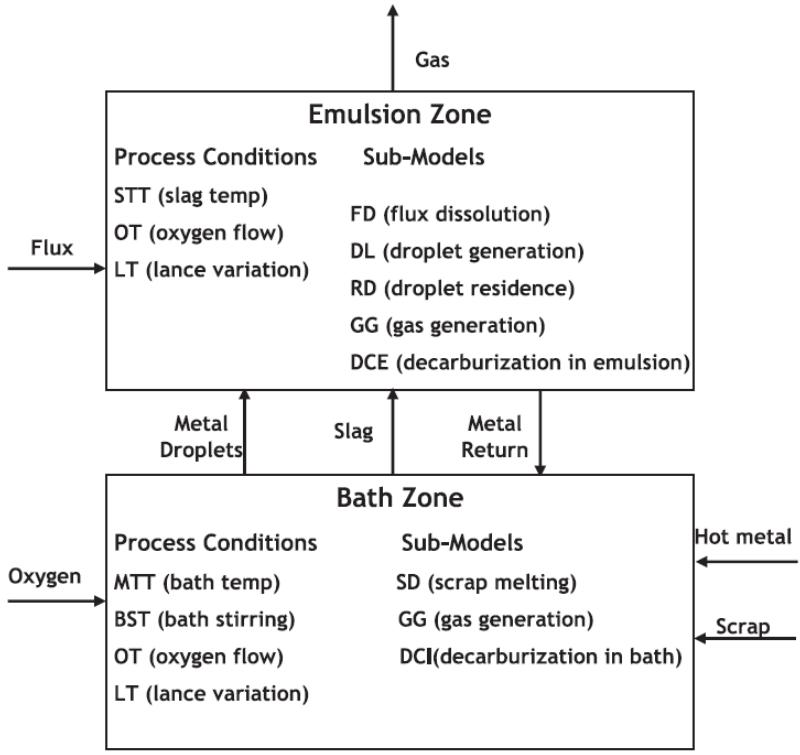

Figure 9.6: Schematic description of the model structure of Dogan et al [23].

To gain better understanding of the interactions in the BOF process, seventeen sub-models (e.g. scrap melting, flux dissolution, etc.) are used. These sub-models have been developed separately and are linked with each other, to model the complete process, as indicated for some on Figure 9.6.

Only decarburisation is considered as refining reaction in the model. A linear temperature profile is imposed upon the bath during the blow. The slag temperature is considered 100°C [15] higher than the metal bath temperature. There is no heat balance nor energy loss considered in the system. Application of linear temperature profiles is often encountered in BOF modelling and is a rather valid assumption with constant oxygen blowing rate. Kattenbelt [43] explains this with a self-regulating temperature assumption. However, possible energy losses to the environment and the sharp decrease in temperature due to the charging of scraps at the start or fluxes during the blow are not considered. On the other hand, it is unlikely that with only the consideration of the reactions with carbon, an applied heat balance would yield realistic results since in reality more reactions will take place.

The slag composition is taken as input by using industrial data as a function of blowing time. Due to the nature of the available data, the calculation only starts two minutes after the start of blowing process. Due to this empirical integration of the slag composition, the model can only be applied for defined operation conditions. This could be seen as a drawback when the interest would be to explore unknown operational conditions before industrial trial.

For iron ore dissolution, unlike for scrap, no kinetics are considered. Dissulution of refractory material is not included. Yet, this is, apart from being complicated, also a slow process as explained by Dogan et al. [23]. The generated gas, due to the decarburisation reaction, is a mixture with a fixed composition of 85% CO and 15% CO_2. The latter originating from the combustion of the CO produced during the process. Results of previous studies by the authors [44] were used to estimate the foam height of the slag as function of the total slag volume. It is assumed that all the generated droplets are also ejected into the emulsion zone. Furthermore, the only possible reaction for carbon in the metal droplets in the emulsion zone is the FeO reduction.

Thorough explanation of the model for the decarburisation in the emulsion zone is given in [24]. The bloating behaviour of droplets is taken into account in this model by its influence on the residence time and the size of the metal droplets. Residence time is calculated with the model of Brooks et al. [21] based upon a ballistic motion principle. A threshold decarburisation rate is introduced to compensate for the density change due to the bloating behaviour. Droplet generation is estimated with the method of blowing number as suggested by Subagyo et al. [16]. Yet, several studies [17]–[19] reported the underestimation of the amount of metal in the emulsion as calculated based upon the

equations proposed by Subagyo and co-workers. Their equation was established under conditions of constant lance height and without considering the effects of flow on the cavity formation. More recent work by Sabah et al. [20] identified the existence of two splashing modes, dependent upon the lance height and operational conditions on one hand and the blowing number on the other. One of their conclusions was the observation that a higher blowing number did not necessarily result into a higher droplet generation rate. Another aspect is that the gas properties by Subagyo and co-workers are calculated at normal temperature and pressure, while the impact of the jet happens at the metal bath and temperatures deviate to a large extent from the normal temperature.

Decarburisation rates in the emulsion zone, are theoretically described with the method of Brooks et al. [45]. Dogan et al. [24] themselves highlighted some critical notes to the used relations to estimate and calculate model parameters. Such as the use of empirical data to fit the parameters of the model by Brooks et al. [45] for the decarburisation rates. Only the overall reaction is considered and no halo formation is taken into account. Finally, it is also assumed that the droplets only contain carbon and no other impurities. The droplet's carbon content, upon ejection from the metal bath, equals this of the liquid bath. This assumption is supported by Dogan et al. due to both the little data available in literature describing the effect of impurities on decarburisation and the lack of information in the considered industrial data on the impurities present in the metal droplets. However, in reality other impurities (e.g. Si, Mn and P) will have an effect upon the kinetics of overall decarburisation. [24]

The decarburisation in the 'Bath Zone' of the model is thoroughly described in [25]. It is assumed that decarburisation takes place in the impact zone. In this reaction zone, two possible reactions for decarburisation are possible: direct reaction with oxygen gas or indirect reaction with CO_2. Both mechanisms have their own kinetics and thus, rate equations [46]–[49]. For situations with carbon content higher than the critical content, these reaction rates govern the kinetics. Once below a critical carbon content, the diffusion of carbon is considered to be the rate determining step, accompanied by a third rate equation [46]. The relevant relations for the rate parameters are calculated based upon a study performed by Lohe [50]. To estimate the dimensions of the cavity created by the gas jet, the relations as proposed by Koria and Lange [8] are used. In the expression of the rate parameter in the liquid iron, the effect of inert gas mixing is taken into account. Diffusivities of carbon in the liquid were calculated based upon temperature and viscosity of the metal with Stokes-Einstein and Eyring equations.

The model is validated to the industrial data from the study of Cicutti et al. [51]. This validation proofs its value for industrial applications and for overall effects on the decarburisation process. Industrial data collected by of Cicutti et al. [51] was for a 200 ton industrial converter with bottom stirring. The bottom stirring is considered within the calculation of the mass transfer coefficients in the metal bath for the 'Bath zone'.

The main objective of the model of Dogan et al. was to study the decarburisation reaction. As such it succeeded. In order to model the complete process also other refining operations should be considered. Thus, this model is only applicable for decarburisation behaviour and not to simulate nor investigate the complete, more complex, BOF process.

Results obtained by the model indicate the behaviour of droplets in the emulsion zone has a crucial impact on the decarburisation kinetics: 60% takes place in the emulsion zone during the main blow and 30% towards the end of blow. In total, it is suggested that 45% of the total carbon is removed in the emulsion zone. A thorough evaluation of some sub-models allowed to conclude that the residence time of the droplets decreases towards the end of the blow and changes of density in the emulsion zone need to be considered to yield decarburisation rates which are realistic compared to industrial plant data. A decrease of lance height results in an increase in decarburisation rate in the emulsion zone.

9.2.2 Multi-zone kinetic model (by Rout et al. [9])

The Dogan model discussed in the previous section was published in 2011. The model described by Rout et al. was published in 2018 and comes from the same research group as the one from Dogan, with mutual co-authors. The newer model considers more aspects of the BOF process than only the decarburisation. However, a lot of the general assumptions (such as droplet generation and jet impact zone) are either the same for both models or modified by Rout et al. based on more recent insights.

Rout et al. [9], [12], [31], [52]–[54] developed a multi-zone kinetic model which is coupled with a dynamic slag generation model to simulate the evolution of both the slag and the hot metal composition during the process. For all assumptions a clear explanation is given, when needed critical remarks are added as well. A schematic overview of their model is given in Figure 9.7. The model is, stripped to its sub-models, built from relative simple and understandable fundamentals. Yet, when put together, the interactions make it a quite complex model.

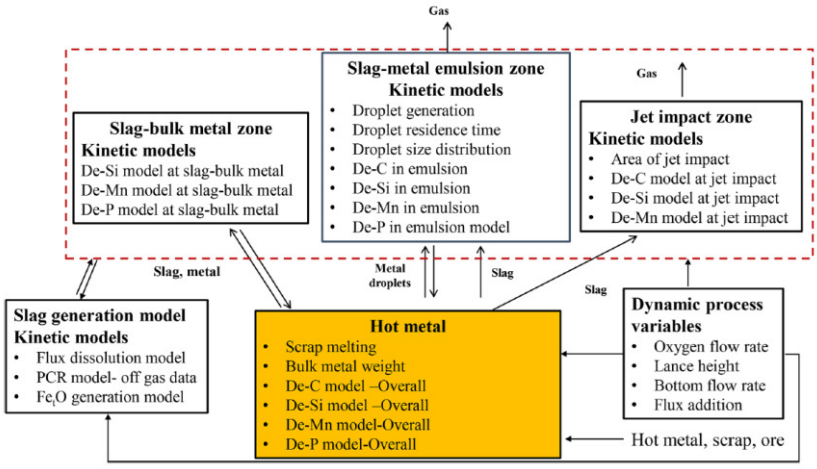

Figure 9.7: A three-zone kinetic model for prediction of metal and slag composition during blowing period of a top/combined blowing steelmaking converter process. Taken from [9].

Three different reaction zones are assumed: the 'jet impact zone', 'the slag – bulk metal zone' and the 'slag – metal – gas emulsion'. Process variables are mathematically incorporated into the model by means of the transient rate parameters. Both micro and macro kinetic approaches are used to be able to model the complete process. Especially, the behaviour of the metal droplets in the emulsion was incorporated in detail in this model. All parts of the model are thoroughly explained in [9]. To simulate the FeO content of the slag correctly an FeO_n generation model was incorporated. The oxygen balance inside the converter was used as starting point for this model. From the kinetic models, it can be calculated at each time step how much oxygen will be consumed for chemical reactions (e.g. oxidation of Si, Mn, P, C , CO and O dissolution). The oxygen which is not consumed in these reactions is considered to be used to oxidize iron, hence resulting in the FeO_n formation. The kinetic models for calculation of the oxygen consumption are constructed for each element separately.

The three separate reaction zones are the only regions in the converter where reactions can take place. Phenomena such as refractory dissolution or creation of slag droplets are not considered. A linear temperature profile (between 1350°C and 1650°C) is imposed upon the bath during blow. The slag temperature is set 100°C [23] higher than the metal bath temperature. As such, there is no heat balance nor loss of energy considered in the system. Rout et al. themselves make the critical note on the simplification they introduce upon doing so. They also indicate that the effect of adding scrap and fluxes on the

temperature profile should be a future addition to the dynamic model. A linear scrap dissolution model is assumed. This is unlikely to hold for all possible real steelmaking practices as also mentioned by Rout et al. themselves. Lime and dolomite are both assumed to be spherical with a fixed, uniform diameter. The dissolution model proposed by Dogan et al. [44] is applied.

All metal droplets generated are assumed to be spherical in shape and are considered to take part in the reactions in the emulsion zone. An inclination angle of 60° is assumed for all the droplets entering the slag. A discretization in computational time steps is imposed on the continuous process. All droplets ejected into the emulsion during a certain time step are assumed to be ejected simultaneously at the start of the computational time step. Finally, the gas volume fraction of the emulsion is set at a fixed value of 0.8 based upon results from Ito and Fruehan [55]. This gas volume fraction is important for the determination of density and viscosity of the emulsion.

The jet impact is assumed to be a paraboloid. Its dimensions are determined based upon the correlations suggested by Koria and Lange [8]. The interfacial area between slag-metal is calculated as the complete geometrical area of the bath with the cavity area, created by the jet impact, subtracted from it. The generation rate of droplets is calculated, based upon a modified blowing number which was developed by Rout et al.[12]. In the modified blowing number, effects of temperature and real jet operation conditions are integrated into the expression. The size of the droplets is not considered uniform, but assumed to follow a Rosin-Rammler-Sperling distribution. The parameters for the distribution function are chosen so that 95% of the droplet sizes lie in the interval of the measured metal droplets from the validation case. As indicated by Rout et al. themselves these are not universal values and adaption might be required for different operational conditions. Even though introduction of a distribution function makes the droplet sizes more realistic than to assume uniform size, it also introduces extra complexity into the model. Difficulty in slag sampling in general and especially during blow, makes it even more tricky to develop a uniform method to gain insight in the precise size distribution of different emulsions. For calculations, different size classes were defined. Residence time of the droplets is based upon the principle of ballistic motion as suggested by Brooks et al. [21]. To estimate the density change in the emulsion, the decarburisation rate is coupled with the equation of motion for the emulsified droplet in the emulsion phase. The bloating behaviour and its effect on area and volume of the droplet is, as proposed in [21], estimated with empirical correlations

for the density and a critical decarburisation rate which acts as a threshold value. The temperature of the droplets is calculated based upon formula's suggested by Chao [56]. To estimate the heat capacity of the slag, a simple weighted linear combination of the individual heat capacities of the oxides is used. The complex post-combustion process is treated with a simplified approach. Two different profiles, based upon industrial data, for post-combustion are defined. One constant profile and one profile where the post combustion decreases until a constant value at the start of the process and increases again to a higher post combustion value at the end of the blow. Both profiles only start at two minutes into the blowing process.

For all possible refining reactions, rate equations and parameters are needed for each relevant reaction zone. Recent work [18], [57] illustrated that simple first-order kinetics with constant rate parameters are not sufficient to describe complex reactions such as oxidation of phosphorus, manganese and carbon. Oxidation of iron is assumed to happen only in the 'jet impact zone'. Because of absence of slag at this 'jet impact zone' due to the impact force of the gas jet, no phosphorus removal is considered in this reaction zone. Oxidation of carbon, silicon and manganese happens in all reaction zones. An overview of the different assumed kinetics is given in Table 9-1. Details for the mathematical models for the oxidation of impurities are thoroughly described in [52] for C, [53] for Si and for [54] Mn. Effect of mixing is included in the mixing energy term in the expression for the mass transfer coefficients for the impurities.

Table 9-1: Summary of the different kinetics per reaction zone.

Zone	Impurtiy	Rate Determining step
Jet impact zone	Si,Mn	*Mass transport in the liquid phase*
	C	*Mixed Kinetics:* *C ≤ 0.3 wt%: Mass transport in the liquid phase* *C > 0.3 wt% : gas transport*
Slag - metal emulsion	Si,Mn,C, P	*Mixed Kinetics: slag and metal mass transport*
Slag - bulk metal	Si,Mn,C, P	*Mixed Kinetics: slag and metal mass transport*

For the refining in the emulsion, a two stage approach is considered: macro- and micro-kinetics. A micro-kinetic approach is used to describe the refining between an individual

droplet and the slag. A model for simultaneous refining kinetics of carbon, silicon, manganese and phosphorus in the emulsion zone, shown in Figure 9.8, was developed. It is assumed that the oxidation of silicon, phosphorus and manganese approaches equilibrium within the first seconds the drop enters the emulsion zone. Decarburisation is as a consequence slowed down by the formation of surface active oxides such as SiO_2 and P_2O_5 which block the reaction sites for carbon and FeO. A macro-kinetic approach is used to describe the overall refining rate by the complete summation over all the droplets present in the emulsion. Such a summation is performed for each time step with consideration of droplet size classes in which one uniform size is defined.

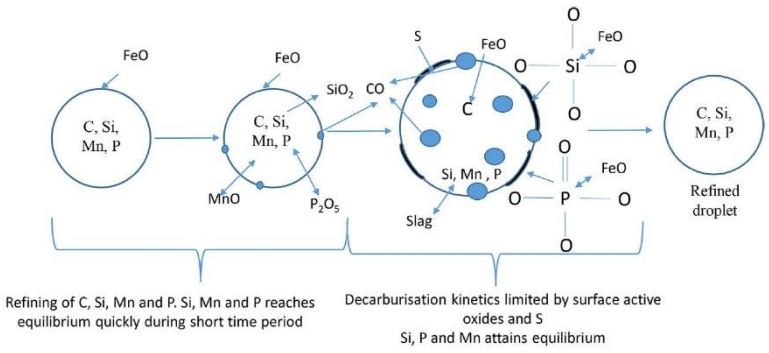

Figure 9.8: Refining mechanism of droplets in the slag-metal emulsion. Taken from [9].

For the reaction zone between the slag and the bulk metal, an instantaneous equilibrium between reactants and products for all impurities per time step is assumed. The bulk metal temperature is used for this equilibrium. Knowledge about the equilibrium concentrations for impurities at the slag-metal interface is required. For the activity of FeO, a regular solution model is used, while for the impurities, different empirical distribution coefficients are considered. For C [58] a polynomial equation as a function of temperature and C content describes equilibrium. For Si [59], Mn [60] and P [61] an equilibrium partition ratio is used.

Finally, the last important aspect is the dynamic slag generation model. A dynamic composition of the slag is required, since the slag composition is used as input for different model parameters. An oxygen balance inside the converter is assumed to develop an FeO_n generation model. [62] Every mole of oxygen entering the converter is consumed in chemical reactions. However, in reality it is likely that the oxygen has a certain efficiency lower than 100%. The amount of oxygen left, reacts with Fe and thus

forms FeO_n. The ratio FeO/Fe_2O_3 is fixed at 0.3 at the slag-metal interface. Several studies indicate dependence of the ratio of Fe^{2+}/Fe^{3+} upon composition [63], [64] and temperature. Yet, a value of 0.3 indicates an oxidised slag. The total slag weight is estimated from the sum of all oxides and the dissolution of added flux at each time step. Saturations limits for CaO and MgO were thermodynamically calculated with Factsage 7.1 [65] and are part of the model input. The input amount of oxygen is the sum of the oxygen blown via the top lance and the oxygen entering as iron ore (Fe_2O_3) in the BOF furnace. Dissolved oxygen in the bulk metal is calculated from the equilibrium reaction with FeO.

A lot of the used parameters and assumptions are fitted to the specific validation case. Even though Rout et al. make critical remarks and indicate this, it still holds that for use in other processes and operational conditions, a lot of parameters need to be verified and possibly refitted. The introduction of geometrical influence from the furnace also makes the model somewhat converter specific. To simulate the BOF process with this model for a plant with several, fundamentally different converters form a geometrical viewpoint, separate models might be necessary. However, it might be questioned whether it is avoidable to introduce geometric specific parameters if the aim is to model the process so fundamentally with the obtained complexity level of Rout's model. Even if the model is converter specific, it might still result in general insights and understanding of the BOF process. Yet, one should always be careful and be aware of the dependence of the parameters on geometric aspects or specific operational modes and working points (e.g. general slag composition) before drawing general conclusions from the model or trying to extrapolate it to fundamentally different working conditions.

The model is validated to the plant data from the study of Cicutti et al. [51]. This validation proves its value for industrial applications and for overall effects upon the refining process. The general conclusion of the model is the importance of the emulsion zone for the refining operation. A significant share of refining is due to the recirculation of the metal droplets ejected from the metal bath into the slag layer. This emulsion zone is a dominant factor in the BOF kinetics. The thermodynamic driving force in the droplets is considered responsible for the high refining rates of silicon, manganese and phosphorus. For these impurities, fast oxidation takes place in the droplets. For carbon, a slightly different story holds. Especially the initial droplet size has an important influence in the decarburisation rate.

9.2.3 Thermodynamic and kinetic model of the converter steelmaking process (Lytvynyuk et al. [66], [67])

Lytvynyuk et al. developed [66], [68] and validated [67] a model for the BOF process considering both thermodynamic and kinetic aspects.

For this model, the converter is approached as a heterogeneous thermodynamic system with one reaction zone. Yet, literature mentions the importance of the droplet generation and the interactions in the metal – slag emulsion for refining. As far as could be verified, there is no mentioning of droplet generation nor of increased interface between slag and metal due to the droplet formation. The final slag metal interface is estimated [68] based upon plant data, because the theoretically calculated interfacial area, based upon mixing energy relations, had a too high value. If the same reasoning was applied in [67], the interfacial area is a fitted value, which would mean the effects of the emulsion zone are incorporated in it.

The blown oxygen is consumed only for the direct oxidation of iron. All other components are assumed to be oxidised by the formed iron oxide, applying the theory of Grum-Grzhimylo [69]. For all components, except carbon, a constant exchange between the slag and metal phase exists due to the successive oxidation and reduction reactions in the process. Carbon is assumed to only form carbon monoxide. This formed gas phase is immediately removed upon formation. Post-combustion is defined as the result of the reaction between the CO-rich off gas and the oxygen sucked in from the atmosphere. For all the oxidation and reduction reactions, a coupled reaction model [70] approach is applied. Relevant reactions are described as combination of the defined system reactions, according to Hess' law. Kinetics of the system are determined by the mass-transfer in the metal and slag phase. The reactions at the interface are assumed to be rapid and to reach equilibrium at any moment.

For the considered reactions, the equilibrium constants are calculated based on expressions formulated in the 'Steelmaking Data Sourcebook' [71]. Subsequently, they are rescaled in terms of the atomic fraction. [68] Activity coefficients for the elements in the metal phase are calculated with a Wagner-Lupis-Elliot method [72]. For the slag components the electron theory [73] is used. The latter one was chosen to be able to integrate the oxidation of vanadium in the system. To calculate the mass transfer coefficients in metal and slag the empirical model developed by Kitamura [74], [75] is used. The argon flow rate (influencing the stirring conditions), CO gas generation rate and solid fraction of the slag were incorporated in the slag's mass transfer coefficient.

For the metal's mass transfer coefficient geometrical parameters and mixing power were integrated. Mixing power will be a function of different technological parameters, such as blowing and bottom stirring parameters. The kinetic and thermodynamic aspects are combined to construct a final nonlinear algebraic equation which needs to be solved to obtain the surface activity of oxygen, from which, in turn, the surface concentrations of hot metal and slag components are calculated.

A heat balance is incorporated to derive the temperature, including heat losses through the vessel lining and mouth. Melting of scrap, ferrosilicon and pellets is integrated in the model. Both diffusion melting and overheating melting mechanisms are considered. The temperature is assumed to be identical for slag and metal phase. However, this is not in correspondence with literature [15] where a considerably higher temperature is reported for the slag. Also the temperatures in the steel bath are not necessarily homogeneous. The oxidation reaction of iron in the jet impact zone of the converter, is reported [4] to result in local temperatures up to 500-1000°C higher than the steel bath at certain moments of the blow.

The dissolution of CaO – and MgO – flux materials is incorporated based on rate equations in which the driving force is the difference between the actual oxide concentration and the saturation concentration. For MgO, the saturation concentrations for different conditions are taken from literature models, while for CaO they are determined with phase diagram calculations, combined with analytic geometry (inverse lever rule).

For validation, the model was applied to data from literature for a 170 and 330 ton converter. For the 170 ton converter also different types of converter heats are tested. Both the 'end of blow' composition and the 'during blow' behaviour of different components are in line with the results found in literature. Especially, the reproduction of the phosphorus and manganese pick up during the process is an interesting feature on which the authors of the model comment. It is possible to examine overall effects with the model, yet it is not possible to investigate micro-kinetics or small scale effects due to the use of macro kinetic parameters. Only mass transfer in the bulk phase is identified as a rate determining step.

9.2.4 Dynamic model for LD converter with gibbs free energy minimization (Sarkar et al. [17])

Sarkar et al. [17] developed a dynamic model for the LD converter to predict slag and steel composition. Chemical reactions are modelled via a Gibbs free energy minimization. The model divides the process into three separate reaction zones. It is assumed each zone can be described as a separate continuous stirred tank reactor. The first zone is the bottom part of the bath, the second, the upper part and the third zone is the slag-metal emulsion. The different reactors (or reaction zones) and the considered material flows are shown in Figure 9.9. The oxygen oxidizes a layer of metal in the 'upper bath' zone and formed oxides are transferred to the 'emulsion' zone. The metal droplets generated due to the impact of the gas jet, are also transferred from the 'upper bath' zone towards the 'emulsion' zone. In the 'emulsion' zone, these droplets undergo chemical reactions and will be refined when they fall back into the bath. Thus, the refining in the 'upper bath' zone is due to the diluting effect of the refined droplets falling back from the 'emulsion' zone. No reactions are considered to take place in the 'lower bath' zone. The refining in this reactor is solely through the exchange of material from the 'upper bath' zone. Refining due to the contact of the bulk slag with the bulk metal phase is not considered in the model. Phosphorus is also not included in this model.

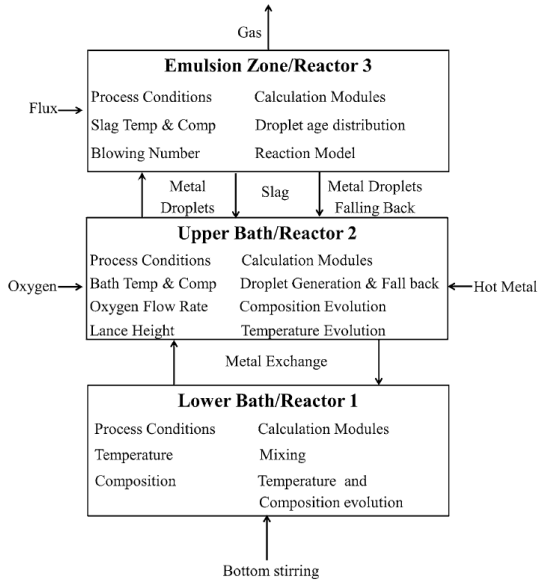

Figure 9.9: Schematic overview from the model of Sarkar et al. [17]

The temperature of the metal bath is assumed to increase linearly during the blowing practice, starting from 1450°C and reaching 1650°C. Figure 9.9, allows to conclude that the characteristics of the emulsion zone reactor are determined by the slag temperature and composition. A description of the evolution of the slag composition is given. It is nevertheless, not mentioned if a different temperature is considered for the slag, compared to the metal. Literature mentions the temperature of the slag usually is, on average, 100°C higher than the metal phase in the converter. This temperature difference will influence the values for the Gibbs free energies of the reactions.

The model starts only one minute after the start of the process, due to the necessity to enter the initial slag composition as input for the model. However, during the first stages of the blow, no slag layer is formed yet and the dynamics of the formation might be considerably different than those assumed during the rest of the process. The oxygen distribution in the impact zone amongst the impurities is based upon the availability of these elements calculated via their weight percentages. All droplets in the emulsion zone are assumed to have the same size and their residence time only depends on the droplets' terminal velocity. The droplet generation rate is calculated based on the blowing number and the empirical relation of Subagyo et al.[16]. It was mentioned earlier that more recent literature argues an underestimation of the amount of metal in the emulsion zone when these formulas are used. An extra model parameter is introduced to yield a higher, more realistic, amount of droplets, resulting in a more accurate amount of metal present in the emulsion zone, whilst preserving the responses of the generation rate as described by Subagyo. The effect of lance height upon the gas velocities is integrated with the correlations formulated by He et al. [13]. Residence time is influenced by the decarburisation of the droplets. It is assumed that the residence time of a droplet in the emulsion is increased with the time needed for decarburisation. However, only until a certain carbon concentration. The refining rate is controlled by the mass transfer of FeO in the slag phase, as long as the carbon content of the droplets exceeds the critical concentration. For droplets with lower carbon content, the residence time is drastically decreased and the refining is, for computational ease, limited to the removal of only carbon from the droplets. The slag is assumed to be well-stirred. No details on scrap melting nor dissolution of fluxes are mentioned.

The main refining operation takes place in the metal – slag emulsion. The model assumes all droplets generated within a certain computational time step will enter an imaginary conceptual box of slag which will have different compositions for different time steps.

Once the droplets fall back to the steel bath, this conceptual box is destroyed. In order to update the composition of the different reactions, a simple mass balance approach is used. Refining in the metal – slag emulsion happens through the FeO – reaction. For each of the reactions, the Gibbs Free energy is defined. A minimization of the summation of all these Gibbs Free energies is used to determine the equilibrium concentrations. Minimization is calculated by the distribution of FeO between the different reactions. A mass balance constraint for each element is also imposed. The needed activity coefficients of the components in the considered reactions are calculated as a function of only slag basicity, as suggested by Turkdogan et al. [76]. The activity coefficient of SiO_2 is set to be constant [77]. Oxygen dissolved in the metal phase is assumed to have an activity equal to its weight percentage. It is unclear whether this also holds for other impurities dissolved in the metal droplets. Even if this is assumed, it might be argued that, in order to be more accurate, also an activity coefficient for these dissolved impurities needs to be considered.

A number of crucial model parameters for mass transport and mixing are assigned to obtain results matching real observation. Sarkar et al. themselves included a section to justify their choices and evaluate the sensitivity of the model response to them. They also made the critical remark that this choice is not unique and that rather the combination of values for these parameters will give satisfactory results.

For validation the data from Cicutti et al. [51] is used. Further development, as also indicated by Sarkar et al., of the model is needed to increase its accuracy and match with real processes. One of the examples is the much lower rate of Si and Mn removal predicted by the model than those observed in actual process.

9.2.5 Mathematical BOF model based upon a Gibbs Energy Minimization Approach (Kruskopf et al. [36])

Kruskopf et al. [36] developed a mathematical model to describe the BOF process. Chemical reactions are modelled with a Gibbs energy minimization approach. In this model, it is assumed the reactions take place in a specified reaction zone. The reaction rates of the species are governed by the mass transfer between reaction volume, bulk slag and metal. Earlier work by these authors already resulted in a model to describe bottom stirring [78] and scrap melting [79]. In [36] emphasis is put on the reactions, equilibria, heat and mass transport in the impact zone. In order to describe the complete BOF process, equilibrium conditions in both the reaction zone and the bulk slag are calculated.

The converter is assumed to have three different bulk phases: gas, metal and slag. The bottom stirring mixes the liquid metal, while the oxygen from the top lance ensures mixing of the slag phase. There is a mass flow from the bulk of these phases towards their interfacial area. Only one reaction zone is considered for all reactions in the process. The pressure in this reaction zone is constant and 1 atm. From literature, it is known that the slag-metal emulsion also plays an important, if not, crucial role, in the refining of the metal bath. More complex assumptions will need to be introduced. The authors mention their intention to do so in the conclusion, e.g. by proposing a reaction volume approach. The evolution of reactions is limited by the mass transfer from the bulk of a phase towards its interface. Mass transfer from the liquid metal towards the interface is only affected by the bottom stirring and not by the top gas jet. For the slag phase, the opposite reasoning holds. No heat transfer between the melt and furnace lining, nor from the injected bottom gas, is considered. For the scrap melting, constant heat and mass coefficients are assumed. The overall system is a simplified five element system consisting of Fe, C, O, Si and Ca.

The reaction zone is defined as the volume close to the interface. At every moment, all the mass inside the reaction zone is assumed to be in thermodynamic equilibrium. Mass and volume fluxes are defined from and towards the interface. The amount of material and energy transported into the reaction zone is determined by the mass transfer coefficients. Calculation strategies for these fluxes contain empirically based functions. For simplicity, the results of Chatterjee et al. [80] for small scale experimental set – up, were used in combination with the upscaling calculations of Sarkar et al. [17] for the mass flow in the validation case. At the start of the process, the mass transfer coefficient does not equal its steady state value, but is gradually increased from a low value to this steady state value during the first 20 seconds of the simulation. The physical reason for this is the time needed for the bulk metal phase to increase momentum due to buoyancy forces. This gradual increase results in the oxidation of iron in the first stages of the blow and the accompanied heat generation. Due to the conservation of energy, the initial temperature of the reaction zone can be estimated. Both the conservation equation of mass and enthalpy for the slag and the metal bulk phase are discretized. In these equations, the heat and mass terms related with scrap melting and lime dissolution are also considered. Details on the involved mathematics are given in [36].

The basis of the BOF model is an in-house developed model to minimize the Gibbs free energy and calculate the equilibrium. Each of the present phases has its own solution

model: ideal for the gas phase, the unified interaction parameter (UIP) formalism for the activity of the steel phase and the modified quasi-chemical model (MQM) for the slag activities. Furthermore, the gas phase only contains CO, CO_2 and O_2, the metal phase Fe, C and Si and the slag SiO_2, CaO and FeO. The equilibrium is calculated using the partitioning of Gibbs energy (PGE) [81] method. In short, this method starts with the definition of the chemical potentials of all species and phases starting from the chemical potentials of the system components. Next, the Gibbs free energy is divided among the system component in such a way that the residuals of the mass balance equations progressively reduce. In order to solve the system, it is, however, required that good initial values are chosen to start the iterative solving methods. A possible method for this is the Leveling and Post-Leveling method [82]. The used thermodynamic data was taken from work by Taylor and Dinsdale [83] and the HSC software. Even though an in-house model gives the possibility to control all model parameters oneself, it is more complex than using commercial software where also Gibbs energy minimization methods are used i.e. ChemApp [84]. Another consideration would be the lack of oxygen dissolved in the metal at the moment. In the current model, the steel phase contains Fe, C and Si. In reality, however, also oxygen will dissolve and play its role in the refining reactions and the thermodynamic equilibria.

First, the thermodynamic model to describe the solution phase of the slag was validated against iso-activity and liquidus lines from the Slag Atlas [85]. The same trends were observed except for the lime saturation line. The calculated lime saturation line is shifted considerably compared to the measured and reported one [85]. Secondly, the BOF model was validated against the reported data from the industrial trial by Cicutti et al. [51]

The results of the model show the increase of FeO content of the slag during the initial stage (first 20-30 s) of the blow. This is explained by the poor mixing in the metal phase at the start of the process. Mathematically this was incorporated into the model by adapting the mass transfer coefficient for the bulk metal.

For the validation the authors also used the models of Sakar et al. [17] and Dogan et al. [25] for comparison. Currently, only silicon an carbon are considered as impurities in the metal bath. To compensate this, the carbon content for the model calculation is taken higher than the one in the industrial trial by Cicutti et al.[51]. Higher accuracy for the compositional trends for this model was found compared to the other two models. Rescaling was taking into consideration for this. For the carbon content the simulation results match, apart from at the start of the blow, with the results from Cicutti et al. [51]

and better than the ones of Sarkar [17] and Dogan [23]. Although it should be mentioned Dogan et al. only focused on decarburisation in their model. In the current discussed model, also the silicon content is much higher during the main part of the blow. If both calculations start from the same amount of oxygen added, this would mean more iron is oxidised. Since, apart from silicon and carbon, this is the only component that consumes oxygen. There is no mentioning of post-combustion. Nevertheless, the current simulation results show the trends, being scaled to a three component slag, rather well. Also the increase in FeO content of the slag, results from a physical assumption made upon the mixing at the start of the blow.

9.2.6 Effective Equilibrium Reaction Zone model (Van Ende et al. [35])

Van Ende et al. [35], [40], [86], [87] developed a more general model for industrial process, in which kinetics and thermodynamics are integrated. Their approach was successfully applied upon the Ruhrstahl Heraeus degassing process [40] and the ladle furnace [86] for which correct chemistry, temperature and inclusions are predicted with minimal tuneable parameters. Application of this approach on the BOF process [35], [87], has been reported in a more restricted way.

The Effective Equilibrium Reaction Zone (EERZ) model divides the process into several reaction volumes linked with the different reaction interfaces. In the predetermined reaction volumes, thermodynamic equilibrium is assumed. The sizes of the reaction volumes are, via physical descriptions or empirical relations, function of process conditions. Computational thermodynamics and reaction kinetics of high temperature processes are coupled. Equilibrium is calculated by means of a CALPHAD type computational thermodynamic database, in this case the Factsage [65] software was used. The integration of the commercially available thermodynamic data and software makes the model straightforward to apply.

The assumption is made that the kinetics of the solutions are dictated by mass transfer in the solution phases. Due to the high temperatures, reactions at the interface are assumed to be fast. With a first order mass transfer equation, the flux of each species is linked with one mass transfer coefficient and the concentration difference between bulk and interface for this species. When the assumption is made that for each species participating in the reactions of the solution, the mass transfer coefficient is identical, the amount of material participating in the reaction can be simplified to equation 9.21.

$$m_{reaction} = k\rho A\,\Delta t \tag{9.21}$$

Where $m_{reaction}$ is the amount of material participating in the reaction, k the overall mass transfer coefficient, ρ the density of the considered phase, A the area of interaction interface and the last term the considered time step. As consequence of this simple expression, complex systems can be divided into a finite number of reaction zones and for each zone the equilibrium is calculated. Subsequently, the formed equilibrium products at the interface diffuse to the bulk of the phase. This is translated into the model with a homogenisation calculation within the phase after the equilibrium calculation between the phases. In order to describe the kinetics of the process, the reaction volumes can be varied. These volumes are tuned based upon mathematical functions for phenomena, properties of the phases, experimental studies, industrial data, etc.

For the equilibrium calculations different Factsage databases are used. To describe the slag and oxide phases present 'FToxid' is used. This database uses a Modified Quasichemical Model [88]–[91] to describe the molten slag solution. Solid solutions are modelled with the Compound Energy Formalism [92]. To model the liquid metal phase, the FTmisc database is used. In this database the liquid metal phase is described with the unified interaction parameter formalism [93] and deoxidation behaviour is described based upon the associate model [94]. Also the FSstel database is used.

For the BOF process, ten different reaction zones are identified, as shown in Figure 9.10. The temperature profile for each phase is calculated based on the heat balances, assuming adiabatic conditions. The possibility exists to incorporate heat losses or gains. Droplet generation is incorporated with the relations proposed by Subayago et al. [16]. For scrap melting, a numerical simulation equation formulated by Gaye et al. [95] is applied. Modified semi-empirical equations are used to calculate the dissolution rates of different fluxes. The thermodynamic driving force, temperature and slag viscosity are considered in these equations. Slag viscosity is calculated based upon the quasi-chemical viscosity [96]–[98] model which uses structural slag information calculated with the FToxid slag database. Other empirical parameters for interfacial reactions are determined based on sampling of industrial data.

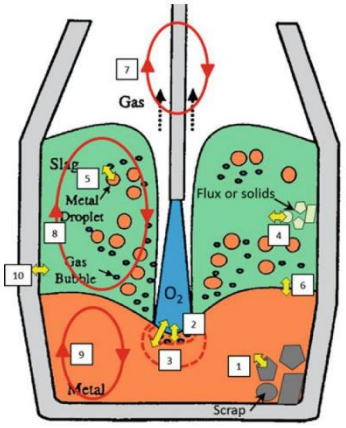

1. Scrap melting in metal bath and heat gain/loss
2. Burning of hot metal surface (O_2/metal reaction for FeO formation)
3. Hot spot (O_2/metal reaction for direct de-C)
4. Flux dissolution in slag
5. Metal droplet/slag reaction
6. Bulk metal/slag reaction
7. Homogenization of the exhaust gas and post-combustion
8. Slag homogenization
9. Bulk metal homogenization
10. Heat loss and gain from vessel

Figure 9.10: schematic overview EERZ concept for BOF from Van Ende et al. [87].

For carbon and manganese, it is already mentioned in literature [57] that first order kinetics description using dynamic equilibrium conditions gives satisfactory results. Yet, from Rout et al. [31] it is known that overall dephosphorization cannot be explained with the simple first order rate equations. Also other works [11], [99] mention complicated kinetics for dephosphorization due to the more complex nature of the refining reaction. However, often the droplets in the slag – metal emulsion are mentioned as key parameter in understanding the dephosphorization. This is one of the reaction volumes identified in the model. For their micro-kinetic approach Rout et al. [9] also assumed first order rate equations at the interface of a single droplet. Depending upon how the emulsified metal droplets were integrated in the current model this might be or not be an issue. However, details on this integration are, up till now, not yet published in available literature.

Validation of the model was performed both upon the industrial data of Cicutti et al. [51] and also with industrial plant data from Hyundai Steel, Posco and VoestAphine, which all have very different operational conditions and process parameters. Finally, it is concluded the model could be used to investigate the impact of various operation conditions on the production path of the BOF process. The example of the effect of lime addition profile on dephosphorization is given.

9.2.7 Additional Models

For completeness, some recent and interesting examples of BOF process simulations are briefly summarized in this section. For these examples either no thorough description in

literature is found by the author or they are only sub-models aiming to describe only a part of the process rather than the complete process.

A BOF model constructed in the context of the BOFdePhos project by Schlautmann et al. [100] and Khadhraoui et al. [99] was developed using the interlinked local equilibria concept. The BOF reactor is described with three reaction zones and one non-reactive slag part where the flux dissolution is incorporated. To calculate the model parameters, such as droplets in the emulsion zone and mass transfer coefficients, a combination of different techniques (CFD – calculations, high and low temperature experiments, calculations linked with the top lance and reactions kinetics) was used. Emphasis is mainly put on the dephosphorization reaction in the BOF in these works [99], [100]. Also Mombelli et al. [10] focused on phosphorus removal in the LD converter. Yet, no full model is built for the complete process and only zones and interactions relevant for phosphorus removal were considered. Pahlevani et al. [101] simulated the steel refining with a model based upon work of Kitamura et al. [74] using a kinetic viewpoint. A coupled reaction model was applied to describe the possible refining reactions and an arbitrary distribution of oxygen for different purposes i.e. decarburisation, iron oxidation and post combustion, was applied.

9.3 Comparisson of the discussed models

Six different models to simulate the BOF process were discussed. This discussion is summarized in Table 9-2. A clear distinction can be made between the ones using a reaction interface model (section 9.2.1, 9.2.2, 9.2.3 and 9.2.4) and those using a reaction volume model (section 9.2.5 and 9.2.6).

The work of Dogan and co-workers [23]–[25], published in 2011, builds a comprehensive model for decarburisation. It is clear that in order to have a thorough evaluation of the BOF process, considering only the decarburisation reaction is not sufficient. The further developed comprehensive model by Rout and co-workers [9] provides a much more detailed and complete model of the BOF process. The many different subsystems and submodels, each with their own set of parameters, make the overall model detailed yet, complex. The level of detail allows to investigate influences upon the process for a range of dimensional scales: from overall macroscopic effects, up to effects on the droplet level in the slag – metal emulsion.

The model by Sarkar and co-workers [17] has only three different reaction zones and is therefore less detailed. Thermodynamics are more fundamentally integrated into this model compared to the model by Rout and co-workers. Sarkar's model uses a Gibbs Energy minimization approach, while Rout's model applies partition ratio's for the different relevant elements formulated in literature.

For these three models no heat balance was considered. The temperature was thus imposed on the system. For all the cases a linear temperature profile was considered. For constant oxygen blow rates, Kattenbelt [43] gave the reasoning for the use of a linear temperature. Rout and Dogan also assumed a higher temperature for the slag. Nevertheless, inhomogeneous temperature profiles might exist in the real BOF process, i.e. the hot spot zone, and can influence local thermodynamics. The cooling effect due to the scrap charged at the start of the process or the fluxes added during the process, was also not considered.

Finally, Lytvynyuk [66], [67] and co-workers also applied a thermodynamic approach in a reaction interface model. Thermodynamics were introduced based upon equilibrium constants and mathematical models were used to calculate the activity coefficients for different components in the slag and metal phase. However, only one reaction zone was considered to describe the process. Additionally, also the size of the interfacial area was a fitted parameter of the model rather than a quantity derived from fundamental considerations. This is different compared to the model of Rout and co-workers who calculate the different interfacial areas based on a fundamental approach.

A completely different approach is used in the reaction volume models. Van Ende and co-workers [35] defined up to ten different reaction zones in the BOF process. For each of them, the size was influenced by operation parameters and process conditions. Kruskopf and co-workers [36] only assumed one reaction zone in the BOF process, but mentioned their intention to use multiple reaction zones for further model development.

The reaction volume models are appealing due to their compatibility with Gibbs free Energy minimization methods. Where Kruskopf's model uses a semi in-house developed method to minimize the Gibbs free energy, Van Ende's model uses commercial software for this purpose. A personal developed database allows for easy personal adaptions, where for commercial software this is less straight-forward. Commercial software is often more a black box, yet the user platform is much larger and application is straightforward. Both models use a heat balance to calculate the temperature.

The models developed by Rout, Lytvynyuk and Van Ende contain all components relevant in BOF steelmaking. This is in contrast to the models described by Dogan where only carbon was considered, by Kruskophf where apart from carbon also silicon and oxygen were part of the metal composition and by Sarkar where carbon, silicon and manganese were considered in the metal phase.

Considering the desired input parameters, the models developed by Dogan and Sarkar require an initial slag composition as input. As such these models avoid the complicated and not yet fully understood formation of the initial slag during the first moments of the blow. For the model of Lytvynyuk the necessity to enter the initial slag composition is not explicitly mentioned. It is mentioned [67] as input for their considered validation cases. However, this might be related to the type of process.

Another striking observation is that all the discussed models, apart from the one of Lytvynuyk and co-workers, use the same industrial experiment described by Cicutti et al. [51] to validate their model. Additionally, Van Ende and co-workers used industrial plant data from different steelplants to validate the model. Kurskopf and co-workers also compared results obtained by their model to those obtained by other models described in literature.

All six models have a certain number of parameters which are either calculated via empirical relations or fitted to experiments or industrial trials. The complexity of the BOF process and the lack of complete and thorough understanding of all its aspects make this inevitable.

As often in modelling, a trade-off exists between the possibilities of the model and the complexity. Depending upon the final purpose of the model and the resources at ones disposal, one model might be more appropriate than the other. Finally, it is up to the reader to decide which approach is most suitable for his specific case. The model by Van Ende et al. gives a straightforward approach to integrate existing thermodynamic software and kinetics, which can be found in literature, to apply on personal research topics. The model by Rout et al. is more complex and has several sub models which on their own have their specifications. This results in a detailed model with a lot of opportunities. Yet, to apply the approach upon personal research topics might be much more challenging.

Table 9-2: Summary of different models.

	Dogan	**Rout**	**Lytvynyuk**
Type	Reaction interface model	Reaction interface model	Reaction interface model
Number of reaction zones	2 Note: Much more subsystems	3 Note: Much more subsystems	1
Integration of thermodynamics	/	Partition ratio from literature	Equilibrium constants + coupled reaction model
Integration of kinetics	Macro and Micro kinetics	Macro and Micro kinetics	Macro kinetics
Temperature	Imposed linear profile $T_{slag} > T_{steel}$	Imposed linear profile $T_{slag} > T_{steel}$	Heat balance
Impurities	C	C, Mn, P, Si	C, Mn, P, Si, Ti, V
FeO concentration peak	Input Measurement t = 2 min	Calculated	Calculated
Publication year	2011	2018	2013
Ref.	*[23]–[25]*	*[9], [52]–[54]*	*[66], [67]*

	Sarkar	**Kruskopf**	**Van Ende**
Type	Reaction interface model	Reaction volume model	Reaction volume model
Number of reaction zones	3	1	10
Integration of thermodynamics	Gibbs free energy minimization	Gibbs free energy minimization	Gibbs free energy minimization
Integration of kinetics	Macro and Micro kinetics	Size reaction volume	Sizes reaction volume
Temperature	Imposed linear profile $T_{slag} = T_{steel}$	Heat balance	Heat balance
Impurities	C, Mn, Si	C, Si	C, Mn, P, Si
FeO concentration peak	Input Measurement t = 1 min	Calculated	Calculated
Publication year	2015	2017	2018
Ref.	*[17]*	*[36]*	*[35]*

9.4 Future opportunities

Experimental measurements during the blow of the converter process are extremely complex. Both from practical and qualitative viewpoint and thus are not straightforward. In more recent literature [18], [51], [100], [102] some attempts are listed. However, the limited data available from such measurements during the converter blow result in a scarce amount of validation data. Attempts to verify the robustness of future BOF models will benefit from more experimental measurements. Furthermore, also verification of the end point composition as calculated by the model with data from different industrial plants might yield opportunities to test the robustness the model. Cooperation with industry could be interesting in this context. However, this could also lead to conflicts with confidentially leading to in results or models which cannot be published in open literature.

Ideally, a fully kinetic approach is connected with a fully thermodynamic approach, combing best of both worlds. Due to the high temperatures in the BOF steelmaking, the assumption that at the interface (or reaction volume) equilibrium is reached and the kinetics are limited by mass transport, is considered valid. This makes thermodynamic approaches which consider all the possible reactions appealing. Especially, the opportunity to use heat balances and calculate temperatures in specific reaction zones rather than imposing temperatures seems interesting. However, reliability of such calculations is unavoidably also linked with the reliability of fundamental thermodynamic and kinetic data. Recent literature [99] mentions the limits of old-established empirical distribution coefficients for phosphorus. Some interesting components such as vanadium and titanium are only limited thermodynamically assessed for steelmaking slags. Additionally, also for the physical slag properties e.g. density, viscosity and surface tension more fundamental knowledge needs to be gained. Some consensus is already found on modelling density [103] and liquid viscosity [96], [97], [104]–[106]. However, modelling the viscosity of real slag systems containing solid particles is still topic of ongoing discussion [107]–[109]. Some attempts to model surface tension are listed in literature [110]–[113]. Yet, surface tension, and its influence, still remains a big unknown in BOF steelmaking.

Coupling thermodynamics and kinetics with CFD modelling to integrate the complex flow pattern could also yield interesting results. Yet, more fundamental understanding needs to be gained in the BOF refining mechanisms and slag properties to ensure reliable

calculations. Also, the difficulty of model validation and calculation times arises for real sized reactor modelling.

To conclude, it is clear still a lot of future challenges exist both on the large scale application of BOF models as well as on the fundamental slag research level.

9.5 References

[1] K. S. Coley, 'Progress in the kinetics of slag-metal-gas reactions, past, present and future', *J. Min. Metall. B Metall.*, vol. 49, no. 2, pp. 191–199, 2013, doi: 10.2298/JMMB121220017C.

[2] Q. Li, M. Li, S. Kuang, and Z. Zou, 'Numerical Simulation of the Interaction Between Supersonic Oxygen Jets and Molten Slag–Metal Bath in Steelmaking BOF Process', *Metall. Mater. Trans. B*, vol. 46, no. 3, pp. 1494–1509, Jun. 2015, doi: 10.1007/s11663-015-0292-3.

[3] N. A. Molloy, 'Impinging jet flow in a 2-phase system-basic flow pattern', *J. Iron Steel Inst.*, vol. 208, p. 943, 1970.

[4] S. Seetharaman, A. McLean, R. Guthrie, and S. Sridhar, *Treatise on Process Metallurgy*, vol. 2. Elsevier, 2013.

[5] H. C. Araújo, E. F. Rodrigues, and E. M. Leal, 'Numerical analysis of the liquid ejection due to the gaseous jet impact through computational fluid dynamics', *REM - Int. Eng. J.*, vol. 71, no. 1, pp. 53–57, Mar. 2018, doi: 10.1590/0370-44672015710079.

[6] N. Asahara, K. Naito, I. Kitagawa, M. Matsuo, M. Kumakura, and M. Iwasaki, 'Fundamental Study on Interaction between Top Blown Jet and Liquid Bath', *Steel Res. Int.*, vol. 82, no. 5, pp. 587–594, 2011, doi: 10.1002/srin.201100041.

[7] R. Sambasivam, S. N. Lenka, F. Durst, M. Bock, S. Chandra, and S. K. Ajmani, 'A New Lance Design for BOF Steelmaking', *Metall. Mater. Trans. B*, vol. 38, no. 1, pp. 45–53, Feb. 2007, doi: 10.1007/s11663-006-9004-3.

[8] S. C. Koria and K. W. Lange, 'Penetrability of impinging gas jets in molten steel bath', *Steel Res.*, vol. 58, no. 9, pp. 421–426, Sep. 1987, doi: 10.1002/srin.198700241.

[9] B. K. Rout, G. Brooks, M. A. Rhamdhani, Z. Li, F. N. H. Schrama, and J. Sun, 'Dynamic Model of Basic Oxygen Steelmaking Process Based on Multi-zone Reaction

Kinetics: Model Derivation and Validation', *Metall. Mater. Trans. B*, vol. 49, no. 2, pp. 537–557, Apr. 2018, doi: 10.1007/s11663-017-1166-7.

[10] D. Mombelli *et al.*, 'Model for Phosphorus Removal in LD Converter and Design of a Valuable Operative Practice', *Steel Res. Int.*, vol. 89, no. 5, p. 1700467, 2018.

[11] K. S. Coley, E. Chen, and M. Pomeroy, 'Kinetics of Reaction Important in Oxygen Steelmaking', in *Celebrating the Megascale*, 2016, pp. 289–302.

[12] B. K. Rout, G. Brooks, Subagyo, M. A. Rhamdhani, and Z. Li, 'Modeling of Droplet Generation in a Top Blowing Steelmaking Process', *Metall. Mater. Trans. B*, vol. 47, no. 6, pp. 3350–3361, Dec. 2016, doi: 10.1007/s11663-016-0773-z.

[13] Q. L. He and N. Standish, 'A Model Study of Droplet Generation in the BOF Steelmaking', *ISIJ Int.*, vol. 30, no. 4, pp. 305–309, Apr. 1990, doi: 10.2355/isijinternational.30.305.

[14] R. Li and R. L. Harris, 'Interaction of gas jets with model process liquids', in *Pyrometallurgy 95 Conference Proceedings*, 1995, p. 107.

[15] B. Deo and R. Boom, *Fundamentals of steelmaking metallurgy*. Prentice-Hall, 1993.

[16] Subagyo, G. A. Brooks, K. S. Coley, and G. A. Irons, 'Generation of Droplets in Slag-Metal Emulsions through Top Gas Blowing', *ISIJ Int.*, vol. 43, no. 7, pp. 983–989, Jul. 2003, doi: 10.2355/isijinternational.43.983.

[17] R. Sarkar, P. Gupta, S. Basu, and N. B. Ballal, 'Dynamic Modeling of LD Converter Steelmaking: Reaction Modeling Using Gibbs' Free Energy Minimization', *Metall. Mater. Trans. B*, vol. 46, no. 2, pp. 961–976, Apr. 2015, doi: 10.1007/s11663-014-0245-2.

[18] Publications Office of the European Union, 'Imphos : improving phosphorus refining.', 14-Dec-2011. [Online]. Available: https://publications.europa.eu/en/publication-detail/-/publication/8aecbb7c-f77f-4ee7-bc38-9ebb13b52faf/language-en. [Accessed: 06-Nov-2018].

[19] H. W. Meyer, W. F. Porter, G. C. Smith, and J. Szekely, 'Slag-Metal Emulsions and Their Importance in BOF Steelmaking', *JOM*, vol. 20, no. 7, pp. 35–42, Jul. 1968, doi: 10.1007/BF03378731.

[20] S. Sabah, M. Alam, G. Brooks, and J. Naser, 'DROPLET GENERATION IN STEELMAKING', in *Scanmet IV 4th International Conference*, Lulea, Sweden, 2012.

[21] G. Brooks, Y. Pan, and K. Coley, 'Modeling of trajectory and residence time of metal droplets in slag-metal-gas emulsions in oxygen steelmaking', *Metall. Mater. Trans. B*, vol. 36, no. 4, pp. 525–535, 2005.

[22] J. Martinsson and D. Sichen, 'Decarburization of Pig Iron in Synthetic BOF Converter Slag', *ISIJ Int.*, vol. 59, no. 1, pp. 46–50, Jan. 2019, doi: 10.2355/isijinternational.ISIJINT-2018-472.

[23] N. Dogan, G. A. Brooks, and M. A. Rhamdhani, 'Comprehensive model of oxygen steelmaking part 1: model development and validation', *ISIJ Int.*, vol. 51, no. 7, pp. 1086–1092, 2011.

[24] N. Dogan, G. A. Brooks, and M. A. Rhamdhani, 'Comprehensive model of oxygen steelmaking part 2: application of bloated droplet theory for decarburization in emulsion zone', *ISIJ Int.*, vol. 51, no. 7, pp. 1093–1101, 2011.

[25] N. Dogan, G. A. Brooks, and M. A. Rhamdhani, 'Comprehensive model of oxygen steelmaking part 3: decarburization in impact zone', *ISIJ Int.*, vol. 51, no. 7, pp. 1102–1109, 2011.

[26] N. Dogan, G. Brooks, and M. Rhamdhani, 'Development of a comprehensive model for oxygen steelmaking', *Fac. Eng. - Pap. Arch.*, pp. 1091–1101, Jan. 2010.

[27] S. C. Koria and K. W. Lange, 'A new approach to investigate the drop size distribution in basic oxygen steelmaking', *Metall. Trans. B*, vol. 15, no. 1, pp. 109–116, Jan. 1984, doi: 10.1007/BF02661068.

[28] E. W. Mulholland, G. S. F. Hazeldean, and M. W. Davies, 'Visualization of Slag–Metal Reactions by X-Ray Fluoroscopy- Decarburization in Basic Oxygen Steelmaking', *J Iron Steel Inst*, vol. 211, no. 9, pp. 632–639, 1973.

[29] C. L. Molloseau and R. J. Fruehan, 'The reaction behavior of Fe-C-S droplets in CaO-SiO2-MgO-FeO slags', *Metall. Mater. Trans. B*, vol. 33, no. 3, pp. 335–344, Jun. 2002, doi: 10.1007/s11663-002-0045-y.

[30] B. Sarma, A. W. Cramb, and R. J. Fruehan, 'Reduction of FeO in smelting slags by solid carbon: Experimental results', *Metall. Mater. Trans. B*, vol. 27, no. 5, pp. 717–730, Oct. 1996, doi: 10.1007/BF02915600.

[31] B. K. Rout, G. Brooks, and M. Rhamdhani, 'Transient Behavior of Dephosphorization Kinetics in Oxygen Steelmaking', in *AISTech 2015 Iron and Steel Technology Conference*, 2015, pp. 3225–3237.

[32] E. Chen and K. S. Coley, 'Kinetic study of droplet swelling in BOF steelmaking', *Ironmak. Steelmak.*, vol. 37, no. 7, pp. 541–545, 2010.

[33] H. Sun, 'Reaction Rates and Swelling Phenomenon of Fe–C Droplets in FeO bearing Slag', *ISIJ Int.*, vol. 46, no. 11, pp. 1560–1569, 2006, doi: 10.2355/isijinternational.46.1560.

[34] K. Gu, N. Dogan, and K. S. Coley, 'The Influence of Sulfur on Dephosphorization Kinetics Between Bloated Metal Droplets and Slag Containing FeO', *Metall. Mater. Trans. B*, vol. 48, no. 5, pp. 2343–2353, Oct. 2017, doi: 10.1007/s11663-017-1002-0.

[35] M.-A. Van Ende and I.-H. Jung, 'Applications of Thermodynamic Database to the Kinetic Steelmaking Process Simulations', in *Computational Materials System Design*, D. Shin and J. Saal, Eds. Cham: Springer International Publishing, 2018, pp. 47–66.

[36] A. Kruskopf and V.-V. Visuri, 'A Gibbs Energy Minimization Approach for Modeling of Chemical Reactions in a Basic Oxygen Furnace', *Metall. Mater. Trans. B*, vol. 48, no. 6, pp. 3281–3300, Dec. 2017, doi: 10.1007/s11663-017-1074-x.

[37] J. Ruuska, A. Sorsa, J. Lilja, and K. Leiviskä, 'Mass-balance Based Multivariate Modelling of Basic Oxygen Furnace Used in Steel Industry', *IFAC-Pap.*, vol. 50, no. 1, pp. 13784–13789, Jul. 2017, doi: 10.1016/j.ifacol.2017.08.2065.

[38] F. He and L. Zhang, 'Prediction model of end-point phosphorus content in BOF steelmaking process based on PCA and BP neural network', *J. Process Control*, vol. 66, pp. 51–58, Jun. 2018, doi: 10.1016/j.jprocont.2018.03.005.

[39] C. Kattenbelt and B. Roffel, 'Dynamic Modeling of the Main Blow in Basic Oxygen Steelmaking Using Measured Step Responses', *Metall. Mater. Trans. B*, vol. 39, no. 5, pp. 764–769, Oct. 2008, doi: 10.1007/s11663-008-9184-0.

[40] M.-A. van Ende, Y.-M. Kim, M.-K. Cho, J. Choi, and I.-H. Jung, 'A Kinetic Model for the Ruhrstahl Heraeus (RH) Degassing Process', *Metall. Mater. Trans. B*, vol. 42, no. 3, pp. 477–489, Jun. 2011, doi: 10.1007/s11663-011-9495-4.

[41] B. Deo and A. K. Shukla, 'Models for oxygen steelmaking process: theoretical analysis versus practical trends', in *5th International Congress on the Science and Technology of Steelmaking*, Dresden,Germany, 2012.

[42] C. Chigwedu, J. Kempken, and W. Pluschkell, 'A new approach for the dynamic simulation of the BOF process', *Stahl Eisen*, vol. 126, no. 12, pp. 25–31, 2006.

[43] C. Kattenbelt, 'Modeling and optimization of slopping prevention and batch time reduction in basic oxygen steelmaking', PhD thesis, University of Twente, Enschede, The Netherlands, 2008.

[44] N. Dogan, G. A. Brooks, and M. A. Rhamdhani, 'Kinetics of Flux Dissolution in Oxygen Steelmaking', *ISIJ Int.*, vol. 49, no. 10, pp. 1474–1482, Oct. 2009, doi: 10.2355/isijinternational.49.1474.

[45] G. A. Brooks, M. A. Rhamdhani, K. S. Coley, Subagyo, and Y. Pan, 'Transient Kinetics of Slag Metal Reactions', *Metall. Mater. Trans. B*, vol. 40, no. 3, pp. 353–362, Jun. 2009, doi: 10.1007/s11663-008-9170-6.

[46] D. R. Sain and G. R. Belton, 'Interfacial reaction kinetics in the decarburization of liquid iron by carbon dioxide', *Metall. Trans. B*, vol. 7, no. 2, pp. 235–244, Jun. 1976, doi: 10.1007/BF02654922.

[47] H. G. Lee and Y. K. Rao, 'Decarburisation and Nitrogen Absorption in Molten Fe–C Alloys. II. Mathematical Model', *Ironmak. Steelmak.*, vol. 15, no. 5, pp. 238–243, 1988.

[48] P. A. Distin, G. D. Hallett, and F. D. Richardson, 'Some reactions between drops of iron and flowing gases', *J Iron Steel Inst*, vol. 206, no. 8, pp. 821–833, 1968.

[49] D. R. Sain and G. R. Belton, 'The influence of sulfur on interfacial reaction kinetics in the decarburization of liquid iron by carbon dioxide', *Metall. Trans. B*, vol. 9, no. 3, pp. 403–407, Sep. 1978, doi: 10.1007/BF02654414.

[50] H. Lohe, 'Warme-und Stofftransport beim Aufblasen von Gasstrahlen auf Flussigkeiten. Fortschritt-Berichte', *VDI-Z. 1967*, vol. 3, no. 3, 1967.

[51] C. Cicutti, M. Valdez, T. Perez, R. Donayo, and J. Petroni, 'Analysis of slag foaming during the operation of an industrial converter', *Lat. Am. Appl. Res.*, vol. 32, no. 3, pp. 237–240, 2002.

[52] B. K. Rout, G. Brooks, M. Akbar Rhamdhani, Z. Li, F. N. H. Schrama, and A. Overbosch, 'Dynamic Model of Basic Oxygen Steelmaking Process Based on Multizone Reaction Kinetics: Modeling of Decarburization', *Metall. Mater. Trans. B*, vol. 49, no. 3, pp. 1022–1033, Jun. 2018, doi: 10.1007/s11663-018-1244-5.

[53] B. K. Rout, G. A. Brooks, Z. Li, and M. A. Rhamdhani, 'Analysis of Desiliconization Reaction Kinetics in a BOF', in *AISTech 2016 Proceedings*, 2016, pp. 1019–1026.

[54] B. K. Rout, G. Brooks, M. Akbar Rhamdhani, Z. Li, F. N. H. Schrama, and W. van der Knoop, 'Dynamic Model of Basic Oxygen Steelmaking Process Based on Multizone Reaction Kinetics: Modeling of Manganese Removal', *Metall. Mater. Trans. B*, vol. 49, no. 5, pp. 2191–2208, Oct. 2018, doi: 10.1007/s11663-018-1306-8.

[55] K. Ito and R. J. Fruehan, 'Study on the foaming of CaO-SiO2-FeO slags: Part I. Foaming parameters and experimental results', *Metall. Trans. B*, vol. 20, no. 4, pp. 509–514, Aug. 1989, doi: 10.1007/BF02654600.

[56] B. T. Chao, 'Transient heat and mass transfer to a translating droplet', *J. Heat Transf.*, vol. 91, no. 2, pp. 273–280, 1969.

[57] A. K. Hewage, B. K. Rout, G. Brooks, and J. Naser, 'Analysis of steelmaking kinetics from IMPHOS pilot plant data', *Ironmak. Steelmak.*, vol. 43, no. 5, pp. 358–370, 2016.

[58] K.-C. Chou, U. B. Pal, and R. G. Reddy, 'A general model for BOP decarburization', *ISIJ Int.*, vol. 33, no. 8, pp. 862–868, 1993.

[59] K. Narita, T. Makino, H. Matusumo, A. Hikosa, and J. Katsuda, 'Oxidation Mechanism of Silicon in Hot Metal', *Tetsu--Hagané*, vol. 69, no. 15, pp. 1722–1729, 1983.

[60] H. Suito and R. Inoue, 'Thermodynamic Assessment of Maganese Distribution in Hot Metal and Steel', *ISIJ Int.*, vol. 35, no. 3, pp. 266–271, 1995.

[61] F. D. Richardson, *Physical chemistry of melts in metallurgy*. Academic Press (Elsevier), 1974.

[62] Y. Ogasawara, Y. Miki, Y. Uchida, and N. Kikuchi, 'Development of high efficiency dephosphorization system in decarburization converter utilizing FetO dynamic control', *ISIJ Int.*, vol. 53, no. 10, pp. 1786–1793, 2013.

[63] S.-M. Jung, C.-H. Rhee, and D.-J. Min, 'Thermodynamic Properties of Manganese Oxide in BOF Slags', *ISIJ Int.*, vol. 42, no. 1, pp. 63–70, Jan. 2002, doi: 10.2355/isijinternational.42.63.

[64] J. M. Park, 'Iron redox equilibria in BOF slag equilibrated with ambient air', *Steel Res.*, vol. 73, no. 2, pp. 39–43, 2002, doi: 10.1002/srin.200200171.

[65] C. W. Bale *et al.*, 'FactSage thermochemical software and databases, 2010–2016', *Calphad*, vol. 54, pp. 35–53, 2016.

[66] Y. Lytvynyuk, J. Schenk, M. Hiebler, and A. Sormann, 'Thermodynamic and kinetic model of the converter steelmaking process. Part 1: The description of the BOF model', *Steel Res. Int.*, vol. 85, no. 4, pp. 537–543, 2014.

[67] Y. Lytvynyuk, J. Schenk, M. Hiebler, and A. Sormann, 'Thermodynamic and kinetic model of the converter steelmaking process. part 2: The model validation', *Steel Res. Int.*, vol. 85, no. 4, pp. 544–563, 2014.

[68] Y. Lytvynyuk, J Schenk, M. Hiebler, and H. Mizelli, 'Thermodynamic and kinetic modelling of the de- vanadization process in the steelmaking converter', in *6th European Oxygen Steelmaking Conference*, Stockholm, Sweden, 2011, doi: 10.13140/2.1.1126.7848.

[69] B. M. Boychenko, V. B. Okhotskiy, and P. S. Kharlashin, 'The Converter Steelmaking', *Dnipro-VAL Dnipropetrovsk Ukr.*, 2006.

[70] S. Ohguchi, D. G. C. Robertson, B. Deo, P. Grieveson, and J. H. Jeffes, 'Simultaneous dephosphorization and desulphurization of molten pig iron', *Ironmak. Steelmak.*, vol. 85, no. 4, pp. 202–213, 1984.

[71] The Japan Society for the Promotion of Science and The 19th Committee on Steelmaking, *Steelmaking Data Sourcebook*. New York: Gordon and Breach Science Publishers, 1988.

[72] G. K. Sigworth and J. F. Elliott, 'The Thermodynamics of Liquid Dilute Iron Alloys', *Met. Sci.*, vol. 8, no. 1, pp. 298–310, Jan. 1974, doi: 10.1179/msc.1974.8.1.298.

[73] V. A. Grigoryan, L. N. Belyanchikov, and A. Y. Stomakhin, 'Theoretical Fundamentals of Electric Steelmaking Processes', *Metall. Mosc.*, 1987.

[74] S. Kitamura, H. Shibata, and N. Maruoka, 'Kinetic Model of Hot Metal Dephosphorization by Liquid and Solid Coexisting Slags', *Steel Res. Int.*, vol. 79, no. 8, pp. 586–590, 2008, doi: 10.1002/srin.200806170.

[75] S. Kitamura, T. Kitamura, K. Shibata, Y. Mizukami, S. Mukawa, and J. Nakagawa, 'Effect of stirring energy, temperature and flux composition on hot metal dephosphorization kinetics', *ISIJ Int.*, vol. 31, no. 11, pp. 1322–1328, 1991.

[76] E. T. Turkdogan, R. J. Fruehan, and R. J. Fruehan, *The Making, Shaping and Treating of Steel, Steelmaking and Refining, Volume 2, ed*. Pittsburgh: AISE Steel Foundation, 1998.

[77] E. T. Turkdogan, 'Assessment of SiO2 Activity Coefficients in Molten Slags Relative to the CaO–SiO2 System', *ISIJ Int.*, vol. 41, no. 8, pp. 930–932, Aug. 2001, doi: 10.2355/isijinternational.41.930.

[78] A. Kruskopf, 'A 2D Axisymmetric Mixture Multiphase Model for Bottom Stirring in a BOF Converter', *Metall. Mater. Trans. B*, vol. 48, no. 1, pp. 619–631, Feb. 2017, doi: 10.1007/s11663-016-0856-x.

[79] A. Kruskopf, 'A Model for Scrap Melting in Steel Converter', *Metall. Mater. Trans. B*, vol. 46, no. 3, pp. 1195–1206, Jun. 2015, doi: 10.1007/s11663-015-0320-3.

[80] A. Chatterjee, N.-O. Lindfors, and J. Wester, 'Process Metallurgy of LD Steel Making', *SEAISI Q July 1976 5-3 6-19*, 1976.

[81] M. H. A. Piro, S. Simunovic, T. M. Besmann, B. J. Lewis, and W. T. Thompson, 'The thermochemistry library Thermochimica', *Comput. Mater. Sci.*, vol. 67, pp. 266–272, Feb. 2013, doi: 10.1016/j.commatsci.2012.09.011.

[82] M. H. A. Piro and S. Simunovic, 'Performance enhancing algorithms for computing thermodynamic equilibria', *Calphad*, vol. 39, pp. 104–110, Dec. 2012, doi: 10.1016/j.calphad.2012.09.005.

[83] J. R. Taylor and A. T. Dinsdale, 'Thermodynamic and phase diagram data for the CaO-SiO2 system', *Calphad*, vol. 14, no. 1, pp. 71–88, Jan. 1990, doi: 10.1016/0364-5916(90)90041-W.

[84] S. Petersen and K. Hack, 'The thermochemistry library ChemApp and its applications', *Int. J. Mater. Res.*, vol. 98, no. 10, pp. 935–945, Oct. 2007, doi: 10.3139/146.101551.

[85] *Schlackenatlas*. Düsseldorf : Stahleisen, 1981.

[86] M.-A. Van Ende and I.-H. Jung, 'A kinetic ladle furnace process simulation model: effective equilibrium reaction zone model using FactSage macro processing', *Metall. Mater. Trans. B*, vol. 48, no. 1, pp. 28–36, 2017.

[87] M.-A. Van Ende and I.-H. Jung, 'A kinetic process Simulation Model for Basic Oxygen Furnace (BOF): Importance of slag chemistry for BOF operation', in *Procedings Asia Steel International Conference 2015*, Yokohama, Japan, 2015.

[88] A. D. Pelton, S. A. Degterov, G. Eriksson, C. Robelin, and Y. Dessureault, 'The modified quasichemical model I—Binary solutions', *Metall. Mater. Trans. B*, vol. 31, no. 4, pp. 651–659, Aug. 2000, doi: 10.1007/s11663-000-0103-2.

[89] A. D. Pelton and P. Chartrand, 'The modified quasi-chemical model: Part II. Multicomponent solutions', *Metall. Mater. Trans. A*, vol. 32, no. 6, pp. 1355–1360, Jun. 2001, doi: 10.1007/s11661-001-0226-3.

[90] P. Chartrand and A. D. Pelton, 'The modified quasi-chemical model: Part III. Two sublattices', *Metall. Mater. Trans. A*, vol. 32, no. 6, pp. 1397–1407, Jun. 2001, doi: 10.1007/s11661-001-0229-0.

[91] A. D. Pelton, P. Chartrand, and G. Eriksson, 'The modified quasi-chemical model: Part IV. Two-sublattice quadruplet approximation', *Metall. Mater. Trans. A*, vol. 32, no. 6, pp. 1409–1416, Jun. 2001, doi: 10.1007/s11661-001-0230-7.

[92] M. Hillert, 'The compound energy formalism', *J. Alloys Compd.*, vol. 320, no. 2, pp. 161–176, May 2001, doi: 10.1016/S0925-8388(00)01481-X.

[93] C. W. Bale and A. D. Pelton, 'The unified interaction parameter formalism: Thermodynamic consistency and applications', *Metall. Trans. A*, vol. 21, no. 7, pp. 1997–2002, Jul. 1990, doi: 10.1007/BF02647247.

[94] I.-H. Jung, S. A. Decterov, and A. D. Pelton, 'A thermodynamic model for deoxidation equilibria in steel', *Metall. Mater. Trans. B*, vol. 35, no. 3, pp. 493–507, Jun. 2004, doi: 10.1007/s11663-004-0050-4.

[95] H. Gaye, M. Wanin, P. Gugliermina, and P. Schittly, 'Kinetics of Scrap Melting in the Oxygen Converter.(Abstract Only)', *Rev Met. Cah Inf Tech*, vol. 82, no. 11, p. 121, 1985.

[96] A. N. Grundy, H. Liu, I.-H. Jung, S. A. Decterov, and A. D. Pelton, 'A model to calculate the viscosity of silicate melts', *Int. J. Mater. Res.*, vol. 99, no. 11, pp. 1185–1194, Nov. 2008, doi: 10.3139/146.101752.

[97] A. N. Grundy, I.-H. Jung, A. D. Pelton, and S. A. Decterov, 'A model to calculate the viscosity of silicate melts', *Int. J. Mater. Res.*, vol. 99, no. 11, pp. 1195–1209, Nov. 2008, doi: 10.3139/146.101753.

[98] A. N. Grundy, I.-H. Jung, A. D. Pelton, and S. A. Decterov, 'A model to calculate the viscosity of silicate melts: Part II: The NaO0. 5–MgO–CaO–AlO1. 5–SiO2 system', *Int. J. Mater. Res.*, vol. 99, no. 11, pp. 1195–1209, 2008.

[99] S. Khadhraoui *et al.*, 'A new approach for modelling and control of dephosphorization in BOF converter', *Metall. Ital.*, vol. 11/12, pp. 5–16, 2018.

[100] M. Schlautmann *et al.*, 'Dynamic on-line monitoring and end point control of dephosphorisation in the bof converter', in *3rd European Steel Technology and Application Days (ESTAD)*, Vienna, Austria, 2017.

[101] F. Pahlevani, S. Kitamura, H. Shibata, and N. Maruoka, 'Simulation of Steel Refining Process in Converter', *Steel Res. Int.*, vol. 81, no. 8, pp. 617–622, Aug. 2010, doi: 10.1002/srin.201000053.

[102] D. Baricová *et al.*, 'Change of the Chemical and Mineralogical Composition of the Slag during Oxygen Blowing in the Oxygen Converter Process', *Metals*, vol. 8, no. 10, p. 844, Oct. 2018, doi: 10.3390/met8100844.

[103] K. C. Mills and B. J. Keene, 'Physical properties of BOS slags', *Int. Mater. Rev.*, vol. 32, no. 1, pp. 1–120, Jan. 1987, doi: 10.1179/095066087790150296.

[104] S. A. Decterov, A. N. Grundy, I.-H. Jung, and A. D. Pelton, 'Modeling the viscosity of aluminosilicate melts', in *AIP Conference Proceedings*, 2007, vol. 963, pp. 404–407.

[105] A. Kondratiev, P. C. Hayes, and E. Jak, 'Development of a Quasi-chemical viscosity model for fully liquid slags in the Al2O3–CaO–"FeO"–MgO–SiO2 system. Part 2. A review of the experimental data and the model predictions for the Al2O3–CaO–MgO,

CaO–MgO–SiO2 and Al2O3–MgO–SiO2 systems', *ISIJ Int.*, vol. 46, no. 3, pp. 368–374, 2006.

[106] G.-H. Zhang, K.-C. Chou, and K. Mills, 'A Structurally Based Viscosity Model for Oxide Melts', *Metall. Mater. Trans. B*, vol. 45, no. 2, pp. 698–706, Apr. 2014, doi: 10.1007/s11663-013-9980-z.

[107] Z. Liu, L. Pandelaers, B. Blanpain, and M. Guo, 'Viscosity of Heterogeneous Silicate Melts: A Review', *Metall. Mater. Trans. B*, vol. 49, no. 5, pp. 2469–2486, Oct. 2018, doi: 10.1007/s11663-018-1374-9.

[108] R. Roscoe, 'The viscosity of suspensions of rigid spheres', *Br. J. Appl. Phys.*, vol. 3, no. 8, p. 267, 1952.

[109] A. Kondratiev and E. Jak, 'Modeling of viscosities of the partly crystallized slags in the Al 2 O 3-CaO-"FeO"-SiO 2 system', *Metall. Mater. Trans. B*, vol. 32, no. 6, pp. 1027–1032, 2001.

[110] M. Hanao, T. Tanaka, M. Kawamoto, and K. Takatani, 'Evaluation of Surface Tension of Molten Slag in Multi-component Systems', *ISIJ Int.*, vol. 47, no. 7, pp. 935–939, 2007, doi: 10.2355/isijinternational.47.935.

[111] Butler John Alfred Valentine and Kendall James Pickering, 'The thermodynamics of the surfaces of solutions', *Proc. R. Soc. Lond. Ser. Contain. Pap. Math. Phys. Character*, vol. 135, no. 827, pp. 348–375, Mar. 1932, doi: 10.1098/rspa.1932.0040.

[112] S.-K. Kim, W. Wang, and Y.-B. Kang, 'Modeling surface tension of multicomponent liquid steel using Modified Quasichemical Model and Constrained Gibbs Energy Minimization', *Met. Mater. Int.*, vol. 21, no. 4, pp. 765–774, Jul. 2015, doi: 10.1007/s12540-015-4619-z.

[113] M. Nakamoto, A. Kiyose, T. Tanaka, L. Holappa, and M. Hämäläinen, 'Evaluation of the Surface Tension of Ternary Silicate Melts Containing Al2O3, CaO, FeO, MgO or MnO', *ISIJ Int.*, vol. 47, no. 1, pp. 38–43, 2007, doi: 10.2355/isijinternational.47.38.

10 Thermodynamic BOF model

To simulate the BOF process of the ArcelorMittal Ghent steel plant, a thermodynamic based model is constructed. The goal of the model is to predict both the end composition as well as to describe the evolution of the process accurately. In this chapter this model is described. Firstly, a motivation is given on the topic of why a more complex model was needed than just a single thermodynamic calculation. Secondly, the implemented model itself is described and its assumptions are discussed.

10.1 Motivation to use thermodynamics

10.1.1 The standard closed calculation

Pyrometallurgical processes are high temperature processes, in steelmaking usually temperatures above 1500°C, and as a consequence it is often assumed that reactions are mostly governed by thermodynamics. Kinetics are stated to be of minor importance because the reaction rates are usually high due to the high temperatures. Especially, at the end of the BOF process (or also called the end of blow), at high temperature (> 1600°C) and due to continuous stirring during the process, a simple thermodynamic calculation could give insight in the process. To illustrate this a set of 66 industrially simulated heats is used. These heats represent the most common and most encountered type of steel grades produced at the ArcelorMittal Ghent (AMG) plant. The AMG results shown in these sections are calculated results. However, these calculations are results from the AMG blowing model which is used as an online tool at the steel plant and thus the predictions of this model are close to the measured reality. The industrially simulated end composition for these heats is compared to a standard closed equilibrium calculation performed with the Factsage 'Equilib' module. A closed equilibrium calculation considers the BOF process as one uniform reactor. Both mass and heat are conserved. The temperature in the thermodynamic (TD) calculation, is set as the final temperature of the heat. Four different databases in Factsage 7.3 [1] were used: FactPS for the gas phase, FToxid for the oxides, FTmisc for high temperature liquid steel and Fsstel for the scrap. In Figure 10.1 it is shown that the calculated slag mass with the standard closed thermodynamic calculation shows a good correlation with the expected industrial slag

mass.[12] However, the thermodynamic calculated slag mass is always higher than the industrially expected one. This is, in this case, due to the so called 'over-oxidation' in the thermodynamic calculation.

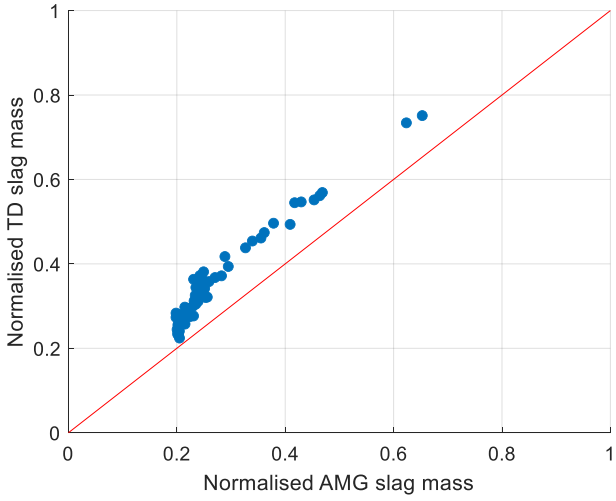

Figure 10.1: Comparison of the AMG calculated slag mass and the thermodynamic calculated slag mass (standard closed calculation).

As can be seen in Figure 10.2, the difference in absolute slag mass is strongly related to the absolute difference in the amount of iron in the slag. This Fe will of course be present in the slag as either FeO or Fe_2O_3. Thermodynamically, a higher Fe content is calculated or more iron is oxidised from the metal bath than industrially observed. One possible explanation is the homogeneous nature of the thermodynamic calculation which implies perfect stirring and unlimited access for the elements to each other. Additionally, the current calculations assume a 100% efficiency for the incoming oxygen, while in industry this efficiency is less.

[12] For confidentiliyt reasons the industrial properties are normalised. This normalisation was required within the context of the current project, as explained in the introduction of the work. Normalisation is done between an industrial relevant minimum and maximum value for each property. These extrema are constant throughout the complete dissertation.

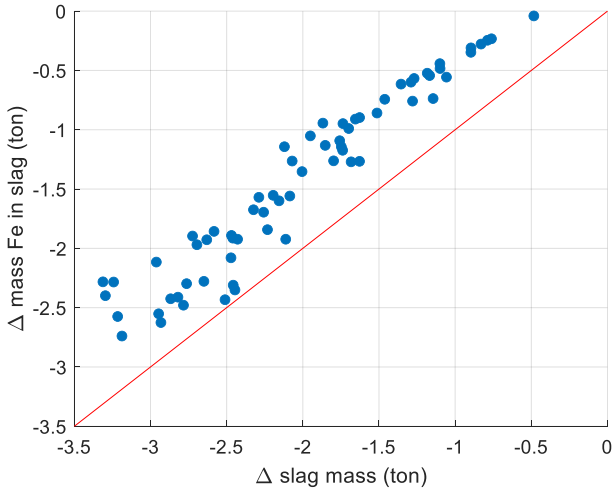

Figure 10.2: The difference in amount of Fe between the AMG simulation and the thermodynamic calculation as a function of the difference in slag mass. The difference is defined as the industrial value minus the thermodynamic value.

Some other important features are shown in Figure 10.3. There is a good correlation between the thermodynamic calculation and the industrial simulation and observations, but the refining of the steel is thermodynamically always better. However, the phosphorus content clearly shows a similar trend, meaning that a heat with a higher phosphorus content in reality will also have a higher calculated thermodynamic phosphorus content. In Figure 10.3 (right) the relation between the obtained carbon content and the dissolved oxygen in the steel phase for the thermodynamic and industrial calculation are compared. For both types of calculation the correlation between these two properties are similar. Although, clearly for the thermodynamic calculation a smaller oxygen content is required to obtain a certain carbon content, indicating that thermodynamically the same carbon content can be achieved with a lower oxygen content. Thermodynamically mixing is considered to be perfect (there are no kinetic or mixing barriers) and each element in the system can react with any other element present. While in reality this is of course not the case and there will be physical barriers for mixing of components.

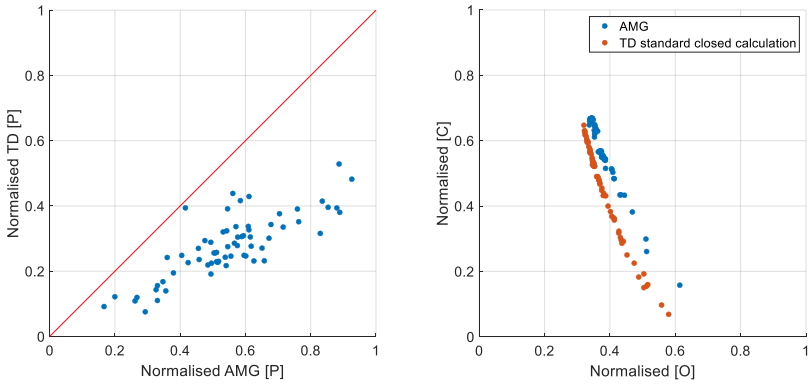

Figure 10.3: Difference in steel composition between the AMG simulations and the standard closed thermodynamic calculation. (left) The TD calculated phosphorus content in function of the industrial phosphorus content. (right) The obtained carbon content as a function of the dissolved oxygen both for the industrial and the thermodynamically calculated data.

Even though the closed standard thermodynamic calculations already seem to give a good indication of the final end composition of the system, they do not give any insight of the slag evolution during the process. A possible solution for this is to apply the concept of an open calculation as explained in the next section.

10.1.2 The standard open calculation

In the previous section the system was considered a closed system with respect to both mass and energy. Furthermore, the complete process was simulated as a one big batch process. In reality oxygen gas is added over time and the gas which is formed will be removed from the vessel, nearly immediately. Thermodynamically, this could be simulated as a simple series of equilibrium calculations in which only a fraction of the total amount of oxygen is added during each calculation step. The formed gas phase is removed from the system. As a consequence, the system is only closed with respect to the mass and energy of the condensed phases. This will have an influence on the equilibrium due to the well-known principle of 'Le Chatelier' that states that upon removal of the product the equilibrium will shift towards the product side. Because the gas phase contains mostly the carbon, it is expected the carbon content of the metal bath for an open calculation will be different compared to a standard closed calculation. The same 66 heats as used in the previous section, are now simulated with an open calculation. A calculation step of 1 ton O_2 is used. The equilibrium calculations are assumed to be adiabatic with respect to the condensed phases, as such the enthalpy of

the condensed system is conserved. This principle is shown in equation 10.1, in which *n* is the current calculation step and ΔH the enthalpy with reference to the standard state.[13] This assumption allows to calculate the equilibrium temperature rather than to impose a temperature.

$$\Delta H_n^{system} = \Delta H_{n-1}^{system} + \Delta H_n^{O_{2,added}} - \Delta H_{n-1}^{gas,formed} \quad (10.1)$$

For these open thermodynamic calculations the Chemapp [2] (V 7.3.2) Gibbs free energy minimiser is used with a database file that is identical to the one used in the closed calculation. In Figure 10.4 the calculated temperature with the open thermodynamic simulation is compared to the AMG temperature for 66 heats. A good match is found between the AMG temperature and the thermodynamically calculated temperature for the larger share of the heats. For higher temperatures, the thermodynamic calculation overestimates the AMG temperature. A larger deviation at higher temperatures might be due to the added fluxes. In this specific dataset, larger amounts of iron ore are generally added to the heats with higher temperature. Possibly, the calculation of the enthalpy of iron ore in the thermodynamic calculation deviates from the one for the AMG calculations. Furthermore, there are also no heat losses considered in this calculation and these losses are higher for higher temperatures (e.g. thermal radiation).

[13] This standard state is the default standard state used by Factsage and ΔH is the value labelled in a Factsage calculation as H. However, strictly speaking the enthalpy is never an absolute value and always with respect to a reference state. Hence, the use of ΔH in the equation.

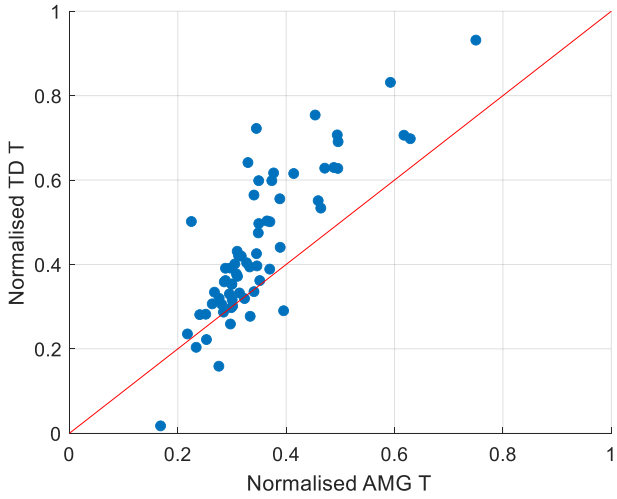

Figure 10.4: The calculated temperature of the open TD simulation at the end of the process, compared to the AMG temperature.

The slag mass calculated with the open calculation is compared both to the AMG slag mass and the closed calculation in Figure 10.5. A good correlation is observed between the thermodynamic and industrial calculated slag masses. Yet, with an open calculation the slag mass is overestimated compared to the AMG results. The results of the open calculation are also higher than those of the closed calculation.

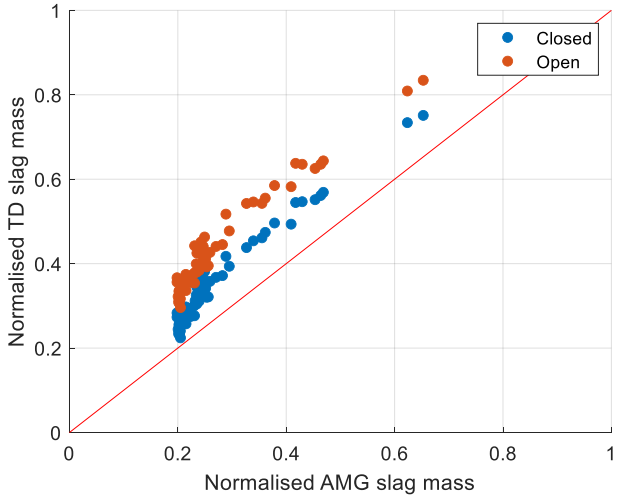

Figure 10.5: Comparison of the AMG calculated slag mass and the thermodynamically calculated slag mass both with the open and closed simulation.

From Figure 10.6, it is clear that this higher slag mass is strongly related to the higher iron content in the slag in the open calculation compared to the closed calculation. Since, for the closed calculation this higher iron content was already identified as the reason for the higher slag masses, this reasoning also applies for the open calculation. As such, the process is 'over-blown' or over oxidised and the oxygen is used in a more efficient way in the current thermodynamic simulations compared to the reality or the closed thermodynamic calculation.

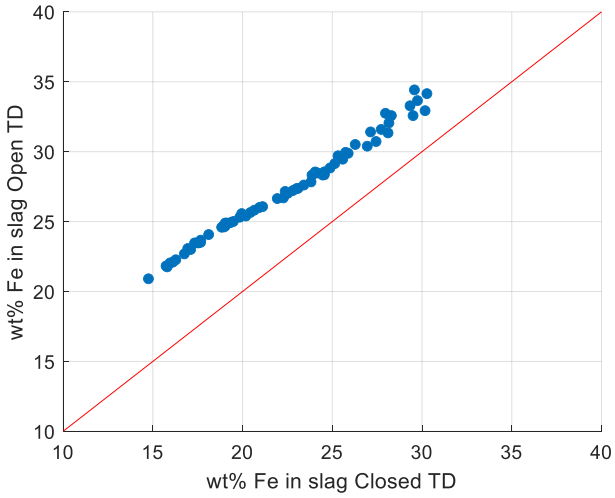

Figure 10.6: The iron content of the slag for the open TD calculation as a function of the closed TD calculation.

As explained earlier, a difference between the gas phase of the closed and the open calculation is expected. In Figure 10.7 (a) the difference in total amount of gas produced is shown. When simulating the process with an open TD calculation about 0.5 ton gas is produced less. Additionally, in Figure 10.7 (b) the carbon content of the steel at the end of the process is given. The steel phase calculated with the open TD calculation clearly contains less carbon and hence, is stronger refined even though all input is identical between the two calculations. Of course, a small deviation exists in the end temperature between the two calculations. Yet, this is not the reason for the difference in carbon content. Via an open calculation, less gas is produced and this gas is richer in C. Thus, the carbon removal is more efficient. Of course, this is to be expected according to the earlier mentioned principle of 'Le Chatelier'.

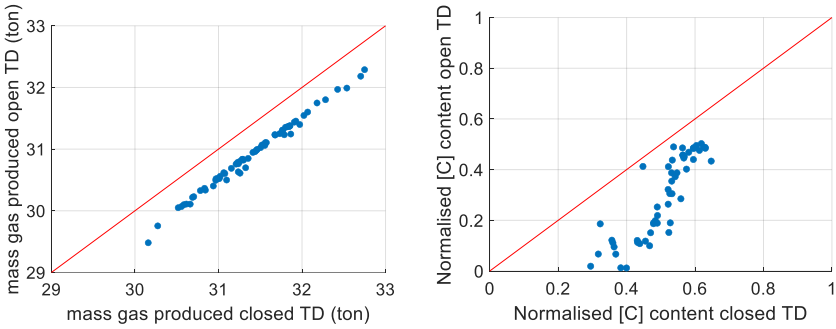

Figure 10.7: Comparison of (left) the amount of gas produced and (right) the carbon content of the steel phase between the open and closed TD calculation. Due to confidentiality the carbon content is normalised.

One of the motivations to simulate the process with an open TD calculation is to get insight in the slag evolution during blow. For the 66 heats the evolution of the average wt% Fe in the slag as a function of the amount of oxygen blown (which on itself is an alternative time axis) is given in Figure 10.8. The black line represents the average iron content and the red dotted lines the standard deviations. From this figure it can be concluded that iron is only observed in the slag at the end of blow. In other words, the iron only oxidises at the end of the process, when nearly all other impurities are removed from the metal bath. From a thermodynamic viewpoint this is to be expected. Consulting any Ellingham diagram (e.g. the one shown in 'chapter 2: BOF process and slag'), proofs the ΔG-value for the oxidation of Fe is considerably higher than the ones for the oxidation of the other common impurities such as Si, P and C: the other impurities have a higher oxygen affinity. Thermodynamically, there will only be a driving force to oxidise iron once the content of the other impurities is significantly reduced.

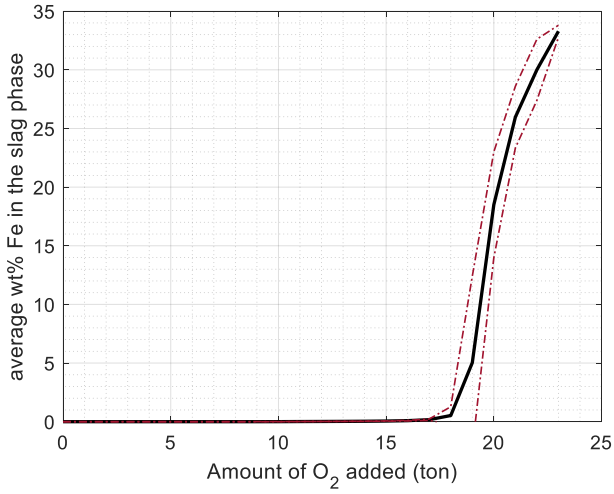

Figure 10.8: Evolution of the iron content of the slag for an open TD calculation. The black line is the average calculated from a set of 66 heats. The red dotted lines show the standard deviation.

Even though this behaviour is perfectly understandable from a thermodynamic view point, it is not what is observed in the reality. In Figure 10.9 (left) the fitted evolutions to the measured data for different heats from the Imphos [3] study are shown. Throughout this European project, slag samples were sampled at different slag heights in a pilot scale set up. During the first two minutes of the process no samples were taken. The exact behaviour, is different for the five different displayed samples. However, it is very clear that the Fe (or FeO_n) content of the slag increases at the very start of the process, to decrease again during the blow and only increase again towards the end of the process. In Figure 10.9 (right) the average evolution of the Fe content in the slag for a set of historical AMG heats is given. These contents were calculated with the model developed during this work and described in Chapter 7. The black line represents the average while the red dotted lines show the standard deviations. An identical behaviour is observed as described for Figure 10.9 (left).

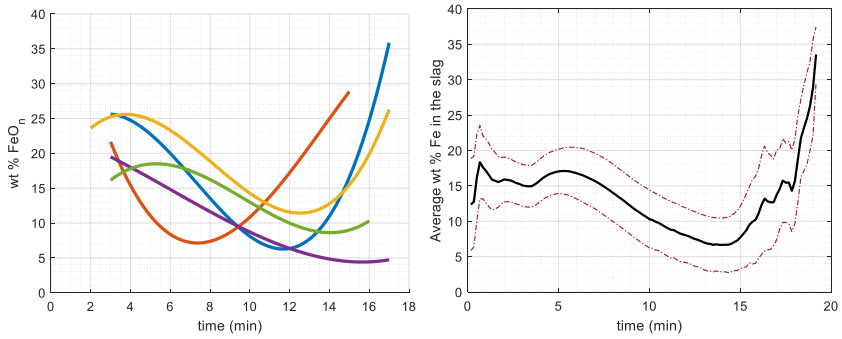

Figure 10.9: The iron content of the slag as observed in real steelmaking process. In (left) fitted curves to the measured Imphos [3] FeO_n content for a 6 ton pilot BOF vessel and (right) average iron content of 96 AMG calculated with the model discussed in 'chapter 7'. The black line is the average, the red dotted ones are the standard deviation.

The focus of the current work is the role of slag in the BOF process. Hence, in understanding this role it is key to get a good simulation or prediction of the slag composition during blow. It is clear, that a simple standard TD calculation is insufficient to model this slag evolution correctly and kinetics need to be considered. Yet, from the discussed results and observations, it can be concluded that thermodynamics give a good indication of the direction the process evolves to. Therefore, a thermodynamic model incorporating kinetic features is proposed.

10.2 An effective equilibrium reaction zone type model: combining kinetics and thermodynamics

10.2.1 General model outline

Van Ende et al. [4]–[7] developed a general model for industrial processes, in which both kinetics and thermodynamics are integrated. This model is known as the 'Effective equilibrium reaction zone' (EERZ) model and details of the model concepts can be consulted in 'chapter 9: Physicochemical models for the BOF process'. The same, or similar models, have been used for this purpose by different researchers [8]–[10] in the steel industry, mainly focussing on ladle furnaces.

The practical implementation of the EERZ model for the BOF process is schematically shown in Figure 10.10. In the first step (**step 1**), the metal and slag bulk phases are two separate phases in contact with each other. Yet, these phases are not in equilibrium with each other. Hence, the phases can have different temperatures and the chemical

potential of the species in the two phases will, in general, be different. For a species X this is shown via its concentration in both phases (red line). Note, that this species will either be iron or any element dissolved in the iron rich metal bath, while for the slag phase this species will be present as an oxide. For simplicity it is assumed that in this example the slag is completely liquid. Within this bulk phase a reaction volume (RV) is defined. In the second step (**step 2**), a thermodynamic equilibrium is assumed for the material present in the RV's. The metal RV and slag RV are at this point in equilibrium with each other. As a consequence, they form one system with one unique temperature and chemical potential for the species. Species X is now redistributed between the slag and metal phase which are formed as result of the equilibrium reaction. The red dotted lines show the concentration of species X in the new metal and slag phase after the equilibrium reaction between the RV's. In the third step (**step 3**), a so called homogenisation reaction for the bulk phases is assumed to take place. The newly formed slag from the RV equilibrium and the part of the original slag which was no part of this RV are now assumed to be at chemical equilibrium. The same reasoning applies for the metal bath. After step 3, the metal phase and the slag phase are again in contact, yet not at equilibrium with each other. However, their temperature and the concentration of species X clearly is different compared to step 1. In each time or calculation step of the EERZ model this principle is applied. Several different reaction zones with specific RV's are defined and the amount of material participating in the reaction is restricted, accounting for the kinetics of the process.

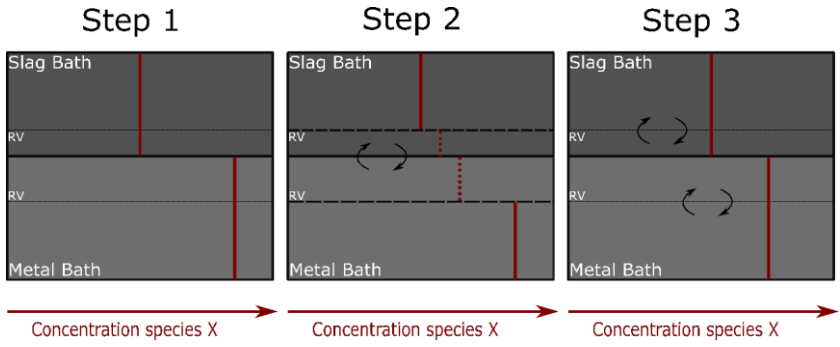

Figure 10.10: Practical implementation of the EERZ model for the BOF process. Inspired on figures from [10]. (RV = reaction volume)

The current EERZ model called the thermodynamic BOF model (TD BOF model) consists out of four reaction volume zones, two homogenisations, one heat transfer calculation

and finally, two thermal homogenisations. The different reaction zones are depicted on Figure 10.11. The calculation sequence is:

1. Jet Impact zone (JIZ): *Reaction of oxygen and the metal bath*
2. Interface zone (IF): *Reaction between the slag and metal at the interface*
3. Emulsion zone (EMU): *Reaction in the Slag – metal – gas emulsion*
4. Scrap melting (SC): *Reaction of the solid metal (scrap) and the liquid metal*
5. Metal homogenisation
6. Slag homogenisation
7. Heat transfer between bulk metal and bulk slag
8. Metal temperature homogenisation
9. Slag temperature homogenisation

A conservation of both heat and mass is assumed for the condensed phases. It is assumed all the formed gas immediately leaves the reaction vessel without any interaction with neither the phases present in the vessel nor the incoming oxygen jet. No heat losses are considered, thus the condensed phases are considered to be a closed thermodynamic system. Temperature for both the slag and metal phase is calculated from the conservation of energy assumption for each phase. The system consists out of 9 different elements: Fe, C, Si, Mn, P, Ca, Mg, Al and O.

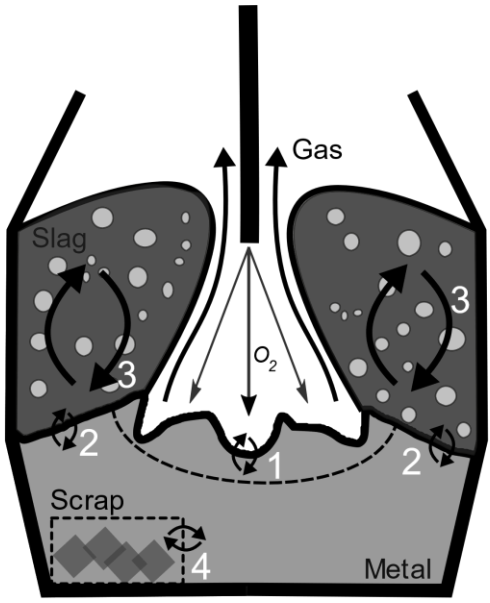

Figure 10.11: Schematic overview of the different reaction zones in the TD BOF model.

10.2.2 Considered material input

Hot metal

Hot metal containing C, Si, P, Mn and Fe is considered. The fraction of Fe is always calculated based upon the C, Si, P and Mn contents to balance the total sum of wt% to 100. The industrial hot metal can also contain other elements e.g. V or S. Yet, these are not considered in the TD calculations. Generally, due to this assumption, the TD Fe content will be slightly higher than the AMG Fe content of the hot metal. However, contents of the impurities left out of the analyses are usually in the order of 100 ppm or less, and for this reason this assumption is considered to be valid. The temperature of the hot metal is the actual measured temperature whenever this is available. Otherwise, a fixed default temperature of 1350°C is used. As a consequence of the allowed variation of hot metal composition and temperature, the enthalpy of the hot metal will always be calculated for each separate batch of hot metal. Yet, to allow the reader to get acquainted with the order of magnitude of the enthalpy of the hot metal, a value for a default composition is given in Table 10-1.

Table 10-1: List of some specific enthalpy values for the different considered inputs. Calculated with Factsage 7.2 or 7.3. The compositions of the input materials cannot be shared due to confidentiality.

Input material	Enthalpy (J/g)	Compounds
Hot Metal	1280.59	Fe, C, Mn, P, Si
Scrap 1	-807.20	Fe, C, Mn, P, SiO_2, Al_2O_3, MgO
Scrap 2	-15.25	Fe, C, Mn, P, SiO_2
Scrap 3	3.21	Fe, C, Mn, P, SiO_2, Al_2O_3
Iron flux 1	-913.06	Fe, SiO_2, Al_2O_3
Iron flux 2	-884.84	Fe, Mn, SiO_2, Al_2O_3, CaO
Iron flux 3	-609.33	Fe, C, P, SiO_2 ,Al_2O_3
Dolo – lime	-12550.20	SiO_2, Al_2O_3, MgO, CaO
Lime	-11464.00	SiO_2, Al_2O_3, MgO, CaO

Scrap

In reality, a wide variety in scrap materials (both composition and size) is used as input material for the BOF process. However, for the TD BOF model the possible variation in scrap input materials is narrowed down to three different scrap types. The compositions of the scrap materials are a mix of metal (Fe, C, Mn and P) and oxides (SiO_2, Al_2O_3 and MgO). Three types of scrap material are defined for the current model: Scrap 1, Scrap 2 and Scrap 3. The Scrap 1 contain a considerable amount of Al_2O_3 and are thus, less clean scrap than Scrap 2 or 3. Scrap 3 will contain more impurities than Scrap 2. For different sets of calculations the exact compositions of these types of scrap might be altered slightly. Yet, the variety of scraps is always limited to three different types. Scraps are added at room temperature (25°C). The corresponding specific enthalpy values are given in Table 10-1 and are calculated with the assumption of a homogeneous metal phase and pure solid oxide phases.

Fluxes

The amount of different fluxes is limited to five: Iron flux 1, Iron flux 2, Iron flux 3, dolomite lime (dolo – lime) and lime. The first three fluxes will contain a large amount of iron and a relatively small fraction of oxides. However, the content of iron and types of

impurities present will differ between the three types. These fluxes also contain some free oxygen. The last two fluxes, dolo – lime and lime, do not contain any metallics and are a mixture of only oxides. The dolo-lime is rich in both CaO and MgO, while lime, as the name suggests, mainly consists out of CaO. The compositions of these fluxes are fixed and never altered. The fluxes are assumed to be added at room temperature and their specific enthalpies are given in Table 10-1 and are calculated with the assumption of a homogeneous metal phase and pure solid oxide phases.

In reality, fluxes are added according to a flux addition profile during the process (an example of such a profile is shown in Figure 7.2). Furthermore, added fluxes will have dissolution kinetics. However, in the current TD BOF model all the fluxes are assumed to be added at the start of the process and no dissolution kinetics are considered, for ease of implementation. This will influence the temperature profile and will also have an effect on the calculated equilibrium. For this equilibrium, it is important to keep in mind that, for most heats, the biggest additions of fluxes are lime and possibly, dolo-lime. The slag will be saturated in CaO, which is one of the important reasons to add oxide rich fluxes, and the effect on the equilibrium is expected to be limited because for the equilibrium the activity is the most important factor and the activity for CaO (s) will be equal to one. The amount of pure precipitated CaO(s) would be different, yet this does not change the activity.

According to AMG observations a yield is considered for each flux. Due to the methods of adding fluxes and the volatility of some components, not all added material will reach the reacting phases in the vessel and some of the material will be removed together with the off gas via e.g. dust.

Oxygen

As mentioned in the discussion of the fluxes, they are a source, be it rather small, of free oxygen. The largest input of oxygen is however, the oxygen jet. This oxygen is assumed to be added to the process at standard conditions.

10.2.3 Considered thermodynamic specifications

Each equilibrium calculation is performed with a Chemapp [2] (V7.3.0) Gibbs free energy minimiser. The thermodynamic data file for the calculation is subtracted from Factsage 7.3 [1]. Four different databases are used: FactPS for the gas phase, FToxid for the slag (both liquid and solids), FTmisc for the liquid metal phase and FSstel for the scrap phases. Following phases were allowed to form at equilibrium:

1. An ideal gas phase
2. CaO(s), MgO(s) and $Ca_3Al_2O_6$(s) from FToxid
3. FSstel-BCC2 for scrap
4. FTmisc-FeLQ for the liquid metal phase
5. FToxid-SLAGA for the liquid slag.
6. FToxid-bC2SA for the calcium silicate phases.
7. FToxid-C2SP for the calcium silicate phase which contains phosphorus.

In the gas phase only species containing either C or O are allowed to form. All the other species in the gas phase are set 'DORMANT'. This has an important influence on the heat balance of the system. In the jet impact zone, very high temperatures (> 2000 °C) can be reached. As a result, a small fraction of iron might evaporate and a considerable amount of heat is lost via the off-gas stream. In reality, this restriction comes down to assuming that any evaporated iron will condense immediately in the same reaction zone. Both CaO (s) and MgO (s) are not modelled as solid solution but as pure substances to reduce the complexity of the model. The solid $Ca_3Al_2O_6$ is only stable at lower temperatures at the beginning of the blow for the current system and from experience it was observed this was the only solid phase containing Al that needed to be considered. The calcium-silicate phases are modelled with solid solutions, due to their importance in the dephosphorisation process. The liquid slag phase is modelled via the SLAGA solution phase, with the assumption that this is one stable phase. The default immiscibility is not used, because it introduced instabilities in the Gibbs Free Energy minimiser for this specific system. However, based on the calculation and analysis of the isothermal sections of the pseudo-ternary phase diagrams, of which some are discussed in Chapter 4, this immiscibility is for the current slag systems only observed at high silicon contents. These silicon contents are not encountered in BOF steelmaking slags. This was also supported with verification calculations for which identical input was used, but one calculation was performed with and one without the default immiscibility. Both types of calculations gave identical results. The liquid metal is described with the FTmisc liquid phase rather than the one in FSstel. The reason for this is that at the start of the PhD research (Factsage 7.1) this was still the advised procedure for high temperature liquid metal in contact with a slag. In the more recent Factsage versions, the FSstel liquid metal phase could also be used for this purpose. Finally, only one scrap phase is considered in the calculation. This BCC scrap phase is considered to be a single phase unlike the default setting for this phase, where an immiscibility is allowed. This scrap phase is set

'DORMANT' for all the calculations apart for the reaction zone in which the scrap melting is considered.

10.2.4 Calculation specifications

The TD BOF model is implemented with a pseudo object oriented structure in Fortran 90, using the Chemapp (V7.3.2) Gibbs Free Energy minimiser to perform equilibrium calculations. The settings for the equilibrium calculation are set via system elements. The '*tqsetc*' routine is used with an imposed enthalpy. Different input files are used giving both information on the incoming material streams for each heat, as well as the dimensions of the different reaction volumes. Apart from the input material streams and the composition for each material stream, also the elemental composition for each heat is required as model input. This elemental input is used to perform a mass balance check for each calculation to ensure the conservation of energy and mass is implemented correctly. For these input files a fixed format is used, given in Appendix B.

10.3 Model concept and mathematical formulation

10.3.1 Calculation at t = 0 s

For every heat, a homogenisation calculation is performed at the start of the process simulation. This calculation considers all the input, apart from the added oxygen gas, which is only blown from t > 0 s onwards. As mentioned earlier, up to three types of scrap can be considered in the system. In a first calculation, the metallic part of all the scrap material is homogenised. After this calculation, only one scrap phase remains with a fixed composition which is used throughout the rest of the process simulation. The oxide mixture, that is also part of the incoming scrap stream, is not considered in this scrap homogenisation and is added, together with the accompanying enthalpy, to the other input products. A general homogenisation is calculated for all this input, creating a first bulk metal and bulk slag phase.

10.3.2 The jet impact zone

The cavity

The jet impact zone (JIZ) is the reaction zone in which the interaction between the oxygen blown on the metal bath and the liquid metal is considered. It is assumed the slag is pushed away by the incoming oxygen jet. Due to the impact of the oxygen jet, a cavity is created that can be described as a parabola in 2D and a paraboloid in 3D. [11], [12] This

is shown in Figure 10.12. Different formulas are proposed in literature to calculate the dimensions of these cavities. [13]

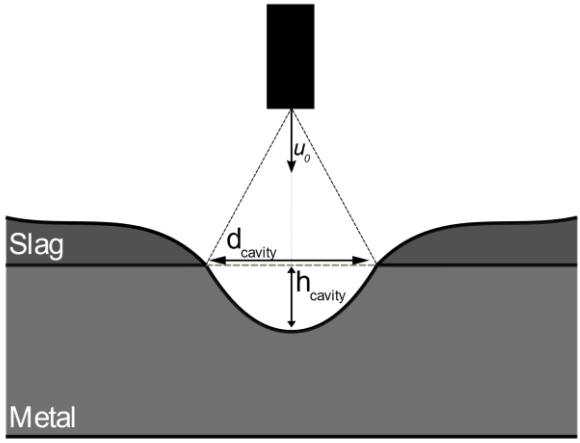

Figure 10.12: Illustration of the formed cavity by the oxygen jet.

The empirical relations of Koria and Lange [14] are used to calculate the dimensions of the paraboloid in the current model. These relations were determined with a lab scale high temperature set up and incorporate the momentum created by the oxygen jet. Recent work by Maia et al. [13] confirmed the applicability of the empirical relations formulated by Koria and Lange [14] in today's steelmaking applications. The formulas to calculate both the diameter and height of the cavity are given in equation 10.2 - 10.4. In these equations *J* is the jet penetrability, h_{cavity} is the height of the formed cavity by a single jet (m) , d_{cavity} is the total diameter of the cavity (m), x is the lance height (m) measured above the liquid bath, α is the inclination angle of a nozzle (indicated on Figure 10.13), ρ is the density of the liquid (kg/m³), g the acceleration due to gravity (m/s²), P_o and P_a are, respectively, the oxygen supply and the ambient pressure (bar). As can be seen on the cross section of the lance tip in Figure 10.13, the diameter of the nozzle is not constant and will vary over the length of the nozzle. In the equations 10.2 and 10.4, d_{nozzle} is the so called throat diameter also indicated on Figure 10.13.

$$J = 1.5887 \left[\frac{0.7854 \cdot 10^5}{\rho\, g} \frac{d_{nozzle}^2}{x^3}\, P_a \left(1.27 \frac{P_o}{P_a} - 1\right)\right]^{0.378} \times \frac{\cos(\alpha)^{0.66}}{[1 \cdot (1 + \sin(\alpha))]^{0.282}} \tag{10.2}$$

$$J = \frac{h_{cavity}}{d_{cavity}} \tag{10.3}$$

$$\frac{h_{cavity}}{x} = 4.469 \left[\frac{0.7854 \cdot 10^5}{\rho\, g} \frac{d_{nozzle}^2}{x^3} P_a \left(1.27 \frac{P_o}{P_a} - 1 \right) \cos(\alpha) \right]^{0.66} \tag{10.4}$$

The lances used at the AMG steel shop are symmetrical with several nozzles which are all positioned under the same inclination angle. According to Koria and Lange [14] the number of created cavities is equal to the number of nozzles in the lance for lances with inclinations angles for each nozzle above 10°. Furthermore, if the inclination angles are larger than 8.5° the jets are noncoalescing. The specifications of the lance at the AMG steel plant, fulfil these requirements and thus, it can be assumed that the total cavity dimension equals the product of the number of nozzles and the cavity created by the oxygen jet of one such nozzle.

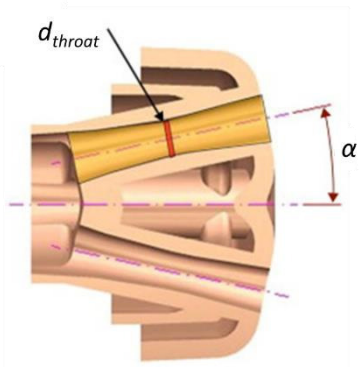

Figure 10.13: Schematic drawing of the cross section of a symmetrical multi nozzle lance tip. Figure taken from [15].

From the calculated cavity dimensions, the contact area between oxygen and steel is calculated as the surface area of the formed paraboloid. However, for the TD BOF model not a surface but a volume is required. The total volume participating in the reaction will depend upon the time step for the calculation as well as the mixing in the metal bath.

The mass transfer coefficient

To account for the mixing, a mass transfer coefficient (k_m) for the bulk metal phase is considered. Different authors have used different methods to either calculate [16], [17] or experimentally [18] determine the mass transfer coefficient in a BOF converter. Values ranging between 0.0004 – 0.02 m/s are reported. A factor 100 difference in this value,

will also result in about a 100 times larger reaction volume and this way largely influence the thermodynamic equilibrium in this reaction zone, since the amount of oxygen is fixed. An accurate determination of the order of magnitude of the mass transfer coefficient is thus crucial. In the current work, the mass transfer coefficient is calculated with the relation proposed by Kitamura [19], shown in equation 10.5. In equation 10.5, ε is the stirring energy (W/kg), T the temperature of metal zone (K), H is the bath depth (cm) and L is the diameter of the furnace (cm). With this expression k_m is calculated in cm/s. The stirring energy due to the oxygen blown via the top lance is calculated with the relation proposed by Nakanishi et al. [20], shown in equation 10.6. In this equation, E_{st} is the stirring energy due to the oxygen blow via the top lance in Watt/ton, Q is the gas flow rate (Nm³/min), W is the weight of the bath (ton), v is the gas velocity at the nozzle exit (m/s) (u_0 in Figure 10.12).

$$\log(k_m) = 1.98 + 0.5 \log\left(\frac{\varepsilon(t) H^2}{100\ L}\right) - \frac{125\ 000}{2.3\ RT} \tag{10.5}$$

$$\varepsilon(t) \cdot 10^{-3} = E_{st}(\mathrm{t}) = \frac{0.0453\ Q(t) v(t)^2 d_{nozzle\ exit} \cos^2(\alpha)}{\mathrm{W}\ x(\mathrm{t})} \tag{10.6}$$

The mixing energy due to bottom stirring is not considered in the calculation of the mass transfer coefficient. Consequently, the calculated mass transfer coefficient is expected to be an underestimation [21] of reality. The stirring energy is time dependent because the lance height will be a function of process time, as well as the volumetric off gas flow of incoming oxygen and thus also the velocity.

From this calculated reaction volume, the mass of steel in the reaction zone is calculated with a fixed density. The amount of oxygen is determined by the size of the calculation step.

10.3.3 The slag – metal interface zone

The interface reaction zone (IF) describes the physical contact between the metal bath and the slag, or slag – metal – emulsion, phase. It is assumed only liquid metal and liquid slag can react with each other. To calculate the dimensions of the reaction volume a flat bath geometry is assumed. The contact area is calculated as the cross section of the industrial converter from which the cross section of the cavity created by the jet impact zone is subtracted. From this area a volume of steel and slag is calculated with a mass transfer coefficient of the phases. For the liquid metal bath, the mass transfer coefficient is calculated as explained previously, using equation 10.5 and 10.6. According to

Kitamura et al. [19] the value for the mass transfer coefficient of the slag can be related to the mass transfer coefficient of steel with a factor 5 to 10. In the current work, the mass transfer coefficient of slag (k_s (m/s)) is calculated according to equation 10.7.

$$k_s(t) = 0.1\, k_m(t) \tag{10.7}$$

This method to calculate the mass transfer of the slag might be straightforward, yet, it does not take any effect of solid particles or viscosity changes of the liquid slag into account. Furthermore, it is important to be aware that the flat interface can be disturbed due the intense mixing of the bath. [22]

From the calculated reaction volumes, the amount of slag and steel is calculated with a fixed density. Within each calculation step (apart from t = 0 s) an IF reaction volume is considered.

10.3.4 The emulsion zone

Due to the impact of the oxygen jet on the metal bath, metal droplets are generated and ejected into the slag. As a result an emulsion zone (EMU) is created [23], that is stated [3], [24], [25] to be crucial for refining due to the large contact area created between the steel and the slag. This phenomenon has been discussed already in detail in 'chapter 2: BOF process and slag' and 'chapter 9: Physicochemical models for the BOF process'. In the current model, the emulsion zone is modelled on macro scale: as a reaction between one metal and one liquid slag phase. The droplet formation and specifications are used to estimate the amount of metal and slag in the reaction volume, yet no individual droplets are assumed for the equilibrium calculation. This means that the emulsion zone will describe the observed average macroscopic effect of the emulsion as one phase, rather than describing the individual effects of droplets on the micro scale.

Amount of metal

Droplet generation and size

The amount of droplets generated in each time step is calculated with the blowing number theory [26]–[28]. In the current work, the blowing number (N_B) as formulated by Li and Harris [27] and Subagyo et al. [26], shown in equation 10.8, is used.

$$N_B = \frac{\rho_G u_G^2}{2\sqrt{\sigma g \rho_L}} \tag{10.8}$$

In this equation ρ_G and ρ_L are the densities (kg/m³) of, respectively, gas and liquid. The surface tension (N/m) of the liquid metal is denoted by σ, g is the gravitational acceleration (m/s²) and u_G is the critical gas velocity (m/s). This velocity is the critical tangential velocity at the liquid metal interface and is related to the axial velocity (m/s) of the impinging gas jet from the lance, u_i, according to the relation described by Li and Harris [27],shown in equation 10.9. The value of 0.447 to link the critical tangential and the axial velocity was determined by Deo and Bloom [29] based on fitting of plant data.

$$u_g = 0.447\, u_i \tag{10.9}$$

A critical unknown value required at this point, is this axial velocity of the impinging gas jet. Process data yields information on the volumetric gas flow. From this property, in combination with the nozzle diameters, it is possible to estimate the gas velocity at the nozzle outlet (u_0). Yet, calculation of u_i from this u_0 value is complex and challenging. In the BOF process, the oxygen gas is supersonically blown. According to literature [30], the gas jet that impinges the molten metal surface has, in general, a Mach number greater than two. Sumi et al. [31] mention that even though the behaviour of a supersonic jet emerging from a nozzle has been thoroughly investigated in the past, this behaviour is not fully understood at the high ambient temperatures in the BOF process (> 1200 °C). Numerical modelling is a possible tool to solve this issue. However, numerical modelling of the supersonic jet was not an available resource in the current work. Hence, empirical relations have to be used. The overview of the calculated impact velocity as function of the lance height as calculated by Rout et al. [28], is given in Figure 10.14. In this figure, different empirical correlations to calculate the impact velocity, ranging from simple to advanced, are compared. The correlations of Standish et al. [32] and Subagyo et al. [26] are simple correlations and identical apart from the used constants. Whereas Standish et al. [32] used a constant suited for cold models, Subagyo et al. [26] used a constant suited for high temperature plant data. The correlations proposed by Li et al. [33], Deo and Bloom [29] and Sumi et al. [31] are more complex and require either knowledge of the ambient temperature of the gas at the metal surface. Furthermore, also the density of the gas at the nozzle exit needs to be known.

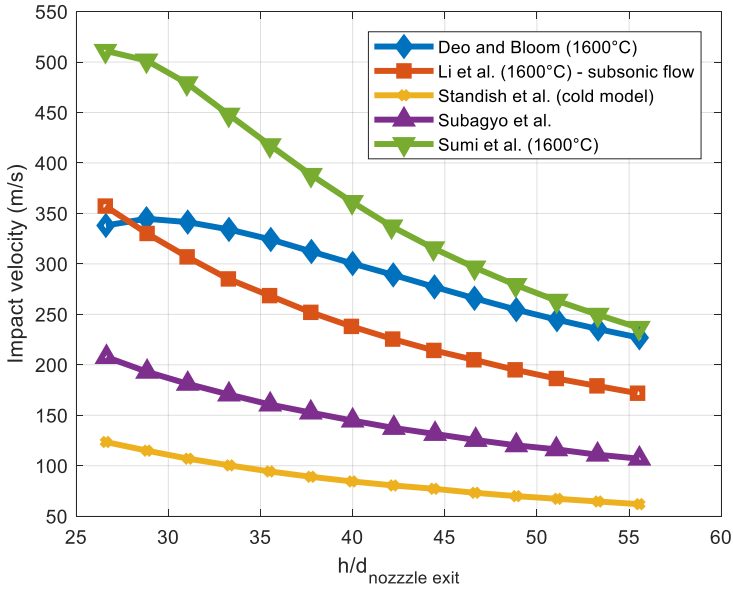

Figure 10.14 Comparison of the impact velocity of the gas in function of the lance height (h). Reconstructed with data from Rout et al. [28].

In the current work, the relation described by Subagyo et al. [26] is used, for its simplicity. The more complex, and quoted [28] to be more accurate, relations require the knowledge of more parameters which are unknown for the current system. Even more so, since the reaction volumes are calculated as input for the TD BOF model, rather than instantaneously calculated, to reduce modelling complexity. The free axial jet velocity at the impingement point is calculated with the correlation given in equation 10.10. In this equation, *a* is an empirical parameter which was determined [26], based upon plant data, to be 0.0393 for the BOF process.

$$u_i(t) = u_0(t)\frac{0.97}{\frac{2ax(t)}{d_{nozzle_{exit}}} + 0.29} \tag{10.10}$$

The relation between the blowing number and the droplet generation rate per unit volume of blown gas is given in equation 10.11. In this equation R_B ,is the number of droplets generated (kg/min) and F_G is the volumetric gas flow rate (Nm³/min). This relationship was empirically established under constant lance height.

$$\frac{R_B}{F_G} = \frac{(N_B)^{3.2}}{[2.6e6 + 2e(-4)(N_B)^{12}\ ]^{0.2}} \tag{10.11}$$

It is assumed all the droplets are uniform and spherical in size. The droplet diameter is set constant as 2 mm. This value for the average droplet diameter is used in multiple research [28], [34] and corresponds to experimental data [35], [36]. Combination of this assumption and the calculated number of droplets, allows to determine the amount of liquid metal ejected from the metal bath into the EMU reaction zone in each calculation step.

Droplet residence time

The droplet residence time in the emulsion phase is another important parameter to determine the amount of metal in the emulsion zone. Different authors[23], [37]–[39] report residence times, determined with laboratory experiments or from plant estimations, ranging between 60 to 120 s. This circulation time was modelled by Brooks et al. [37] based on a ballistic motion principle. The residence time of the droplet is, among other things, a function of its size and density. Brooks et al. [37] concluded that dense droplets have very short residence times of less than 1 s. Yet, due to the droplet swelling/bloating phenomenon [40] and hence the reduction of the droplet's density as result of decarburisation of the metal, the residence times increase significantly to 20 - 200 s.

In the current model the time step is a model parameter. However, usually time steps of about 8 s (referring to circa. 0.2 ton O_2) are used to combine a sufficiently fast and accurate enough calculation. It is assumed that for all the droplets generated, a variation in residence time will exist. Some droplets will have very short residence times, which are smaller than the time step of the calculation, while others might have residence times up to 120 s and thus, exceeding the time step of the calculation. Due to the description of the emulsion zone as the equilibrium reaction between one metal and slag phase, rather than assuming individual droplets, the metal in the reaction zone is considered as a bulk phase anyway. This means that the result will describe rather the average macro scale effect than the individual droplet micro scale effects. Based on these arguments, it is assumed that the residence time of the droplets can be modelled via the fraction of metal that is left in the reaction zone after the equilibrium calculation. This fraction is denoted as f_{emu}, after the equilibrium reaction $100\ (1 - f_{emu})$ % of the metal in the reaction volume will return to the bulk metal phase, while $100\ f_{emu}$ % remains in the emulsion phase. A value for f_{emu} will be determined based upon fitting of the model results to the industrial observations.

Total amount of metal

The total amount of metal in the emulsion zone for a random calculation step i, is given in equation 10.12. In this equation, $m_{metal}^{emu}(i)$ is the amount of metal in the reaction volume for calculation step i, $m_{new\ droplets}(i)$ is the amount of metal originating from the newly generated metal droplets in the calculation step and $m_{metal}^{emu,R}(i-1)$ is the mass of metal which was the result of the emulsion zone equilibrium calculation in the previous calculation step, hence the superscript 'R'.

$$m_{metal}^{emu}(i) = m_{new\ droplets}(i) + f_{emu}\, m_{metal}^{emu,R}(i-1) \tag{10.12}$$

Even though both $m_{new\ droplets}$ and $m_{metal}^{emu,R}$ are called liquid metal, it is important to be aware that the composition of these two types of metal might be completely different. Whereas $m_{new\ droplets}$ is metal from the bulk metal phase, thus high C and P contents, $m_{metal}^{emu,R}$ is refined metal already present in the emulsion zone for which the C and P content will be lower compared to the bulk in physically relevant cases. It is estimated that 10% to 25% of the metal in the BOF vessel is present in the slag-metal emulsion. [23]

Amount of slag

To calculate the maximal amount of slag in this reaction zone, it is assumed the droplets are homogeneously distributed in the slag phase, and there is no interaction between the different metal droplets. For one droplet, the amount of slag that can react with the droplet is calculated from the time step, the mass transfer coefficient of the slag phase and the surface area of the droplets. The total amount of slag participating in the EMU reaction zone, is hence calculated as the product of the amount of slag per droplet and the total number of metal droplets. From this reasoning the expression in equation 10.13 is derived, to calculate the amount of slag in this reaction zone.

$$m_{slag}^{emu} = 3000\, \frac{\rho_{slag}}{\rho_{metal}}\, k_s\, m_{metal}^{emu} \tag{10.13}$$

The slag is formed during the process, due to the oxidation of iron and silicon and the dissolution of the fluxes. Unlike the steel bulk phase, which is always present in abundance, the slag and liquid fraction will vary from very small amounts till 20 – 30 ton slag at the end of the process (on average). As a consequence, the calculated m_{slag}^{emu} is rather a maximum value. For certain calculations, the amount of liquid slag present in the system and thus the slag available to react will be lower than the calculated value. In such cases, all the available slag is assumed to react. The amount of slag considered in

the emulsion zone reaction is thus the minimum of m_{slag}^{emu} and the amount of liquid slag present (after considering the IF reaction zone).

10.3.5 Scrap melting zone

On Figure 10.15, both a typical scrap composition and a hot metal (HM) composition are indicated on the Fe-C phase diagram. Due to this large difference in composition (C content), the scrap melting is a complex process compared to melting process of materials with identical composition and only a difference in temperature. Generally, scrap melting due to the difference in carbon composition is known as diffusion melting, whereas scrap melting due to heat transfer (when the scrap has identical C content as the hot metal, or when the hot metal temperatures exceeds the scrap melting temperature) is known as forced scrap melting. Details on these processes and the stages in which they happen can be found in the recent (2019) review on scrap melting by Penz and Schenk [41]. The final scrap melting behaviour will be influenced by the dimensions of the used scrap, its weight, its carbon content and the set-up of the BOF-process.

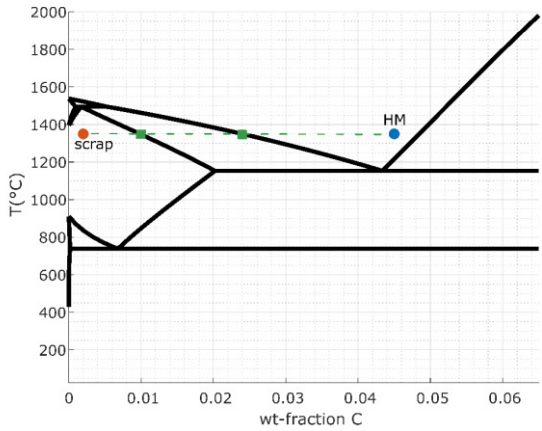

Figure 10.15: Fe-C phase diagram with HM composition and Scrap-composition point indicated at traditional HM charging temperatures.

In the current model, solid pig iron is not considered. Consequently, all the considered scrap types have carbon contents considerably lower than the carbon content of the liquid hot metal. The scrap melting is assumed to be only governed by the thermodynamic driving force due the difference in carbon content between the scrap phase and the metal bulk phase. As a consequence, size and weight of scrap is not considered. At t = 0 s, the uniform composition of the scrap phase is determined, as discussed earlier. However, all the scrap is assumed not to be part of the thermodynamic

system at this point in the model. In each calculation step, the maximal amount of scrap than can dissolve in the metal bath is calculated. For this calculation, different thermodynamic settings are used compared to the other equilibrium calculations in the model. All possible phases (both solutions and solids) are set 'DORMANT' apart from FSstel-BCC2 and FTmisc-FeLQ. Once this maximal amount is determined, this amount of material (with accompanying composition and enthalpy) is included to the thermodynamic system. It is assumed the scrap dissolves in the metal bulk phase.

10.3.6 Homogenisation

For each calculation step, a homogenisation (HOM) calculation is performed for the bulk metal phase as well as for the slag. This is an equilibrium reaction between the phases formed in the reaction zones and the liquid metal or liquid slag and solid oxides which are not part of any reaction zone volume. In Figure 10.16, the concept of homogenisation calculations is shown. For simplicity, only one reaction zone, the jet impact zone, is considered. A certain amount of liquid metal, with composition and enthalpy of the previous calculation step $(i-1)$, is used as reaction volume for JIZ. In this reaction zone, equilibrium is assumed. As a result, a new equilibrium state is calculated containing: gas, liquid metal and oxides. The gas is immediately removed from the system. The newly formed liquid metal, '*Liquid metal JIZ*' has a different composition and potentially also different temperature, than the original bulk metal. In the homogenisation reaction, the equilibrium between this metal from the reaction zone and the left over bulk metal is calculated. The result is a new composition and temperature for the bulk metal of calculation step i compared to $(i-1)$. This principle is also explained in Figure 10.10. Analogous reasoning applies to the slag bulk phase.

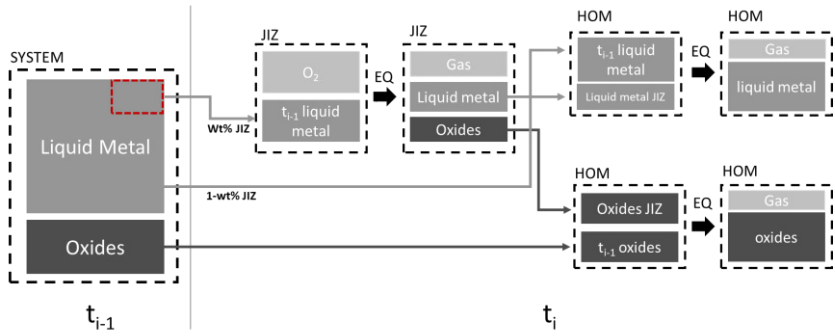

Figure 10.16: Schematic concept of the homogenisation calculations.

10.3.7 Heat transfer between metal and slag phase

After homogenisation, two bulk phases with each a unique temperature are present in the simulated vessel. Up till this point in the calculation cycle, the only possibility for heat transfer is via chemical equilibrium reactions. In a reaction zone, a new equilibrium state is calculated with a new temperature. As a result, after homogenisation the new bulk metal and slag will have a different composition and temperature than the state in the previous calculation step. In reality, due to the difference in temperature between the two phases, a heat transfer will exist between them. Additionally, without integration of a heat transfer, the temperature can only change via the equilibria phases in the reaction zones. To understand the consequence of this, let's have a closer look at a simplified example with only the jet impact reaction zone (given in Figure 10.16). If we would assume an extreme case with only very little metal in the reaction zone then here is an abundance of oxygen compared to the metal phase and as a result, a lot of iron is oxidised. In such a case, the new equilibrium state will be a CO rich gas phase, oxides with a very high temperature due to the strongly exothermic character of the iron oxidation and there is no or little refined metal left at equilibrium. Subsequently, a homogenisation reaction is performed first for the metal phase. However, little metal is formed in the JIZ, and thus the bulk metal composition does not change, nor does its temperature increase. Next, a homogenisation of the slag phase is performed. Due to the high temperature of the oxide phase formed in JIZ, the bulk slag phase increases in temperature. At the end of the process simulation, the temperature of the slag phase is extremely high (> 1800°C), while the metal phase has nearly not increased in temperature compared to the original hot metal temperature. Even though this is an extreme example, it demonstrates the necessity to implement an additional heat transfer between the bulk phases. This is supported by the result shown in Figure 10.17. Without a heat transfer between the metal and slag bulk phase, a strong dependency can be observed between the amount of metal in the JIZ and the final steel temperature for a heat. This dependency is not related to the other reaction volume sizes. Due to the implementation of heat transfer, this dependency is strongly decreased.

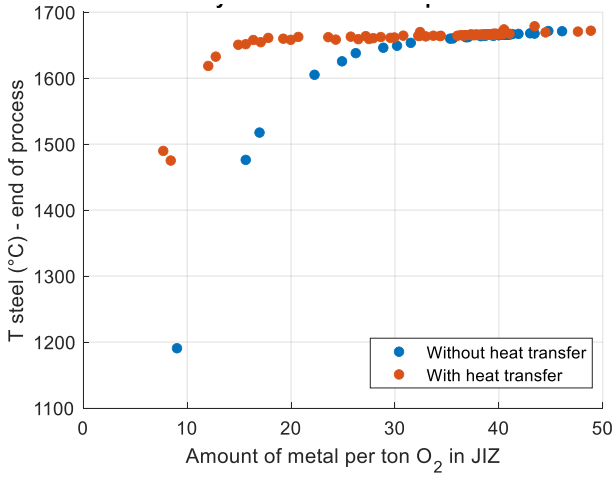

Figure 10.17: The effect of the amount of metal in the JIZ on the calculated steel temperature at the end of the process for one heat.

A rather simple, pragmatic heat transfer is incorporated in the model. A flat bath surface is assumed between the metal and the slag phase. It is assumed the heat transfer can be described via forced convection with a simplified convection coefficient $h = \frac{k'}{\delta}$ (W/m² K) with k' (W/m K) the conduction coefficient and δ (m) the thermal boundary layer thickness. To calculate this thermal boundary layer thickness, the Reynolds (Re) number of the phases in the BOF process is required. In literature [42], [43] different values can be found for the Re number of the BOF process ranging between 10^7 – 10^9. A value of 10^9 will be used in this work due to the similar geometrical set up and blowing parameters in the work of Singh et al. [43] and the BOF process at the ArcelorMittal Ghent steel shop. For the current estimations of the thermal boundary layer it is assumed this value holds both for the steel and slag phase. For laminar flow across a flat plate, the expressions to calculate the thermal boundary layer thickness are well known. [44] Because they are dependent on the Prandtl number, the value for the steel and the slag phase will be different. However, for turbulent regimes, which clearly applies to the BOF process since Re > 10^3, determining thermal boundary layer thickness is much more complex. [44], [45] In Table 10-2 some values for thermal boundary layers are calculated for different situations. Based on these results, a constant thermal boundary layer thickness of 100 µm is assumed both for the slag and steel phase.

Table 10-2: Calculated boundary layer thickness

	$\boldsymbol{\delta\ (\mu m)}$
Laminar, steel *[44]*	811
Laminar, slag *[44]*	144
Turbulent *[45]* *(both steel and slag)*	55

The amount of heat transfer from the slag to the steel phase is calculated with equation 10.14. It is assumed the heat transfer only happens in the thermal boundary layer. Outside this layer, the heat redistributes immediately (in the temperature homogenisation step) and the temperature of the phase is homogeneous.

$$Q = 4.61 \cdot 10^5 \left(T_{slag}^{hom} - T_{steel}^{hom}\right) \Delta t \qquad (10.14)$$

10.3.8 Temperature homogenisation

As a final step, the new temperatures of the slag and metal phase are calculated with integration of the heat transported from the slag towards the steel phase. Potentially, some gas might form during the temperature homogenisation. If this is the case, the gas is immediately removed from the system and the mass balance of the system is updated.

10.4 Summary of the main model assumptions

During the model description a lot of assumptions are made. The most important ones are summarized here, since they will be crucial in evaluation of the model results.

- The system consists out of nine components: Fe, C, Mn, P, Si, Al, Mg, Ca and O.
- All fluxes are added immediately at the start of the process. There is no delay due to dissolution assumed.
- Both the CaO and MgO rich solid phases are described thermodynamically as pure solid phases rather than as solid solutions. It is possible that for a certain set of conditions (composition and temperature) the solution phase would have been stable, while the pure compound is not yet. However, it is assumed that for most of the cases, a system in which the solid solution precipitates out of the slag, this will also be the case for the pure compound. Although, numerical differences might exists between both conditions. As can be seen on Figure 10.18 for CaO, the effect of this assumption is minor on the isothermal section

of the pseudo-ternary phase diagram. However, from a computational perspective assuming pure solids is beneficial for the TD BOF model implementation.

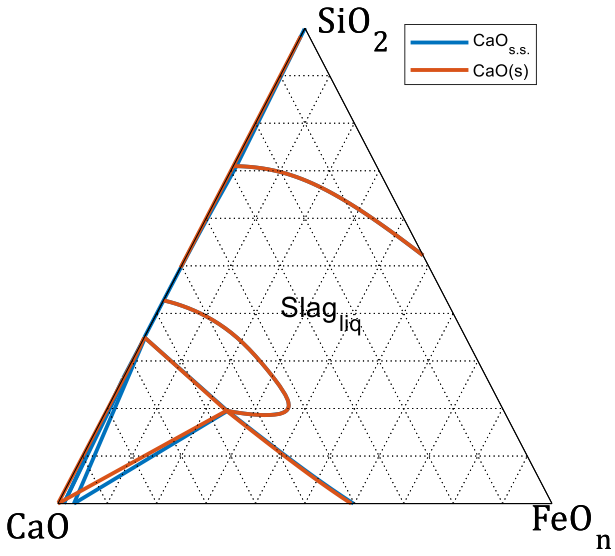

Figure 10.18: Basis phase diagram at 1650 °C calculated with two different thermodynamic settings: CaO described as solid solution and as pure solid.

- The gas phase only contains C and O (all possible species are allowed). Thermodynamically the gas phase is described as an ideal gas.
- The formed gas leaves the vessel immediately. There is no interaction with any other reaction zone or phase present in the vessel. The effect of post combustion is thus also not integrated in the model.
- Heat losses to the environment are only considered via the off gas. Losses via the vessel or due to radiation are not considered.
- The mass transfer coefficient for the steel phase mainly depends on the mixing energy for which only the momentum due to the top blown oxygen jet is considered. Bottom stirring is not taken into account in this model.
- The mass transfer coefficient of the slag phase is assumed to be related to the mass transfer coefficient of the steel phase with a constant factor 0.1 during the complete process. Variations in the slag viscosity and liquid fraction are not considered even though in reality there is a considerable variation calculated for these properties, as shown in Figure 10.19.

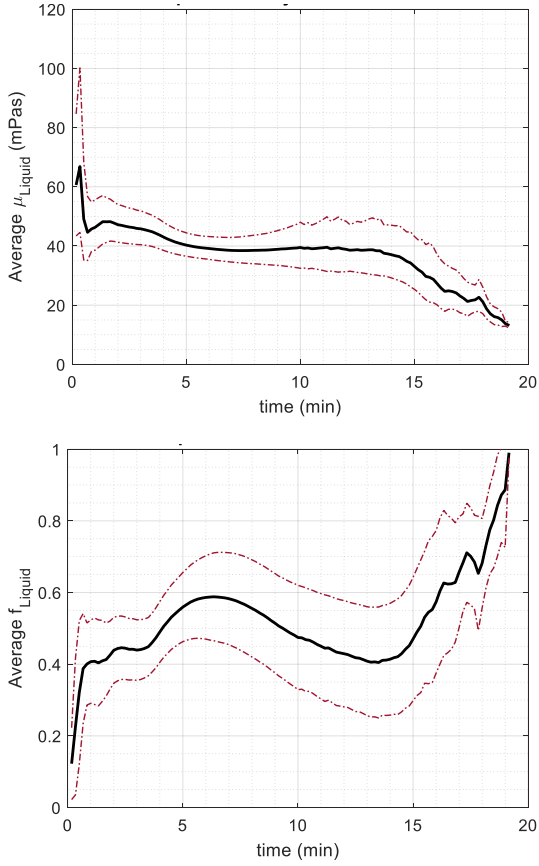

Figure 10.19: Evolution of (top) the average calculated liquid viscosity and (bottom) liquid fraction for 96 AMG heats. The black line is the average, the red dotted ones are the standard deviation.

- All the physical properties (e.g. density, surface tension, etc.) of both the metal and the slag are assumed to be constant during the complete process. Thus, they are both temperature and composition independent. The used values for these properties are given in Table 10-3. Apart from the density of the slag, the values are taken from Rout et al. [11]. The slag density is taken as the average slag density from slag evaluations calculated with the model described in 'chapter 7: Model to calculate slag compositions during blow of historical heats'. The value was verified with the slag densities calculated from the evolutions reported in literature [3], [46].

Table 10-3: Overview of the default material properties in the TD BOF model

Property	value	Unit
ρ_{metal}	7000	kg/m³
ρ_{slag}	3100	kg/m³
k_{metal}	40.0	W (m K)$^{-1}$
k_{slag}	1.7	W (m K)$^{-1}$
σ_{metal}	1.7	N m^{-1}

10.5 Conclusion

At the start of this chapter the possibilities to examine the industrial BOF process via thermodynamics are discussed. Even though, simple thermodynamic calculations give good indications of the direction in which the process evolves, their description of the evolution of the slag and steel phase during the process is not accurate. A model that not only considers thermodynamics but also kinetics is required. A thermodynamic based model with integration of kinetics via different reaction zones, known as an EERZ – model was developed for this purpose.

10.6 References

[1] C. W. Bale *et al.*, "FactSage thermochemical software and databases, 2010–2016," *Calphad*, vol. 54, pp. 35–53, 2016.

[2] S. Petersen and K. Hack, "The thermochemistry library ChemApp and its applications," *Int. J. Mater. Res.*, vol. 98, no. 10, pp. 935–945, Oct. 2007, doi: 10.3139/146.101551.

[3] Publications Office of the European Union, "Imphos : improving phosphorus refining.," Dec. 14, 2011. https://publications.europa.eu/en/publication-detail/-/publication/8aecbb7c-f77f-4ee7-bc38-9ebb13b52faf/language-en (accessed Nov. 06, 2018).

[4] M.-A. Van Ende and I.-H. Jung, "Applications of Thermodynamic Database to the Kinetic Steelmaking Process Simulations," in *Computational Materials System Design*, D. Shin and J. Saal, Eds. Cham: Springer International Publishing, 2018, pp. 47–66.

[5] M.-A. Van Ende and I.-H. Jung, “A Kinetic Ladle Furnace Process Simulation Model: Effective Equilibrium Reaction Zone Model Using FactSage Macro Processing,” *Metall. Mater. Trans. B*, vol. 48, no. 1, pp. 28–36, Feb. 2017, doi: 10.1007/s11663-016-0698-6.

[6] M.-A. Van Ende and I.-H. Jung, “A kinetic process Simulation Model for Basic Oxygen Furnace (BOF): Importance of slag chemistry for BOF operation,” presented at the Asia Steel International, Yokohama, Japan, 2015.

[7] M.-A. van Ende, Y.-M. Kim, M.-K. Cho, J. Choi, and I.-H. Jung, “A Kinetic Model for the Ruhrstahl Heraeus (RH) Degassing Process,” *Metall. Mater. Trans. B*, vol. 42, no. 3, pp. 477–489, Jun. 2011, doi: 10.1007/s11663-011-9495-4.

[8] A. Harada, N. Maruoka, H. Shibata, and S. Kitamura, “A Kinetic Model to Predict the Compositions of Metal, Slag and Inclusions during Ladle Refining: Part 1. Basic Concept and Application,” *ISIJ Int.*, vol. 53, no. 12, pp. 2110–2117, 2013, doi: 10.2355/isijinternational.53.2110.

[9] J. H. Shin, Y. Chung, and J. H. Park, “Refractory–Slag–Metal–Inclusion Multiphase Reactions Modeling Using Computational Thermodynamics: Kinetic Model for Prediction of Inclusion Evolution in Molten Steel,” *Metall. Mater. Trans. B*, vol. 48, no. 1, pp. 46–59, Feb. 2017, doi: 10.1007/s11663-016-0734-6.

[10] A. N. Grundy *et al.*, “A Kinetic and Thermodynamic Description of the Steel Making Process using Thermo-Calc and the CALPHAD Database TCOX,” p. 9.

[11] B. K. Rout, G. Brooks, M. A. Rhamdhani, Z. Li, F. N. H. Schrama, and J. Sun, “Dynamic Model of Basic Oxygen Steelmaking Process Based on Multi-zone Reaction Kinetics: Model Derivation and Validation,” *Metall. Mater. Trans. B*, vol. 49, no. 2, pp. 537–557, Apr. 2018, doi: 10.1007/s11663-017-1166-7.

[12] D. Mombelli *et al.*, “Model for Phosphorus Removal in LD Converter and Design of a Valuable Operative Practice,” *Steel Res. Int.*, vol. 89, no. 5, p. 1700467, 2018.

[13] B. Maia, R. Tavares, S. Balajee, and J. Cappel, “Practical Approach of Penetration Index Equations for Use in BOF Blowing Pattern Design,” in *Iron & Steel Technology*, Mar. 2019, vol. 16.

[14] S. C. Koria and K. W. Lange, “Penetrability of impinging gas jets in molten steel bath,” *Steel Res.*, vol. 58, no. 9, pp. 421–426, Sep. 1987, doi: 10.1002/srin.198700241.

[15] B. T. Maia, R. K. Imagawa, A. C. Petrucelli, and R. P. Tavares, “Effect of blow parameters in the jet penetration by physical model of BOF converter,” *J. Mater. Res. Technol.*, vol. 3, no. 3, pp. 244–256, Jul. 2014, doi: 10.1016/j.jmrt.2014.06.010.

[16] Y. Lytvynyuk, J Schenk, M. Hiebler, and H. Mizelli, “Thermodynamic and kinetic modelling of the de- vanadization process in the steelmaking converter,” presented at the 6th EOSC, Stockholm, Sweden, 2011, doi: 10.13140/2.1.1126.7848.

[17] Y. Ogasawara, Y. Miki, Y. Uchida, and N. Kikuchi, “Development of high efficiency dephosphorization system in decarburization converter utilizing FetO dynamic control,” *ISIJ Int.*, vol. 53, no. 10, pp. 1786–1793, 2013.

[18] S. K. Ajmani and A. Chatterjee, “Cold model studies of mixing and mass transfer in steelmaking vessels,” *Ironmak. Steelmak. Lond.*, vol. 32, no. 6, pp. 515–527, Dec. 2005.

[19] S. Kitamura, T. Kitamura, K. Shibata, Y. Mizukami, S. Mukawa, and J. Nakagawa, “Effect of stirring energy, temperature and flux composition on hot metal dephosphorization kinetics,” *ISIJ Int.*, vol. 31, no. 11, pp. 1322–1328, 1991.

[20] K. Nakanishi, K. Saito, Y. Kato, H. Nakamura, K. Suzuki, and T. Emi, “Stirring Intensity and Metallurgical Reactions in Combined Blowing,” *Jpn. Soc. Promot. Sci. 19th Comm. Steelmak.*, pp. 19–10303, 1980.

[21] A. K. Shukla, B. Deo, S. Millman, B. Snoeijer, A. Overbosch, and A. Kapilashrami, “An Insight into the Mechanism and Kinetics of Reactions In BOF Steelmaking: Theory vs Practice,” *Steel Res. Int.*, vol. 81, no. 11, pp. 940–948, Nov. 2010, doi: 10.1002/srin.201000123.

[22] Subagyo, Brooks, and Coley, “Interfacial area in top bloxn oxygen steelmaking,” in *Ironmaking Conference Proceedings*, 2002, p. 14.

[23] G. Snigdha, B. N. Bharath, and N. N. Viswanathan, “BOF process dynamics,” *Miner. Process. Extr. Metall.*, vol. 128, no. 1–2, pp. 17–33, Apr. 2019, doi: 10.1080/25726641.2018.1544331.

[24] J. Martinsson and D. Sichen, “Decarburization of Pig Iron in Synthetic BOF Converter Slag,” *ISIJ Int.*, vol. 59, no. 1, pp. 46–50, Jan. 2019, doi: 10.2355/isijinternational.ISIJINT-2018-472.

[25] H. W. Meyer, W. F. Porter, G. C. Smith, and J. Szekely, “Slag-Metal Emulsions and Their Importance in BOF Steelmaking,” *JOM*, vol. 20, no. 7, pp. 35–42, Jul. 1968, doi: 10.1007/BF03378731.

[26] Subagyo, G. A. Brooks, K. S. Coley, and G. A. Irons, “Generation of Droplets in Slag-Metal Emulsions through Top Gas Blowing,” *ISIJ Int.*, vol. 43, no. 7, pp. 983–989, Jul. 2003, doi: 10.2355/isijinternational.43.983.

[27] R. Li and R. L. Harris, “Interaction of gas jets with model process liquids,” in *Pyrometallurgy 95 Conference Proceedings*, 1995, p. 107.

[28] B. K. Rout, G. Brooks, Subagyo, M. A. Rhamdhani, and Z. Li, “Modeling of Droplet Generation in a Top Blowing Steelmaking Process,” *Metall. Mater. Trans. B*, vol. 47, no. 6, pp. 3350–3361, Dec. 2016, doi: 10.1007/s11663-016-0773-z.

[29] B. Deo and R. Boom, *Fundamentals of steelmaking metallurgy*. Prentice-Hall, 1993.

[30] N. Y. Doh, “Multiphysics modelling of the steelmaking converter,” Jan. 2012, Accessed: Jul. 30, 2019. [Online]. Available: https://hal.univ-lorraine.fr/tel-01749372.

[31] I. Sumi, Y. Kishimoto, Y. Kikuchi, and H. Igarashi, “Effect of High-temperature Field on Supersonic Oxygen Jet Behavior,” *ISIJ Int.*, vol. 46, no. 9, pp. 1312–1317, 2006, doi: 10.2355/isijinternational.46.1312.

[32] N. Standish and Q. L. He, “Drop Generation due to an Impinging Jet and the Effect of Bottom Blowing in the Steelmaking Vessel,” *ISIJ Int.*, vol. 29, no. 6, pp. 455–461, 1989, doi: 10.2355/isijinternational.29.455.

[33] Q. Li, M. Li, S. B. Kuang, and Z. Zou, “Computational study on the behaviours of supersonic jets and their impingement onto molten liquid free surface in BOF steelmaking,” *Can. Metall. Q.*, vol. 53, no. 3, pp. 340–351, Jul. 2014, doi: 10.1179/1879139514Y.0000000124.

[34] A. Kadrolkar and N. Dogan, “Model Development for Refining Rates in Oxygen Steelmaking: Impact and Slag-Metal Bulk Zones,” *Metals*, vol. 9, no. 3, p. 309, Mar. 2019, doi: 10.3390/met9030309.

[35] C. Cicutti *et al.*, “Sudy of slag-metal reactions in an LD-LBE converter,” in *Proceedings of the Sixth International Conference on Molten Slags, Fluxes and Salts*, Stockholm-Helsinki, 2000, pp. 69–78.

[36] I. Hahn and D. Neuschütz, “Investigations on the ejection of steel and slag droplets from gas-stirred steel melts,” 2000.

[37] G. Brooks, Y. Pan, and K. Coley, “Modeling of trajectory and residence time of metal droplets in slag-metal-gas emulsions in oxygen steelmaking,” *Metall. Mater. Trans. B*, vol. 36, no. 4, pp. 525–535, 2005.

[38] J. SCHOOP, S. J, R. W, and M. G, “REACTIONS OCCURRING DURING THE OXYGEN TOP-BLOWN PROCESS AND CALCULATION OF METALLURGICAL CONTROL PARAMETERS.,” *React. Occur. Oxyg. TOP-BLOWN PROCESS Calc. Metall. CONTROL PARAMETERS*, 1978.

[39] P. Kozakevitch and T. G. John, “Foams and emulsions in steelmaking,” *JOM*, vol. 21, no. 7, pp. 57–68, 1969.

[40] N. Dogan, G. A. Brooks, and M. A. Rhamdhani, “Comprehensive model of oxygen steelmaking part 2: application of bloated droplet theory for decarburization in emulsion zone,” *ISIJ Int.*, vol. 51, no. 7, pp. 1093–1101, 2011.

[41] F. M. Penz and J. Schenk, “A Review of Steel Scrap Melting in Molten Iron-Carbon Melts,” *Steel Res. Int.*, vol. 90, no. 8, p. 1900124, 2019, doi: 10.1002/srin.201900124.

[42] M. J. Luomala *et al.*, “Physical Model Study of Selective Slag Splashing in the BOF.,” *ISIJ Int.*, vol. 42, no. 11, pp. 1219–1224, 2002, doi: 10.2355/isijinternational.42.1219.

[43] V. Singh, J. Kumar, C. Bhanu, S. K. Ajmani, and S. K. Dash, “Optimisation of the Bottom Tuyeres Configuration for the BOF Vessel Using Physical and Mathematical Modelling,” *ISIJ Int.*, vol. 47, no. 11, pp. 1605–1612, 2007, doi: 10.2355/isijinternational.47.1605.

[44] J. R. (viaf)56695352 Welty, G. L. Rorrer, C. E. (viaf)49307720 Wicks, and R. E. (viaf)281796437 Wilson, *Fundamentals of momentum, heat, and mass transfer*, 5th ed. Chichester : Wiley, 2008.

[45] H. Schlichting, *Boundary-layer theory*. New York: McGraw-Hill, 1979.

[46] E. T. Turkdogan, *Fundamentals of steelmaking*. London: The Institute of Materials, 1996.

11 Fitting of TD BOF model parameters and model validation

In the previous chapter a thermodynamically based model to simulate the BOF process (TD BOF model) was described. The current chapter explains the necessity to define a set of model parameters which can be varied to obtain a good fit between the model and the industrially measured properties. The methodology to fit the model to industrial data is explained and the obtained results are discussed. A new dataset of heats is defined for validation purposes. The TD BOF model is validated and both its strong and weak points are discussed.

11.1 Motivation for fitting

To verify the possible predictive nature of the described TD BOF model, a set of five already executed heats (historical heats) is selected. These heats are selected based on a regular blowing practice (e.g. no blowing interruptions) and minimal amount of material input streams. The main variation for the selection was the silicon content of the liquid hot metal and the final measured dissolved oxygen of the steel phase. In the model description it is mentioned that the value for the recirculation metal in the emulsion zone (f_{emu}) needs to be fitted to industrial plant data. For a first trial calculation, the value is set at 50%. A calculation step of 0.2 ton O_2 is used which corresponds to 110 till 130 calculation steps.

The results of the TD BOF model are compared to the measured plant data. An example is shown in Figure 11.1. During the industrial process, the volumetric flow of the off gas is measured, as well as its composition. With this combination, a decarburisation profile is constructed during the process for monitoring purposes. This decarburisation profile gives insight in the amount of carbon removed from the vessel at any point in the process. The decarburisation profile calculated with the TD BOF model is compared to the measured one for the second heat of the dataset. The TD predicted profile is much lower than the measured one. As a result, the carbon content of the steel at the end of the simulation is still about 3 wt%, while values around 500 ppm (always on weight basis) or less are observed in real industrial practice. Furthermore, it is observed the final steel

temperatures are predicted around 1100°C. This is much lower than the real steel temperatures around 1650°C. The reason for these results is the ratio of steel over O_2 in the jet impact zone (JIZ). The value of about 1.5 ton of steel per ton oxygen gas, is too small and will result in complete oxidation of the metal in the JIZ. As a result, the equilibrium state of the JIZ only contains gas, although this is only a little amount due to the small amount of C present in the reaction zone, and a liquid slag rich in FeO_n. The calculated equilibrium temperatures for this reaction zone are around 2450 °C.

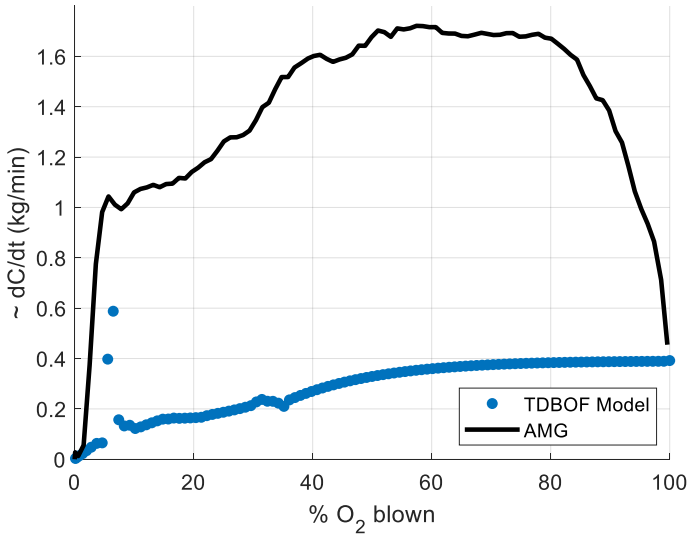

Figure 11.1: Comparing the modelled results to the industrially measured results for the decarburisation profile/rate of one heat. The decarburisation rate (dC/dt) is normalised using a fixed constant value instead of using the conventional normalisation method, hence ~dC/dt.

The results of this first calculation indicate that using theoretical and empirical formulae to estimate the dimensions of the reaction volumes might not be accurate or suited enough to model the real process kinetics. To calculate the dimensions of the cavity at the jet impact, the empirical relations of Koria and Lange [1] are used. Even though the applicability of these relations for steel applications have been stated [2], this does not necessarily mean they are applicable for the EERZ model. Due to the physical background of these relations compared to other expressions, which often contain scaling constants that are plant specific, they are very suitable to evaluate qualitative changes in the dimensions of the cavity due to process or geometrical changes (e.g. effect of difference in lance heights). Yet, for an EERZ model the dimensions of the reaction volume are

crucial because they will govern the complete equilibrium state of the reaction zone and hence, influence the outcome of the model to a great extent.

Increasing the ratio of metal over oxygen gas in the JIZ from 1.5 to 15, which corresponds to the stoichiometric amount of C for the considered calculation step, gives much more reliable results for the process, as is shown in Figure 11.2. On this figure, also the effect of variation of the amount of metal circulating in the emulsion is visible. First, the differences between the simulated results and the measured decarburisation rates are discussed. The simulated results show a jump around 20% oxygen blown into the process and a peak appears between 20 – 40% oxygen blown.

The jump in the simulated curves is due to the contribution of the homogenisation reaction. Even though this homogenisation is considered for each calculation step, it is only when the bulk metal is sufficiently refined in silicon that the reaction between the refined metal from the reaction zones and the unreacted bulk metal which is less refined, will contribute to the carbon removal. The observed peak in the curve is due to the changes in the amount of slag that is involved in the emulsion reaction zone. Due to changes in the lance height, the amount of metal in the emulsion zone increases and with this also the slag limit. At first, this causes an increase in carbon oxidation in this reaction zone. More FeO_n is consumed, yet the FeO_n formation does not increase at the same rate at this moment in the process for the current simulations. Hence, the slag is depleted in FeO_n and the amount of carbon that can be removed decreases until a steady state between creation of FeO_n and consumption is obtained. This corresponds to the observations for the FeO_n content during the first part of the process, which is discussed in Figure 11.3.

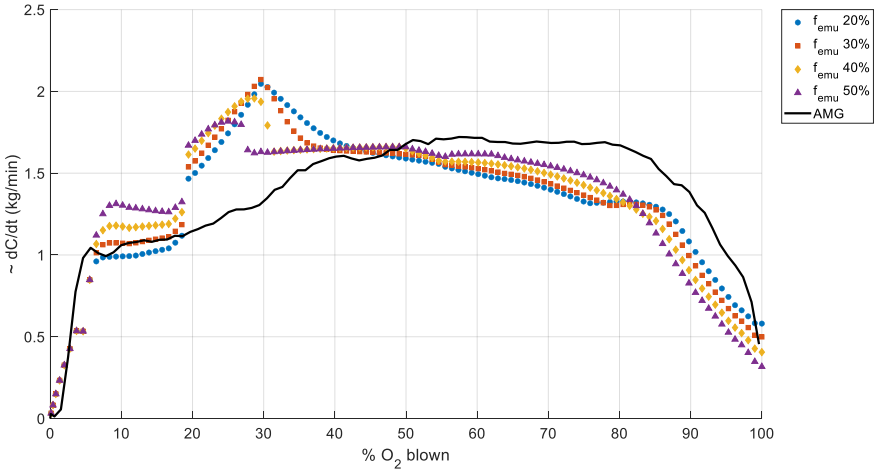

Figure 11.2: Comparing the modelled results for the decarburisation profile/rate to the industrially measured results, with variation for circulating fraction in the emulsion zone.

A higher f_{emu} value, corresponding to more material in the emulsion zone for these calculations, increases the rate of decarburisation. The decarburisation rate corresponding to f_{emu} 50% is higher than the rate for f_{emu} 20% for the majority of the datapoints. Two exceptions are seen: the maximum observed after sudden steep increase of carbon removal around 20% O_2 blown in the process and the very last part of the curve. The explanation of the latter is straightforward, due to the higher carbon removal rates during the process for this calculation, the carbon content will reach the critical value, after which the driving force for decarburisation decreases due to the lower carbon content in the steel, at an earlier point in the process compared to the other calculations. The difference in the peak height is due to the faster depletion in FeO_n when more material is present in the emulsion reaction zone.

The FeO_n content of the slag is a crucial parameter to describe the evolution of the slag during the process accurately. However, there are no direct measurements of the slag composition during the process at the AMG steel plant. Yet, the conventional profile of the FeO_n content in the slag, is a much discussed topic in literature and multiple examples have been discussed already throughout this dissertation (see Figure 10.9). Additionally, the slag compositions during blow have been estimated with the model described in chapter 7: 'Model to calculate slag compositions during blow of historical heats'. The current TD BOF model result for the FeO_n content of the slag during the process for two different values of circulating fraction are shown in Figure 11.3. One of the major assumptions of the model is that all the fluxes are added at the start of the process. To

compare the FeO_n content of the TD BOF model simulations to the well-known profiles, the calculated slag compositions are corrected to compensate for the assumptions. For the considered heats, the flux addition profiles in function of process time are known and can be used for this purpose.

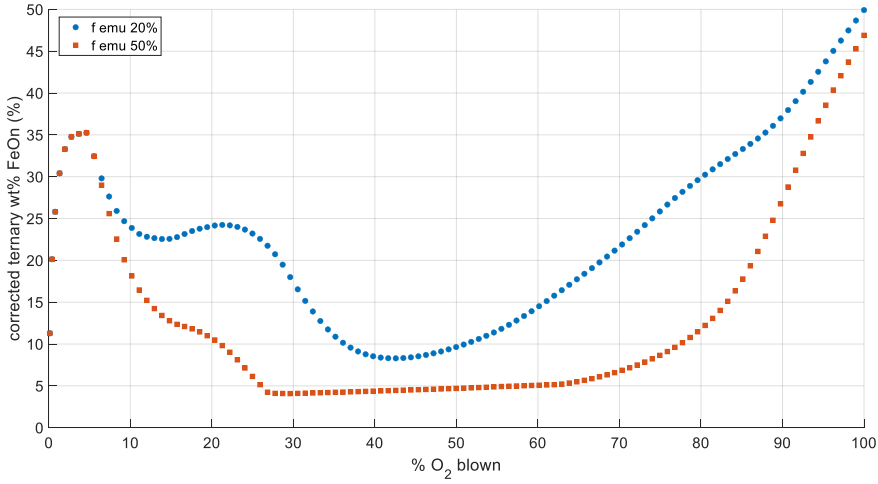

Figure 11.3: Effect of variation of the circulating fraction in the emulsion zone on the calculated corrected ternary FeO_n content of the total slag.

At the start of the process, before the emulsion zone is formed, the contents in Figure 11.3 are identical. This is due to the absence of the emulsion zone for both simulations at this early stage of the process. Hence, the simulations are identical at this point in time. Around 8% of the oxygen blown in the process, the evolution of the iron content starts to differ between the simulations. An emulsion zone has been formed and because the amount of newly generated droplets for each time step is identical between the two simulations, a higher fraction of material left to circulate in the emulsion zone, directly corresponds to more material in this reaction zone. Thus, more FeO_n will be consumed and the content will decrease faster. At the end of the process, the increase in FeO_n content is steeper for the simulation with f_{emu} 50% compared to 20%. Even though these evolutions are clearly different during the process, the final fractions FeO_n are similar.

Apart from the process evolution, also the prediction of these final conditions (composition, temperature, phase amounts) is important. Firstly, in Figure 11.4, the results for the end temperatures are shown. In Figure 11.4 (top) the calculated final steel temperature, with the TD BOF model, is compared to the measured temperature of each heat. The dotted lines, show the acceptable deviation for the calculated steel

temperature. This is based on the deviation of the models used at the ArcelorMittal Ghent steel plant. These models, as discussed earlier in this dissertation, have been strongly optimised during the years and give reliable prediction for the end of blow properties of the process for the familiar working areas. From this figure, it is clear the temperature is nearly identical for the two simulations. Furthermore, based on the limited data used in the comparison, the prediction of the temperature seems to follow the correct trend. Yet, the calculated temperature is lower than the measured one, and only for two heats this value lies within the acceptable deviation of the measured temperature.

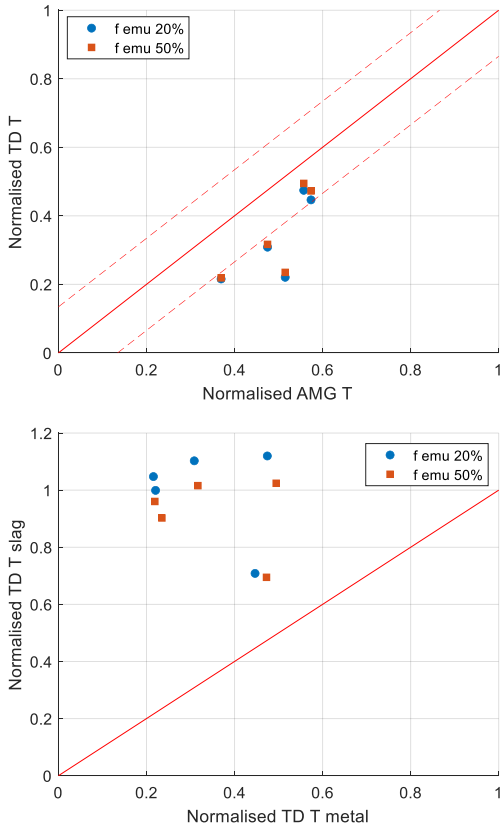

Figure 11.4: The calculated final steel and slag temperature of the process. In (top) the calculated steel temperature is compared to the measured temperature of the heat. The acceptable deviation is indicated with the dotted lines. In (bottom) the calculated steel temperature is compared to the calculated slag temperature. For confidentiality reasons the values are normalised.

In Figure 11.4 (bottom), the calculated slag and steel temperature are compared. The calculated slag temperature is for all the five heats higher than the calculated steel

temperature for both the simulations. Industrially, a higher slag temperature is expected. Unlike the final steel temperature there is a clear difference between the calculated final slag temperature for different circulating fractions. The absolute temperatures exceed the maximal expected steel temperature and hence the normalised value exceeds one.

Apart from the final temperature the content of impurities in the final steel is also of crucial importance. In Figure 11.5, both the final calculated carbon and phosphorus content of the steel phase are compared to the measured ones. The acceptable deviation for the calculated contents is again given by the dotted lines. For both species there is a considerable difference between the simulations with f_{emu} 50% and 20%. The simulation with a circulating fraction of 50% has more material in the emulsion zone, hence a larger contact between the steel phase and the slag and thus, a better refining as result. Both for carbon and for phosphorus the final steel composition is better predicted with a value of 50% for f_{emu}.

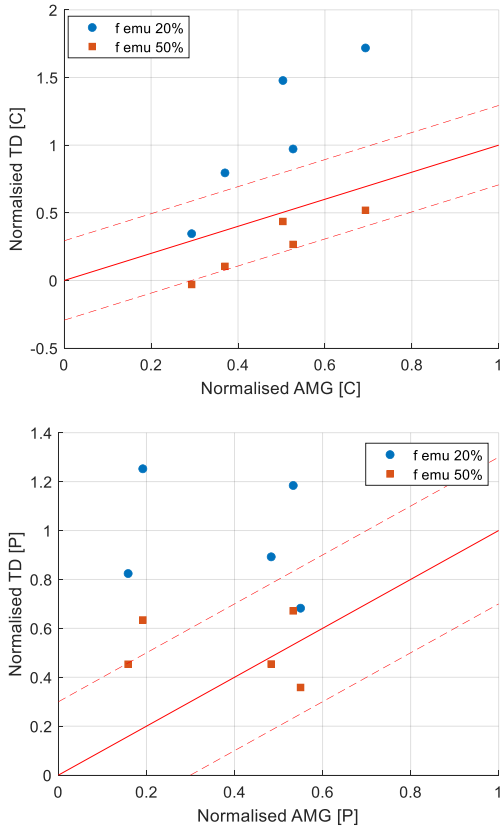

Figure 11.5: Comparison of the end of blow steel composition of the thermodynamic calculation to the industrial compositions. In (top) the final carbon content is shown

and (bottom) the final phosphorus content of the steel phase. The acceptable deviation is indicated with the dotted lines.

The calculated carbon content, in Figure 11.5 (top), shows a good correlation with the measured values. This is not the case for the phosphorus content. From the measured contents, it is clear that for phosphorus there is a high and a low [P] content group (around the normalised values 0.2 and 0.5) while for the calculated values this is not observed. It should be kept in mind however, that currently only five heats are discussed.

Generally, from the results displayed in Figure 11.2 - Figure 11.5 it seems that with an adapted size for the jet impact reaction zone and the theoretical sizes for the interfacial (IF) and emulsion (EMU) reaction zones reasonable results are obtained. Yet, the results are not sufficient nor accurate enough at this point to use the TD BOF model as described so far. It is clear that for the jet impact zone a factor is needed to be able to run sensible simulations. This factor was reasoned at a value of 10 yet, this does not necessarily yield the most accurate results. Furthermore, it could be argued that the origin for deviations between the calculated reaction volume for the JIZ, are also present in the calculations for the other two reaction zones: IF and EMU. Calculation of the interfacial reaction volume involves, apart from the cross section of the cavity created by the oxygen jet, also the mixing coefficient and the assumption of a flat bath geometry. Furthermore, for the calculation of the emulsion zone reaction volume a simplified correlation is used to calculate some of the necessary velocities. Additionally, several studies [3]–[6] reported the underestimation of the amount of metal in the emulsion as calculated with the blowing number theory (discussed in the introduction chapters of this work and Chapter 9). For the amount of metal that circulates in the emulsion zone, it was put forward, in the model description, that this value will be determined with a comparison of the model results with the AMG results. Based on these arguments, it is decided to fit a set of four model parameters (3 reaction volume factors and f_{emu}) to industrial data and results to obtain an optimal model to simulate the BOF process. The final size of each reaction volume is the result of the product of the theoretically calculated size and the determined corresponding model parameter.

11.2 Fitting methodology

To determine the four model parameters, which were put forward in the previous section, the model is fitted to the industrial data. To do this, this problem is handled as an optimisation problem and practically the minimum of a function needs to be

determined. This function is called the error function ($\varepsilon(\boldsymbol{x})$, with $\boldsymbol{x} = [factor\ 1\ (jiz), factor\ 2\ (if), factor\ 3\ (emu), f_{emu}]$) and describes the deviation between the model and the industrial measurements.

11.2.1 Defining the error function

Global error

The definition of the function that will be minimised is crucial and will influence the finally obtained optimal result. Firstly, it is important that the model results at the end of the process approach the measured values. However, a balance is necessary between fitted properties and properties for which the model gives accurate results without specific parameter fitting. Five properties are put forward, for which an accurate end prediction is crucial: steel temperature (T_{steel} (°C)), carbon content of the steel phase ($[C]$ (ppm)), phosphorus content of the steel phase ($[P]$ (ppm)), the liquid steel mass (m_{steel} (ton)) and the Fe content of the slag ($(wt\%\ Fe)$ (wt%)) . Yet, due to the conservation of mass in the TD BOF model, a good fit for the steel mass, which primarily consists out of Fe, automatically equals a good fit of the Fe content in the slag. For this reason $(wt\%\ Fe)$ is left out of the set of properties used to define the error. Secondly, it is also important to describe the evolution of the process accurately. Even though a lot of industrial data is collected during the process, not that much data relates to the phases or the composition of these phases in the BOF vessel. The off gas produced during the process is measured as well as its composition and this results in a rate of decarburisation, also called a decarburisation profile or curve ($\frac{dC}{dt}$ (kg/min)), which is monitored during the process. This type of data has been displayed already in Figure 11.1 and Figure 11.2. This decarburisation profile will be used to evaluate the model simulation during the process. Ideally, if the TD BOF model predicts the decarburisation profile accurately, the amount of carbon removed from the bath in reality and as predicted by the TD BOF model should be equal. If the calculated mass of steel equals the industrial steel mass, the carbon contents in reality and as simulated with the TD BOF model should also be equal. Hence, if the decarburisation curve is already used in the definition of the error the carbon content of the steel can be left out of the analyses.

This results in four properties that will be used to define an error function:

- T_{steel}
- $[P]$
- m_{steel}
- $\frac{dC}{dt}$

These four properties all have a unique unit and deviation from each of them will thus mean something different. A deviation of 1 ton of steel will have a different consequence than 1 °C or 1 ppm phosphorus. Consequently, each property will have a different 'cost' attributed to it. This so called cost is determined based on the AMG model accuracies (apart for $\frac{dC}{dt}$). For this, both the deviation between the average AMG model calculations and the average measured value for each property as well as the standard deviation for each of the properties of the AMG calculation is considered as accuracy. The reasoning being that if the largely optimised and continuously maintained AMG model allows a larger variation for a property, this variation is also tolerated in reality. The values for these accuracies cannot be given due to confidentiality. However, both methods give nearly identical costs for the properties. To give an idea, a deviation of 1 ton of steel is 15 times worse than a deviation of 1 °C. For the decarburisation curve, there is no predicted value by the AMG model, hence for this property arbitrary costs were used. In the final optimisation the value of this cost was set at 0.1. The finally defined error function is given in equation 11.1.

$$\begin{aligned}\varepsilon(\boldsymbol{x}) = \; & c_1 \cdot (T_{steel}^{AMG} - T_{steel}^{TD})^2 \\ & + c_2 \cdot (m_{steel}^{AMG} - m_{steel}^{TD})^2 \\ & + c_3 \cdot ([P]^{AMG} - [P]^{TD})^2 \cdot \mathbb{H}\big(-([P]^{AMG} - [P]^{TD})\big) \\ & + 0.01 \cdot c_3 \cdot ([P]^{AMG} - [P]^{TD})^2 \cdot \mathbb{H}\big(([P]^{AMG} - [P]^{TD})\big) \\ & + 0.1 \cdot \left| \frac{dC^{AMG}}{dt}(t) - \frac{dC^{TD}}{dt}(t) \right|\end{aligned} \tag{11.1}$$

In this equation c_i is the earlier explained cost for the property. These costs are constant and fixed values. Even though, from a first glance at equation 11.1, it would appear there are two different contributions for phosphorus, this is not the case due to the Heaviside functions which cause one of the two terms to be zero. Due to the introduction of the Heaviside function ($\mathbb{H}$) the contribution will be larger if the calculated [P] is higher than the industrially measured one as opposed to if it would be smaller than the industrially

measured value. The reason is because from a refining viewpoint, reaching the target value is sufficient and furthermore, it was already mentioned in this work that purely thermodynamically an improved refining will be predicted as compared to the observed reality. The norm used to describe the contribution of the deviation between the calculated and measured rate of decarburisation is given in equation 11.2, with k the maximum calculation step.

$$\left|\frac{dC}{dt}^{AMG}(t) - \frac{dC}{dt}^{TD}(t)\right| = \sum_{i=1}^{k}\left|\frac{dC}{dt}^{AMG}(i) - \frac{dC}{dt}^{TD}(i)\right| \qquad (11.2)$$

To gain some insight in the concept, the calculated error values for two different simulations are given in Figure 11.6. These error values correspond to the simulations with a factor 10 for JIZ, the theoretical RV size for IF and EMU and f_{emu} set at 20% and 50%. In Figure 11.6 (a) the calculated error for each heat with f_{emu} 20% is shown, while in Figure 11.6 (b) this value is 50%. Clearly, the simulation with a circulating fraction of 50% gives better results (note the difference in y-axis range between the two figures), based on the defined general error, than the simulation with 20%. Especially the high P contents for the latter contribute to a large error. Interestingly, for both simulations heat 3 has the highest error and, in both cases, the largest deviation in [P] out of the five heats.

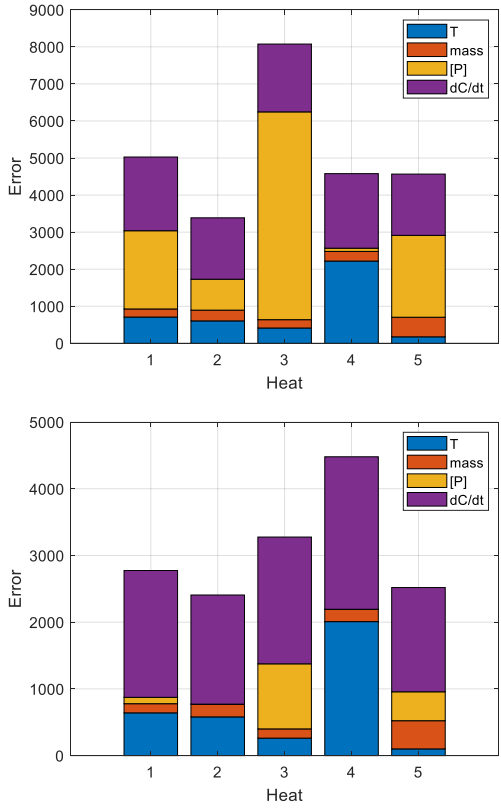

Figure 11.6: Example of the contributions to the general error function for two set of simulations with varying circulating fraction. In (top) the results for x = [10, 1, 1, 0.2] and thus a circulation fraction of 20% are shown, in (bottom) the results for x = [10, 1, 1, 0.5] and thus a circulation fraction of 50% are shown. Note the difference in limit on the y-axis.

Alternative error

Apart from the general error, with contributions for both the final conditions and the evolution, a second alternative error is introduced ($\varepsilon_a(\boldsymbol{x})$). It is mentioned in literature [7], that especially for the beginning of the blow there is a lack of understanding in the process. Yet, this early stage will be crucial, a.o. due to the initial increase in FeO_n content of slag. This is not only important to describe the slag composition accurately, but has also been mentioned [8] to be important for the Mn and P removal as well as for the temperature evolution. To focus on the early stage of the blow, the alternative function only focusses on the first half of the blow. There are no samples of steel or slag from during the blow and as a consequence only the rate of decarburisation can be used. The

definition of the alternative error is given in equation 11.3 in which $t_{50\%}$ denotes the time halfway through the process.

$$\varepsilon_a(\boldsymbol{x}) = \left| \frac{dC^{AMG}}{dt} \quad (t < t_{50\%}) - \frac{dC^{TD}}{dt} \quad (t < t_{50\%}) \right| \tag{11.3}$$

In Figure 11.7 an example is given in the value of the alternative error for two simulations with a varying f_{emu}. Unlike the general error the alternative error is rather similar for both simulations. However, when comparing the corresponding decarburisation curves, in Figure 11.2, the two simulations have clearly different decarburisation curves. Unavoidably, some information will be lost when a curve is transformed into a single value, which is nicely demonstrated here.

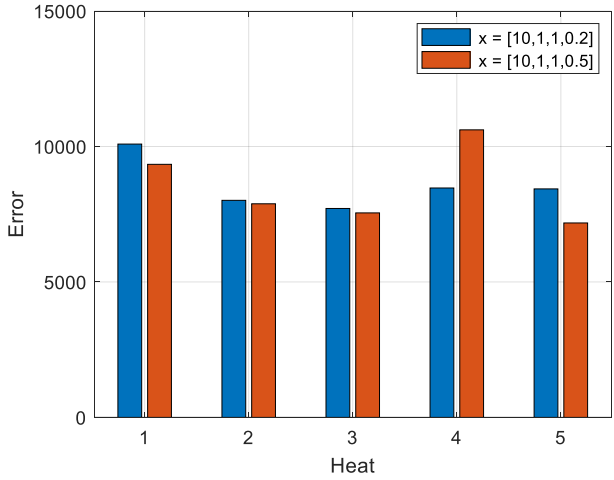

Figure 11.7: Example of the value for the alternative error for two sets of simulations with varying circulating fraction (20% versus 50%).

11.2.2 Optimisation solver

A standard MATLAB optimisation solver is selected. Even though a variation of solvers is investigated and has been used, for the final optimisation the '*surrogateopt*' function is used. This choice was made due to its suitability for time consuming objective functions (the TD BOF model) and because the starting point is not user defined. The constraints for the sampled space are [5, 0.5, 0.5,0.1] as lower boundary and [35, 15, 15, 0.6] as upper boundary. Additionally, the total amount of liquid metal in the reaction zones is constrained to be smaller than the maximum amount of liquid metal. This maximum amount is set at a conservative value of 300 ton. All the function settings, of the

'*surrogateopt*' function, are kept at their default. If due to physical/chemical impossibilities during the calculation, the equilibrium cannot be calculated for a heat, the results are set to be 'NaN'.

For optimisation, the earlier described five heats are used. The solver requires a unique value for the optimised function. With the definition of the error functions so far, each heat has its specific error. The final error is the average value of the individual error values. This approach of averaging over the five heats, has been used rather than to optimise for one heat. As a consequence, it is expected that the final optimal input for the model parameters will not give a perfect result for each heat, rather give an overall good result for all the heats.

11.3 Fitting results

The results of the optimisation are given in Table 11-1. Both optimal points have a nearly identical factor for the interfacial reaction zone (IF). A clearly different value is obtained for the jet impact zone (JIZ) as well as for the emulsion zone (EMU). The total amount of metal in the emulsion is determined both by the factor of the emulsion zone and the recirculating value and this can be formulated as a geometric progression. Consequently, the total amount of metal in the emulsion zone can be calculated as the theoretic reaction volume multiplied with the limit (for infinite number of calculation steps) of the geometric progressions. This limit can be calculated and equals Factor 3 (EMU) divided by f_{emu}. This value is also listed in Table 11-1 and is clearly larger for the general error optimisation. Generally, it can be concluded that a larger reaction volumes and thus more reacting metal and slag are necessary to optimise both the final properties and complete decarburisation profile compared to only modelling the first 50% of the decarburisation profile accurately.

Firstly, the solution obtained for the general error (ε) is considered. In Figure 11.8 the different contributions to the total error for each heat are shown. From the results shown in Figure 11.8 (top) it is clear that the simulation will give a similar total deviation (for both end point data as well as decarburisation profile) for all the heats apart for heat 4. This heat has clearly a larger error than the other heats. Especially for the final steel temperature a larger deviation from the industrial measurement is observed. From Figure 11.8 (bottom) it can also be seen that for all the heats the deviation between the model results and the end of blow measurements is largest for the temperature. However, for heat 4 this is a different order of magnitude. Furthermore, for heat 5 also

a large deviation between the calculated mass and the AMG steel mass is observed. However, this could be attributed to the industrial value for this property in this specific case.

Table 11-1: Overview of the solutions of the optimisation. In this table $\varepsilon(\boldsymbol{x})$ corresponds to the general error (considering the decarburisation profile for 100% oxygen blown and end compositions), while $\varepsilon_a(\boldsymbol{x})$ corresponds to the alternative error (only considering the first half of the decarburisation curves).

	Factor 1 (JIZ)	Factor 2 (IF)	Factor 3 (EMU)	f_{emu}	$\frac{\text{Factor 3}}{f_{emu}}$	$\varepsilon(x_{min})$
$\varepsilon(\boldsymbol{x})$	26.06	0.72	3.03	0.39	4.97	1752.5
$\varepsilon_a(\boldsymbol{x})$	17.58	0.78	0.50	0.28	0.69	6094.0

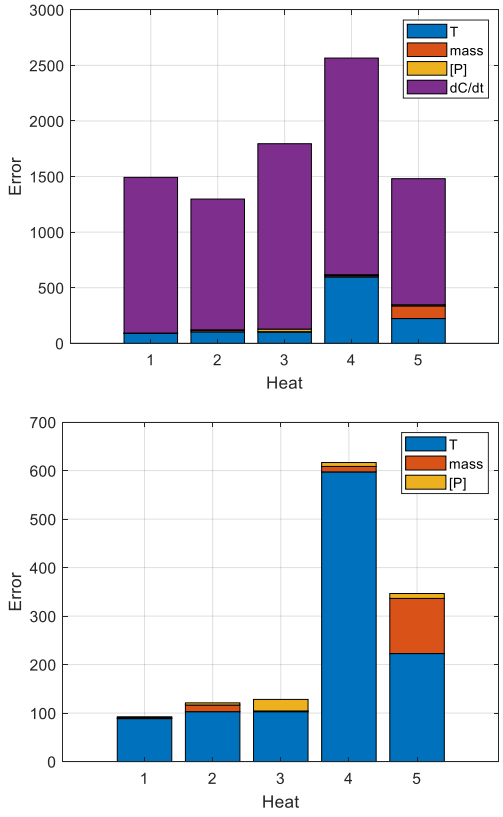

Figure 11.8: Contributions to the general error for each heat. In (top) all contributions are shown, in (bottom) only the contributions of the end properties are shown.

Because the largest deviation between the model and the final measured properties is related to the temperature, this property is further scrutinised. In Figure 11.9 the calculated value of the TD BOF model is compared to the measured temperature as well as to the expected temperature calculated with the AMG model for the known used input. It is important to be aware that for any real industrial heat, there could be a difference between the known used input and the real input. For example, scrap materials are assumed to have a certain composition yet, sometimes the real composition might deviate or the scrap mixture could be heterogeneous. Or due to sculling an extra unknown material stream enters the vessel. A difference between the calculated and measured AMG temperature is thus certainly possible. For heat 4, the calculated AMG temperature is also lower than the measured one. However, the TD calculation always predicts a temperature in the range of the deviation of the AMG model. The contributions to the error are thus acceptable.

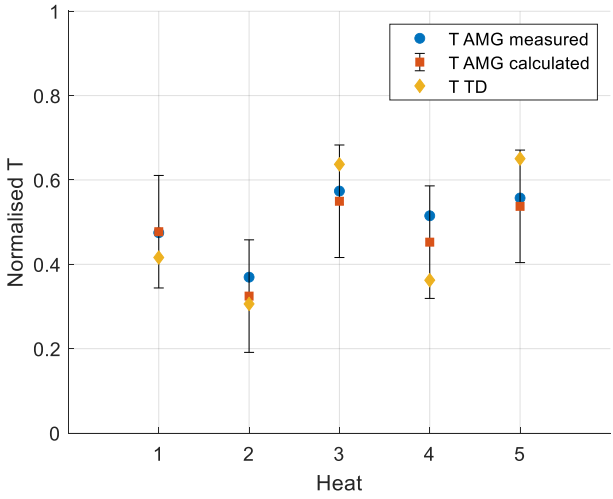

Figure 11.9: Comparing the TD calculated final steel temperature to the measured AMG temperature and the calculated AMG temperature.

In Figure 11.10 the calculated rate of decarburisation is compared to the measured profile, for two different heats. At the start of the blow the (blue) curve clearly predicts a much higher decarburisation rate. This will also have an effect on the slag evolution. For the second part of the profile, where the rate reaches a plateau value, the current set of model parameters gives a good match between the measured curve and the calculated one. The behaviour of both is identical yet, the absolute value of the roughly constant decarburisation rate, between around 35% and 90% O_2 blown, will be lower for the TD calculation.

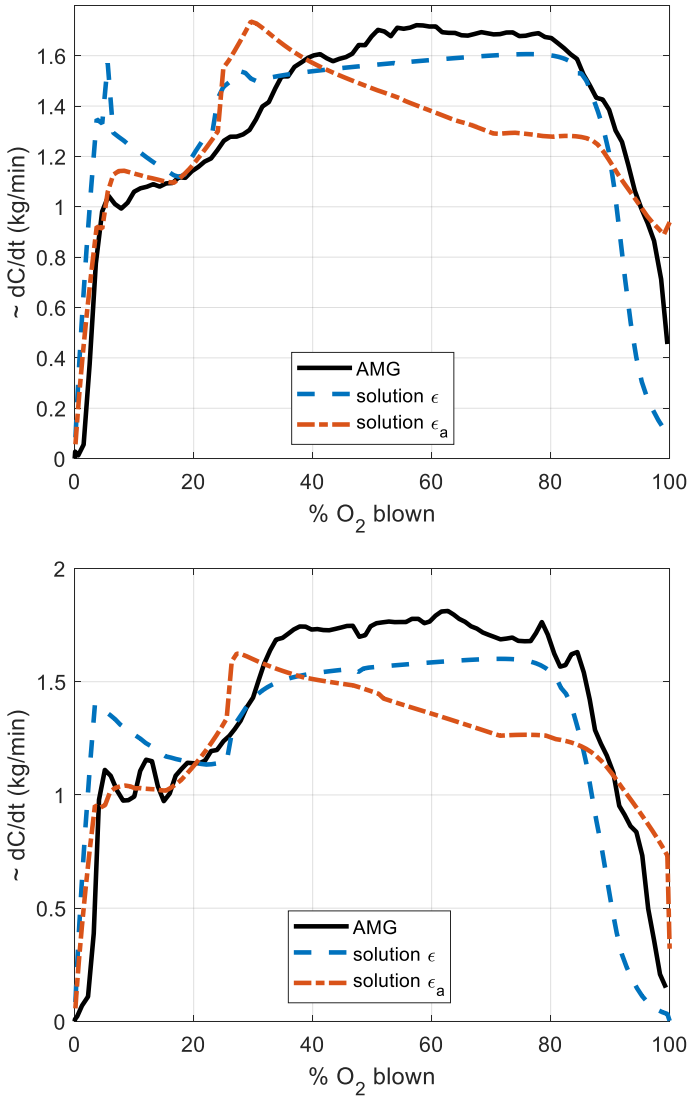

Figure 11.10: Decarburisation profiles for two different heats. Both the results for the parameter set obtained with the general and the alternative error are shown, together with the industrially measured decarburisation rate.

Secondly, the solution obtained for the alternative error (ε_a) is considered. In Figure 11.10 the calculated decarburisation profiles for the solution of the alternative error, which only considers the rate of decarburisation during the first half of the process, are shown for two heats. Clearly, with this set of model parameters the onset of the decarburisation is more accurately described. This is important to get a proper description of the slag evolution and steel refining during the process. However, unlike

measured the modelled decarburisation rate never reaches a plateau value. As a consequence, the final calculated carbon content is too high (> 1 wt%) and the final process conditions are not predicted accurately with this set of model parameters.

Comparing the two different solutions and their effect on the rate of decarburisation shows that to simulate the start of the process accurately a different set of parameters is required than to simulate the overall process and the final end of blow properties. For a good description of the start of the process, smaller reaction volumes are required than to get an overall good description. The same conclusion can be formulated from the calculated FeO_n contents in Figure 11.11. The model described in chapter 7 that estimates the simplified slag composition during the blow based on industrial input and output data is used to evaluate the FeO_n evolution profiles calculated with the TD BOF model. Unfortunately, only heat 2 fulfils all the requirements to use the model of chapter 7. Furthermore, it was assumed in the TD BOF model that all the fluxes are added at the start of the process. To be able to compare the results of the two models, the results of the TD BOF model are corrected with compensation for the flux addition profile for the most significant fluxes. From this comparison, in Figure 11.11, it is seen that the simulation with the model parameters determined with the alternative error (orange curve), gives a rather good description of the behaviour of FeO_n at the beginning of the blow. The predicted values are not identical. Nevertheless, the behaviour matches rather good for a predictive model. This of course is only the case until 40 – 50 % of the oxygen blown into the process. The alternative error was only defined in this interval and the decarburisation profiles already prevailed a poor fit for the second part of the process. On the other hand, the simulation with the model parameters determined with the general error (blue curve) describes the FeO_n behaviour very poorly. The high decarburisation rates at the start of the process already indicated more oxygen is consumed for the removal of carbon and hence, less Fe is oxidised. Although a peak in FeO_n content is observed at the beginning, the FeO_n content decreases very fast due to the larger reaction volumes and the corresponding larger consumption of FeO_n in the refining reactions. Even though, the FeO_n evolution is described very poorly during the largest part of the process, the final behaviour is more or less a good prediction. From the previous discussion it was already known that for this set of parameters, the final conditions show a rather good match.

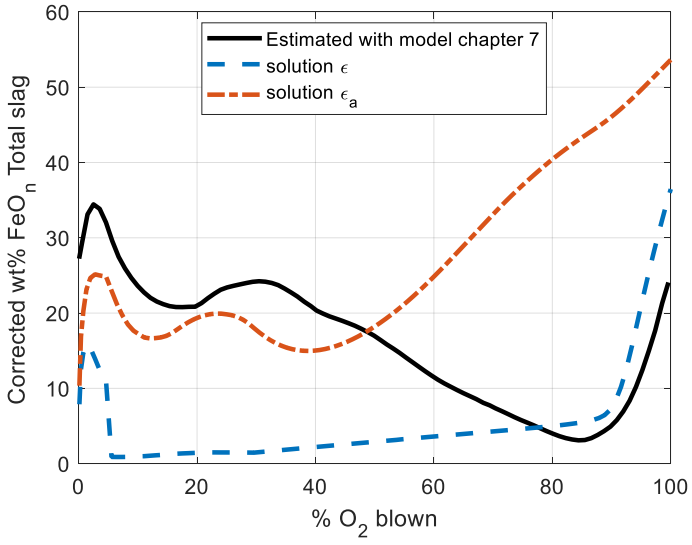

Figure 11.11: Calculated FeO_n content with the model described in chapter 7 based on industrial plant data and two different simulations of the TD BOF model with the two different set of model parameters obtained via the fitting of the general error and the alternative error.

It seems from the above that it is impossible, with the current optimisation, to find a good set of constant model parameters to give satisfactory results for the complete process. Either the start until 40 – 50% O_2 blown is well predicted but the rest of the process is described very poorly or only the final end of blow conditions and the last part of the process (> 90% O_2) is well described and the onset of the process is not accurately predicted. For industrial research questions this can be tackled by using the two different set of model parameters separately and depending upon the research question use one or the other. There are multiple arguments on why there is need for variable model parameters over process time (apart from general model construction assumptions such as number of reaction zones). Possibly, the stirring coefficients will need a different correction at different times in the process, for instance due to different lance heights or due to differences in bottom stirring (which is not incorporated in the current model). Possibly, the current formulas to calculate the stirring coefficients are applicable during the process when oxygen is steady blown, but not as accurate in describing the start. The stirring coefficients are also calculated as a function of the stirring energy but viscosities are not considered. For the steel phase, the variation in viscosity is expected to be minimal but for the slag a larger variation in viscosities can be expected. Furthermore, certain authors have argued that the existence of the emulsion zone is also related to the blowing regime (so called hard versus soft blowing) and hence is also related to the lance

height. In the current model this is not incorporated. Moreover, the ratio of the reaction volume of slag over metal in the emulsion zone is calculated based on some assumption of droplet sizes and mixing coefficients. Even if the average droplet diameter of 2 mm is a good estimate, it remains an average value and using a more complex droplet size distribution could give different results. Possibly, the current method to define the amount of slag reacting in the emulsion zone is not accurate enough. Additionally, it was mentioned in the previous chapter that the number of droplets ejected from the metal bath is calculated with the blowing number for which a simple velocity calculation was used. In Figure 10.14 the dependency of this velocity on the lance height was shown. The deviation between the simple, used velocity calculation and the more accurate yet, complex velocity calculations might be different as function of the lance heights as well.

11.4 Model validation

For the model validation a new set of AMG simulated heats is created. This dataset contains 71 heats with variation in amongst others scrap types, scrap amount and fluxes. Unlike the heats used in the fitting routine, explained above, these heats are simulated and have never been produced. The big advantage of this type of simulations is the cleanliness of the data and the possibility to impose variations as desired. The disadvantage is that the results are calculated rather than measured and that there is no information of the process evolution, but only for the final conditions of the process. The validation of the model is split in two different validations, one for each of the solutions of the fitting.

11.4.1 Validation for parameter set [26.06; 0. 72; 3.03; 0.39]

The parameter set [26.06; 0. 72; 3.03; 0.39] is the solution for the optimisation of the general error and it was concluded earlier that this set of parameters gives a good description of the final conditions of the BOF process, thus at the end of blow. Consequently, for this validation only the final calculated properties by the TD BOF model are considered. In Figure 11.12 the masses of the condensed bulk phases present at the end of blow for the AMG and TD BOF simulation are compared. The calculated steel mass for both simulations is nearly identical. For the slag, the TD BOF model slightly overestimates the amount for small slag masses. Yet, a good correlation is observed for this property as well. That both properties are well predicted is crucial yet, is an obvious consequence of the imposed conservation of mass for iron. The larger deviations between both simulations for the slag mass could be linked to the AMG simulation of the

slag mass. Theoretically, this simulation predicts a slag mass in between the liquid slag mass and the total slag. This is due to the slag sampling method for real heats, on which some of the AMG slag simulations are strongly based, where only the liquid slag is sampled rather than the complete slag.

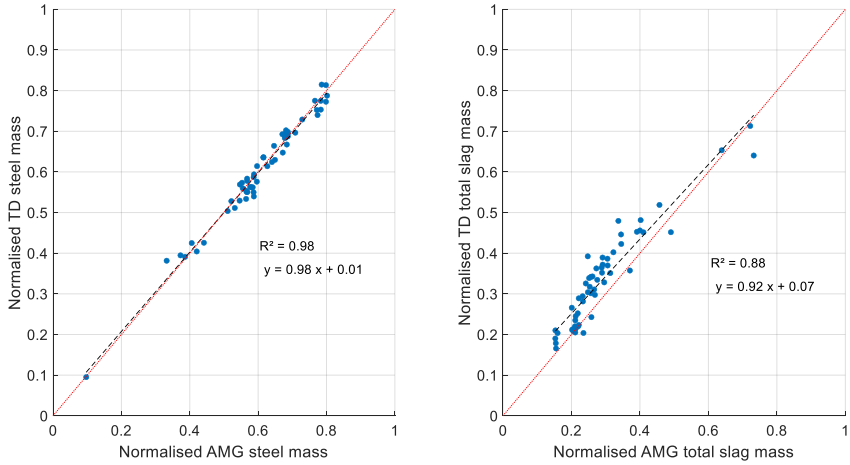

Figure 11.12: Comparison of the thermodynamically calculated amount of (left) steel and (right) total slag present at the end of blow to the industrial amounts.

The results shown in Figure 11.13 illustrate the difference between a simple open TD calculation and the more complex TD BOF simulation (in essence also based on an open TD calculation). Even though, for both types of thermodynamic calculations a good correlation is observed with the AMG simulated slag mass, the TD BOF model clearly predicts more accurate slag masses if the AMG slag mass is set as the reference value. This demonstrates again the importance of a more complex TD BOF model and shows an importance difference between the TD BOF model simulations and the simple standard TD calculations.

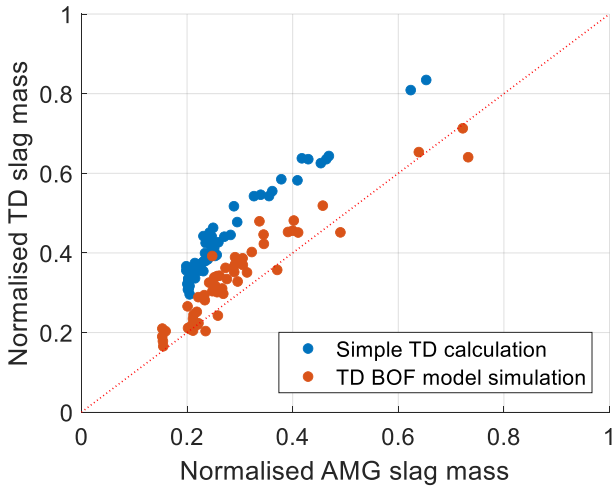

Figure 11.13: Comparison of the thermodynamically calculated slag mass to the AMG simulated slag mass. Both the results of a simple TD calculation (general open calculation as explained in the earlier chapter) and the complex TD BOF simulation (with parameter set of the general error) are shown.

In the TD BOF simulation the slag and steel phase have a different temperature. For the AMG simulation only the steel temperature is available. However, from literature and industrial measurements it is generally known that the slag temperature should be larger than the steel temperature. A comparison between the calculated steel temperature from the AMG simulation and the TD BOF simulation is shown in Figure 11.14. For most of the heats the TD BOF model predicts a lower temperature than the AMG simulation. Some of these temperatures are even lower than the lower limit temperature for the normalisation (which is a fixed value throughout this complete work) and as a result also negative normalised temperatures are shown. There is a correlation between the two simulations yet, not as convincing as the correlations observed for the masses. However, temperature calculations are more complex. They depend on a heat balance which is strongly dependant on the correct calculation of the enthalpy of the input material streams. Furthermore, heat streams in the model are uniquely linked to material streams apart for the temperature homogenisation steps, where the imposed additional heat balance is a strong simplification of reality. Finally, it is also assumed there is no interaction between the formed gas and the phases in the BOF vessel, thus also for the heat balance the enthalpy related to the formed gas phases is removed from the system's total enthalpy.

The deviation between the AMG and TD BOF temperature is strongly linked with the enthalpy for the hot metal in the TD BOF model, as shown in Figure 11.14 (b). The heats with the largest temperature underestimation have the smallest total enthalpy for the liquid hot metal. This enthalpy is both a function of the amount of hot metal considered for the heat and the specific enthalpy for the hot metal that is charged for the heat. This enthalpy will mainly be influenced by the temperature and Si content of the hot metal. Especially, the low hot metal temperatures appear to be the dominant cause for the low steel temperature for the heats with the largest steel temperature deviation between the simulations.

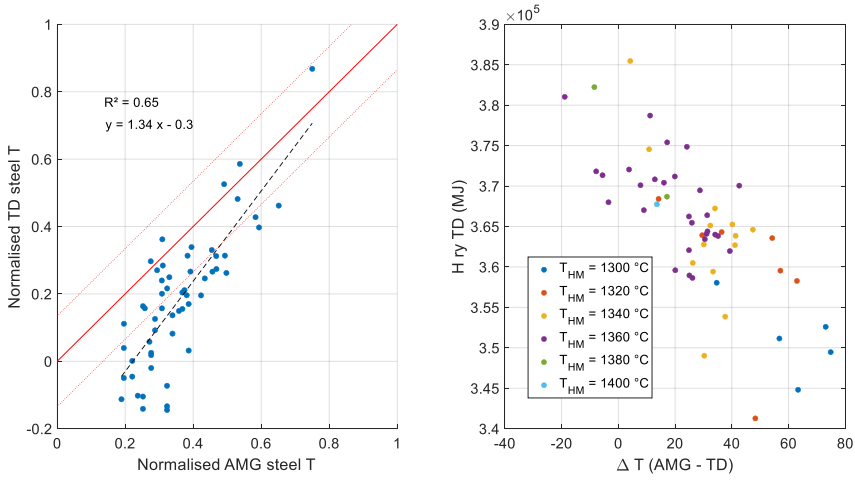

Figure 11.14: (left) Comparison of the steel temperature calculated with the TD BOF model to the simulated AMG steel temperature. The acceptable deviation, based on AMG model data, is indicated with the red dotted line. (right) The hot metal enthalpy calculated for the TD BOF model as a function of the difference in steel temperature between the industrial and thermodynamic simulation. The hot metal initial temperature interval is indicated as well on the figure (T_{HM} = 1300°C corresponds to $T_{HM} \epsilon$ [1300, 1320[ )

Even though a larger temperature for the slag is expected this is only the case for 27% of the heats. Even though some significant differences in input material streams are observed between the heats with and without a correct trend for the steel and slag temperature (e.g. addition of dolomitic lime and amount of oxygen blown), it is impossible to explain the difference between these two groups of heats based on the input. Furthermore, with a different set of model parameters (for the alternative error) the slag temperature is for all the heats calculated to be higher than their steel temperature. This indicates that possibly not the input for the heat balance is the reason

for the lower slag temperatures but rather the description of heat exchange between the different reaction zones and the imposed heat transfer. In the model description it was already mentioned that the current heat transfer equation is a strong simplification of reality. The current results indicate that the description of heat exchanges in the model can be further improved.

Focussing on the steel composition, in Figure 11.15, it is clear that even more variation is observed on the calculation of the content of the important impurities. For the carbon content, a large share of the heats is thermodynamically predicted to have a lower carbon content than industrially simulated. This result is expected and for this group the two simulations seem to show identical trends. However, some heats show a different behaviour and their thermodynamic carbon content lies in the range of the industrial carbon contents. Furthermore, these heats seem to have a fixed and constant industrial carbon content, while thermodynamically variation is calculated. This group of heats (both normalised AMG [C] ≈ 0.7 and 0.95) are heats for which industrially the FeO_n content is a fixed and constant value while thermodynamically this FeO_n content will vary as well. This is strongly correlated to the observations for the oxygen content. For most of the heats a higher oxygen content is thermodynamically observed, yet for this set of heats the thermodynamic oxygen content matches the industrial content. In Figure 11.16 a good correlation for the product of the carbon and oxygen content is observed. From this data (Figure 11.16), it is also clear the thermodynamically simulated oxygen contents are much higher than the AMG simulated ones. Hence, generally the much lower predicted thermodynamic carbon contents. For the group of heats with their thermodynamic carbon content is predicted in the range of the industrial expected values, the thermodynamic oxygen content lies within the range of the industrial calculated ones, yet also lower than the AMG value. The AMG simulations are performed with a statistically based model, which has a fundamental basis but which will also incorporate effect of kinetics due fitting to measured values. As explained earlier, the TD BOF model integrates kinetics, yet does certainly not incorporate all the kinetic aspects. Specifically, for this case, the relation between the iron content of the slag and the oxygen content for very low FeO_n contents in the slag, is different between the TD BOF model and the AMG model. As a consequence, for this group of heats a deviation in trends for oxygen and carbon content is observed.

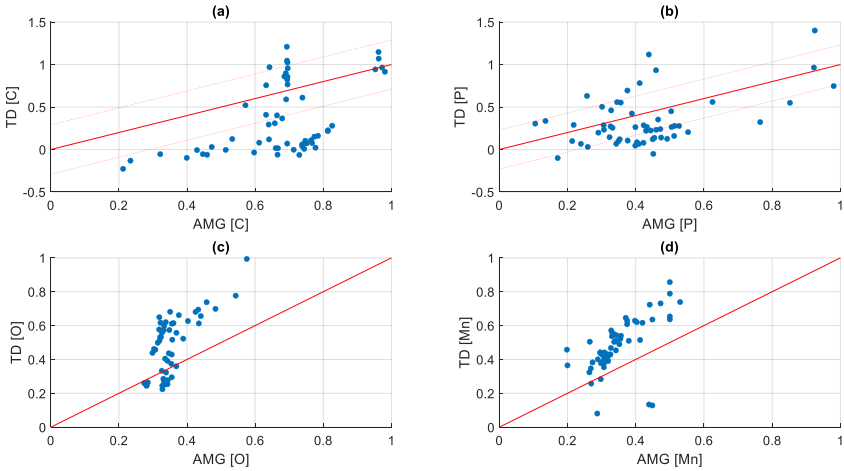

Figure 11.15: Comparison of the thermodynamically calculated steel composition at the end of blow with the TD BOF model to the industrial simulated ones: (a) carbon content, (b) phosphorus content, (c) oxygen content and (d) manganese content.

The thermodynamically calculated phosphorus content for the steel phase, Figure 11.15, seems to lie within the range of industrial calculated values. However, there is no strong trend between the two simulations. For the manganese content, most of the heats show a very poor thermodynamic simulation. Absolute values of the manganese content reach values of 2700 ppm for some heats and the steel is thus, not really refined for this property. In conclusion, the carbon content for most heats shows a good correlation between the two simulations with of course, stronger refining predicted according to the TD BOF model. The phosphorus content is roughly well predicted and values within the industrial ranges are observed. Yet, there is no strong correlation for this property between the two simulations. For manganese the TD BOF model seems not suitable to give accurate results of the final Mn content.

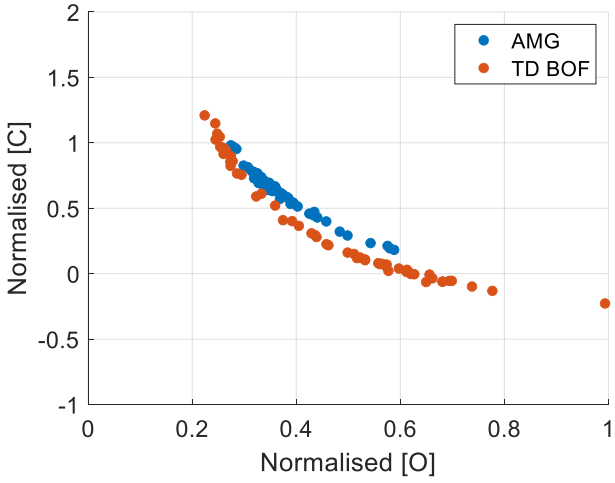

Figure 11.16: The relation between the carbon and oxygen content of the steel, shown for both the industrial simulated heats (AMG), which corresponds to the measured relation in the BOF vessel, as well as for the TD BOF model simulations.

For the slag composition the ternary slag compositions are compared in Figure 11.17. The AMG simulated iron content in the slag is strongly related to the measured slag samples from the industrial process. These types of samples are dipping samples and will, as a consequence, mainly sample the liquid slag instead of the complete slag existing out of liquids and solids. For this reason, for the TD ternary slag composition the liquid slag composition rather than the complete slag composition is used. For the AMG ternary composition the available calculated ternary composition is used. Both ternary slag compositions show great similarities. The thermodynamic slag composition has a slightly smaller basicity and some of the slags have a higher FeO_n content compared to the AMG ternary slag compositions. Yet, overall the thermodynamic predicted ternary slag composition matches well to the industrial composition. Both basicity and iron content are further analysed in Figure 11.18. The AMG basicity is either calculated with the CaO and SiO_2 content of the slag or the absolute masses of these components. Both methods give similar results. The basicity related to the thermodynamically calculated liquid slag is clearly lower than the ones of the AMG simulation. This corresponds to the observations from Figure 11.17. The variation for this specific basicity is also larger than the variations of the AMG basicities. If the total thermodynamic basicity is calculated then this value is in line with the calculated AMG basicities and higher than the basicity of the liquid slag. The difference between the liquid and the total slag is that for the total slag also the solids, usually pure CaO and sometimes pure MgO, are considered. The silicon content, in the dominator, remains constant but the amount of CaO will increase

if the total slag is considered, resulting in a larger basicity. The industrial calculation for the CaO and SiO_2 contents of the slag are strongly dependent on the system's mass balances with incorporation of some statistics. Thus, the industrial basicity should be compared to the thermodynamic total slag basicity. For this value the thermodynamic observations correspond well to the industrial ones. The main source of deviation in the total mass of CaO and SiO_2 between the AMG simulations and the TD simulations is due to the presence of AMG model constants, due to the statistical nature of this model, for these masses.

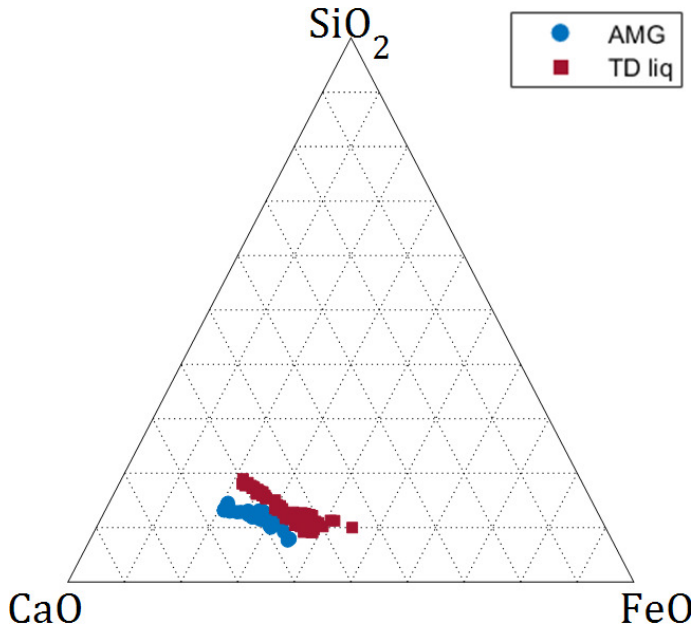

Figure 11.17: Ternary slag compositions for the total slag at the end of blow for the industrial (AMG) and TD BOF simulations (TD liq).

For the iron content of the slag, in Figure 11.18, a good correlation is observed for most of the heats between the two simulations. As expected, the iron content of the TD calculation is usually higher than the industrially calculated iron content.

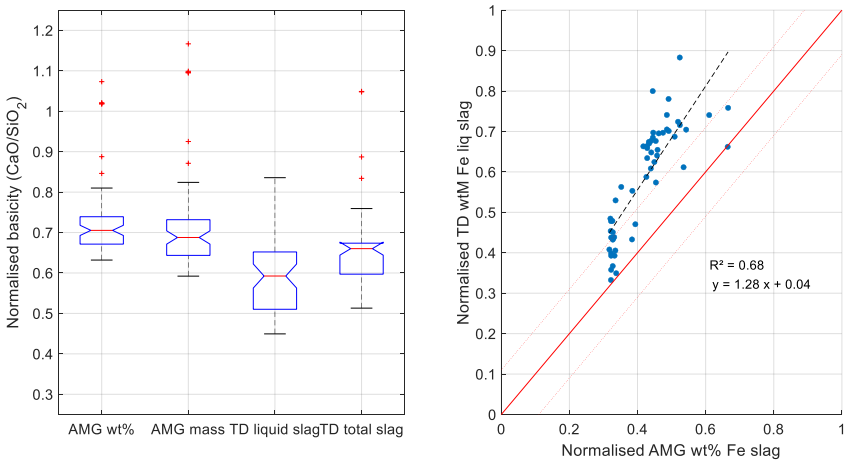

Figure 11.18: (left) The comparison of different basicities. The boxplot shows the median values for the set of heats simulated, as well as the first and third quartiles. The outliers are displayed as red crosses. (right) The iron content of the liquid slag phase calculated with the TD BOF model compared to the results of the AMG simulations. The linear regression is indicated (black dashed line) as well as the acceptable deviations according to the AMG models (red dotted lines).

Finally, in Figure 11.19 the MgO and Al_2O_3 contents for the two simulations are compared. For Al_2O_3, most of the industrial simulations predict a constant value while thermodynamically variation is calculated. Yet, for heats with industrially very low alumina contents in their slags, the thermodynamic calculated values are also lower. The largest group of heats has an industrial normalised Al_2O_3 content of 0.81 (±0.00). For this group the average thermodynamic content is 0.7 (±0.10). For MgO similar conclusions can be formulated. However, for MgO two larger groups of industrial MgO contents exist: around 0.3 and fixed at 0.9. For the thermodynamic data the same groups are observed although the content is again lower. For the first group, low MgO content, the average normalised AMG content is 0.30 (±0.03) while the average normalised TD content is with a value of 0.17 (±0.03) much lower. For the second group of heats, high MgO content, the average normalised AMG content is 0.91 (±0.00) and the TD content 0.61 (±0.03). The reason for the systematic underestimation of both slag components in the thermodynamic simulation compared to the AMG simulation is the presence of extra correction constants in the formulas to calculate the contents in the latter. Additionally, for MgO the refractory wear is not included in the TD model and a slightly different input is used between the two simulations due to differences in the compositional matrices for fluxes used in both simulations. These differences are minor.

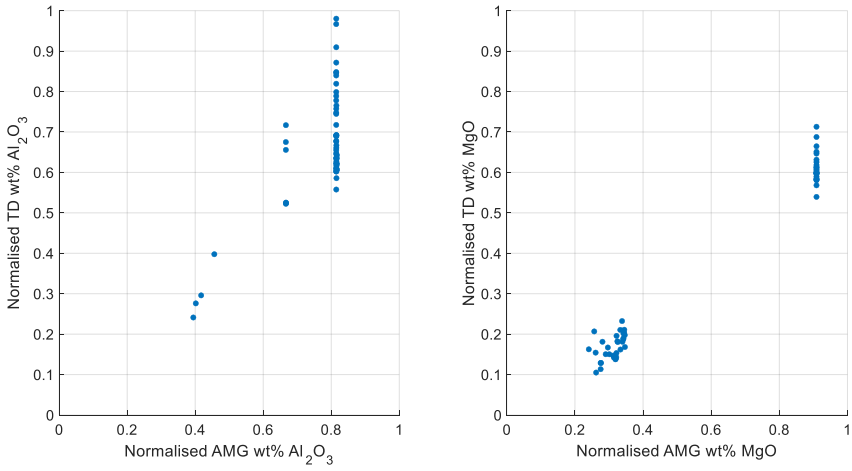

Figure 11.19: (left) Comparison of the Al_2O_3 contents of the liquid slag phase as calculated with the TD BOF model to the industrially simulated ones. (right) Comparing the TD calculated MgO content of the liquid slag phase to the industrial content.

For this set of model parameters it can be concluded that the thermodynamic model gives an accurate description of the masses of the different phases in the converter. The temperature for both steel and slag is underestimated yet, the steel temperature seems to correlate well to the AMG temperatures. The slag composition is rather well predicted by the thermodynamic model, considering the use of model constants and parameters in the industrial simulation. The TD BOF model can, however, not be used to simulate the refining of manganese.

11.4.2 Validation for parameter set [17.58; 0. 78; 0.50; 0.28]

The parameter set [17.58; 0. 78; 0.50; 0.28] is the solution for the optimisation of the alternative error and it was concluded earlier that this set of parameters gave a good description of the early stages of the BOF process. Consequently, for this validation only the results of TD BOF model in the interval between 0% and 40% oxygen blown into the process are considered. However, the industrial simulations do not give any information on the evolution of the properties. For the fitting of the model parameters already executed industrial heats have been used. Thus, for these heats flux addition profiles are known and the decarburisation rate is measured allowing to estimate the slag evolution during blow. For the current simulations, used to validate the model, these evolutions are unknown. Hence, it is impossible to evaluate the overall slag composition due to the lack of information on flux additions and it is also impossible to calculate the industrial

slag evolutions. Consequently, only trends can be investigated. This validation is thus not a strictly quantitative one but is on a qualitative basis.

The evolution of different impurities in the steel phase are shown in Figure 11.20. These evolutions are calculated as the average evolution for a component based on the results of the 71 heats in the dataset. To calculate the average and standard deviations, the Matlab function '*grpstats*' has been used. Grouping, required for this function, has been performed per calculation step. The average for these heats are displayed with a black solid line while the standard deviations are shown with a red dotted one. Typical evolution of these components was briefly discussed in Chapter 2 in Figure 2.3. As discussed earlier for the previous set of model parameters, the TD BOF model is not able to predict the manganese content at the end of the process. From the results in Figure 11.20 (d) it appears the TD BOF model is also not able to describe the evolution of the manganese content during the blow either. The manganese is only removed from the steel bath at the end of the blow according to the TD simulation while in reality a profile just like for phosphorus is expected with a decrease and a pick up of Mn during the blow. It is unclear why the model predicts the Mn-removal so poorly. Multiple factors could be the reason: the thermodynamic description of Mn – MnO in the used thermodynamic databases, the assumptions of the necessary reaction zones in the TD BOF model (e.g. the bottom stirring is not considered), the assumptions on the sizes of the implemented reaction zones (e.g. different kinetics might be involved in Mn removal), etc. For the other important components (C, Si and P) the trends in the evolutions are as expected: a steady decrease for C (Figure 11.20 (a)), a steep decrease for Si at the beginning (Figure 11.20 (b)) and for P a decrease followed by a pick up of the P content (Figure 11.20 (c)).

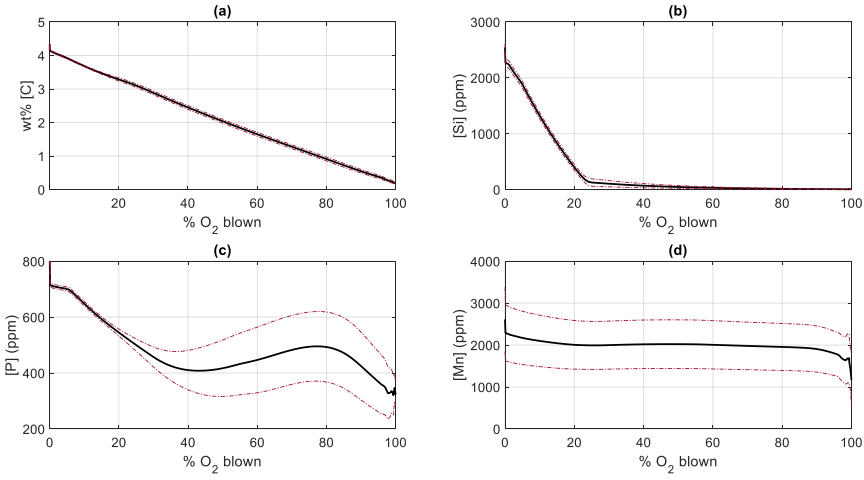

Figure 11.20: Average steel composition evolution for TD BOF simulated heats as function of the %O_2 blown into the process. The red dotted lines are the standard deviations. The average is calculated for the validation dataset with the 'grpstats' function of Matlab, grouping the data per calculation step. Figure (a) shows the carbon content of the steel, (b) the silicon content, (c) the phosphorus content and (d) the manganese content

To validate the slag composition only the three major slag components are considered: FeO_n, CaO and SiO_2. For these components the expected trends are well known and can be consulted in Chapter 2. In Figure 11.21 (left) the average evolution of the Fe content in the liquid slag is shown. As expected a steep increase at the start of the process is observed while after some time the iron content decreases, not reaching zero, to increase again towards the end of the process. This kind of behaviour is expected for a BOF steelmaking slag (e.g. ref. to Figure 10.9). The average composition of the three major slag components in the liquid slag is also as expected, as shown in Figure 11.21 (right). The FeO_n behaviour affects the ternary slag composition as expected: the slag mostly consists out of CaO and FeO_n and only around 10 wt% SiO_2. Even at the first stages of the process, this is as expected. Hence, the average trends in slag evolution for the ternary components seem to be trustworthy. Especially, during the first part of the process, for which this set of model parameters is intended.

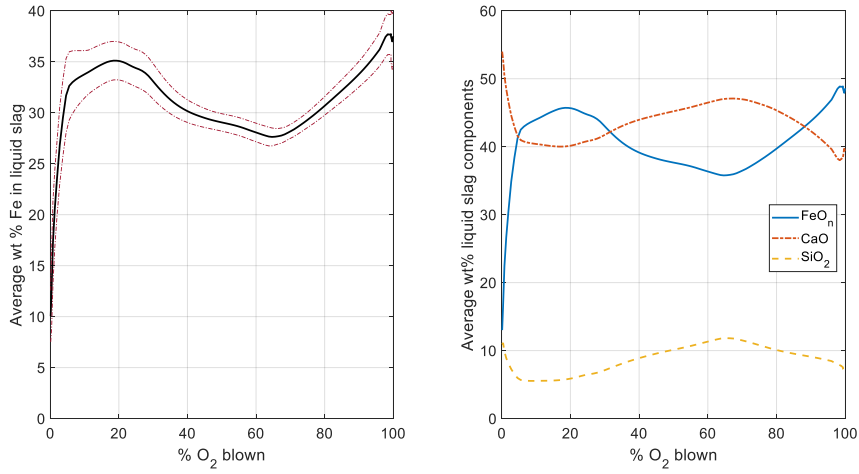

Figure 11.21:(left) The average iron content of the liquid slag and the average liquid slag composition. The red dotted lines, in the figure of the Fe content evolution, are the standard deviations. (right) The evolution of the average ternary composition of the liquid slag phase, as calculated with the TD BOF model. The average is calculated for the validation dataset with the 'grpstats' function of Matlab, grouping the data per calculation step.

Finally, the decarburisation rates for the simulated heats need to be evaluated. This is shown in Figure 11.22. For the overall average decarburisation profile a good description at the start of the process is observed. There is an initial lower constant decarburisation rate followed by a steady increase until the maximum decarburisation rate. However, unlike industrially observed this maximal value is not maintained for the rest of the blow. This discrepancy has already been discussed in the fitting evaluation and it was one of the arguments to state that the current set of model parameters only allows to describe the first 40% of the process. The results in Figure 11.22 merely confirm this earlier observation. Furthermore, the industrial data revealed a strong correlation between the moment during the blow where the decarburisation rate increases after the first constant decarburisation rate and the silicon content of the liquid hot metal. Industrially, this increase started at a higher % O_2 blown in the process for higher silicon contents in the liquid hot metal. As can be seen in Figure 11.22, thermodynamically the same behaviour is observed. This shows the TD BOF model is not only able to describe the decarburisation quite accurately at the start of the process, but also the major effect of differences in the input material streams is described correctly.

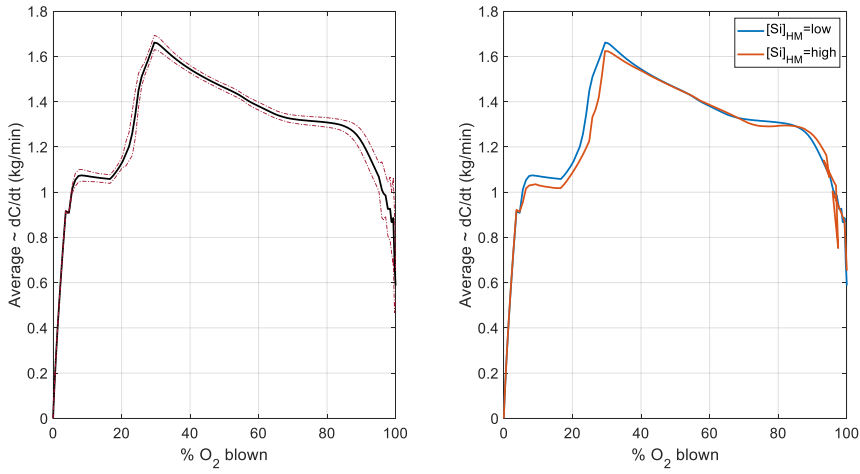

Figure 11.22: (left) Average decarburisation profile for the heats simulated with the TD BOF model. The standard deviations are indicated with red dashed lines. (right) The effect of the Si content of the hot metal on the average decarburisation profile. The average is calculated for the validation dataset with the 'grpstats' function of Matlab, grouping the data per calculation step.

A final critical note should be added before formulating the conclusion of the chapter. The discrepancy between the TD BOF model with the theoretical calculated reaction volumes and the measured industrial reality is solved via introduction of correction parameters that are fitted to industrial data. This approach results in a TD BOF model with two different set of parameters that simulates the process properties rather well for most components. However, the current model is very interesting for industrial oriented research, which is clearly within the scope of the current work, but cannot be used for fundamental research. The results of the model are similar to industrial measurements yet, that does not necessarily mean the kinetics and dynamics of the process are fundamentally correctly modelled.

11.5 Conclusion

The results of the TD BOF model with reaction volumes with their theoretically calculated size are discussed at the beginning of this chapter. It is clear that these theoretical reaction volume sizes are not suited to describe the process correctly. To solve this, a set of model parameters is introduced to compensate for certain deviations between the model assumptions, under which these theoretical volumes are calculated, and the observed reality. A fitting between the model, with variation of the set of model parameters, and industrially executed heats is described. This fitting is handled as an

optimisation between simulated and measured data and two different error functions are defined to describe the discrepancy between the TD BOF model and the AMG measurements. For both error functions a different solution is found after minimalization of the error value for five heats. The first set of parameters gives an accurate description of the end of blow properties, yet is unable to describe the very start of the process. The second set of parameters describes the start of the process very accurately however, is unable to give an accurate description of the second half of the process nor of the end of the process properties. It is concluded that it is impossible, with the current model description, to define one unique set of model parameters constant during the process to describe the complete process. Finally, both sets of model parameters are validated with a new set of industrially simulated heats. Most important general process aspects are simulated acceptably to good with the TD BOF process. The major observed deviations are the underestimation of the final steel and slag temperature and that the behaviour of manganese in the process is not described accurately at all. Overall, the current model is an interesting tool for industrial oriented research, which fits perfectly to the context of the current work. The model can be used to identify potential new working areas for the BOF process at AMG. In case the results are promising, the simulations could be verified with carefully designed industrial trials. In the next chapter, the potential use of the current TD BOF model is demonstrated with a case study on the addition of MgO. Yet, for more fundamental research or for a more widely applicable model, a more fundamental approach would be necessary on the level of the implemented reaction volumes.

11.6 References

[1] S. C. Koria and K. W. Lange, “Penetrability of impinging gas jets in molten steel bath,” *Steel Res.*, vol. 58, no. 9, pp. 421–426, Sep. 1987, doi: 10.1002/srin.198700241.

[2] B. T. Maia, R. K. Imagawa, A. C. Petrucelli, and R. P. Tavares, “Effect of blow parameters in the jet penetration by physical model of BOF converter,” *J. Mater. Res. Technol.*, vol. 3, no. 3, pp. 244–256, Jul. 2014, doi: 10.1016/j.jmrt.2014.06.010.

[3] R. Sarkar, P. Gupta, S. Basu, and N. B. Ballal, “Dynamic Modeling of LD Converter Steelmaking: Reaction Modeling Using Gibbs’ Free Energy Minimization,” *Metall. Mater. Trans. B*, vol. 46, no. 2, pp. 961–976, Apr. 2015, doi: 10.1007/s11663-014-0245-2.

[4] Publications Office of the European Union, “Imphos : improving phosphorus refining.,” Dec. 14, 2011. https://publications.europa.eu/en/publication-detail/-/publication/8aecbb7c-f77f-4ee7-bc38-9ebb13b52faf/language-en (accessed Nov. 06, 2018).

[5] H. W. Meyer, W. F. Porter, G. C. Smith, and J. Szekely, “Slag-Metal Emulsions and Their Importance in BOF Steelmaking,” *JOM*, vol. 20, no. 7, pp. 35–42, Jul. 1968, doi: 10.1007/BF03378731.

[6] B. K. Rout, G. Brooks, Subagyo, M. A. Rhamdhani, and Z. Li, “Modeling of Droplet Generation in a Top Blowing Steelmaking Process,” *Metall. Mater. Trans. B*, vol. 47, no. 6, pp. 3350–3361, Dec. 2016, doi: 10.1007/s11663-016-0773-z.

[7] J. Biswas, S. Ghosh, N. B. Ballal, and S. Basu, “A Dynamic Mixed-Control Model for BOF Metal–Slag–Gas Reactions,” *Metall. Mater. Trans. B*, Mar. 2021, doi: 10.1007/s11663-021-02094-w.

[8] G. Snigdha, B. N. Bharath, and N. N. Viswanathan, “BOF process dynamics,” *Miner. Process. Extr. Metall.*, vol. 128, no. 1–2, pp. 17–33, Apr. 2019, doi: 10.1080/25726641.2018.1544331.

12 Case study: The effect of MgO

In the previous chapters a thermodynamic BOF model was developed and described. The current chapter shows some firsts results, exploring and demonstrating the use of the model for the industrially oriented research questions of this dissertation. A case study on the MgO addition is used to verify whether the thermodynamic simulations give similar results and effects as industrially expected.

12.1 Methodology

To show the potential of the thermodynamic BOF model (TD BOF) described in the previous chapters, it has been decided to focus on the role of MgO in the process. The reason is twofold. Firstly, MgO is industrially observed to be important for refining, interaction with refractory and foaming as well. This makes it an ideal component to evaluate the three roles of the slag in the BOF process. Secondly, the addition of MgO in the process can be easily monitored by adding dolomitic lime (dolo – lime). This flux is either added or not. For other interesting components, such as Al_2O_3, the variation in the added amount is less controllable due to the fact that an important source for alumina are the scrap materials, which will be added to all the heats. Yet, not necessarily in the same amounts which results in differences in Al_2O_3 content for the end of blow slag.

Two sets of heats are defined. One set of heats with addition of dolo - lime and one without this flux addition. To generate industrially relevant input material streams for each heat, the AMG model is used. The two datasets contain the same heats but in one dataset the input of the heat is calculated with the possible addition of the dolo – lime, while in the second dataset the input of the same heat is calculated without the addition of the dolo – lime. The dataset contains 65 heats.

For the TD BOF model two different sets of parameters are used, shown in Table 12-1. Set A is obtained after fitting to the alternative error and is found to give a good description of the onset and first part of the BOF process. Set B is obtained after fitting of the general error and gives better results for the general process and especially for the final conditions of the process.

Table 12-1: Overview of the solutions of the optimisation

	Factor 1 (JIZ)	Factor 2 (IF)	Factor 3 (EMU)	f_{emu}
Set A	17.58	0.78	0.50	0.28
Set B	26.06	0.72	3.03	0.39

The volumetric gas flow and the lance height pattern used in the TD BOF model are based on the industrial common practices for these types of heats. They cannot be shown due to confidentiality. A calculation step of 0.2 ton O_2 was used, corresponding to 110 till 130 calculations steps for each heat. This was also the calculation step used in the fitting of the model parameters. A calculation step of this size allows to give enough details of the process, combined with acceptable calculation time.

12.2 Results and discussion

To discuss the effect during the process, parameters of Set A are used. The results are shown as average results for the 65 heats. It is important to stress that even though the complete process time is shown (0 – 100% O_2 blown) on these figures, the simulated results are only trustworthy until 40% O_2 blown. This was thoroughly discussed in the previous chapter on parameter fitting and model validation. The reason to show the complete process time nevertheless, is to allow to discuss the trends of the evolution. The effect at the end of the blow are analysed with simulations with parameters of Set B. For most of the discussion in this chapter calculations with Set A are used, in the case Set B was used this is clearly stated.

12.2.1 Interaction with refractory

Earlier in this dissertation, section '4.2.1 Effect of MgO', the effect of MgO on refractory wear was discussed. It was explained that due to the use of MgO-based refractory materials, the saturation of the slag in MgO is important to decrease the refractory wear. Thus, it is expected that slags with an activity of solid MgO equal to 1, or slags in which solid MgO is precipitated, will be beneficial for refractory wear. The saturation in MgO is most easily visualised via the amount of precipitated solid MgO, shown in Figure 12.1.

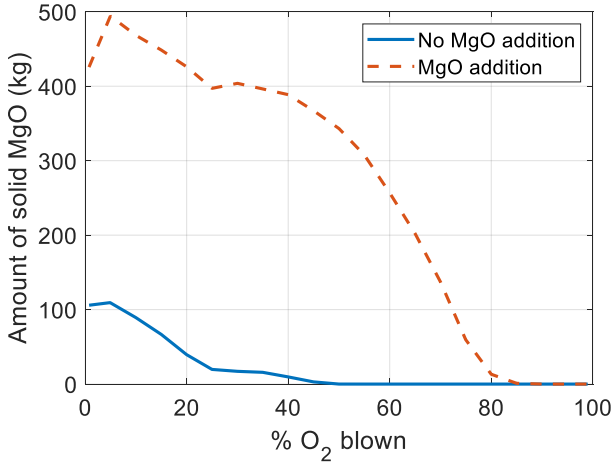

Figure 12.1: The average total amount of solid MgO for the dataset with and without addition of the MgO rich flux. The average is calculated from the selected dataset with the 'grpstats' function of Matlab, grouping the data per calculation step

From the two evolution profiles in Figure 12.1, it is observed that the dataset with the addition of the MgO rich flux has slag evolutions for which this MgO saturation is observed for a longer period during the process. This is expected. Whereas the heats without addition of the MgO rich flux are no longer saturated in MgO around 40% O_2 blown, the heats with addition of the MgO rich flux are still saturated. The MgO dissolution is strongly linked with the FeO_n content of the slag. Hence, it is impossible to verify with the current simulation limitations if the trends after 40% O_2 blown are correct. Considering only saturation, and assuming that once saturated in MgO this is sufficient to protect the refractory material, also for the heats without the addition of the MgO rich flux, the refractory material is protected at the early stages of the process from a thermodynamic viewpoint. For future work, it might be interesting to consider the effect of different components, e.g. Al_2O_3, on this MgO saturation.

Apart from saturation also the viscosity of the liquid slag could be important for the interaction with the refractory. [1] If a slag has a very low viscosity, the possibility to interact and penetrate in the pores of the refractory material could be higher. The results in Figure 12.2 indicate however, that the liquid slag viscosities for both datasets are nearly identical. The compositions of the liquid slags are too similar to have a distinct different viscosity.

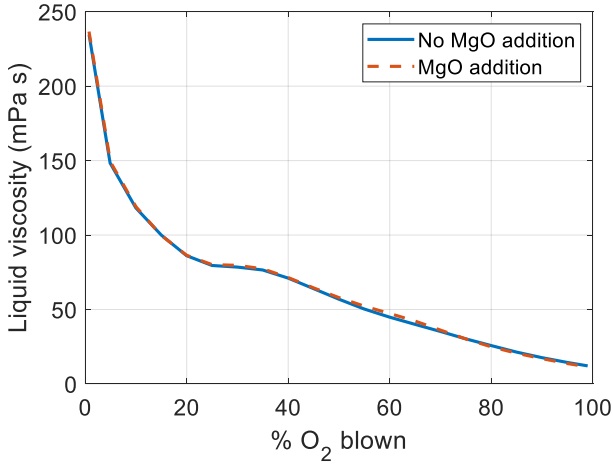

Figure 12.2: The average liquid viscosity for the dataset with and without addition of the MgO rich flux. The average is calculated from the selected dataset with the 'grpstats' function of Matlab, grouping the data per calculation step

12.2.2 Foaming behaviour

As described earlier in this work, chapter 8, the foaming of a heat is industrially monitored with an acoustic measurement. A high acoustic signal means that there is little damping and hence, there is less slag foaming. Analysis of the acoustic signals for a large dataset of executed heats, showed that there is a difference in behaviour when the MgO rich flux is added or not. In Figure 12.3 (left) it is demonstrated that the acoustic signal is, on average, lower for heats with addition of the MgO rich flux compared to heats where this flux is not added. The lower signal corresponds to more foamy slags. Hence, from industrial observations it is concluded that addition of MgO increases the foaming behaviour of the slag.

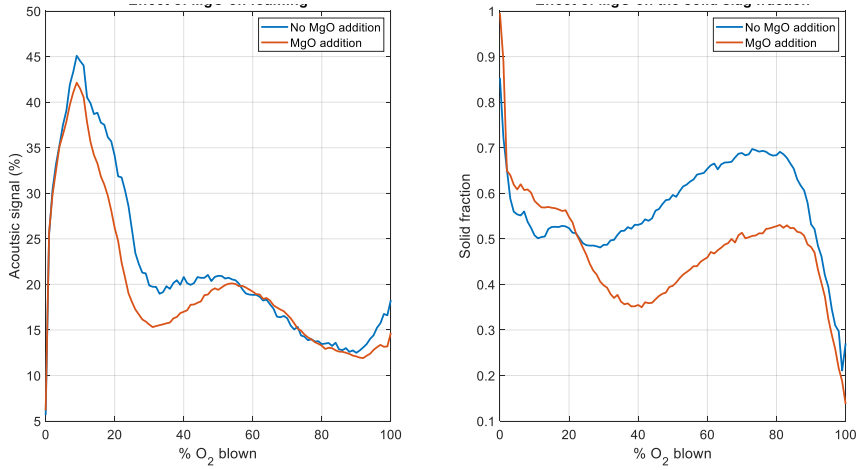

Figure 12.3: (left) Industrially observed difference in acoustics signal and (right) difference in industrially expected solid fraction (based on the off-gas analyses described in chapter 7) between heats with and without the MgO rich flux. These are averages calculated for a large set of actual executed heats.

In chapter 8, it was concluded that it is impossible to link the foaming uniquely to slag compositions and properties. Yet, the liquid slag viscosity was identified as the most important physical slag property to consider when discussing foaming. From the results shown in Figure 12.2, it is clear that there is no significant difference in the calculated liquid slag viscosities for heats with and without the addition of the MgO rich flux. Apart from liquid viscosity, also the solid fraction and the gas evolution will be important. The role of solids in foaming is ambiguous: more solids increase the apparent viscosity but a too high solid fraction will have a destructive effect on foaming. [2], [3] Because foaming is an effect of retained gas, difference in gas evolution could also be the reason for differences in foaming behaviour. [4], [5] Both the solid fraction and the gas evolution, via decarburisation rates, are shown in Figure 12.4.

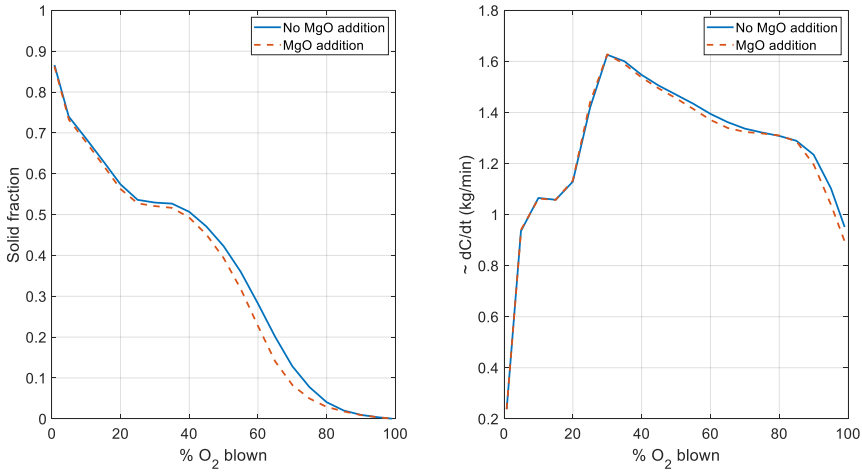

Figure 12.4: (left) average evolution of the solid fraction and (right) average decarburisation rates for the dataset with and without addition of the MgO rich flux. The average is calculated from the selected simulation dataset with the 'grpstats' function of Matlab, grouping the data per calculation step. The decarburisation rate is normalised by dividing the absolute value by a fixed constant.

There is no relevant difference observed between the average decarburisation profiles of the heats with and without the MgO rich flux addition. The gas evolution rates are for both types of heats nearly similar and cannot be used to explain the difference in industrially observed foaming behaviour. The average solid fraction evolutions show a different behaviour. The heats with addition of the MgO rich flux have on average a smaller solid fraction thus less solids present in the slag. This is potentially a reason for different foaming behaviour: if for both types of heats the solid fraction is considered too high and to have a negative effect on the foaming. Yet, due to the ambiguous effect of the solids it is impossible to quantify this with the current knowledge on foaming and role of the solids. Additionally, this difference in solid fraction was also observed from analysis of the heats used to describe the foaming behaviour in chapter 8, as is shown in Figure 12.3 (right). The differences in solid fraction are more pronounced though on this figure compared to the results of the current TD BOF simulations shown in Figure 12.4 (left).

It is an interesting result that the MgO rich heats have a lower solid fraction and thus a higher liquid fraction for the thermodynamic simulations, while the results in Figure 12.1, clearly indicate the absolute mass of solid MgO is higher for these heats. The reason for this is the difference in working point when the MgO rich flux, dolo – lime, is added. Industrially, as a standard method, lime (containing mainly CaO and only minor amounts

of MgO) is added to the process to ensure protection of the vessel lining. When dolo – lime is added the amount of lime added to the process is decreased. Heats with the addition of dolo – lime will thus contain less lime. This results in a different standard basicity (considering only CaO) for these heats, as shown Figure 12.5, while the difference in alternative basicity (considering both MgO and CaO) between the two types of heats is smaller. Consulting the phase diagram shown in chapter 4, Figure 4.2, illustrates how a higher basicity results in a higher solid fraction for identical iron content in the slag and identical slag system. For MgO additions a strong reduction of the liquidus area was observed in Figure 4.5. Nevertheless, it seems that the difference in basicity and hence, in CaO content of the slag, is more dominant in the effect on solids than the added MgO for the current considered systems. Note that the basicities on Figure 12.5, at the very beginning of the process are very high due to the ongoing formation of SiO_2.

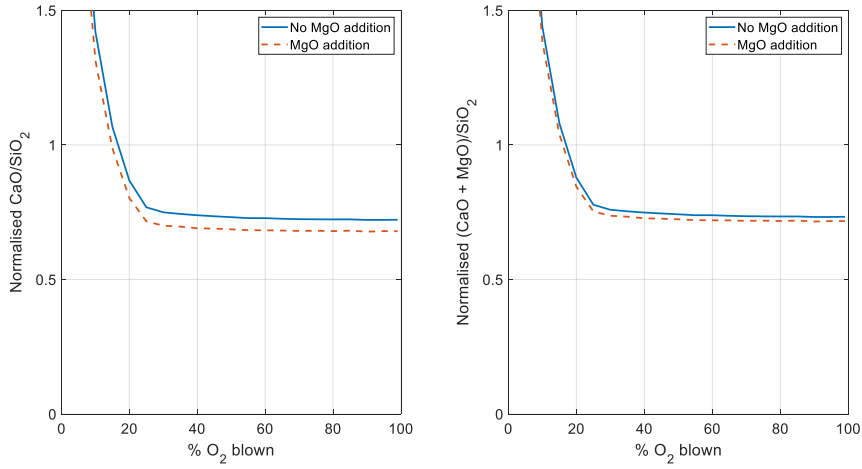

Figure 12.5: (left) average standard total basicity and (right) average alternative total basicity for the dataset with and without addition of the MgO rich flux. The average is calculated from the selected dataset with the 'grpstats' function of Matlab, grouping the data per calculation step

12.2.3 Effect on refining

The effect of MgO on refining, especially dephosphorisation, was already discussed in chapter 4. The most important effect is shown in Figure 12.6. For a higher MgO content in the end of blow slag, the phosphorus distribution coefficient between slag and steel decreases. A less good dephosphorisation is observed for heats with higher MgO contents.

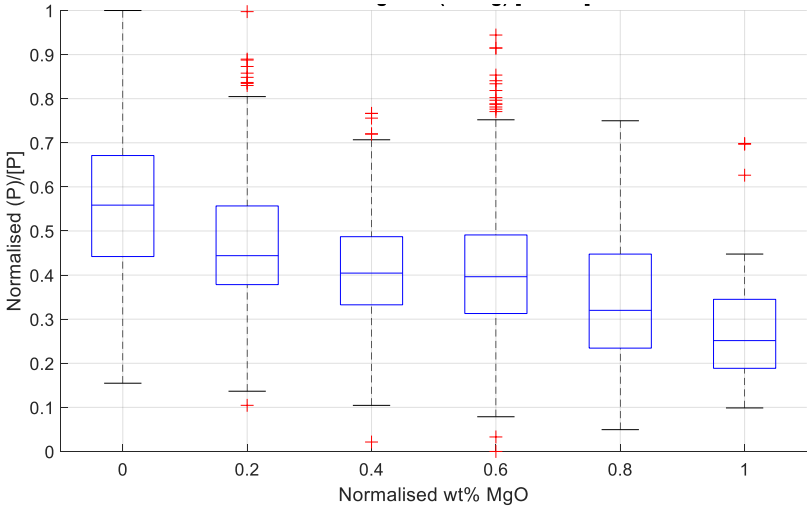

Figure 12.6: Effect of MgO content of the slag on the phosphorus distribution coefficient ($(P)_{slag}/[P]_{steel}$)) from industrial ArcelorMittal Ghent data for a fixed temperature interval around 1650°C. The box plots show the median value with indication of the first and third quartile. The error bars the lowest and largest datapoints without the outliners. The outliners are shown with red crosses. Both variables are normalised between the industrial relevant minimum and maximum value.

The data shown in Figure 12.6 are the median and deviations calculated from a large set (data of more than a year) of actual executed heats, showing the overall effect of higher MgO content in the slag. In reality, not only MgO content but also temperature and the FeO_n content of the slag are crucial parameters to calculate the phosphorus content for the industrial simulation. Comparing the data on dephosphorisation according to the thermodynamic calculation, for which Set B is now used, since end of blow data is required, for the dataset with and without addition of the MgO rich flux only makes sense if the other important parameters are also similar. This is not the case for the largest share of the heats. Especially, the iron oxide content, and hence the oxygen content of the steel to which the dephosphorisation is linked, is very different for the largest part of the heats as shown on Figure 12.7. This is data for only 65 heats and thus not sufficient to perform sensible statistical analysis as the one shown in Figure 12.6. Consequently, to discuss the effect of MgO on the dephosphorisation the data is limited to the eight heats with low, and nearly identical, Fe content in the slag between the simulation with and without the MgO rich flux addition. The difference in temperature between these heats is maximal 5°C, thus the temperature effect on dephosphorisation can be neglected for this group of heats as well.

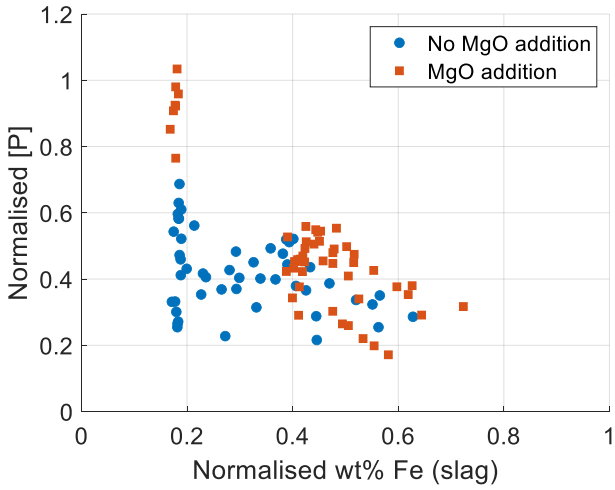

Figure 12.7: The phosphorus content of the steel phase as a function of the iron content of the slag. Due to confidentiality, both variables are normalised.

The effect of the MgO content in the slag on the dephosphorisation is shown in Figure 12.8 for the industrial and thermodynamic calculation. The average phosphorus content in the steel increases clearly for both types of simulations when the MgO content of the slag is higher. For the thermodynamic calculation a larger variation is calculated for this set of eight heats. The thermodynamically calculated phosphorus content has more variation than the industrial one. Considering only the effect of MgO, the thermodynamic model predicts the same trends on dephosphorisation behaviour as industrially observed.

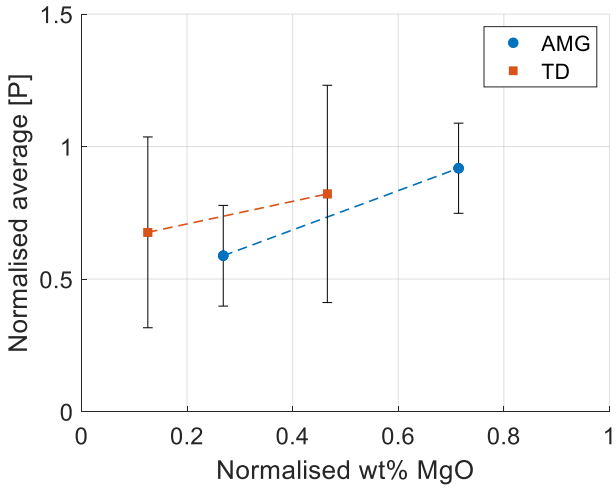

Figure 12.8: The effect of MgO content in the slag on the phosphorus content of the steel phase.

The thermodynamic model allows to investigate the effect of adding the MgO rich flux on the evolution of the slag. Hence, apart from the final phosphorus content, calculated with the parameters of Set B, also the evolution of the phosphorus distribution coefficient can be examined, calculated with the parameters of Set A, as is shown in Figure 12.9. On average, a slightly higher coefficient, hence better dephosphorisation, is observed for the heats with the MgO rich flux added from 0 till 40 % O2 blown into the process. Afterwards, the phosphorus distribution coefficient decreases, thus there is a less good dephosphorisation, for the heats with the MgO rich flux added.

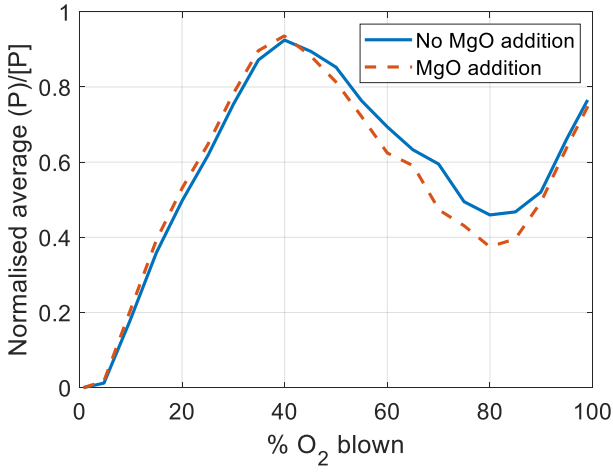

Figure 12.9: Average evolution of the phosphorus distribution coefficient ($(P)_{slag}/[P]_{steel}$) during the process. The average is calculated from the selected dataset with the 'grpstats' function of Matlab, grouping the data per calculation step.

The phosphorus is either present in the liquid slag as phosphorus oxide (P_2O_5) or in the calcium silicate solid solution (C_2S-C_3P). Figure 12.10 shows both the fraction of the calcium silicate containing phosphorus, as well as the fraction of P_2O_5 in the total slag. For the heats with addition of the MgO rich flux, the amount of calcium silicates is initially higher, while the phosphorus oxide content is either similar or lower compared to the heats without this flux. At 40% O_2 blown, the fraction of calcium silicates decreases for the heats with the MgO rich flux, while for the heats without there is still an increase at that point in the process. Later on, the fraction of calcium silicates also decreases for these heats, but the total fraction of calcium silicates present in these systems is higher. The calcium silicates are also stable up to a later point in the blowing process. At the same time, the fraction of P_2O_5 is always lower for the heats with the MgO rich flux added. This explains the observed difference in distribution coefficient during the process. It should be noted though that from the validation in chapter 11, it was concluded the results of the current TD BOF model are only trustworthy till 40% O_2 blown. For a thorough evolution of these effects, the TD BOF model needs to be adapted to be able to describe the complete process accurately.

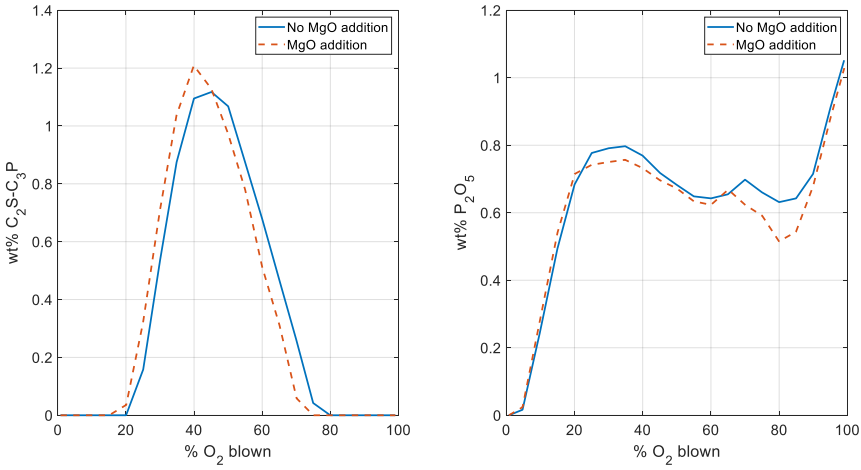

Figure 12.10: (left) Average fraction of calcium silicates containing P as function of the oxygen blown into the process. (right) Average fraction of P_2O_5 during the process. The average is calculated from the selected dataset with the 'grpstats' function of Matlab, grouping the data per calculation step.

12.3 Conclusion

In this chapter some preliminary results of the TD BOF model with the fitted parameters from Set A or Set B are discussed. The effect of MgO was selected as case study because it allows to describe the effect on all the three defined roles of slag: refining, refractory interaction and foaming. An industrial dataset was used as input for this case study. The thermodynamic simulation confirmed the results which were expected from industrial observations. However, it is also clear that for a full analysis a more accurate description of the slag evolution is required. This is the topic of the next chapter.

12.4 References

[1] R. Sarkar and H. Y. Sohn, "Interactions of Alumina-Based and Magnesia-Based Refractories with Iron Melts and Slags: A Review," *Metall. Mater. Trans. B*, vol. 49, no. 4, pp. 1860–1882, Aug. 2018, doi: 10.1007/s11663-018-1300-1.

[2] A. P. Luz, T. A. Ávila, P. Bonadia, and V. C. Pandolfelli, "Slag Foaming: Fundamentals, Experimental Evaluation and Application in the Steelmaking Industry," *Refract. WorldForum*, vol. 3, p. 91, 2011.

[3] R. A. M. de Almeida *et al.*, “Slag Foaming Fundamentals - A Critical Assessment,” *Mater. Res.*, vol. 20, no. 2, pp. 474–480, Apr. 2017, doi: 10.1590/1980-5373-mr-2016-0059.

[4] J. J. Bikerman, *Foams*. Springer Science & Business Media, 2013.

[5] V. Cnockaert, I. Bellemans, K. Verbeken, T. Crivits, and B. Blanpain, “On the origin of sudden slag foaming during copper smelting,” presented at the Copper 2019, Vancouver, 21/08 2019.

13 Towards a more advanced TD BOF model

In the previous chapters the TD BOF model, parameter fitting for the model and model results have been discussed. From the parameter fitting it was concluded that with the current model implementation it is impossible to find one set of model parameters to describe the complete process accurately. Either, the set of parameters describes the start of the process well or it describes the final properties in a good way. In this chapter, possible solutions to combine the different set of parameters, and hence, implement a model with a set of model parameters that is variable over time, are discussed. Some examples are shown and their results are discussed.

13.1 The combination of different set of model parameters

For the TD BOF model different reaction zones with corresponding reaction volumes are defined. Preliminary results showed however, that with theoretically calculated reaction volumes the thermodynamic simulations show significant discrepancies with the industrial process (both evolution and final conditions). Different reasons were put forward for this in previous chapters (see '11.1 Motivation for fitting'). To tackle part of these reasons, a set of model parameters was introduced which act as a correction for the theoretic reaction volumes. These parameters were determined via a fitting of the TD BOF simulation results to industrial measurements. Details on the meaning of these parameters and the performed fitting can be consulted in earlier chapters (see chapter 11). From the original fitting of the TD BOF model to industrial data two different solutions for the set of parameters were put forward and are shown in Table 12-1. Set A is obtained after fitting to the alternative error and is found to describe the onset and first part of the BOF process rather well. Set B is obtained after fitting of the general error and gives better results for the general process and especially for the final conditions of the process. To evaluate the possibility to combine the different sets of the model parameter, the industrial heats used for the fitting of the model parameters are considered. For these five heats, industrial information on their evolution as well as the measured end properties are known.

Table 13-1: Overview of the solutions of the optimisation

	Factor 1 (JIZ)	Factor 2 (IF)	Factor 3 (EMU)	f_{emu}
Set A	17.58	0.78	0.50	0.28
Set B	26.06	0.72	3.03	0.39

13.1.1 Piecewise combination of the parameter sets

To predict the complete process evolution better, rather than work with two different sets of parameters depending on the specific research topic, a combination of the two sets of process parameters is proposed. A first, straightforward, idea to combine these parameters could be to do this depending on the time in the process, according to equation 13.1. The threshold value of 50% O2 blown into the process is chosen because this is the defined threshold value for the error function used in the fitting to obtain Set A.

$$Set = \begin{cases} Set\ A & \%O_2 < 50\% \\ Set\ B & \%O_2 \geq 50\% \end{cases} \tag{13.1}$$

Although, seemingly a combination of two different parameter sets, the implemented combination shows an abrupt change in behaviour of the different properties during the process and hence there is no real effect of the combination. This is shown in Figure 13.1. This is to be expected because there is an immediate change between the two different sets of parameters. Due to the big increase in the amount of metal in the reaction zones when switching from Set A to Set B, nearly all the FeO_n in the slag is consumed immediately. The slag composition changes drastically and abruptly. The decarburisation curve shows a few out-of-line points, where the decarburisation rate is significantly higher than measured or otherwise calculated. This method to combine the different parameters, clearly does not give any better results than using the separate set of model parameters. The only advantage is that from a calculation time viewpoint the amount of calculation is decreased by a factor two. To ensure a smoother transition from one set of parameters to the other, a gradual combination of the different parameter sets is proposed.

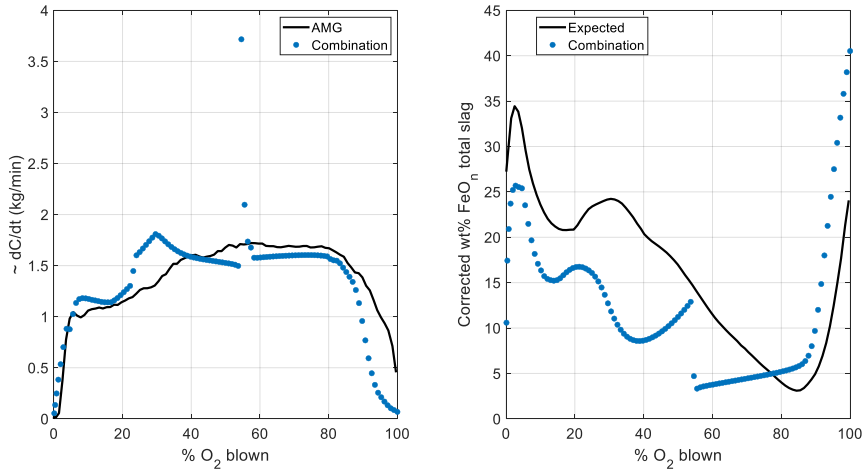

Figure 13.1: (left) Decarburisation profile and (right) FeO_n evolution[14] measured or expected according to AMG data versus the TD BOF simulation with a piecewise combination of the parameter sets.

13.1.2 Linear combination of the parameter sets

Unlike the method mentioned above, the current method gradually changes the used set of parameters from Set A to Set B with the method shown in equation 13.2. For the first part of the process, 100% of Set A is assumed. Next, from a certain threshold value (x) onwards the used set is a combination of Set A and Set B until a second threshold value (y). For the final part of the process Set B is used.

$$Set = \begin{cases} Set\ A & \%O_2 \leq x \\ (100\% - a) * Set\ A + a * Set\ B & x < \%O_2 < y \\ Set\ B & \%O_2 \geq y \end{cases} \qquad (13.2)$$

A linear profile is used to determine the value of the parameter a between the two threshold values x and y. This principle is schematically shown with the example in Figure 13.2 for the gradual change from Set A to Set B for the reaction volume of the Jet Impact zone (JIZ).

[14] Corrected wt% FeO_n : To compare the FeO_n content of the TD BOF model simulations to the industrial profiles, the calculated slag compositions are corrected to compensate for the assumptions on the flux addition.

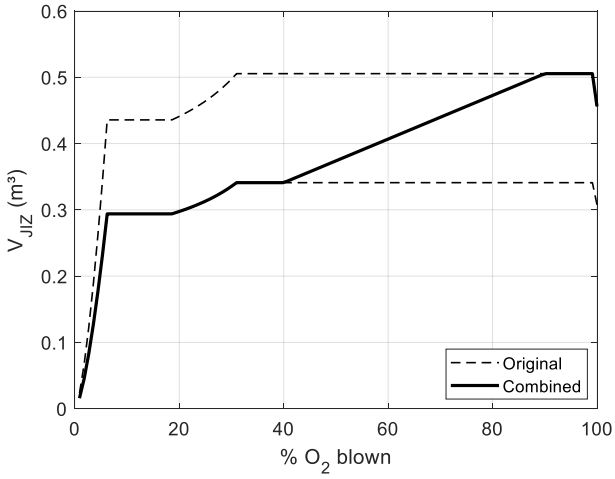

Figure 13.2: Illustration of the gradual change (linear profile) from Set A to Set B for the Jet Impact zone.

The second threshold value, y, is fixed at a value of 90% O_2 blown. The reason is that during the discussion of the model results for parameter Set B it was concluded the simulations gave good results from 90% O_2 onwards. For the first threshold value, x, different options are considered. Firstly, the fitting for Set A has been performed with the error function defined between 0% and 50% O_2 blown in the process. This makes 50% a logical first value for the threshold. However, during analyses of the results, it was concluded that for Set A the simulations with the TD BOF model gave rather good results till 40% O_2 blown. Finally, for a complete investigation of this value, it is decided to also discuss the results at 30% O_2 blown and evaluate whether identical trends are observed for the model.

From the results shown in Figure 13.3 it is clear that a more gradual transition is observed in the decarburisation profiles. Upon changing the value of the parameter set from Set A to the combination of Set A and Set B, an increase in decarburisation rate is observed. This can be explained due to the increase in reaction volume. However, due to the fact that with this method the increase from the reaction volume size is less steep than with the previous method, the increase in decarburisation rate is also less exaggerated. The decarburisation rate decreases afterwards and reaches the expected value for the TD BOF simulation at about 60% O_2 blown. The decarburisation rate, at the end of the process, decreases slightly earlier in the process compared to the simulation with set B. Considering the FeO_n content of the slag, in Figure 13.4, similar results are observed. Unlike the simulation for Set A, a decrease in FeO_n content is observed when the

combined set is used. This decrease is gradual until the FeO_n content corresponds to the one calculated with the simulation using Set B. This happens around a value of 50% O2 blown in the process. This corresponds to the maximal reached decarburisation rate of this simulation.

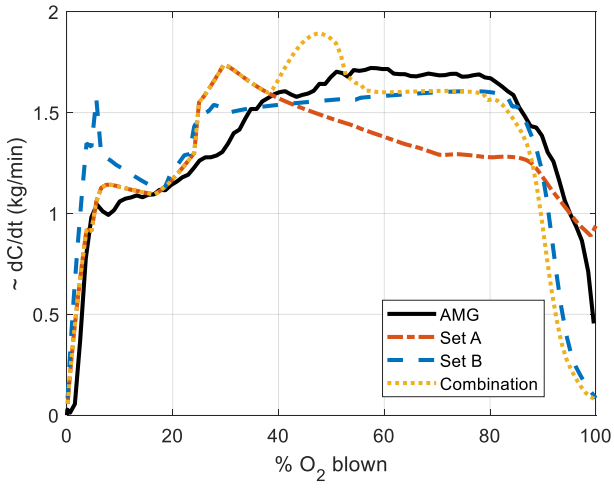

Figure 13.3: Comparison of the measured decarburisation profiles and the simulated profiles for one heat. Simulations with different model parameters are shown. The combination in this figure is a linear combination with threshold x = 40% and y = 90% O_2.

The transition peak in decarburisation rate is due to a peak in the amount of indirect carbon oxidation via FeO_n. As long as Set A is used, the amount of metal in the reaction is small and the corresponding slag limit is small as well. The amount of liquid slag present is larger than the slag limit and not all the FeO_n formed in the JIZ reacts. Using the combined set, increases the amount of metal present in the emulsion zone and thus, as well the value for the slag limit. More metal and liquid slag react in the emulsion zone and the decarburisation rate increases. However, as the amount of metal keeps increasing, the slag limit value also increases until the moment that this limit is larger than the liquid slag present in the system and thus all this liquid slag, and all FeO_n, reacts in the emulsion zone, resulting in consumption of nearly all the FeO_n formed in the JIZ. From this point on, the amount of liquid slag present in the system will be the dominant factor for the amount of carbon that can be removed via indirect reduction. This is the case until the carbon content decreases strongly towards the end of the process. Together with the decrease in carbon content at the end of the process the decarburisation rates decrease as well. As important side note, the total carbon removal

is not only determined by the indirect carbon oxidation, also the direct oxidation of carbon both in the JIZ and during homogenisation of the metal phase (refined metal droplets from the emulsion zone will react with the unrefined metal bulk) contributes to the carbon removal.

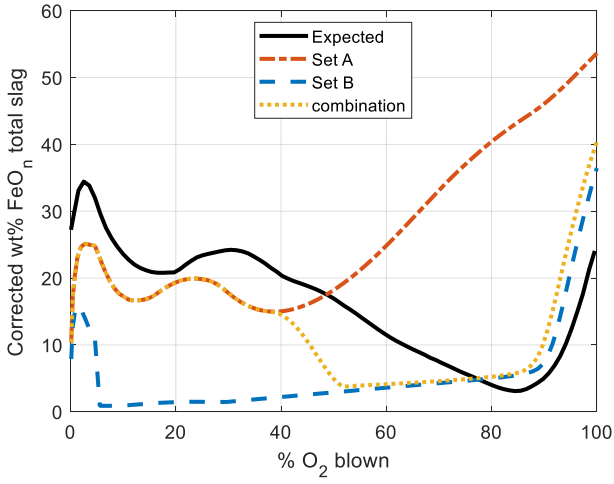

Figure 13.4: The iron content of the total slag for one heat: expected versus simulated with different model parameters. The combination is a linear combination with threshold x = 40% and y = 90% O_2.

Identical trends are observed if the onset threshold (*x*) is varied to 30% or 50% O_2 as can be observed in Figure 13.5. Although, from these figures it seems that for the considered heat the simulation with onset on 40% O_2 blown, gives the results closest to the familiar expected evolutions for both properties. To evaluate this quantitatively and for five heats instead of just one, the same error function as for the fitting ('11.2.1 Defining the error function') is used. Considering both the deviation between the decarburisation curves and the important end of blow properties. The average deviation between the decarburisation curves is considered separately as well. The results are shown in Figure 13.6.

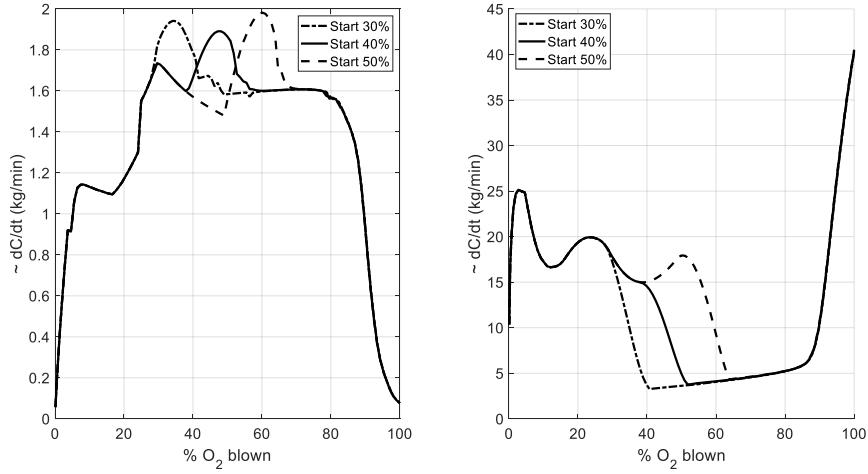

Figure 13.5: Effect of the variation of threshold value x on (left) the decarburisation and (right) FeOn profile for one heat.

The results in Figure 13.6 (only considering the blue round data points at this instance) indicate that the deviation between the measured and simulated decarburisation rate (as shown in the right part of the figure) is indeed, for the three simulations with a combined set of model parameters, smallest for the simulation with the threshold for the linear combination for the parameters at 40% O_2 blown. This is as expected from the discussed evolutions. Additionally, the smaller deviations indicate that overall these simulations predict better decarburisation rates for all the heats. Considering the general error, and thus also the final properties of the simulations, an increase of general error is observed for the simulations with the combined set of parameters compared to the constant use of Set B. This is an increase of about 100 and mainly due to a slightly larger deviation in the calculated steel temperature. The simulations with the combined parameters, predict a smaller steel temperature than the one with constant use of Set B. Furthermore, the deviation for the simulations with combined parameters is also larger, indicating that for some heats the general error will be relatively small, while for others much larger.

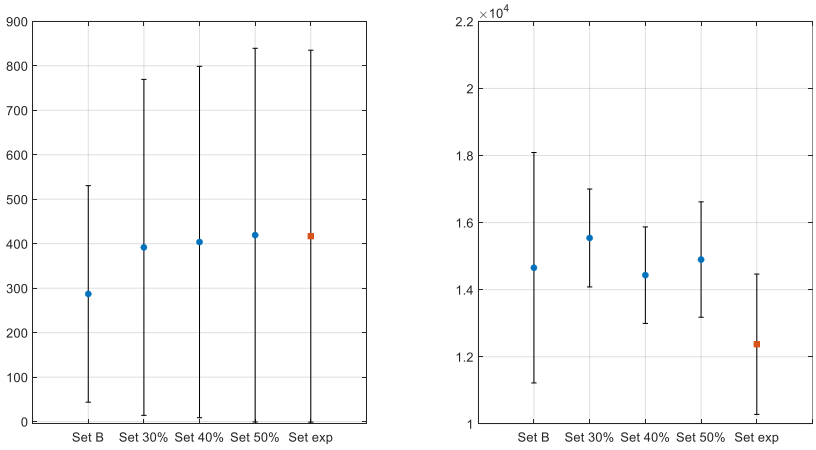

Figure 13.6: Average general error (considering final conditions and decarburisation) and average deviation between decarburisation curves between simulations and industrial measurements for five heats.

13.1.3 Exponential combination of the parameter sets

From the results discussed so far, it is concluded that the combined simulation gives best results for an onset x of 40% oxygen blown into process. However, the discussed profiles show that the change in parameter values might even still be too drastically to simulate the slag evolution correctly. Even though the change is more gradual, there is still the observed increase in decarburisation rate although it is continuous while the piecewise combination gave some very high and out-of-line rates at the transition from one set of parameters to the other. To insure an even more gradual change of parameters, an exponential profile instead of a linear one is proposed. The used exponential function g is given in equation 13.3.

$$g(\%O_2) = \frac{\ln(0.05)}{y - x}(\%O_2 - y) \tag{13.3}$$

Based on the results of the linear combination it is determined to set the threshold values at 40% and 90%. This principle is shown on Figure 13.7.

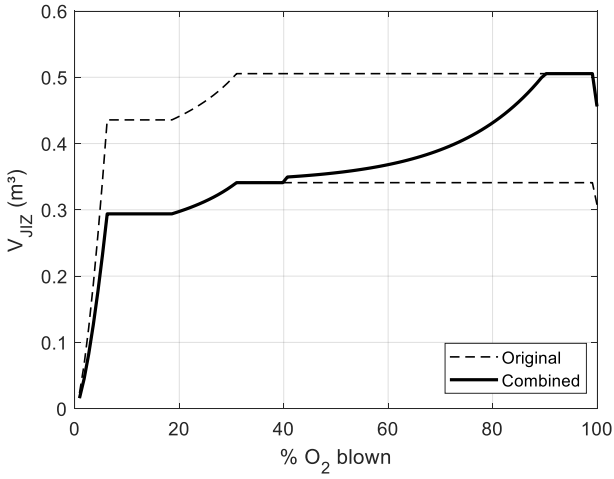

Figure 13.7: Illustration of the gradual change (exponential profile) from Set A to Set B for the Jet Impact zone.

The results of the exponential combination of model parameters are compared to the simulations with the constant set of parameters and the measured decarburisation rate in Figure 13.8.

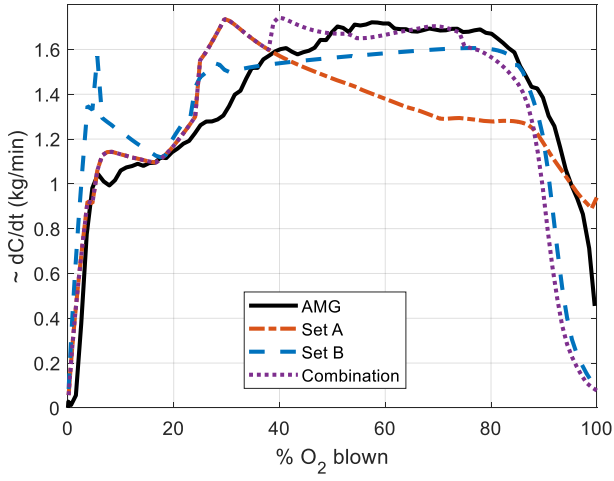

Figure 13.8: Decarburisation profiles for one heat: Measured versus simulated with different model parameters, the combination is the exponential combination with threshold x = 40% and y = 90% O_2.

In the combined simulation, shown in Figure 13.8, an increase in decarburisation rate is observed due to the increase in parameters and hence, the increase in amount of material in de the reaction zones. Next, a nearly constant decarburisation rate is

observed, which starts to decrease towards the end of the process yet, earlier than the original simulation with Set B.

A similar comparison for the evolution of the FeO_n content of the slag is shown in Figure 13.9. A gradual decrease in FeO_n content is observed for the interval between the start of the combination of parameters sets and about 75% O_2 blown. After this point, the FeO_n content of the slag is identical for the combined simulation and the original simulation with a constant use of parameter Set B. This point also corresponds to the first decrease in decarburisation rate, as shown in Figure 13.8. The same explanation as earlier for the link between these observations is applicable. The major difference is that for the current simulation the depletion of the FeO_n from the liquid slag phase is slower due a more gradual increase of the slag limit, which determines the amount slag material in the reaction. At 90% O_2 blow, the iron content of the combined simulation increases slightly faster than for the simulation with Set B.

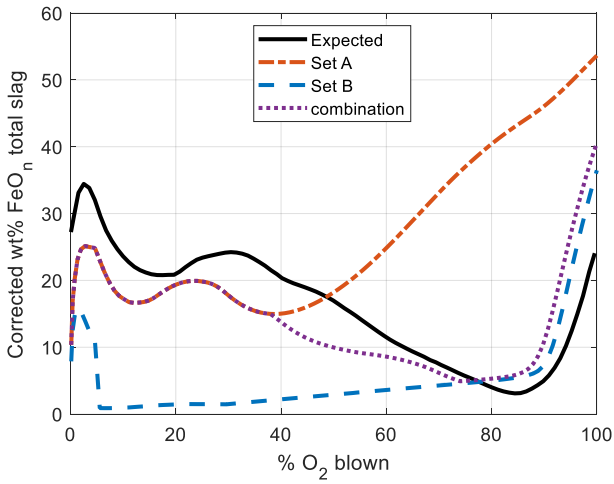

Figure 13.9: The iron content of the total slag for one heat: expected versus simulated with different model parameters. The combination is exponential with threshold x = 40% and y = 90% O_2.

13.1.4 Comparing different combinations

The behaviour of the simulation with the linear and exponential method to combine parameter sets are compared in Figure 13.10. Both for decarburisation rate and FeO_n evolution the simulation with the exponential results gives results closer to the industrially measured or expected values. Furthermore, in Figure 13.6 the general error and deviation between the decarburisation curves are quantitatively compared (round

blue points are for the linear combinations and square orange points are for the exponential combination). The combination of parameter sets with the exponential profile, gives a significant better match between simulated and measured decarburisation profiles. For the general error, thus also considering final process properties, similar results are observed between the two types of combinations. Due to a better match with the decarburisation profile, a more gradual trend in FeO_n consumption and hence the evolution of this property closer to the expected values and similar general error between the exponential and linear combination, it is decided the exponential combination is the best option from the ones considered. For the small set of heats considered, the obtained results are very promising. In the next section, the possibility to use the exponentially combined parameter set is further investigated.

However, a critical note needs to be added to this method. Just as with the fitting of model parameters, this method allows to obtain an elegant solution for the TD BOF model simulation. Yet, this does not mean that the model is able to describe the process correctly from a fundamental viewpoint. The introduction of model parameters, compensates for the errors, yet it is not clear what their origin is and whether the dynamics of the process are described accurately. However, it gives an interesting tool for industrially oriented research allowing to describe the effect of variation of the input material streams.

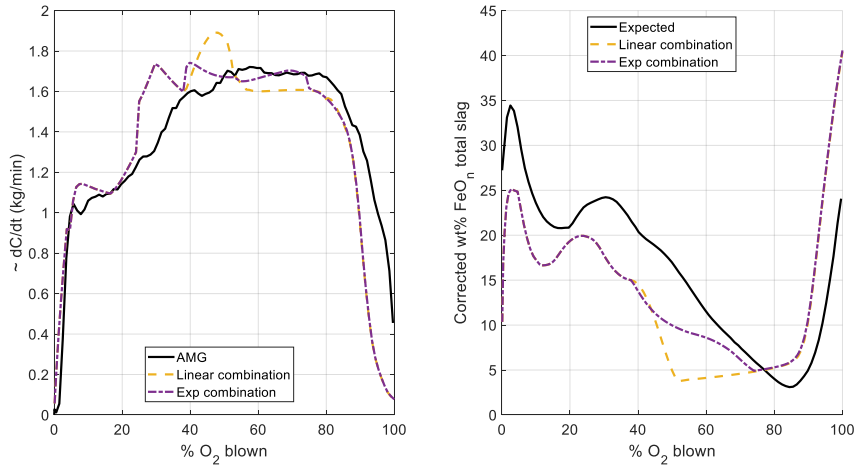

Figure 13.10: Comparison of the linear and exponential combination of parameter sets. (left) the simulated decarburisation rates and the industrially measured rate during the

process for one heat. For confidentiality, the decarburisation rate is normalised. (right) The evolution of the iron oxide content[15] of the slag during the process.

13.2 Validation results

For thorough validation of the combined parameter set, the same validation database as in the previous chapters, is used. Thus, the industrial results shown from here on forward are industrially simulated results and not measured ones as in the previous sections of this chapter. The goal of the validation, is to verify whether accurate results both for evolutions during the process, as well as final conditions are simulated with the current TD BOF model.

Firstly, the end of blow properties are considered. As can be seen in Figure 13.11, the steel mass is underestimated with the current TD BOF mode simulation. However, just as for the previous results of the TD BOF model, there is a good correlation between the industrially calculated steel mass and the thermodynamically (TD) calculated one. The total slag mass is overestimated with the TD BOF simulation, which is also shown on Figure 13.11, although again there is a good correlation between the industrial and TD simulation.

[15] Corrected wt% FeO_n : To compare the FeO_n content of the TD BOF model simulations to the industrial profiles, the calculated slag compositions are corrected to compensate for the assumptions on the flux addition.

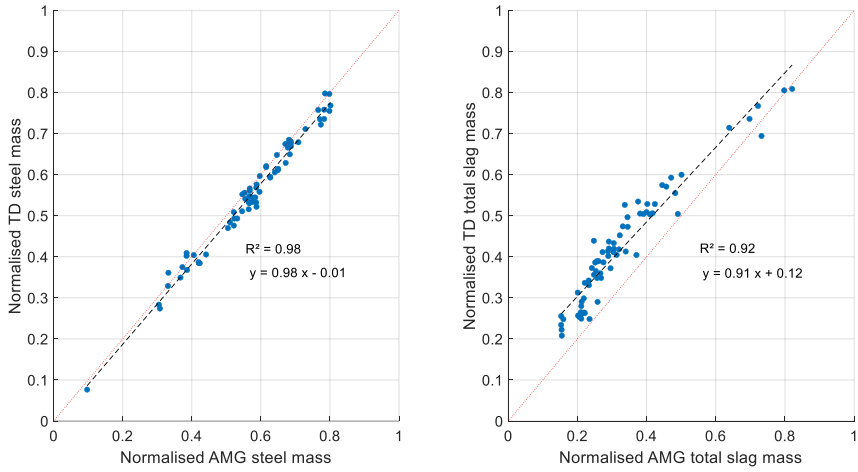

Figure 13.11: (left) Comparison of the simulated steel mass with the combined parameterset and the industrial mass. (right) Comparison of the simulated slag mass with the combined parameter set and the industrial slag mass.

There is a larger deviation between the calculated final masses for the phases compared to the simulation with Set B (see previous chapters, Figure 11.12). This difference in steel and slag mass could already be expected from the decarburisation rates and FeO_n evolution profiles, shown earlier in this chapter. On Figure 13.8 and Figure 13.9, the decarburisation rate, at the end of the process, decreases earlier for the TD BOF simulation with the combined set of parameters compared to the one with parameter Set B. Correspondingly, the oxygen content of the steel phase will be higher and also more iron will oxidise resulting in an earlier increase in FeO_n content of the slag. Finally, for the combined TD BOF simulation more iron will be present in the slag, increasing its mass compared to the calculation with Set B, and less iron will be in the steel phase, decreasing its mass compared to the calculation with Set B. In Figure 13.12, the difference in amount of iron in the slag between the two different TD BOF simulations are shown to support this reasoning.

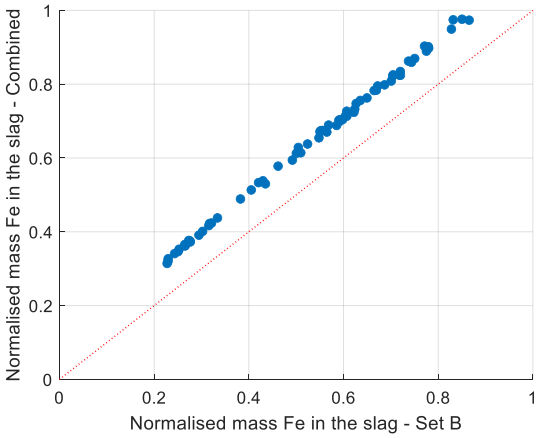

Figure 13.12: Difference in the total amount of iron in the slag between the TD BOF simulation with Set B and the combined parameter set.

The steel temperature as calculated with the TD BOF model is an underestimation compared to the industrially calculated steel temperature, as shown in Figure 13.13. This was also the case for the earlier simulations with the TD BOF model. Although, with the current combined parameter set the temperatures are predicted 7°C lower than with parameter Set B. On the other hand, for 48% of the heats, the slag temperature is calculated to be higher than the steel temperature of the heat. For the TD BOF simulation with Set B this is only for 27% the case. Yet, it is important to keep in mind that even though the slag temperature is higher than the steel temperature they will both be an underestimation of reality. The current TD BOF simulated temperature shows the same correlation with the industrial data as the previous simulations with Set B.

Next, the steel composition is considered in Figure 13.14. The thermodynamically calculated carbon content is lower than the industrial carbon content for the largest part of the heats. There is a group of heats for which the thermodynamically calculated carbon contents lies within the industrial expected range. This is identical to the earlier described behaviour of the TD BOF model (see Figure 11.15).

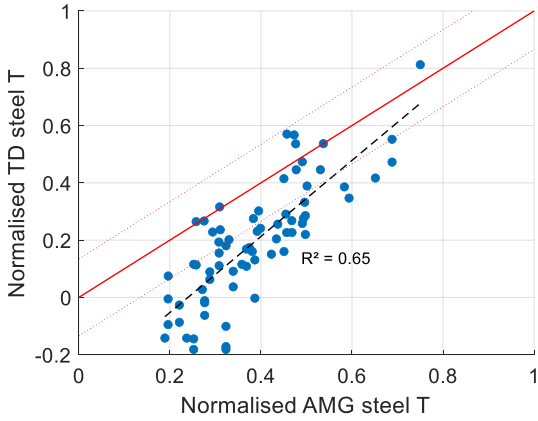

Figure 13.13: The simulated steel temperature with the TD BOF model and the combined parameter set as a function of the industrial steel temperature. The first bisector is indicated with a solid red line, the acceptable deviations, according to the industrial models, are indicated with red dotted lines.

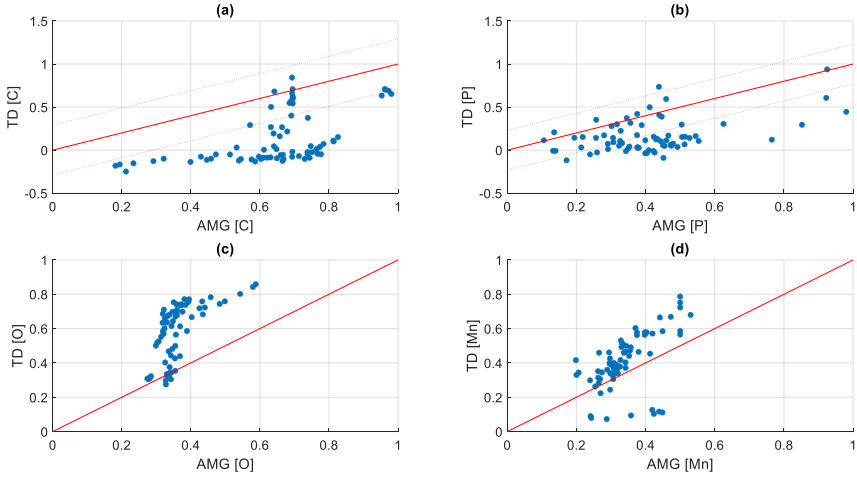

Figure 13.14: The simulated steel compositions with the TD BOF model as a function of the industrial steel composition: (a) carbon content, (b) phosphorus content, (c) oxygen content and (d) the manganese content. Acceptable deviations are indicated with red dotted lines. The contents are normalised due to confidentiality.

Comparing the carbon contents simulated with the TD BOF model with the combined parameter set and Set B, shown in Figure 13.15, the current simulation predicts lower carbon contents than the earlier simulations. Again, this is also visible on the

decarburisation profiles, shown in Figure 13.8, where for the combined parameter set, the decarburisation rates at the end of the process decrease earlier. Indicating the carbon content decreases faster and hence, the final contents will also be lower.

The thermodynamically calculated phosphorus content is either also lower than the industrial phosphorus content or lies within the range of industrial expected values. From the comparison between the simulation with the combined parameter set and Set B in Figure 13.15, it is clear that with the current simulation the phosphorus contents are predicted to be lower than with the previous simulation. This difference can be explained by a stronger dephosphorisation at the end of the process for the current simulation.

Finally, the thermodynamically calculated oxygen content of the steel phase is higher than the industrial oxygen contents. For the manganese contents, the current simulation gives better results than the simulation with the constant parameters of Set B: for more heats an acceptable manganese content is calculated. Still, for heats with a normalised industrial manganese content of 0.3 or higher, the thermodynamically calculated contents strongly deviate from the industrial ones. For some heats absolute thermodynamic values of over 2000 ppm are still predicted. The TD BOF model is not able to predict the manganese contents accurately since, the large deviations for this property of some heats cannot be explained.

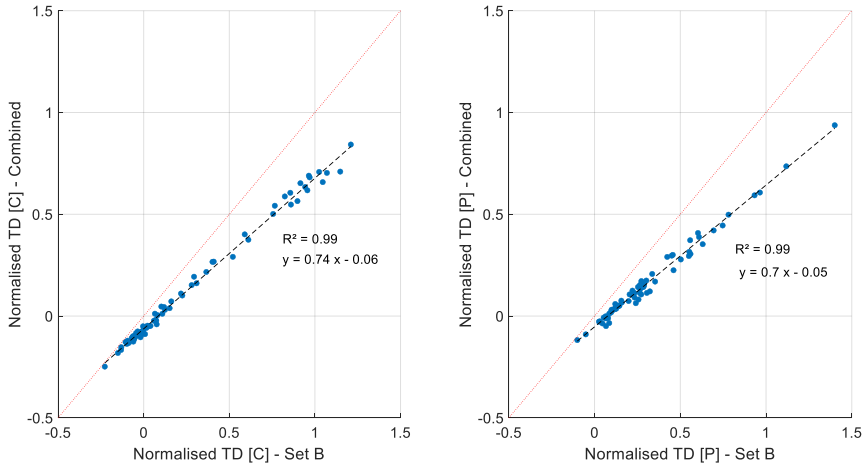

Figure 13.15: Comparing the thermodynamically calculated carbon and phosphorus content of the steel phase with the TD BOF model with Set B and the combined parameter set: (left) the carbon content and (right) the phosphorus content.

The evolutions of these impurities are shown in Figure 13.16. The same procedure as explained in Chapter 11, is used to determine the averages and the standard deviations for these impurities for the dataset of heats. Just as in Chapter 11, the validation of the compositions during the process are qualitatively based.

For the carbon content the evolution is as expected and unlike the earlier simulations with Set A which were suited for description of the evolution until 40% oxygen blown (see Figure 11.20), they are also accurate for the final stages of the process. For the silicon content the profile remains unchanged, because all the silicon is removed before 40% O_2 blown in the process. The phosphorus content shows the initial decrease, followed by the phosphorus pick up. For the manganese content, the profile is identical to the earlier simulations. Yet, for manganese a similar profile as for phosphorus is expected. The TD BOF model is thus able to describe the carbon, silicon and phosphorus behaviour during the process but not the behaviour of manganese.

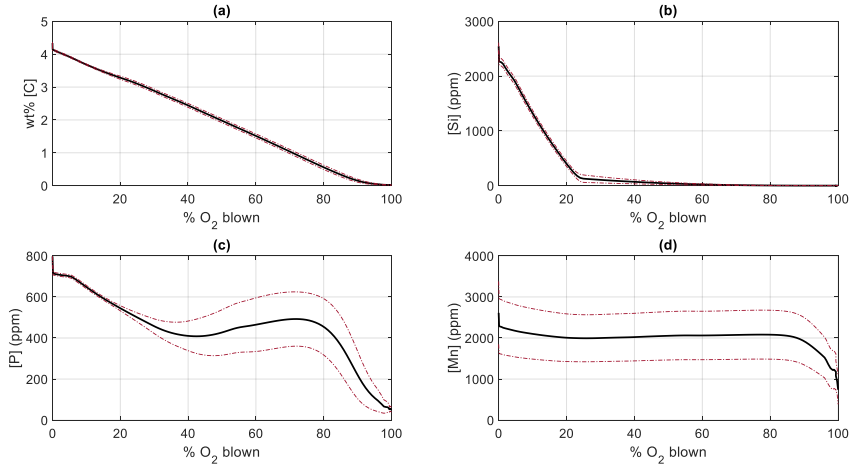

Figure 13.16: Average steel content evolution for simulated heats: (a) the carbon content, (b) the silicon content, (c) phosphorus content and (d) manganese content. The red dotted lines are the standard deviations. The average is calculated for the validation dataset with the 'grpstats' function of Matlab, grouping the data per calculation step.

The average iron content of the slag, shown in Figure 13.17, shows a nice description of the expected behaviour for this component. The decrease of iron content is gradually and only at the end of the process the iron content increases again. The evolution of the three major slag components, also shown in Figure 13.17, is as expected.

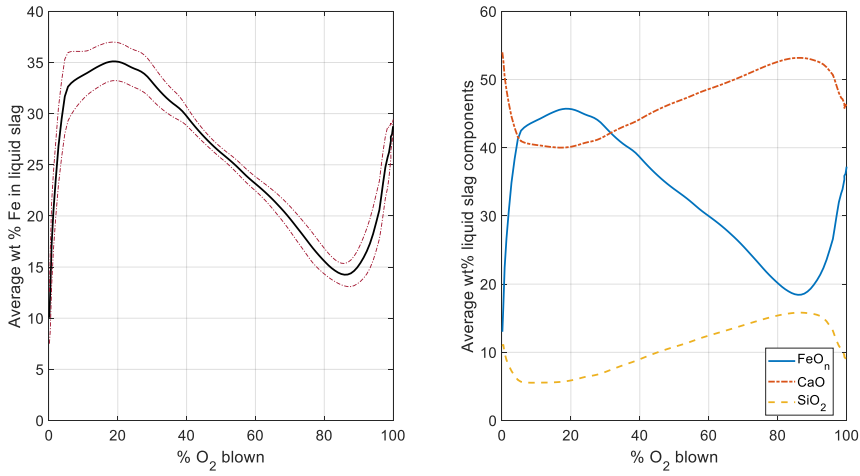

Figure 13.17: (left) The average evolution of the iron content of the liquid slag. The red dotted lines are the standard deviations. (right) The average ternary liquid slag composition during the process. The average is calculated for the validation dataset with the 'grpstats' function of Matlab, grouping the data per calculation step.

As a last step in the validation, the decarburisation profiles are shown in Figure 13.18 (left). The calculated profiles are as industrially expected. The industrially observed trend that for a higher silicon content of the hot metal, the onset for the decarburisation rate increase (around 20% O_2 blown) is situated at a later point during the blow, is also observed on Figure 13.18 (right).

The results discussed in this validation section show the potential of the TD BOF model with a set of combined parameters that are not constant during the complete process. Currently, the time dependency is introduced via a combination of constant parameters with a specific combination profile. However, more advanced methods could be used to determine a unique parameter set as function of process time. It could be an idea to fit the parameter set as function of the lance height since it has been discussed in earlier chapters that the lance height is mentioned to be a crucial factor in many process dynamics according to literature. Or more advanced fitting methods could be used, allowing to fit a variable parameter over time. Nevertheless, care should be taken when further fitting these parameters. The result is a model with thermodynamic fundamentals that is interesting for industrially oriented research yet, the model cannot be used to gain fundamental insights in the process. The fitting allows for elegant solutions which look good and correct but the mechanisms are not necessarily correct. The stronger the fitted contribution to the model, the less the model can be used outside

well known working area's (to which parameters are of course fitted). For fundamental insights, a thorough investigation is needed on why exactly the theoretical reaction volumes deviate from reality. For this, more fundamental research on the BOF vessel would be necessary.

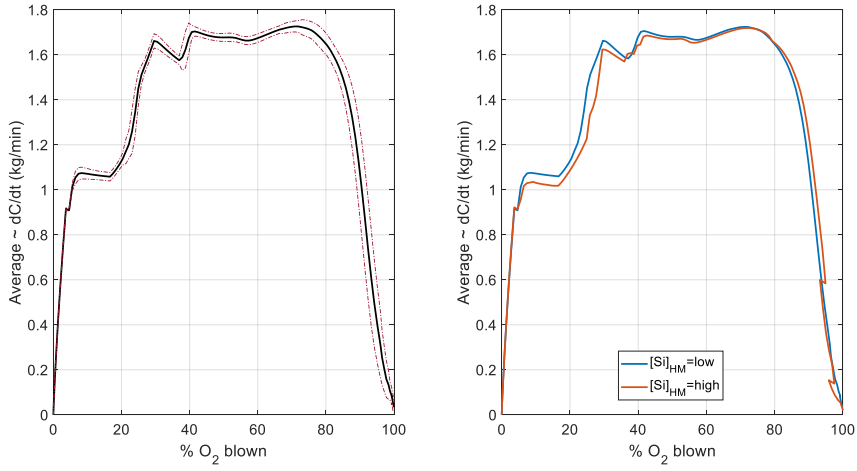

Figure 13.18: (left) Average decarburisation profile for the simulated heats. The red lines are the standar deviations. (right) The effect of the Si content of the hot metal on the average decarburisation profile. The average is calculated for the validation dataset with the 'grpstats' function of Matlab, grouping the data per calculation step.

13.3 Conclusion

Previously, two different sets of parameters for the TD BOF model were put forward: one for an accurate description of the onset and first stages of the process and one for an accurate description of the final conditions of the process. In this chapter it is shown that a combination of the parameters can be used to get an accurate description of the complete process: both evolution and final conditions. From the investigated combinations, the exponential combination of the parameter sets gives the best results because the decrease of FeO_n content in the slag is more gradual compared to other combinations, due to the more gradual change of one parameter set to the other. Validation of these simulations shows that both the evolution as well as the final conditions of the process are described just as accurately as with the constant, fitted, parameter sets. However, even though the results of these simulations seem promising it is important to stress that this gives an interesting model for industrial oriented research but, it is not because the results appear to be good that the underlying

mechanisms, kinetics and dynamics of the process are modelled correctly. For more fundamentally oriented research the model cannot be used.

V. Conclusion and future work

Dat heb ik geleerd. Nog ben ik jong
Maar ik ben oud. Al wat ik bezong
Verschrompelt vlug, wat ik bemin
Bestaat, hoewel ik het verzin
En door mijn woorden waadt het einde
Nader, duidelijker dan het begin

Wat ik bemin – Junkieverdriet – Jotie T'Hooft

14 General conclusion and outlook for the future

14.1 Conclusion

Even though there is general agreement on the importance of the slag and its functions in steelmaking, a profound and complete understanding of slags is hitherto lacking. Within the context of the current work three main areas of importance for the slag were defined: refining, refractory interaction and foaming. To examine the role of slag for these three different aspects of the process, a modelling approach was proposed. Within the first chapters of the work, the relevant literature was mentioned and then, the potential of thermodynamically based models was investigated, via isothermal sections of phase diagrams, and promising results were observed. However, it also became clear that for real complex slag systems (containing more than four different types of oxides and covering a range of temperatures during the process) the use of phase diagrams was insufficient to gain the necessary fundamental understanding of the slag in the process. Hence, the use of more complex models was proposed. Two different types of models were constructed.

A model to calculate the slag evolution during the blow for already executed heats. This model was described and results were discussed in part 'III. Foaming' – Chapters 7 and 8. This model is not meant to have a predictive nature and only already executed heats are examined with it.

The foaming behaviour of the slag was investigated via both the industrially measured acoustic signals, used to monitor foaming, and the theoretical concept of a foaming index. The foaming index of a slag was calculated with the slag's liquid viscosity, density and surface tension. These physical properties were determined for the calculated slag composition during the process.

- Within the framework of the current research it was not possible to link the foaming behaviour in the real industrial converter at the ArcelorMittal Ghent steel plant uniquely to the slag composition or the slag's physical properties.
- From the result of the current work it was concluded that the liquid viscosity is the dominant physical slag property to consider for slag foaming indices.
- The role of solids in the slag's foaming behaviour was not investigated in detail in the current work. This is due to the ambiguous role the solids are stated to

have on the slag's foaming behaviour and due to the lack of full understanding of the effect of these solids on the total viscosity of the slag.

A predictive model to calculate the slag evolution during the blow starting from input material streams. This model was described and results were discussed in part 'IV. Thermodynamic BOF model' – Chapters 9, 10, 11, 12 and 13. This model is meant to have a predictive nature and unknown heats, and hence unfamiliar combinations of material input, could be examined with it.

A thermodynamic BOF model (TD BOF model) with integration of the process kinetics via the EERZ principle, was used in this work. Kinetics are integrated via reaction zones and the sizes of these reaction zones are thus crucial for an accurate description of the process. The sizes of these reaction zones were first calculated based on theoretical and empirical relations for the BOF process. However, it was observed that these relations were not suited to describe the process accurately. To solve this, correction factors, called parameters, for the reaction zone sizes were introduced and a fitting of the model results to the industrial observations was used to determine the parameters. It was impossible to define one unique constant set of the parameters for the complete process. To describe the onset of the process accurately, a different set of parameters is required than to describe the final properties at the end of blow. Different reasons for this were discussed.

The potential application of this model was demonstrated with a case study comparing the thermodynamically calculated and industrially observed effect of MgO in the slag. Finally, a future potential extension of the model is investigated to describe the evolution of the full process more accurately.

Generally, the following conclusions can be formulated for the simulations with the TD BOF model:

- The refining of carbon, phosphorus and silicon showed expected behaviours during the process. For the removal of manganese from the steel phase, the TD BOF simulation did not give satisfactory results. The origin of this last observation is not clear.
- For the industrial partner, the calculated steel composition at the end of the process showed a sufficiently good correlation with their observations of the steel composition in the AMG plant. Apart for manganese for which also the

refining profiles during blow were not as expected from literature. The origin of this observation is not clear.

- The calculated temperature at the end of the process was an underestimation of the industrially expected temperature. The temperature of the slag was for part of the heats predicted to be higher than the steel phase. This is as expected. However, for the other heats, this was not the case. The limited heat transfer between different reaction volumes and phases in the current version of the TD BOF model is put forward as possible reason for this. For future work, this deviation in temperature should be assessed.
- The model results showed the expected trends for FeO_n content in the slag evolution during the process.
- The calculated ternary slag composition, at the end of blow, showed a sufficient correlation with the AMG observations of the ternary slag composition. For the final MgO content of the slag the TD BOF simulation also showed two types of heats: those with high and those low MgO content. This corresponds to the AMG observations. For Al_2O_3 more variation on the final calculated content in the slag was thermodynamically predicted than industrially expected.

Both models allow to calculate the slag evolution during the process. At the start of the PhD project, information on these compositions was lacking at the ArcelorMittal Ghent steel shop. Hence, this is an important contribution of the current work. This allows to consider the slag composition during the process instead of only considering the end of blow slag composition.

14.2 Conclusions with respect to the research questions

In the first chapter of this work, the general introduction, the research objectives and specific research questions were defined. In this section, the conclusions with respect to these research questions and general objective are summarised.

What is the effect of slag composition on refining?

The analysis of the calculated isothermal sections of the pseudo-ternary phase diagrams indicated that MgO has a negative influence on the stability of the calcium silicate phase, which is often mentioned in literature to be of crucial importance for optimal dephosphorisation. This observation, was also discussed in the case study on the effect of MgO with the TD BOF model. Furthermore, the thorough literature review on different

physiochemical models to simulate the BOF process, gave both the industrial and the academic partner of the project insight in modelling possibilities for future research.

What is the effect of slag composition on the interaction with the refractory material?

In this work, the chemical refractory wear is linked with the MgO saturation of the slag. The calculated isothermal sections of the pseudo-ternary phase diagrams gave a clear explanation, for the industrial partner, regarding the existence of a threshold value for MgO additions and its protective effect with respect to refractory wear.

Is it possible to characterise industrial foaming via the slag compositions?

A literature review on calculation of physical slag properties resulted in the implementation of a model to calculate the surface tension and the density of the slag. For the slag's viscosity, the viscosity model as described in literature was implemented to calculate the viscosity of BOF slags.

A model to calculate the slag evolution during the process, for historical heats was developed. The results of this model in combination with the implemented models to calculate the slag's physical properties was used to calculate the foaming indices for relevant slag compositions. Based on these calculations, and the study of the possibility to use the foaming index to identify industrial foaming, the slag's liquid viscosity was identified as the most important parameter. In the context of this work, it was not possible to link the industrial foaming to the theoretical foaming index. Solids were not integrated in the analysis due to their ambiguous role on foaming and the limitations of the conventional Einstein-Roscoe equations to calculate the total viscosity.

In summary, the general goal to gain scientific insights in the role of the slag in the BOF process at the steel plant of the industrial partner, has been met. Both literature review and modelling results contributed to the knowledge of the industrial partner on the role of slag in the process. A large part of the project was devoted to model implementation of two different models to make it possible to estimate the slag composition during the process. This information was lacking before the start of this project. Further calculations and development of the TD BOF model should increase the insights with respect to the research questions. This is further discussed in the next section on future work.

14.3 Outlook for future work

The current version of the TD BOF model shows promising results for industrial research yet, there is definitely room for improvement. An onset is given in chapter 13. More complex methods to allow time dependent parameters for the model could be investigated. Nevertheless, as a first step the discrepancies between the model results and industrial observations (e.g. manganese content and temperature) should be assessed. Additionally, the validation has been performed with a limited set of simulated heats. For industrial research, some more validation cases with real produced heats would be interesting. For fundamental research it would be more interesting to investigate the exact origin of the deviations between the calculated reaction volumes and the observed reality.

The possibility to link the concept of the TD BOF model to CFD calculations could be an interesting future opportunity. Expanding the number of reaction volumes and also integrating bottom stirring and post combustion is another point for future work. The dissolution kinetics for fluxes and scrap melting behaviour are already thoroughly described in literature. For future improvements of the TD BOF model these phenomena should be integrated more accurately instead of assuming this happens thermodynamically as in the current version of the model.

Furthermore, also the time dependency of different parameters such as both the steel's and slag's density and the slag's viscosity should be integrated in future versions of the model. The current implemented heat balance in the TD BOF model should be re-evaluated. However, this is a complex topic for which more fundamental research on heat transport for the BOF vessel is needed.

In general more reliable measurements of the evolution of both the slag composition and the steel composition during the process are required for validation purposes. It is striking that most state-of-the-art physiochemical BOF models rely on the same industrial data for validation. Both measurements from pilot scale set-up (such as the Imphos project) as well as measurements from industrial vessels would be interesting. Although for the latter, measurements during the process are understandably difficult due to the harsh process conditions and the economic cost of blow interruptions.

To gain more insight on the role of solids in the slag foaming behaviour there is need for more fundamental research on the effect of solids in the total slag viscosity. Often Einstein-Roscoe equations are mentioned to integrate the effect of solids. Yet,

fundamentally these equations only allow to integrate limited solid fractions. It would be interesting to verify if different amounts or types of solids can be described via the same Einstein-Roscoe parameters or if differentiation is required.

Generally, it seems that to describe the complex BOF process via modelling, more fundamental research and more validation data, are needed to be able to describe all the smaller subaspects of the process more accurately.

Appendices

Appendix A: Additional figures assessement of the foaming index

A. Additional figures for 'Relation foaming index and composition during blow'.

In Figure 8.7 the relation between foaming index and acoustic signal during blow is only shown for group 1 and 3. In Appendix - Figure 1, the relation between those two properties is shown for the other investigated groups (group 2,4 and 5). To enhance readability only five heats were randomly selected to be shown for each group. In Figure 8.9 the relation between foaming index and weighted acoustic signal during blow is only shown for group 1 and 3. In Appendix - Figure 2, the relations between these two properties is shown for the other investigated groups (group 2,4 and 5). To enhance readability only five heats were randomly selected to be shown for each group.

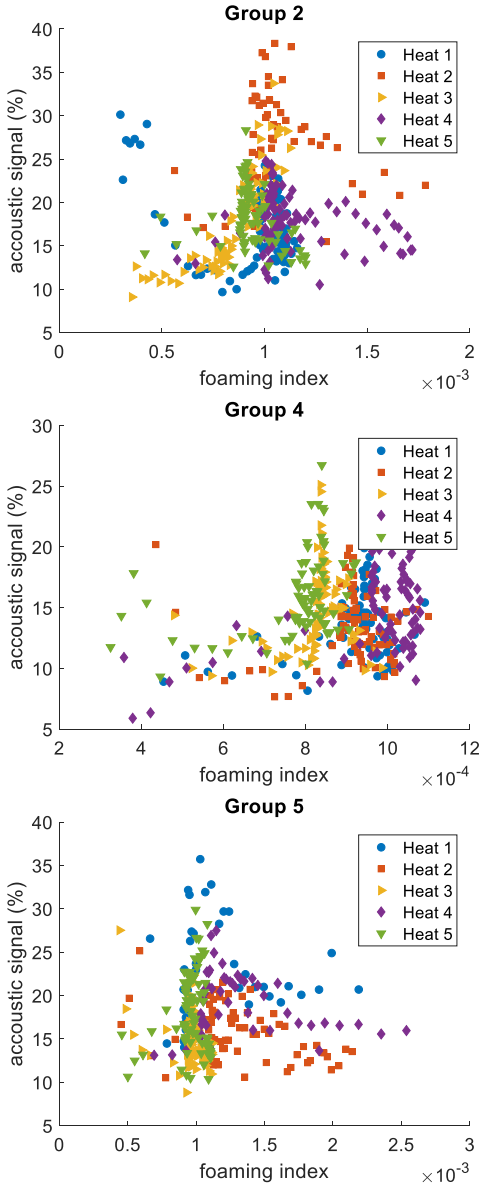

Appendix - Figure 1: foaming index of the liquid slag as function of the acoustic signal for five random selected heats in group 2, 4 and 5.

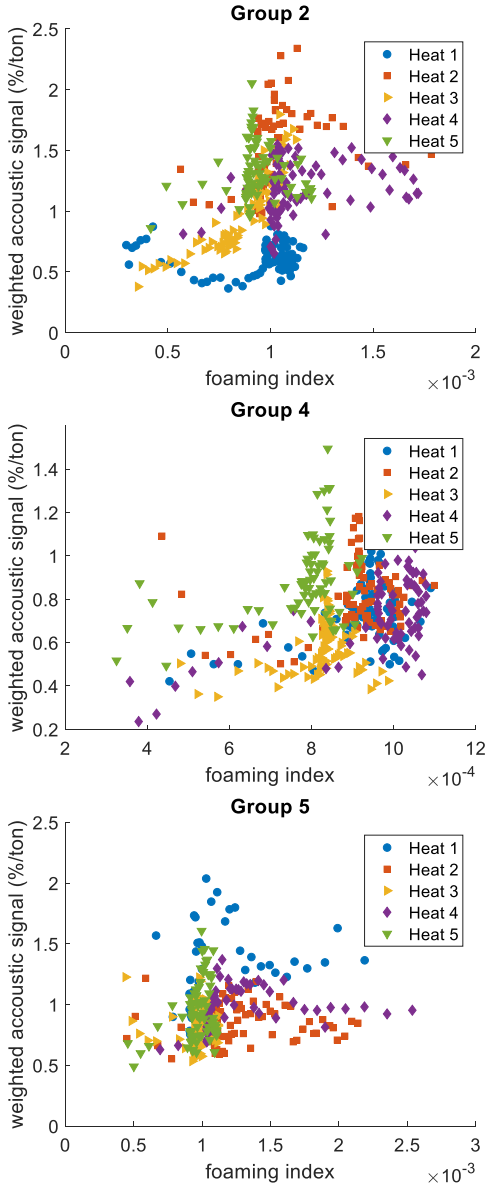

Appendix - Figure 2: foaming index of the liquid slag as function of the weighted acoustic signal for five random selected heats in group 2, 4 and 5.

B. Analysis of the effect of MgO saturation

Some authors distinguish between MgO saturated and CaO based slags in their description of the foaming index. The calculation of the foaming indices is identical for both types, yet the scaling factor changes drastically (999 for MgO saturated slags, compared to 214 for CaO based slags). For group 1 the heats are divided into those which are saturated with MgO at the end of blow and those who are not. The industrial composition at the end of blow is used to distinguish between the two groups. For both groups the relation between foaming index and acoustic signal during blow is shown in separate figures, as can be seen in Appendix - Figure 3, to determine whether there is a clear effect of the MgO saturation on their relation. However, as already stated in the body text of this work and supported here with these two figures, no clear relation can be established between the foaming indices and the acoustic signals.

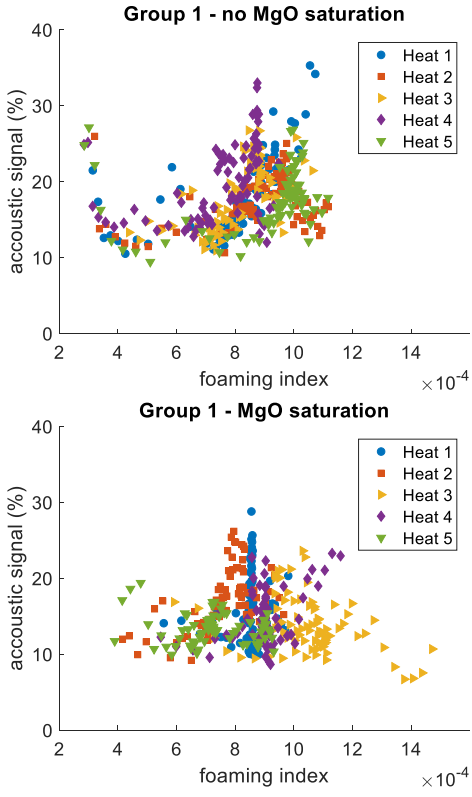

Appendix - Figure 3: foaming index of the liquid slag as function of the acoustic signal for group 1, separation has been made between the heats by MgO saturation.

Appendix B: Input format TD BOF model

General input:

1	2	3	4	5	6	7	8	9	10	11	12
Number	AMG number for the heat	Mass hot metal (ton)	Mass Hot metal 2 (ton)	Mass Scraps (ton)	Mass scrapA (ton)	Mass scrap B (ton)	Mass iron ore (ton)	Mass recuperated briquettes (ton)	Mass briquettes (ton)	Mass Dolo Lime (ton)	Mass Lime (ton)

13	14	15	16	17	18	19	20	21	22	23
Mass O_2 bown (ton)	Mass total O_2 (ton)	Final obtained T (°C)	Pressure (atm)	$T_{hot\ metal}$ (°C)	$[Fe]_{hot\ metal}$	$[C]_{hot\ metal}$	$[Si]_{hot\ metal}$	$[Mn]_{hot\ metal}$	$[P]_{hot\ metal}$	$H_{hot\ metal}$ (J/g)

***Note**: O_2 blown is the amount of oxygen blown via the top lance. O_2 total is the amount of oxygen added via the top lance and the amount added via the fluxes.*

***Note 2**: Calculation from volume to mass under normal conditions (1 atm, 0°C)*

Elemental input:

1	2	3	4	5	6	7	8	9	10	11
Numberr	AMG number	Fe	C	Mn	P	Si	Al	Mg	Ca	O

***Note**: For the fluxes O is only the oxygen present as element thus not oxygen added as O_2.*

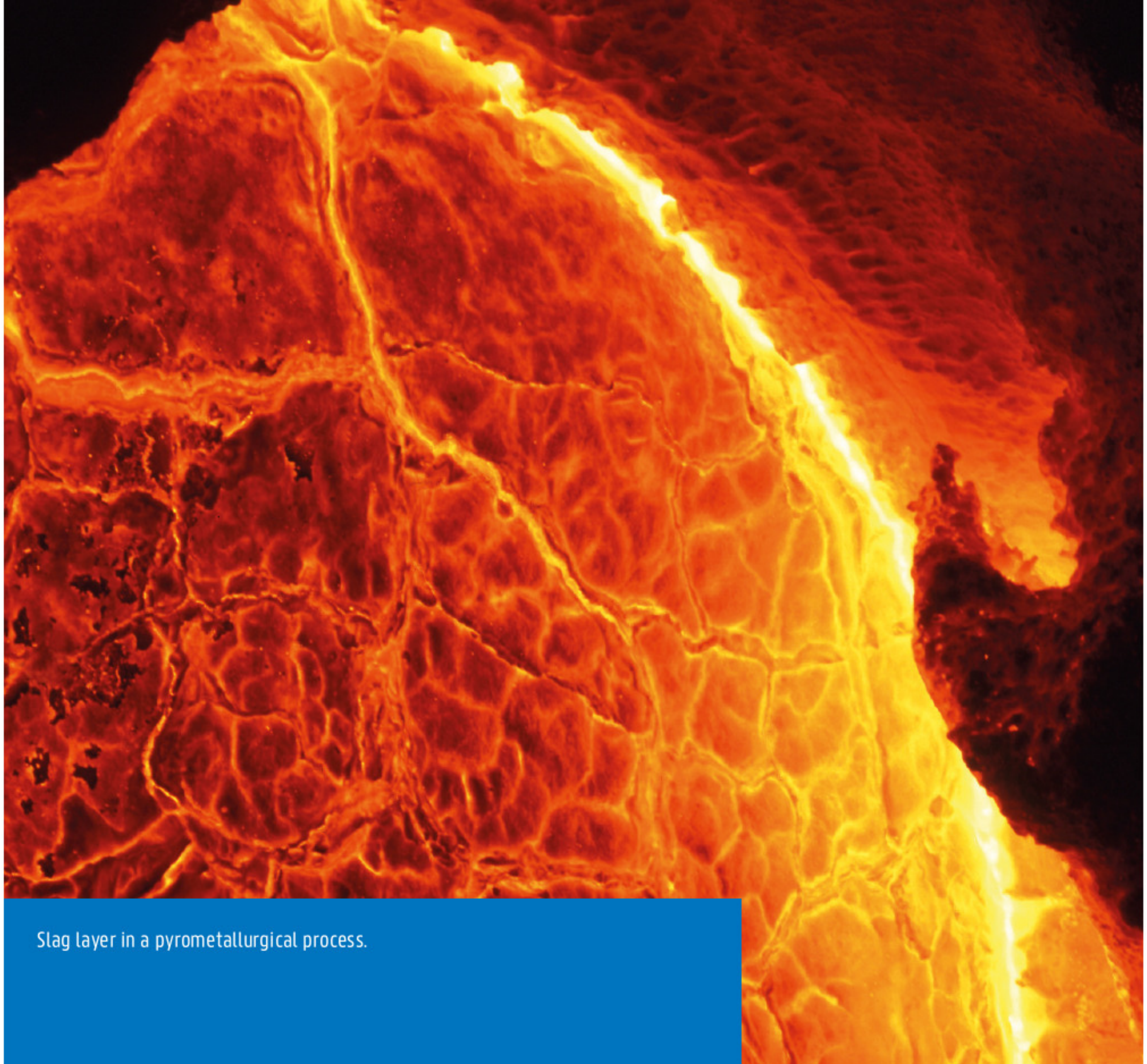

Slag layer in a pyrometallurgical process.